Optimum Topology for Power Handling in Dual Bandpass Filters

Rucha A. Paradkar Smith

School of Electronics and Electrical Engineering
University of Leeds

Submitted in accordance with the requirements for the degree of
Doctor of Philosophy

April 2020

Declaration

The candidate confirms that the work submitted is her own, except where work which has formed part of jointly-authored publications has been included. The contribution of the candidate and the other authors to this work has been explicitly indicated below. The candidate confirms that appropriate credit has been given within the thesis where reference has been made to the work of others.

The work presented in Chapters 3 and 4 is a combined work with Dr. Evaristo Musonda. The dual band synthesis technique was developed by Dr. Musonda. The candidate is responsible for the formulation of the generalised multi-band synthesis technique in the transformed frequency plane and for the design of the two multi-band prototype filters. Dr. Richard Parry provided intellectual insight, useful suggestions and corrections to this work. My supervisor, Professor Ian Hunter provided useful suggestions and editorial comments on the relevant publication.

The candidate is responsible for the idea, implementation of the clustering algorithm and analysis of the results presented in Chapters 5 and 6. Prof. Hunter provided intellectual insight into the analysis and presentation of the results and provided editorial comments on the relevant publication.

<div align="right">

Rucha A. Paradkar Smith

April 2020

</div>

Acknowledgements

First and foremost, I would like to express my utmost gratitute to my supervisor, Professor Ian Hunter, for his invaluable guidance and encouragement throughout my doctoral work. I am also grateful to Dr. Nutapong Somjit for his exceptional role as my co-supervisor and for his role as my supervisor after Professor Hunter's retirement.

I would like to thank the Engineering and Physical Sciences Research Council (EPSRC) for funding my research. I am also thankful for the support and facilities provided at the University of Leeds.

My utmost gratitude goes to Radio Design Ltd., in particular Dr. Richard Parry, Dr. Martin Gostling and Liz Phillips for their technical support and invaluable guidance throughout this research work.

I am extremely grateful to Dr. Evaristo Musonda with whom the collaborated work was carried out. I wish to thank him for sharing his knowledge and expertise in the field, as well as for his guidance. I also wish to thank Dr. Mustafa Bakr for the helpful discussions and support.

I am forever grateful to my parents for their continuous support and encouragement. I also wish to thank my husband Elliott for his support, enouragement and patience throughout the period of my PhD research. My PhD would not have been as memorable and enjoyable without my friends and collegues Elly, Mateusz, Rowan, Nick and Thomas.

Abstract

The design of microwave filters begins by deriving an equivalent filter network that approximates the desired filter response. The technique for the synthesis of single band filters is well-established. However, the new generation of advanced wireless systems demand filters capable of supporting multiple passbands.

A linear optimisation technique for the synthesis of dual bandpass filters is presented in this thesis. It is applicable to the direct synthesis of symmetric and asymmetric transfer functions in the lumped or distributed domain. The technique is extended to allow synthesis of multi-bandpass filters with improved numerical accuracy. It allows arbitrary placement of transmission zeros, providing full control over the stopband rejection levels. It also permits large band-to-band separation due to the frequency-variant nature of the inter-resonator couplings. Synthesis examples are given to demonstrate the technique. Combline realisations of a 7th-degree dual bandpass filter and a 10th-degree triple bandpass filter are designed, fabricated and tested successfully to validate the theory.

The power handling capacity of microwave filters is limited by the internal peak electric fields that can cause multipaction or ionisation breakdown. The peak time-averaged stored energy in the equivalent filter network is related to the internal peak electric fields. A given power transfer function can be realised using multiple filter topologies. Although the total time-averaged stored energy in the filter network is constant, its distribution varies depending upon the chosen topology. This part of the research focuses on establishing guidelines that help predict the optimum power handling topology for a given transfer function.

The k-means clustering algorithm is implemented to discover patterns that aid prediction of the filter topology that demonstrates the lowest peak time-averaged stored energy for a given transfer function. Key characteristics of large data sets comprising of several single band transfer functions and corresponding topologies are determined by analysing the results of the clustering algorithm. The application of this algorithm has further been extended to discover patterns in the stored energy distribution of filter topologies realising dual bandpass transfer functions. In order to validate the obtained patterns, a comparison of the peak electric fields

in the EM simulation of two filter topologies realising the same dual bandpass power transfer function is provided. The two topologies are such that: 1) a topology that constitutes the optimum topology as determined using the established patterns, and 2) a topology typically chosen by a microwave filter engineer for the transfer function at hand. Simulated results were in good agreement with the theory.

Table of contents

Abbreviations

CQ   Cascaded quartet

CT   Cascaded triplet

EM   Electromagnetic

FIR   Frequency-invariant reactance

HPA   High power amplifier

ISB   Inner stopband

ISBR   Inner stopband ratio

ITU   International Telecommunications Union

LNA   Low noise amplifier

LSB   Lower stopband

PA   Power amplifier

PB   Passband

PBR   Passband ratio

RF   Radio frequency

RTR   Relative transmission zero position ratio (for dual bandpass functions)

RTZR   Relative transmission zero position ratio (for single bandpass functions)

S.C   Silhouette coefficients

t.a.s.e   Time-averaged stored energy

t.z   Transmission zero

TEM   Transverse electromagnetic

TSR   Transmission zero separation ratio

USB   Upper stopband

WCSS   Within cluster sum of squares

List of figures

List of tables

Chapter 1

Introduction

1.1 Background

The radio frequency (RF) and microwave region of the electromagnetic spectrum (EM) supports a wide range of applications, such as mobile communications systems, radar systems, remote sensing and radio astronomy, to name a few [6]. As the RF and microwave spectrum is a finite resource, it must be used judiciously. Each application is allocated a fixed frequency range/s that it must adhere to. The national goverments and the regulatory bodies such as the International Telecommunications Union (ITU), determine the national and international spectrum allocations, respectively [7]. Consequently, the available bandwidths for the various standards employed for mobile communications systems are limited by the availability of the spectrum. Subsequently, the capacity of the communications channels is also limited.

The new generation of wireless communications systems aims at providing a better connectivity between more devices than ever before, resulting in a continual increase in the demand for high capacity. As a consequence, higher frequency bands are being allocated for mobile communications systems to satisfy the increasing demands. In order to make efficient use of the microwave spectrum, the filtering requirements imposed in microwave filters are becoming more and more critical. A brief review of the applications of microwave filters in communications systems are presented below.

1.1.1 Microwave filters in communications systems

Microwave filters are an integral part of all communications systems. Their purpose is to transmit signals in the desired frequency range/s and to reject the unwanted signal frequencies [2, 8].

In satellite communication systems, microwave filters are integrated into input/output multiplexers to facilitate channelisation of a composite wideband signal [1, 9]. A simplified block diagram of the payload satellite system is depicted in Fig. 1.1. Dielectric and waveguide filters are utilised for satellite applications as they provide very low loss (high Q-factor) and can be minitiaturised by exploiting multi-mode design techniques.
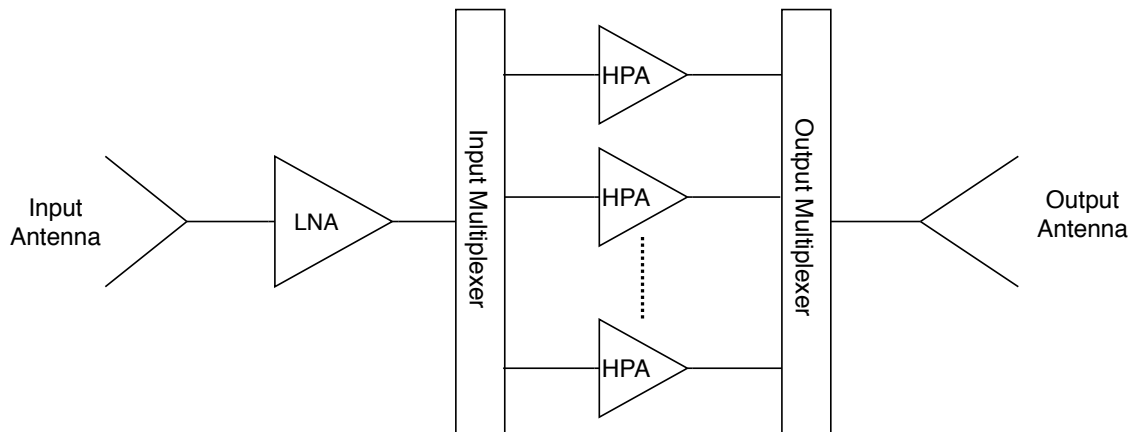
Fig. 1.1 A simplified block diagram of a satellite payload system [1].
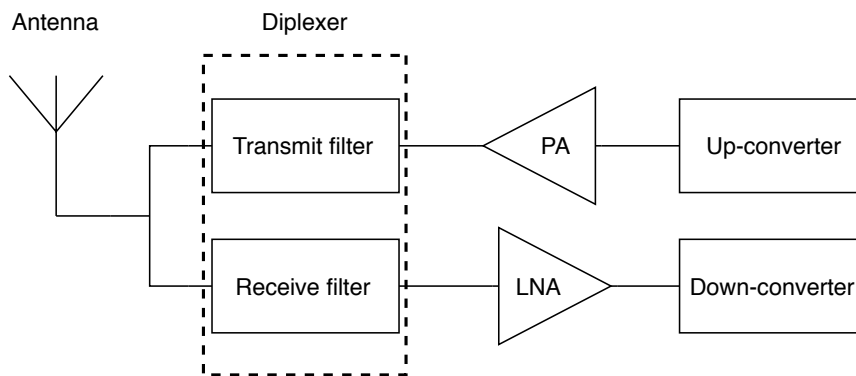
Fig. 1.2 A simplified block diagram of the RF front-end at cellular base station [2].

A simplified block diagram of the RF front-end at a cellular base station is depicted in Fig. 1.2. The transmit and receive filters are connected at a common port and incorporated as diplexers. The up-converters and the transmit power amplifiers produce unwanted signal

frequencies that must be filtered out by the transmit filter. This is achieved by the transmit filter having high attenuation levels in the receive band. Similarly, the receive filter must have high attenuation levels in the transmit band to achieve high isolation from the transmit channel. In addition, both filters must demonstrate low passband insertion loss.

This desired selectivity can be achieved by introducing transmission zeros on one side of the passband. Coaxial filter technology is exploited extensively for cellular base station applications. These filters are easy to implement in the desired configurations, have high power handling capacity and a large spurious window [10]. They have higher losses (lower unloaded Q-factors) as compared to some of the other filter technologies, such as dielectric and waveguides. However, the loss requirements for cellular base station applications are not as stringent as those for satellite communication applications.

1.2   Motivation

As alluded to previously, the new generation of wireless communications systems demand high data rates and improved connectivity. This necessitates development of the RF front-end architecture along with new and improved design techniques for the various RF components, such as microwave filters.

The design of RF and microwave filters begins with the synthesis of a circuit model that approximates the transfer characteristics of the practical filter. The circuit model is then transformed to an equivalent physical structure in an EM modelling software where the higher-order and parasitic effects are taken into consideration. Broadly speakly, research in the field of microwave filters is, therefore, focussed on one of the following aspects: 1) filter synthesis techniques that achieve the desired transmission and reflection characteristics, and 2) implementation of different structures and materials to enhance the filter performance and characteristics.

The development of the multi-band RF front-end architecture has paved way for multi-band filters. Incorporation of multiple passbands in a single filter unit provides reduction in size, cost and power consumption of the RF front-end. Therefore, a new synthesis technique for multi-bandpass filters was developed. The highest degree of filter network that can be synthesised is typically limited by the numerical inaccuracies that arise in the intermediate steps of the synthesis procedure. This presents a problem for multi-band filters where higher degree filter networks are desired. Thus, the multi-band synthesis technique

was re-formulated in the transformed variable plane, which results in improved numerical accuracy.

An important aspect in the practical design of microwave filters is their power handling capacity. The peak internal electric fields in the filter cavity can result in breakdown, rendering the device useless. In order to avoid the risk of a breakdown, the peak internal electric fields can be minimised by choosing a suitable filter topology. The suitable filter topology is such that the peak time-averaged stored energy in the equivalent circuit model is at a minimum. The choice of the optimum filter topology for power handling is strongly dependent on the transfer function to be realised. Hence, guidelines to predict the optimum filter topology for various single and dual band transfer functions were determined using the k-means clustering algorithm.

The work presented in this thesis is, therefore, focussed on two main topics: 1) synthesis of multi-band filters, and 2) improvement of power handling capacity of single and dual band filters by choosing an optimum filter topology.

1.3   Thesis Overview

The thesis is arranged into seven chapters, the first one being an introduction. Chapter 2 provides the background knowledge on the filter synthesis theory and analysis. The characteristics of the various filtering functions are briefly reviewed. The coupling matrix synthesis approach, which has been used extensively throughout this work, is briefly explained. Methods for construction of the transversal coupling matrix for lowpass and bandpass filter networks are described. A brief overview of the physical implementation of microwave filters is provided. The material discussed in this chapter forms the prerequisite for the work presented in the succeeding chapters.

Chapter 3 introduces a novel dual bandpass synthesis technique. The chapter commences with a discussion of the motivation behind the research in the area and a review of the existing techniques in the literature. The presented technique is a linear optimisation technique in which a system of linear independent equations is solved iteratively to optimise the in-band critical frequency points so as to meet a specified convergence criteria. Formulation of the system of linear independent equations and the iterative procedure used for optimisation has been described in detail. The technique is applicable to the direct synthesis of symmetric as well as asymmetric generalised Chebyshev transfer functions in the lumped or distributed domain. Large band-to-band separations are permitted due to the frequency-variant nature of

the inter-resonator couplings. Dual bandpass synthesis examples are presented to demonstrate the technique. A combline prototype has been designed to validate the theory. Finally, the limitations of the technique in terms of numerical accuracies are reviewed.

In Chapter 4 the entire linear optimisation technique introduced in Chapter 3 is re-formulated in the transformed frequency plane, i.e., the z-plane, in order to deal with the numerical inaccuracies. The optimisation techique is also generalised to allow for multi-bandpass synthesis in the z-plane. The formulation maps the passbands and the inner stopbands (a stopband between two passbands) to the imaginary axis and the outer two stopbands to the real axis of the z-plane. The roots of the characteristic polynomials are, therefore, spread across the entirity of the two axes resulting in an improved numerical accuracy. Formation of the bandpass transversal coupling matrix in the z-plane is also reviewed. A synthesis and design example of a triple bandpass filter is presented. This technique is exploited in Chapters 5 and 6 to generate single and dual bandpass transfer functions and corresponding coupling matrices.

The work presented in Chapters 3 and 4 is a combined work with Dr. Evaristo Musonda. The dual band synthesis technique was developed by Dr. Musonda. The candidate is responsible for the formulation of the generalised multi-band synthesis technique in the transformed frequency plane and for the design of the two multi-band prototype filters.

Chapter 5 discusses implementation of the k-means clustering algorithm to obtain patterns that aid in the prediction of optimum network topology for power handling for a given single bandpass transfer function. The k-means clustering algorithm, which is one of the most commonly used unsupervised pattern recognition algorithms, is reviewed. Generation of the input data sets for the clustering algorithm that comprise of data points representing the specification, the filter topology and its peak time-averaged stored energy (used as an indicator of the power handling capacity) is discussed in detail. By application of the clustering algorithm on the data sets, K clusters are obtained. Analysis of these clusters is presented. From the clustering analysis, patterns for prediction of the optimum power handling topology are determined. The established patterns for the data sets are described in a clear and concise manner. In addition, the motivation for research in this area and a literature review are presented at the beginning of this chapter.

In Chapter 6, the k-means algorithm is applied to data sets representing cascaded topologies for various dual bandpass transfer functions. Formation of the input data sets is described. Clustering analysis for the data sets is presented, from which the patterns for predicting the optimum dual bandpass topology for power handling are determined. The practicality of the obtained patterns is validated by comparision of the peak electric fields in the EM simulation

of two filter topologies: 1) the optimum topology predicted using the obtained patterns, and 2) a topology that would typically be implemented by a microwave filter engineer.

The candidate is responsible for the idea, implementation of the clustering algorithm and analysis of the results presented in Chapters 5 and 6.

Finally, a conclusion and suggestions for future work are given in Chapter 7.

Chapter 2

Filter Synthesis and Design

2.1 Overview of filter design and synthesis procedure

The filter synthesis and design procedure aims at achieving a physical realisation of an approximated circuit model that satisfies the desired specifications. The typical filtering specifications include the range of passband and stopband frequencies, maximum insertion loss and minimum return loss levels in the passband and the minimum attenuation levels in the stopband.

Firstly, the transmission and reflection functions, that collectively describe the filter characteristics, are determined. These mathematical expressions, that are in the form of rational functions, must satisfy the desired set of specifications. Lumped or distributed lowpass circuit models employing a suitable topological configuration can be derived from the transmission and reflection functions. The lowpass prototype element values can then be denormalised in terms of frequency and impedances. Depending upon the technology of implementation, an inital physical realisation of the filter is modelled in an EM simulation software. The EM model is optimised with an aim to match the circuit model approximation. Finally, the filter is fabricated and if necessary, fine-tuned until a satisfactory response is achieved. An illustration of the filter synthesis and design procedure is presented in Fig. 2.1.

In the following sections, an extensive description of the theoretical background that forms the prerequisite for the consecutive chapters is presented. Throughout this work, it is assumed that a filter network is composed of passive and lossless elements. The synthesis procedures described are thereby restricted to lossless networks.
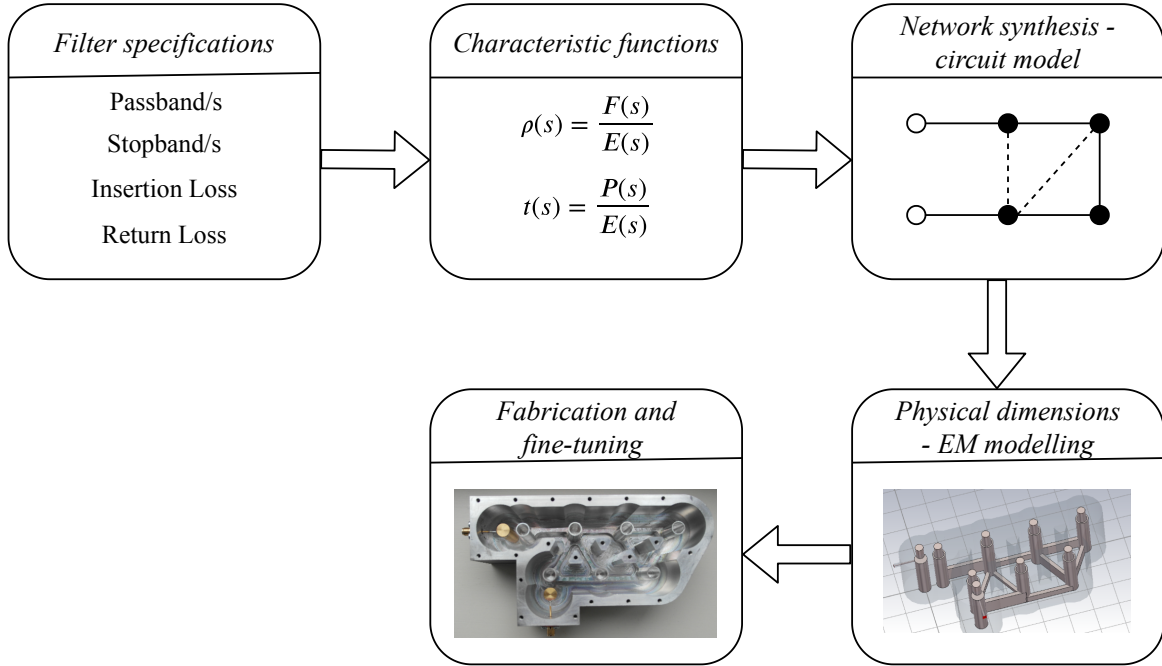
Fig. 2.1 Illustration of the filter synthesis and design procedure [3].

2.2   Filter Transfer Function and Characteristic Polynomials

The filter response of a two-port passive lossless network can be approximated using mathematical expressions that are in the form of rational functions. These rational functions are represented as functions of the complex frequency variable s which is related to the angular frequency variable ω by the following equation:

$$s = \sigma + j\omega \tag{2.1}$$

For lossless networks, the attenuation $\sigma = 0$, giving $s = j\omega$. Suppose a_1 and a_2 are the incident signals and b_1 and b_2 are the emerging signals at the source and load ports (Fig. 2.2), respectively, of a lossless filter network composed of inductive and capacitive elements. The scattering parameters for such a two-port network can be defined using the following equation [7]:

$$\begin{bmatrix} b_1 \\ b_2 \end{bmatrix} = \begin{bmatrix} S_{11} & S_{12} \\ S_{21} & S_{22} \end{bmatrix} \begin{bmatrix} a_1 \\ a_2 \end{bmatrix} \tag{2.2}$$

The power incident at a port can either be transmitted to the other port (transmission coefficients) or be reflected back (reflection coefficients). S_{21}, S_{12} represent the forward
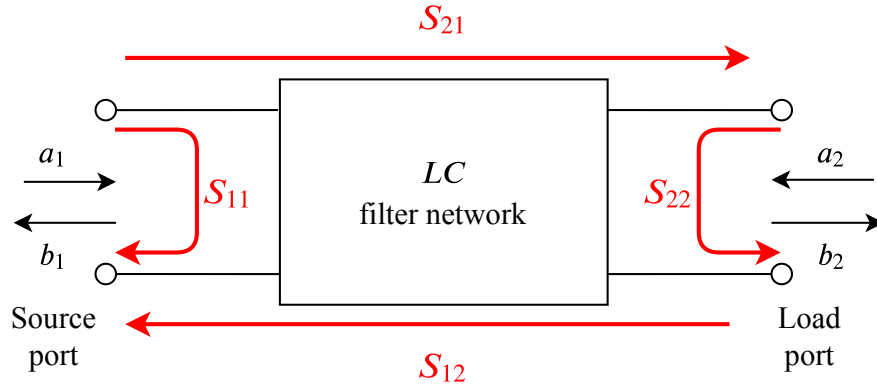
Fig. 2.2 Scattering parameters for a two-port network.

and reverse transmission coefficients, whereas S_{11} and S_{22} represent the input and output reflection coefficients. As the filter network is reciprocal,

$$S_{21}(s) = S_{12}(s) \tag{2.3}$$

Note that the S-parameters can be expressed as functions of the complex frequency variable. As the network is passive, lossless and reciprocal, it must obey the two conservation of energy equations and an orthogonality condition.

$$S_{11}(s)S_{11}(s)^* + S_{21}(s)S_{21}(s)^* = 1 \tag{2.4a}$$

$$S_{22}(s)S_{22}(s)^* + S_{12}(s)S_{12}(s)^* = 1 \tag{2.4b}$$

$$S_{11}(s)S_{12}(s)^* + S_{21}(s)S_{22}(s)^* = 0 \tag{2.4c}$$

where, the asterisks operator (*) indicates a paraconjugation operation [11]. The parameters S_{11} and S_{21} expressed in decibels represent the return loss (L_R) and the insertion loss (L_A) of the filter network, respectively.

$$L_R = -10\log_{10} \mid S_{11}(s) \mid^2 \text{ (dB)} \tag{2.5a}$$

$$L_A = -10\log_{10} \mid S_{21}(s) \mid^2 \text{ (dB)} \tag{2.5b}$$

2.2.1   Characteristic Polynomials

The amplitude-squared power transfer function can be expressed mathematically as a function of the complex frequency variable [4]:

$$| S_{21}(s) |^2 = \frac{1}{1 + K^2(s)} \tag{2.6}$$

Here, $K(s)$ is the characteristic function of the filter network defined by the ratio of the reflection and transmission polynomials.

$$K(s) = \varepsilon \frac{F(s)}{P(s)} \tag{2.7}$$

where, ε is the ripple factor used to control the passband ripple level. The reflection and transmission polynomials are both monic polynomials, i.e., the coefficient of their highest order term is unity. For lowpass prototypes, the degree of the reflection polynomial $F(s)$ is usually equal to the degree of the filter network, i.e., N. Similarly, the degree of the transmission polynomial $P(s)$ is N_{TZ}, where $N \geq N_{TZ}$ for physical realisability. The roots of $F(s)$ represent the frequency points at which all power incident on the source port is transferred to the load port. As no reflection occurs at these frequency points, they are termed as reflection zeros. The roots of $P(s)$ represent the frequency points of maximum power reflection. These frequency points are called transmission zeros or attenuation poles. Therefore, the zeros of the characteristic function are the reflection zeros and the poles of the characteristic function are the transmission zeros. Typically, the position of these transmission zeros is prescribed so as to achieve a desired rejection level in the stopband. Using the reflection and transmission polynomials along with a third polynomial, the S-parameters can be expressed as rational functions:

$$S_{11}(s) = \frac{F_{11}(s)/\varepsilon_R}{E(s)} \tag{2.8a}$$

$$S_{21}(s) = \frac{P_{21}(s)/\varepsilon_T}{E(s)} \tag{2.8b}$$

$$S_{22}(s) = \frac{F_{22}(s)/\varepsilon_R}{E(s)} \tag{2.8c}$$

where, ε_R and ε_T are normalising constants for reflection and transmission polynomials, respectively and are related to the ripple factor by $\varepsilon = \varepsilon_T/\varepsilon_R$. Note that $S_{21}(s) = S_{12}(s)$ by reciprocity. $E(s)$ is a monic polynomial of degree N. In order to satisfy the stability condition,

the roots of the $E(s)$ must lie in the left-half of the complex frequency plane, implying that it is a Hurwitz polynomial. The transmission and reflection polynomials, together with the Hurwitz polynomial are referred to as the characteristic polynomials.

As a result of the orthogonality condition in equation (2.4c), the polynomial $F_{22}(s)$ must be such that

$$F_{22}(s) = (-1)^N F_{11}(s)^* \tag{2.9}$$

In addition, the transmission polynomial must be multiplied by j if $N - N_{TZ}$ is even. By substituting the mathematical expressions in (2.8) into the conservation of energy equation in (2.4a), the following relationship can be derived:

$$E(s)E(s)^* = \frac{F_{11}(s)F_{11}(s)^*}{\varepsilon_R^2} + \frac{P_{21}(s)P_{21}(s)^*}{\varepsilon_T^2} \tag{2.10}$$

where, $E(s) = (-1)^N E(s)^*$. If $F_{11}(s)$ and $P_{21}(s)$ are known, the Hurwitz polynomial can be computed using the alternating pole method in [7, 12]. In general, if any two characteristic polynomials are known, the third characteristic polynomial can be computed.

The roots of the characteristic polynomials must comply to certain properties in order to enable physical realisability using passive lumped or distributed elements. The roots of the reflection polynomial must lie at dc or occur in conjugate pairs on the imaginary axis of the s-plane. Therefore, the reflection polynomial is a purely odd or purely even polynomial. For lowpass prototype synthesis, the roots of the transmission zero polynomial can be located at infinity, or lie symmetrically on the $j\omega$-axis or the real axis or occur as complex quad on the s-plane. If the synthesis is carried out directly in the bandpass domain (as in all of the following chapters), at least a single transmission zero must be placed at dc. The roots of the Hurwitz polynomials are complex in nature and occur in complex conjugate pairs in the left-half of the complex frequency plane.

The normalising constants in equation (2.10) can be computed using the monic characteristic polynomials in the ω-plane [7]. The expressions in equations (2.11)-(2.12) are evaluated at a frequency point where the return loss (L_R) value is known or specified, for example at the cut-off frequency. In general, for $N < N_{TZ}$,

$$\varepsilon_T = \frac{1}{\sqrt{10^{L_R/10} - 1}} \left| \frac{P(\omega)}{F(\omega)} \right| \Bigg|_{\omega = \omega_c} \tag{2.11a}$$

$$\varepsilon_R = 1 \tag{2.11b}$$

and for fully canonical functions, i.e, $N = N_{TZ}$,

$$\varepsilon_T = \sqrt{1 + \left(\frac{1}{\sqrt{10^{L_R/10} - 1}} \left\| \frac{P(\omega)}{F(\omega)} \right\| \bigg|_{\omega = \omega_c} \right)^2} \qquad (2.12a)$$

$$\varepsilon_R = \frac{\varepsilon_T}{\sqrt{\varepsilon_T^2 - 1}} \qquad (2.12b)$$

Depending upon the nature of the roots of the characteristic function, an approximation can be classified as Butterworth, Chebyshev, generalised Chebyshev, Elliptic, etc. The approximation theory for single bandpass filters has been well covered [13, 14]. The Butterworth approximation is the simplest approximation in which all zeros of the characteristic function are located at dc and all poles are located at infinity. The Chebyshev approximation provides an equiripple response in the passband. The characteristic function of this approximation is typically denoted by the symbol T_N. The numerator polynomial of the Chebyshev characteristic function can be derived using the recursive relationship in [13]. The poles of the Chebyshev characteristic function are located at infinity, and hence this approximation is also known as an all-pole Chebyshev approximation. For generalised Chebyshev approximation, the attenuation poles can be prescribed at finite frequencies, thus, allowing the synthesis of asymmetric filter responses. The equiripple passband behaviour is achieved by generating the reflection polynomial using the recursive technique described in [15]. The generalised Chebyshev approximation allows for high selectivity and group delay equalisation by permitting arbitrary placement of transmission zeros in the complex frequency plane. In addition, it is relatively insensitive to the element value tolerances [16]. Hence, the synthesis techniques described in this thesis are focussed on this approximation.

A filter network is described in terms of its amplitude and phase (or group delay) responses. The phase response of a filter network typically refers to the phase of the transmission coefficient, which can be computed using

$$\phi_{21} = \tan^{-1} \frac{Im\{S_{21}(s)\}}{Re\{S_{21}(s)\}} \qquad (2.13)$$

The group delay of the filter can be described as the delay experienced by the various sinusoidal frequency components of the propagating signal. It can be defined by the following equation:

$$\tau_g = -\frac{d\phi_{21}}{d\omega} \qquad (2.14)$$

A constant group delay can be obtained if ϕ_{21} is a linear function of frequency. A non-linear phase versus frequency response results in signal distortion [17]. Hence, in applications where the passband phase response of the filter network is of importance, complex transmission zeros are introduced to achieve group delay equalisation [18, 19].

2.2.2   Immittance Inverters

Another important concept in the circuit synthesis theory is that of immittance, i.e., impedance and admittance, inverters. These are introduced in coupled resonator circuits to enable realisation using purely series or purely shunt elements. Introduction of an immittance inverter implies an effective phase shift of $\pm 90°$ [4]. An impedance inverter can be defined using its transfer matrix

$$\begin{bmatrix} A & B \\ C & D \end{bmatrix} = \begin{bmatrix} 0 & jK \\ j/K & 0 \end{bmatrix} \tag{2.15}$$

where, K is the characteristic impedance of the inverter. The characteristic admittance of an inverter is denoted by J. Immittance inverters are frequency-invariant networks and hence, are restricted to narrowband approximations. However, the bandpass coupling matrix synthesised in section 2.3.1 employs frequency-variant coupling inverters. The lumped element immittance inverters are depicted in Fig. 2.3. The negative elements are absorbed in the adjacent resonator nodes.

2.2.3   Richard's Transformation

A lumped element network can be converted to its equivalent distributed network using Richard's transformation [20]. For lossless networks, the real distributed variable t is defined by

$$t = \tan \theta \tag{2.16}$$

where, θ is the electrical length expressed in radians. The corresponding complex distributed variable ρ is given by

$$\rho = \tanh \theta = j \tan \theta = jt \tag{2.17}$$

The variable θ is related to the real frequency variable ω by

$$\theta = \frac{\omega l}{v_p} = a\omega = \frac{\theta_0}{\omega_0}\omega \tag{2.18}$$
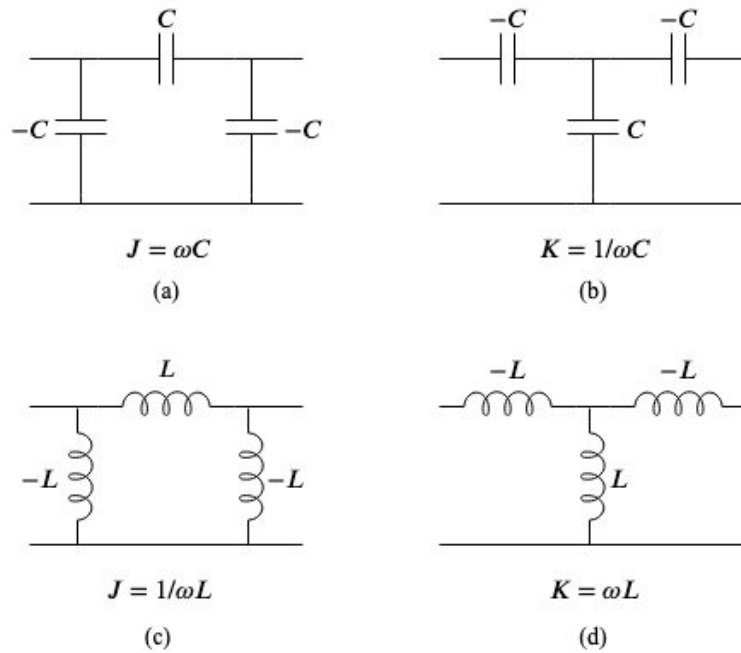
Fig. 2.3 Equivalent network for lumped element immittance inverters [4].

where, θ_0 is the electrical length of the transmission line at a known frequency point ω_0, typically taken as the centre frequency of the passband. The physical length of the commensurate transmission line is denoted by l and v_p is the phase velocity of the propagating wave. Note that the latter expression in equation (2.18) is valid under the assumption that the phase velocity of the propagating wave is independent of frequency [4]. The correspondence between the lumped and distributed elements through Richard's transformation is illustrated in Fig. 2.4. Z_0 (or Y_0) is the characteristic impedance (or admittance) of the short- or open-circuited stubs. Note that the impedances of the lumped and the corresponding commensurate line
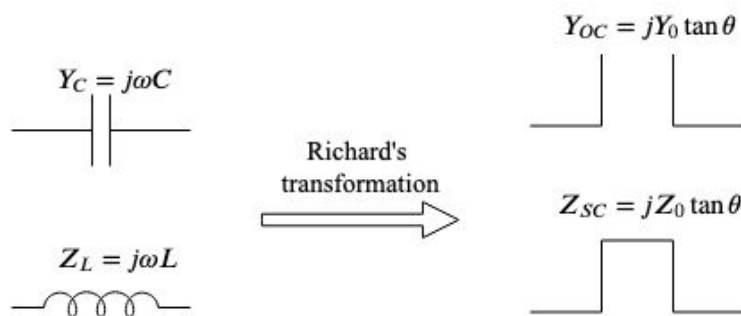
Fig. 2.4 Correspondence between lumped and distributed elements through Richard's transformation.

elements are equal at the centre frequency ω_0 at which the electrical length is set to θ_0. From

the expressions for immittances of the lumped and equivalent distributed elements in Fig. 2.4, it can be observed that: 1) the reactances of the lumped circuit elements are linear functions of frequency, whereas 2) the reactances of the distributed elements are periodic functions of variable θ.

By transforming the lumped variable (i.e., ω or s) to the distributed variable (i.e., t or ρ), the techniques described in this chapter are applicable to the direct synthesis of distributed elements. The critical frequencies and the prescribed transmission zeros can be transformed to the t- (or ρ) plane at the beginning of the synthesis procedure. The synthesis procedure thereafter is the same for directly distributed filters, with subtle differences in the form of the characteristic polynomials. A comprehensive description of direct synthesis in the distributed domain is given in [21, 7]. Examples of direct synthesis in the distributed domain for various relisations have been presented in [22, 23] and in Chapter 3 of this thesis.

2.3 Coupling Matrix Synthesis

The obtained characteristic polynomials can be translated into a prototype circuit using one of the two synthesis methods, viz., the classical cascade synthesis method or the modern direct coupling matrix synthesis method. The traditional cascade synthesis approach involves extraction of elements one-by-one from the input (or output) impedance or admittance function. This method is covered extensively in several textbooks [24–26] and has been reviewed in [27]. Exploiting the $[ABCD]$-matrix for element-by-element extraction [7] can be advantageous when using software packages such as MATLAB. The coupling matrix synthesis method, on the other hand, is a simplified modern approach in which the filter network is modelled in a matrix form. Thus, by performing simple matrix operations such as similarity transformations, the filter network can be easily reconfigured to a different topology. It is also amenable to implementation in MATLAB and other programming packages. Thus, the coupling matrix synthesis method has been used extensively throughout this thesis.

The coupling matrix approach was introduced by Atia and Williams in the 1970's [28] and was further simplified by Cameron [5]. The coupling matrix is a mathematical representation of a multi-coupled resonator network. The synthesis of the $N + 2$ coupling matrix for a lowpass prototype, composed of shunt capacitors or series inductors coupled through immittance inverters, is discussed in section 2.3.1. In order to allow for asymmetric filter responses, hypothetical frequency-invariant reactance (FIR) elements [29] are introduced in the lowpass prototype. The FIR elements offer frequency offsets form the centre frequency of a lowpass prototype, i.e., from $\omega = 0$. These fictitious elements can only be realised

when transformed from lowpass prototype to the corresponding bandpass or bandstop filter network. A method for the generating the coupling matrix for directly synthesised bandpass filters, may it be single or multi-band, is presented in section 2.3.1.

The coupling matrix synthesis approach is based on computing the short-circuited admittance parameters of a canonical filter network in two different ways: 1) from the coefficients of the characteristic polynomials, and 2) from the circuit elements of the canonical filter network [30]. By equating the two admittance matrices, the filter element values are related to the coefficients of the characteristic polynomials.

2.3.1   Direct synthesis of $N + 2$ coupling matrix

The $N + 2$ coupling matrix is synthesised from a filter network in its canonical form, i.e., transversal [31], arrow [5] or folded [19] form. Typically, the transversal topology is used as it is easy to synthesise and can be reconfigured to any of the other canonical forms by performing similarity transformations. The short-circuited two-port parameters for a lossless, passive, reciprocal and symmetrical network can be derived from the characteristic polynomials using the following equations:

$$Y_{11n}(s) = \frac{1}{2}[E(s) - E(s)^*] \tag{2.19a}$$

$$Y_{12n}(s) = -P_{21}(s) \tag{2.19b}$$

$$Y_{21n}(s) = -P_{21}(s) \tag{2.19c}$$

$$Y_{22n}(s) = \frac{1}{2}[E(s) - E(s)^*] \tag{2.19d}$$

$$Y_{den}(s) = \frac{1}{2}[E(s) + E(s)^* + 2F_{11}(s)] \tag{2.19e}$$

The overall two-port short-circuited $[Y]$-parameters matrix can be written as:

$$[Y] = \frac{1}{Y_{den}(s)} \begin{bmatrix} Y_{11n}(s) & Y_{12n}(s) \\ Y_{21n}(s) & Y_{22n}(s) \end{bmatrix} \tag{2.20}$$

where, all parameters share a common denominator polynomial.

Coupling matrix for an ideal lowpass prototype

Using partial fraction expansion, the short-circuited admittance parameters of the form (2.20) can be expressed in terms of their eigenvalues and residues. For a lowpass prototype of

degree N, the $[Y]$-matrix in terms of its eigenvalues and residues takes the form:
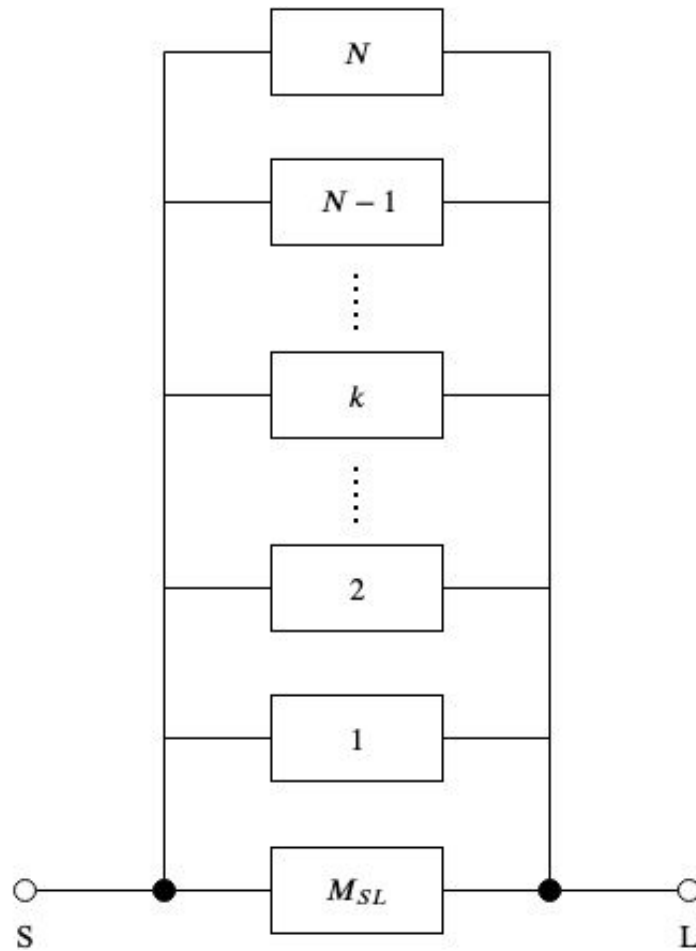
(a) A canonical transversal network composed of N resonators.
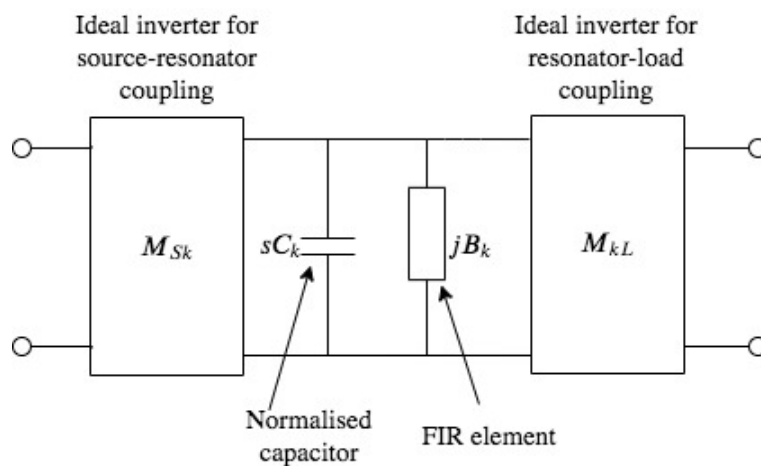
(b) Equivalent circuit of the kth resonator .

Fig. 2.5 Lowpass transversal filter network composed of N resonators [5].

$$[Y] = \frac{1}{Y_{den}(s)} \begin{bmatrix} Y_{11n}(s) & Y_{12n}(s) \\ Y_{21n}(s) & Y_{22n}(s) \end{bmatrix}$$

$$= j \begin{bmatrix} 0 & K_\infty \\ K_\infty & 0 \end{bmatrix} + \sum_{k=1}^{N} \frac{1}{(s - j\lambda_k)} \begin{bmatrix} r_{11k} & r_{12k} \\ r_{21k} & r_{22k} \end{bmatrix} \qquad (2.21)$$

Here, $r_{11k}, r_{12k}, r_{21k}$ and r_{22k} are the kth residues with a corresponding eigenvalue of λ_k. K_∞ is a real constant which is equal to zero for all cases except for where $N = N_{TZ}$. The eigenvalues are purely real and can be obtained by factorising the denominator polynomial $Y_{den}(s)$. The residues of the $[Y]$ matrix are also purely real and can be computed as follows [7, 32]:

$$r_{21k} = \left. \frac{Y_{21n}(s)}{Y'_{den}(s)} \right|_{s=j\lambda_k} \qquad r_{22k} = \left. \frac{Y_{22n}(s)}{Y'_{den}(s)} \right|_{s=j\lambda_k} \qquad k = 1,2,,\cdots,N \qquad (2.22)$$

The transversal array network for a lowpass prototype is illustrated in Fig. 2.5. It is composed of N 1st-degree parallel-connected resonant sections coupled to the source and the load using inverters. The kth resonant section consists of a shunt capacitor, typically normalised to unity, and an FIR element with a susceptance of jB_k. The two-port short-circuited admittance matrix for the transversal network in terms of its circuit elements can be found by summing the $[Y]$-matrices for the N individual resonant sections. The $[Y]$matrix for an individual section can be computed from its $[ABCD]$-matrix, i.e.,

$$[ABCD]_k = \begin{bmatrix} 0 & j/M_{Sk} \\ jM_{Sk} & 0 \end{bmatrix} \begin{bmatrix} 1 & 0 \\ sC_k & 1 \end{bmatrix} \begin{bmatrix} 1 & 0 \\ jB_k & 1 \end{bmatrix} \begin{bmatrix} 0 & j/M_{kL} \\ jM_{kL} & 0 \end{bmatrix}$$

$$= - \begin{bmatrix} \frac{M_{kL}}{M_{Sk}} & \frac{(sC_k+jB_k)}{M_{Sk}M_{kL}} \\ 0 & \frac{M_{Sk}}{M_{kL}} \end{bmatrix} \qquad (2.23)$$

The matrix in (2.23) can be converted to the equivalent $[Y]$-parameters using the standard $[ABCD]$ to $[Y]$ transformations [33].

$$[Y]_k = \frac{1}{(sC_k + jB_k)} \begin{bmatrix} M_{Sk}^2 & M_{Sk}M_{kL} \\ M_{Sk}M_{kL} & M_{kL}^2 \end{bmatrix} \qquad (2.24)$$

For N resonant sections, the overall $[Y]$-matrix is given by:

$$[Y] = j \begin{bmatrix} 0 & M_{SL} \\ M_{SL} & 0 \end{bmatrix} + \sum_{k=1}^{N} \frac{1}{(sC_k + jB_k)} \begin{bmatrix} M_{Sk}^2 & M_{Sk}M_{kL} \\ M_{Sk}M_{kL} & M_{kL}^2 \end{bmatrix} \qquad (2.25)$$

By equating the matrices in (2.21) and (2.25),

$$C_k = 1, \quad B_k = -\lambda_k$$
$$M_{kL} = \sqrt{r_{22k}}, \quad M_{Sk} = r_{21k}/\sqrt{r_{22k}} \tag{2.26}$$

The source-load coupling $M_{SL} = K_\infty$, which is zero for all cases except fully canonical. The input couplings M_{Sk} are entered into the first row and column of the $N+2$ coupling matrix M. Similarly, the output couplings are entered into the last row and column of the $N+2$ coupling matrix. The FIR susceptances represent the frequency offsets from the centre frequency and are entered into the main diagonal. The remaining entries are zero. The constructed $N+2$ coupling matrix is represented in Fig. 2.6. The diagonal elements $M(k,k) = jB_k$ for

	S	1	2	3	$\cdots\cdots$	k	$\cdots\cdots$	$N-1$	N	L
S		M_{S1}	M_{S2}	M_{S3}	$\cdots\cdots$	M_{Sk}	$\cdots\cdots$	$M_{S,N-1}$	M_{SN}	
1	M_{S1}	M_{11}								M_{1L}
2	M_{S2}		M_{22}							M_{2L}
3	M_{S3}			M_{33}						M_{3L}
$\vdots$	$\vdots$				$\ddots$					$\vdots$
k	M_{Sk}					M_{kk}				M_{kL}
$\vdots$	$\vdots$						$\ddots$			$\vdots$
$N-1$	$M_{S,N-1}$							$\ddots$		$M_{N-1,L}$
N	M_{SN}								$M_{N,N}$	M_{NL}
L		M_{1L}	M_{2L}	M_{3L}	$\cdots\cdots$	M_{kL}	$\cdots\cdots$	$M_{N-1,L}$	M_{NL}	

Fig. 2.6 Construction of the $N+2$ transversal coupling matrix.

$k = 2,3,\cdots,N,N+1$. The unity capacitances can be used to form a capacitive coupling matrix, denoted by M_C, where the diagonal elements $M_C(k,k) = 1$ for $k = 2,3,\cdots,N,N+1$. The overall coupling matrix for a lowpass prototype can, therefore, be expressed by:

$$M_{LP} = sM_C + M \tag{2.27}$$

Coupling matrix for a bandpass filter network

The synthesis techniques presented in Chapters 3 and 4 of this thesis are pertinent to direct synthesis in the bandpass domain. This implies that the characteristic polynomials are generated to represent the filter characteristics in the bandpass domain. Hence, construction of the $N+2$ transversal array coupling matrix for a bandpass filter is described in this section. The technique is applicable to single as well as multi-bandpass filters.

The transversal network array for directly synthesised bandpass filters consists of N parallel-connected resonant sections as in Fig. 2.5a. The equivalent network of the resonant sections, however, is composed of a shunt LC resonator (a 2nd-degree resonant network) as in Fig. 2.7. The shunt capacitor is normalised to unity. Note that for a bandpass filter network of degree N, the reflection and Hurwitz polynomials are of degree $2N$. The degree of the transmission polynomial is NTZ, where NTZ may be even or odd depending upon the number of transmission zeros located at finite frequencies and at dc. As alluded to in section 2.2.1, the transmission zeros at finite frequencies always occur in pairs. Those at dc and inifinity need not occur in pairs. The degree of the characteristic function is, therefore, always even for directly synthesised bandpass filters. As in the case of lowpass prototype functions, it is assumed that the number of finite transmission zeros is less than the degree of the filter network. This implies that direct coupling between the source and the load does not exist.
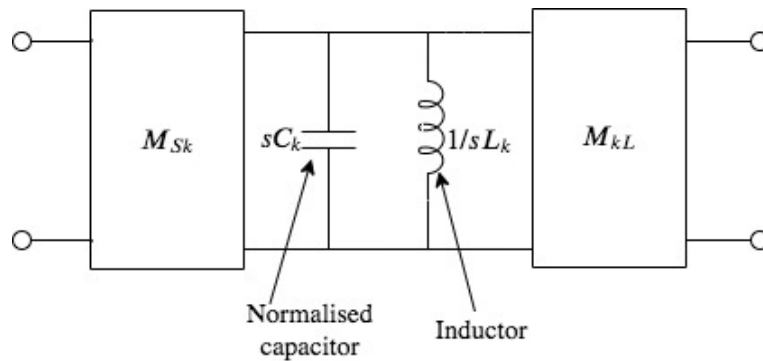
Fig. 2.7 Equivalent network of the kth bandpass resonator.

Equations (2.19b)-(2.19e) were used to calculate the short-circuited admittance parameters of the bandpass filter network. Using partial fraction expansion, this $[Y]$-matrix was re-written

in terms of its eigenvalues and corresponding residues as:

$$[Y] = \frac{1}{Y_{den}(s)} \begin{bmatrix} Y_{11n}(s) & Y_{12n}(s) \\ Y_{21n}(s) & Y_{22n}(s) \end{bmatrix}$$

$$= \sum_{k=1}^{N} \frac{1}{(s^2 - p_k^2)} \begin{bmatrix} 2r_{11k}s & 2r_{12k}s \\ 2r_{21k}s & 2r_{22k}s \end{bmatrix} \qquad (2.28)$$

where, the roots of the denominator polynomial $Y_{den}(s)$ are purely imaginary are occur in conjugate pairs, i.e., $p_k = \pm j\lambda_k$. The eigenvalues λ_k and the residues are purely real. Next, the $[ABCD]$-matrix for the kth section can be computed by cascading the $[ABCD]$ matrices of the individual elements.

$$[ABCD]_k = \begin{bmatrix} 0 & j/M_{Sk} \\ jM_{Sk} & 0 \end{bmatrix} \begin{bmatrix} 1 & 0 \\ Y_k & 1 \end{bmatrix} \begin{bmatrix} 0 & j/M_{kL} \\ jM_{kL} & 0 \end{bmatrix}$$

$$= - \begin{bmatrix} \frac{M_{kL}}{M_{Sk}} & \frac{Y_k}{M_{Sk}M_{kL}} \\ 0 & \frac{M_{Sk}}{M_{kL}} \end{bmatrix} \qquad (2.29)$$

where, Y_k is the admittance of the shunt LC resonator given by

$$Y_k = sC_k + \frac{1}{sL_k} = \frac{s^2C_k + 1/L_k}{s} \qquad (2.30)$$

Using the standard $[ABCD]$ to $[Y]$ transformations, the admittance matrix for the kth section can be obtained.

$$[Y]_k = \frac{s}{(s^2C_k + 1/L_k)} \begin{bmatrix} M_{Sk}^2 & M_{Sk}M_{kL} \\ M_{Sk}M_{kL} & M_{kL}^2 \end{bmatrix} \qquad (2.31)$$

The overall $[Y]$-matrix can be obtained by summing the $[Y]$ matrices of the N individual resonant sections.

$$\therefore [Y] = \sum_{k=1}^{N} \frac{1}{(s^2C_k + 1/L_k)} \begin{bmatrix} M_{Sk}^2 s & M_{Sk}M_{kL}s \\ M_{Sk}M_{kL}s & M_{kL}^2 s \end{bmatrix} \qquad (2.32)$$

Equating the right hand sides of equations (2.28) and (2.32) yields,

$$C_k = 1, \quad 1/L_k = -p_k^2$$

$$M_{kL} = \sqrt{2r_{22k}}, \quad M_{Sk} = 2r_{21k}/\sqrt{2r_{22k}} \qquad (2.33)$$

The $N+2$ transversal array coupling matrix can be reconstructed in the same manner as that for the lowpass coupling matrix. The input couplings M_{Sk} are entered in the first row and column, whereas the output couplings M_{kL} are entered in the last row and column of the coupling matrix M. The shunt inductances form the main diagonal of the coupling matrix. The overall bandpass coupling matrix can be written as the sum of three individual $N+2$ matrices, i.e.,

$$\mathrm{M_{BP}} = \mathrm{M_T} + s\mathrm{M_C} + \frac{1}{s}\mathrm{M_L} = s\mathrm{M_C} + \mathrm{M} \tag{2.34}$$

Here, the input couplings are entered in the first row and column and the output couplings are entered in the last row and column of the $\mathrm{M_T}$ matrix.

$$\mathrm{M_T} = \begin{bmatrix}
0 & M_{S1} & M_{S2} & \cdots & M_{Sk} & \cdots & M_{S,N-1} & M_{SN} & 0 \\
M_{S1} & 0 & 0 & \cdots & 0 & \cdots & 0 & 0 & M_{1L} \\
M_{S2} & 0 & 0 & \cdots & 0 & \cdots & 0 & 0 & M_{2L} \\
\vdots & \vdots & \vdots & \ddots & \vdots & \vdots & \vdots & \vdots & \vdots \\
M_{Sk} & 0 & 0 & \cdots & 0 & \cdots & 0 & 0 & M_{kL} \\
\vdots & \vdots & \vdots & \vdots & \vdots & \ddots & \vdots & \vdots & \vdots \\
M_{S,N-1} & 0 & 0 & \cdots & 0 & \cdots & 0 & 0 & M_{N-1,L} \\
M_{SN} & 0 & 0 & \cdots & 0 & \cdots & 0 & 0 & M_{NL} \\
0 & M_{1L} & M_{2L} & \cdots & M_{kL} & \cdots & M_{N-1,L} & M_{NL} & 0
\end{bmatrix} \tag{2.35}$$

The $N+2$ capacitive coupling matrix $\mathrm{M_C}$ is such that $\mathrm{M_C}(i,i) = 1$ for $i = 2, 3, \cdots, N, N+1$. The remaining entries in this matrix are equal to zero.

$$\mathrm{M_C} = \begin{bmatrix}
0 & 0 & 0 & \cdots & 0 & \cdots & 0 & 0 & 0 \\
0 & 1 & 0 & \cdots & 0 & \cdots & 0 & 0 & 0 \\
0 & 0 & 1 & \cdots & 0 & \cdots & 0 & 0 & 0 \\
\vdots & \vdots & \vdots & \ddots & \vdots & \vdots & \vdots & \vdots & \vdots \\
0 & 0 & 0 & \cdots & 1 & \cdots & 0 & 0 & 0 \\
\vdots & \vdots & \vdots & \vdots & \vdots & \ddots & \vdots & \vdots & \vdots \\
0 & 0 & 0 & \cdots & 0 & \cdots & 1 & 0 & 0 \\
0 & 0 & 0 & \cdots & 0 & \cdots & 0 & 1 & 0 \\
0 & 0 & 0 & \cdots & 0 & \cdots & 0 & 0 & 0
\end{bmatrix} \tag{2.36}$$

The inductive coupling matrix M_L is an $N+2$ coupling matrix with the diagonal elements $M_L(i,i) = 1/L_i$ for $i = 2, 3, \cdots, N, N+1$.

$$M_L = \begin{bmatrix} 0 & 0 & 0 & \cdots & 0 & \cdots & 0 & 0 & 0 \\ 0 & 1/L_1 & 0 & \cdots & 0 & \cdots & 0 & 0 & 0 \\ 0 & 0 & 1/L_2 & \cdots & 0 & \cdots & 0 & 0 & 0 \\ \vdots & \vdots & \vdots & \ddots & \vdots & \vdots & \vdots & \vdots & \vdots \\ 0 & 0 & 0 & \cdots & 1/L_k & \cdots & 0 & 0 & 0 \\ \vdots & \vdots & \vdots & \vdots & \vdots & \ddots & \vdots & \vdots & \vdots \\ 0 & 0 & 0 & \cdots & 0 & \cdots & 1/L_{N-1} & 0 & 0 \\ 0 & 0 & 0 & \cdots & 0 & \cdots & 0 & 1/L_N & 0 \\ 0 & 0 & 0 & \cdots & 0 & \cdots & 0 & 0 & 0 \end{bmatrix} \tag{2.37}$$

2.3.2 Reconfiguration of the coupling matrix

The transversal coupling matrix is not suitable for practical implementation. Hence, it has to be reconfigured into a topology more suitable for practical realisation. The transversal coupling matrix is first transformed to one of the other two canonical forms, i.e., arrow or folded, and then transformed to other topologies such as cascaded n-tuplets for implementation. A series of similarity transformations are applied to the transversal coupling matrix to reconfigure it into the folded or arrow topologies. The coupling matrix M is pre- and postmultiplied by a rotation matrix R and its transpose R^T such that a single rotation can be represented by:

$$M_r = R_r \cdot M_{r-1} \cdot R_r^T \tag{2.38}$$

A series of such rotations, i.e., similarity transformations, are performed on the coupling matrix to annihilate the unwanted coupling elements. The transformations are such that the eigenvalues and the eigenvectors of the original coupling matrix are preserved. The capacitive coupling matrix remains unaffected by the rotations and hence, is not included in the main coupling matrix M representation above. The $N+2$ rotation matrix is such that the main diagonal entries $R(i,i) = 1$ for $i = 2, 3, \cdots, N, N+1$. For a pivot $[i, j]$, where $i \neq j$, the elements $R_{i,i} = R_{j,j} = \cos\theta$, $R_{i,j} = -R_{j,i} = -\sin\theta$. The angle θ is calculated analytically using the coupling matrix elements [30]. The remaining non-diagonal entries are equal to zero.

The transversal network can be transformed to the arrow topology from which it can be reconfigured into cascaded n-tuplet topologies [34, 35]. A similar approach as in [34] has been used to calculate the rotation angle for cascaded triplets in bandpass filters in [21]. The

folded, cascaded triplet and cascaded quartet configurations are illustrated in Fig. 2.8 using coupling routing diagrams. A comprehensive description of reconfiguration of the transversal
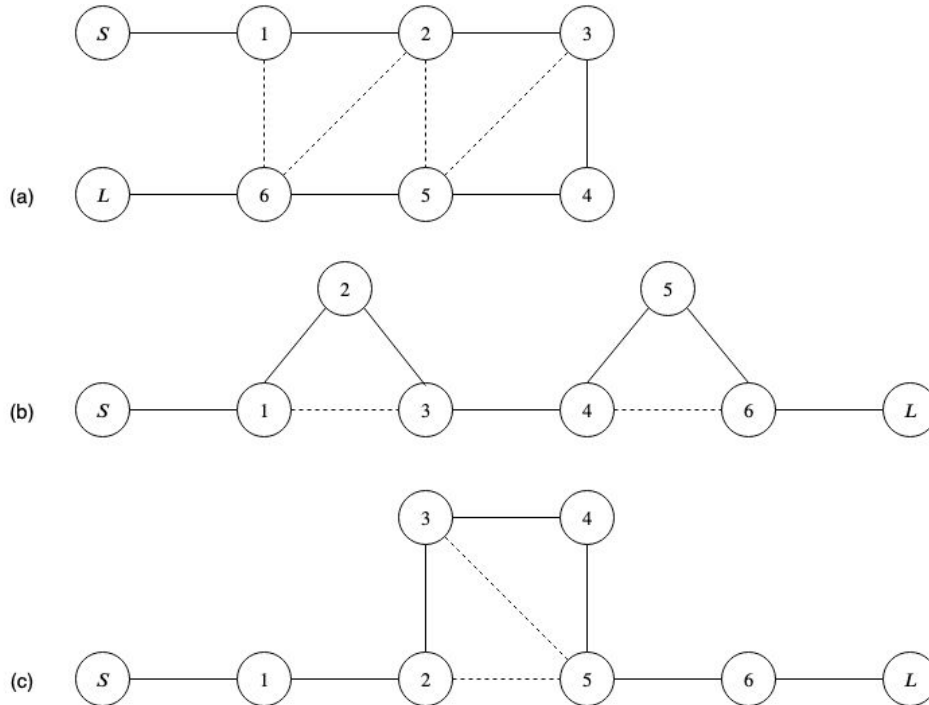
Fig. 2.8 Coupling routing diagrams for (a) Folded topology (b) Cascaded triplet topology (c) Cascaded quartet topology for 6th-degree filter networks.

coupling matrix into various configurations can be found in [7].

The bandpass coupling matrix represented by the formulation in (2.34) assumes inductive coupling elements. In some cases, however, one or more of the computed element values in the inductive coupling matrix M_L may be negative. This implies that the particular coupling is capacitive in nature. For narrow bandpass filters, a brute-force approximation of replacing the inductive coupling by a capacitive coupling of the same value may be sufficient. For wide band filters, however, this approximation will result in an erroneous response and will require optimising of the element values to retain the original response. A better approach involves eliminating the inductive coupling element in the M_L matrix using simple matrix operations whilst introducing a capacitive coupling in the M_C matrix.

2.3.3   Coupling matrix analysis

Once the coupling matrix, may it be lowpass or bandpass, has been reconfigured into a practically realisable topology, almost all source/load-resonator couplings are annhiliated.

Typically, only the source-first resonator and N^{th} resonator-load couplings are present in the $N+2$ coupling matrix. These coupling admittances are equivalent to the source and load terminating conductances (or resistances):

$$G_S = (M_T(1,2))^2 = 1/R_S \tag{2.39a}$$

$$G_L = (M_T(N+1,N+2))^2 = 1/R_L \tag{2.39b}$$

The $N+2$ coupling matrix can then be transformed to a $N \times N$ coupling matrix of the form:

$$\mathbf{Y}_{\text{LP}} = \mathbf{M}_{\text{Ts}} + s\mathbf{M}_{\text{Cs}} + j\mathbf{M}_{\text{Ks}} \tag{2.40}$$

for lowpass prototypes and

$$\mathbf{Y}_{\text{BP}} = \mathbf{M}_{\text{Ts}} + s\mathbf{M}_{\text{Cs}} + \frac{1}{s}\mathbf{M}_{\text{Ls}} \tag{2.41}$$

for bandpass transfer functions. Here, $\mathbf{M}_{\text{Ts}}$ is the $N \times N$ terminating coupling matrix with all its elements equal to zero except $M_T(1,1) = G_S$ and $M_T(N,N) = G_L$. $\mathbf{M}_{\text{Cs}}$ is the $N \times N$ capacitive coupling matrix. $\mathbf{M}_{\text{Ks}}$ is the remnant coupling matrix with the self coupling elements occuping the principal diagonal. $\mathbf{M}_{\text{Ls}}$ is the inductive coupling matrix with composed of self and mutual couplings.

The $N \times N$ matrices in equations (2.40) and (2.41) can be related to the S-parameters using the following equations [21]:

$$S_{11} = 1 - 2 \cdot G_S \cdot [\mathbf{Y}^{-1}]_{1,1} \tag{2.42a}$$

$$S_{21} = 2\sqrt{G_S G_L} \cdot [\mathbf{Y}^{-1}]_{N,1} \tag{2.42b}$$

where $\mathbf{Y} = \mathbf{Y}_{\text{LP}}$ for lowpass prototype filters and $\mathbf{Y} = \mathbf{Y}_{\text{BP}}$ for bandpass filters. Note that the bandpass analysis of the coupling matrix is valid for the analysis of a multi-bandpass coupling matrix.

2.4 Physical implementation

The circuit elements of the synthesised lowpass prototype network can be transformed to the desired lowpass, highpass, bandpass or bandstop network elements using the standard transformations [36]. For directly synthesised bandpass networks, this step is redundant. If

the filter network is synthesised in the lumped domain, it can be transformed to the distributed domain using Richard's transformations outlined in section 2.2.3. This transformed filter network can be realised using various technologies. Irrespective of the technology of physical implementation, the underlying circuit synthesis theory is common for all filters.

The choice of technology of physical implementation depends on a range of factors, such as the operating frequency range, the desired power handling capacity, physical size constraints, Q-factor requirements, spurious window, temperature drift and cost. The two main technologies employed for cellular base station applications are coaxial cavity resonator filters and dielectric resonator filters [37]. Coaxial cavity resonator filters have Q-factors in the range of 1000-5000. They are widely used due to their low cost production and ease of implementation. Dielectric resonator filters can achieve higher unloaded Q-factors of upto 50,000. They demonstrate good temperature stability and can be miniaturised using multi-mode techniques. They have close out-of-band spurious response and relatively low power handling capacity [10].

As mentioned previously, the filter synthesis theory is an approximation of the electromagnetic theory as described by Maxwell's equations. In the past, the filter design methodology involved a lot of experimental cut-and-try work to obtain the desired filter response [38]. These days EM simulation softwares that are capable of analysing various phenomena that are not represented by the circuit models, viz., parasitic coupling effects or higher-order mode effects, are exploited to achieve an optimised physical hardware.

The initial physical dimensions can be determined from the circuit elements of the coupling matrix and from the isolated EM resonator pair models. Dishal [39] first identified that a narrow-bandpass lumped or distributed element filter network could be described using three fundamental parameters: 1) the synchronous frequency of each resonator, 2) a measure of the coupling between a pair adjacent resonators, i.e., the coupling coefficient, and 3) the external unloaded Q-factor [40]. An approach that combines Dishal's theory with the modern day EM software has been presented in [41, 42]. Computation of the external couplings and the inter-resonator couplings for asynchronously tuned lumped element circuit models are described in [43]. A similar approach was adopted in Chapter 1 of [21] to derive explicit formulae for computation of the inter-resonator and external couplings for mixed lumped-distributed element models. An isolated pair of resonators is modelled in the EM simulation software, as shown in Fig. 2.9, for measurement of the inter-resonator couplings. Similarly, the external coupling mechanism (typically, tapped or transformer input for coaxial filters) along with the first (or last resonator) is modelled in the EM software to measure the external coupling. The measurements of the EM models are then mapped to the corresponding theoretical results
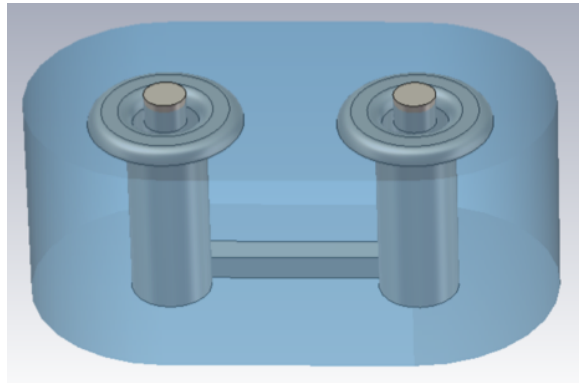
(a) An EM model of a resonator pair for magnetic coupling measurement. A rib is introduced between the two resonators to achieve a strong magnetic coupling.
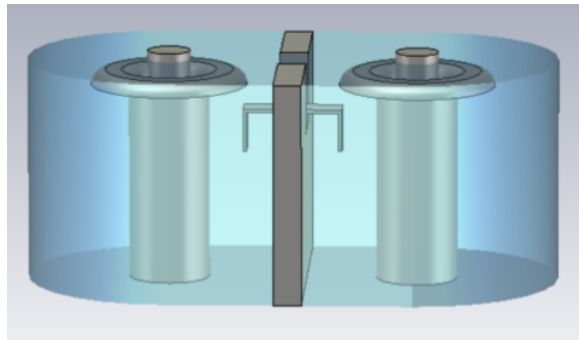
(b) An EM model of a resonator pair for capacitive coupling measurement. The capacitive coupling is achieved by the introducing a wall with copper strip between the two resonators.

Fig. 2.9 Examples of EM modelling of two resonators for inter-resonator coupling measurement.

to obtain the initial physical dimensions. The dimensions of the complete filter model can be optimised using the advanced design techniques that exploit the coarse model, i.e., the lumped or distributed circuit model, the fine model, i.e., the EM model. Examples of such methods include the space mapping technique [44–47] and the Cauchy method [48]. Once the physical dimensions of the EM model are optimised so that a satisfactory response is obtained, the filter can be fabricated and fine-tuned.

Chapter 3

Synthesis of Dual Band Filters

3.1 Motivation

The transmission of multiple frequency bands and services is, conventionally, enabled by the use of diplexers and multiplexers. The employment of a diplexer at RF front-end of a cellular base station for two different applications is illustrated in section 1.1.1. Although multiplexers allow for a modular design, their implementation requires the use of additional hardware. For example, the most commonly used multiplexer configurations include the use of manifold junctions to compensate for the interchannel interactions or the use of circulators or hybrids to couple the different channels. Thus, the multiplexer approach accounts for additional costs and an increase in the size of the filters.

An alternative approach to multiplexers is the incorporation of separation of multiple frequency bands in a single physical hardware, i.e., a multi-band filter. The employment of multi-band filters results in reduced mass, volume and cost of the RF-front end. It also simplifies the base station system architecture. A typical RF-front end employing two diplexers composed of single bandpass filters and a single diplexer composed of two dual band filters is depicted in Fig. 3.1. Given the advantages, multi-band filters have become an active area of research in the past decade.

Several approaches for realising multi-band filters have been reported in the literature. One of the approaches is to cascade a wide bandpass filter with multiple narrow bandstop filters [49, 50]. The bandwidths of each of the passbands are determined by the characteristics of the bandstop filters. Using this approach, filter responses with closely spaced passbands can be realised. Subsequently, it is difficult to realise filter responses with large band-to-band
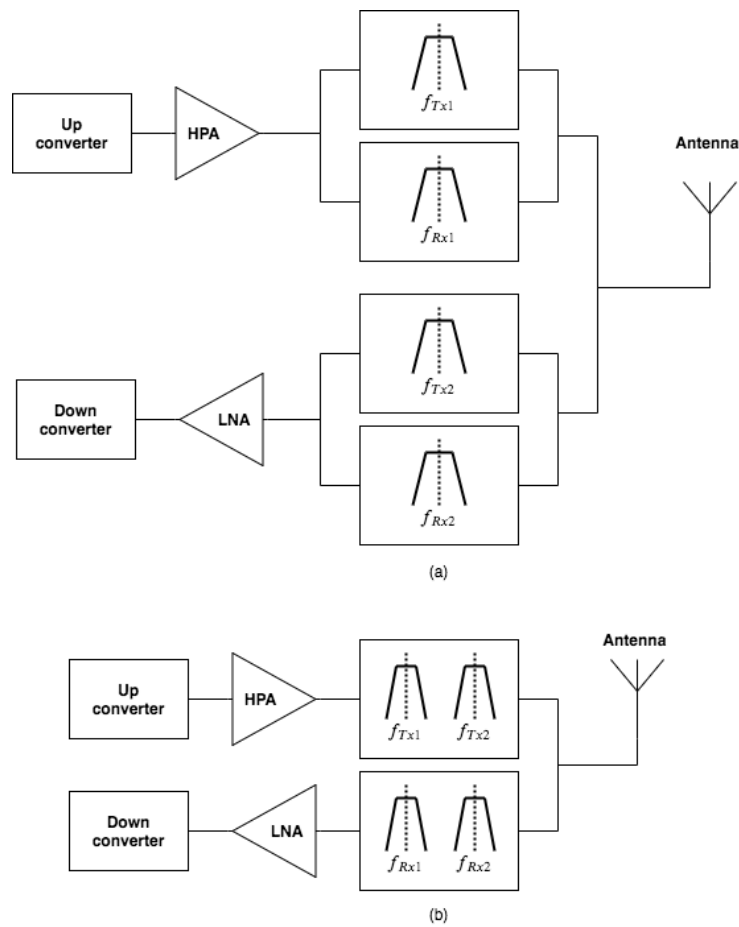
Fig. 3.1 (a) Two diplexers employing parallel-connected single bandpass filters (b) A diplexer employing dual bandpass filters (courtesy of Radio Design Ltd.)

separation. To enable integration of the individual bandpass and bandstop filters into a single unit, matching is required.

Multi-mode resonators can be exploited to design multi-band filters. A multi-mode resonator can support multiple resonances, each of which serve as an operating mode for a single passband. Therefore, they offer a significant reduction in the size of the filter. Triple conductor combline filters supporting two modes have been studied in [51]. Dual-mode dielectric resonators employing dual-band filters have been reported in [52]. The challenge with multi-mode multi-band resonator filters lies in controlling the the various filter parameters, viz., passband centre frequencies, bandwidth of each passband, external and inter-resonator couplings. The choice and position of tuning mechnasim in these filters is also a limiting factor. Traditional synthesis procedures are not applicable to these type of filters, which makes the design process relatively challenging.

Synthesis of multi-bandpass filters using advanced optimisation techniques have been reported in [53, 54]. The number of poles and zeros is imposed and determined through numerical optimisation. The disadvantage is the tradeoff between the passband return loss levels and control over the stopband rejection levels. Also, convergence of the system is not always guaranteed. Synthesis of dual and triple bandpass filters by performing frequency transformations on suitable lowpass prototypes have been reported in [55–57]. The suggested methods allow synthesis of symmetric and asymmetric filters. However, frequency transformations are only applicable to narrow band approximations due to the dispersive nature of the couping elements.

Direct synthesis methods for dual bandpass filters have been investigated in [58, 59]. As the coupling elements obtained using direct synthesis methods are frequency variant, they provide a better approximation for wide bandpass filters. In [58], characteristic functions for two single band filters are synthesised in the bandpass domain and are superimposed to obtain the dual band characteristic function. The characteristic function of each passband is synthesised with transmission zeros positioned suitably close to the band-edges. The transmission zero positions of the overall dual band characteristic function are altered and additional transmission zeros are generated in the process. Thus, there is no direct control over the position of transmission zeros, and consequently, over the stopband rejection levels. The technique in [59] involves linear combination of lower order basis functions to generate the dual band characteristic function. Although this method allows some control over the stopband transmission zeros, each basis function generates a pair of dependent transmission zeros. Therefore, there is no efficient control over the placement of transmission zeros.

A new direct synthesis method for the generation of generalised Chebyshev polynomials is explained in this chapter. The given linear optimisation technique is applicable to the synthesis of symmetric, as well as, asymmetric dual band filter responses. As the coupling elements obtained using the direct synthesis technique are frequency variant, the method can be applied to filters with wide bandwidths and large band-to-band separation. It allows full control over the stopband rejection levels by permitting arbitrary placement of transmission zeros. The method can be modified to include the synthesis of general multi-band filters.

3.2   Generalised Chebyshev Characteristic Function

In order for the dual bandpass characteristic function to pass through the desired frequency points, it is necessary that at least one of the transmission zeros is dependent. Thus, it is important to understand that moving to the synthesis of dual bandpass filters reduces the degree of freedom in terms of the characteristic function specifications.

Consider a filter with two passbands of degrees N_1 and N_2, respectively. The degree of the dual bandpass filter, N, can be given by the summation of individual degrees of the two passbands, i.e., $N = N_1 + N_2$. The generalised Chebyshev dual bandpass characteristic function, $T_{2N}(\omega)$, is defined by the ratio of the reflection characteristic polynomial, $F_{2N}(\omega)$, and the transmission characteristic polynomial, $P_{NTZ}(\omega)$. The transmission and reflection characteristic polynomials are, both, monic polynomials. Therefore, the characteristic function can be expressed mathematically as:

$$
\begin{aligned}
T_{2N}(\omega) &= \frac{F_{2N}(\omega)}{P_{NTZ}(\omega)} \\
&= \frac{\omega^{2N} + f_{N-1}\omega^{2N-2} + f_{N-2}\omega^{2N-4} + \cdots + f_1\omega^2 + f_0}{\varepsilon(\omega^2 - \omega_d^2)P_{rem}(\omega)}
\end{aligned}
\tag{3.1}
$$

where,
$f_{N-1}, f_{N-2}, f_{N-3} \cdots f_1, f_0$ are the N unknown coefficients of $F_{2N}(\omega)$,
ε is the scalar normalisation parameter,
ω_d is the dependent transmission zero position in rad/s, and
$P_{rem}(\omega)$ is the polynomial whose roots are the prescribed transmission zeros of the dual bandpass filter network.

For direct bandpass realisation, the degree of the characteristic function and the reflection polynomial is $2N$, i.e., twice the degree of the filter network. The degree of the transmission polynomial $P_{NTZ}(\omega)$ is NTZ, where $NTZ \leq 2N$. Consequently, the degree of the polynomial $P_{rem}(\omega)$ is at most $2N - 2$. The prescribed transmission zeros that form the $P_{rem}(\omega)$ polynomial can occur at finite frequencies (real, imaginary or complex), at dc or at infinity. In order to be able to realise the filter using lumped or distributed elements, the finite transmission zeros and the reflection zeros must always occur in pairs. This is not a necessary condition for the transmission zeros at dc and infinity as they can be extracted individually with a single lumped or distributed element.
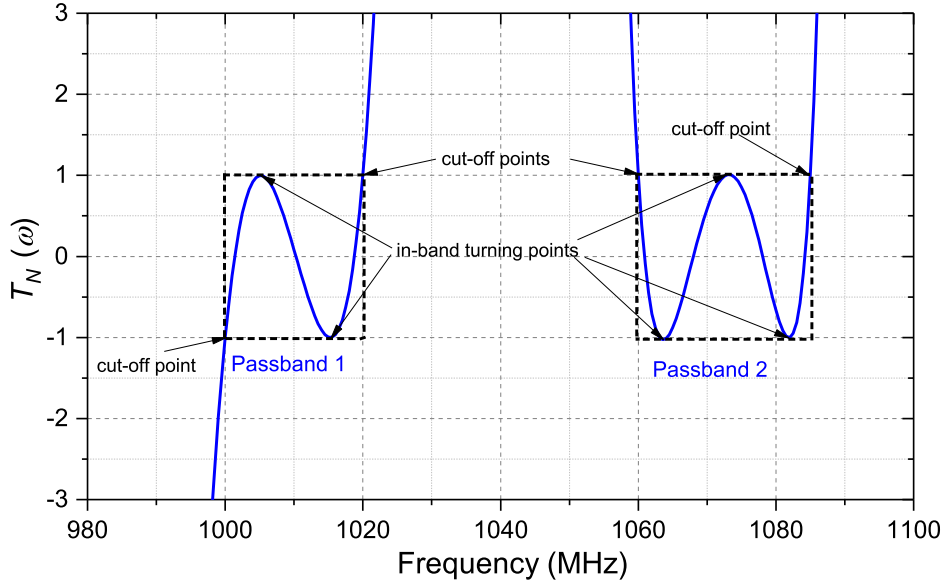
Fig. 3.2 An example of a 14th-degree characteristic function with four cut-off frequency points and five in-band turning points (critical points).

3.3 Linear optimisation technique for synthesis of characteristic polynomials

3.3.1 Formulation of the linear system of equations

Consider the dual band generalised Chebyshev characteristic function defined by equation (3.1). This equation is defined in $N+2$ unknown parameters, viz., the N reflection polynomial coefficients, the normalisation parameter ε and the dependent transmission zero ω_d. A linear system of equations can be formed by re-writing equation (3.1) as:

$$F_{2N}(\omega) - T_{2N}(\omega) \cdot P_{NTZ}(\omega) = 0 \tag{3.2}$$

Substituting for $F_{2N}(\omega)$ and $P_{NTZ}(\omega)$ yields,

$$\begin{aligned} [\omega^{2N} + f_{N-1}\omega^{2N-2} + f_{N-2}\omega^{2N-4} + \cdots + f_1\omega^2 + f_0] - \\ [T_{2N}(\omega)\varepsilon(\omega^2 - \omega_d^2)P_{rem}(\omega)] = 0 \end{aligned} \tag{3.3}$$

Consider the dual bandpass characteristic function displayed in Fig. 3.2. As discussed in section 2.2, the zeros of the characteristic function are the reflection zeros. These are the frequency points where the characteristic function value is zero. The in-band frequency

points where the characteristic function has its extremes are called the in-band turning points. The characteristic function ripples between $+1$ and -1 (normalised values as per convention) at these frequency points. The in-band turning points, together with the cut-off frequency points constitute the critical points for a given passband.

For a passband of degree N_1, there exists $N_1 - 1$ in-band turning points and two cut-off frequency points that define the passband. Thus, a single passband of degree N_1 has $N_1 + 1$ critical points. Consequently, for a dual bandpass characteristic function, there exist $N + 2$ critical points comprising of $(N_1 - 1) + (N_2 - 1) = N - 2$ in-band turning points and 4 cut-off frequency points. If the in-band frequency points were assumed to be known, then substituting $\omega = \omega_{cp}$, where ω_{cp} is a $N + 2$ by 1 column matrix comprising of the critical points, in equation (3.3) yields,

$$[f_{N-1}\omega_{cp}^{2N-2} + f_{N-2}\omega_{cp}^{2N-4} + \cdots + f_1\omega_{cp}^2 + f_0] - [T_{2N}(\omega_{cp})P_{rem}(\omega_{cp})\varepsilon\omega_{cp}^2]$$
$$-T_{2N}(\omega_{cp})P_{rem}(\omega_{cp})\varepsilon\omega_d^2] = -\omega_{cp}^{2N} \tag{3.4}$$

Note that in the above equation, the characteristic function $T_{2N}(\omega)$ and the $P_{rem}(\omega)$ polynomial are also functions of ω_{cp}.

Equation (3.4) represents a system of $N + 2$ linear independent equations, where the N reflection polynomial coefficients, ε and ω_d form the $N + 2$ unknown parameters and the $N + 2$ critical points form the known parameters. The $N + 2$ linear system of equations in (3.4) can be represented in a matrix form as:

$$Ax = B \tag{3.5}$$

where, A is a $N + 2$ by $N + 2$ square matrix defined as:

$$A = \begin{bmatrix} \omega_{cp}^{2N-2} & \omega_{cp}^{2N-4} & \cdots \omega_{cp}^2 & 1 & -T_{2N}(\omega_{cp})P_{rem}(\omega_{cp})\omega_{cp}^2 & -T_{2N}(\omega_{cp})P_{rem}(\omega_{cp}) \end{bmatrix} \tag{3.6}$$

B is a $N + 2$ by 1 column matrix defined as:

$$B = \begin{bmatrix} -\omega_{cp}^{2N} \end{bmatrix} \tag{3.7}$$

and x is a $N + 2$ by 1 column matrix of the unknown variables, defined as:

$$x = \begin{bmatrix} f_{N-1} & f_{N-2} & \cdots & f_1 & f_0 & \varepsilon & \varepsilon\omega_d^2 \end{bmatrix}^T \tag{3.8}$$

For a well-defined system of linear independent equations of the form (3.5), the solution for a well-conditioned square matrix A can be found using

$$x = A^{-1}B \qquad (3.9)$$

For an ill-conditioned matrix A, the solution to (3.5) may be found by using a direct method to solve for the unknown vector matrix x (for example, by Gaussian elimination).

In order to solve the linear system of equations in (3.5), the position of the critical points and the value of the characteristic function at these critical points must be known. The four cut-off frequency points for the dual bandpass filter are defined by the specifications. The $N-2$ in-band turning points, however, are not known. Thus, an initial estimation of the critical points is made so that the solution to (3.5) can be found. Once the unknowns in x are solved, the new turning points can be computed by equating the derivative of the characteristic function to zero. These new in-band turning points are used to solve the linear system in (3.5) to find the new unknowns. The procedure is repeated iteratively till the convergence criterion is met. Before reviewing the iterative procedure in detail, the following sub-sections review the methods used for determining the critical points and the characteristic function value at these critical points.

3.3.2   Determination of the critical points

The critical points comprise of the four cut-off frequency points that define the two passbands and the $N-2$ in-band turning points. As the cut-off points for both passbands are defined by the specifications, the problem reduces to determining the in-band turning points.
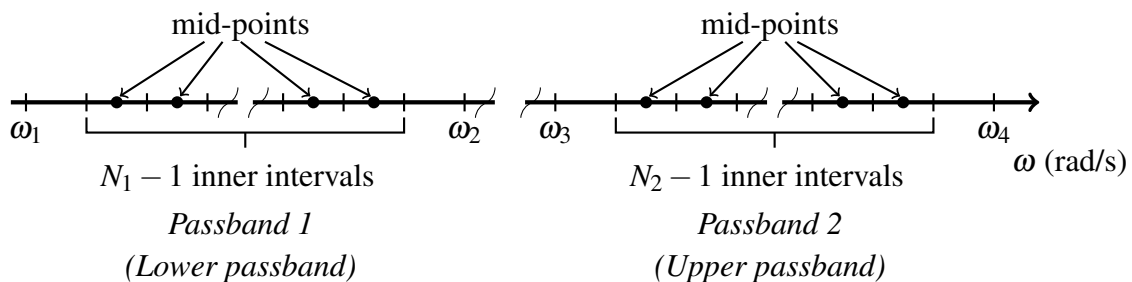
Fig. 3.3 Determination of the $N-2$ initial set of in-band turning points to form the $N+2$ column of critical points.

In order to do so, the first passband (lower passband) is divided into $N_1 + 1$ equal frequency intervals in the range $[\omega_1, \omega_2]$. Similarly, the second passband (upper passband) is divided into $N_2 + 1$ equal frequency intervals in the range $[\omega_3, \omega_4]$. The initial in-band turning points for the lower passband are determined by computing the mid-points of the inner $N_1 - 1$ frequency intervals (as illustrated in Fig. 3.3). Likewise, the mid-points of the inner $N_2 - 1$ frequency intervals form the in-band turning points for the upper stopband. The $N + 2$ by 1 column matrix containing all the critical points can be written as:

$$\omega_{cp} = \begin{bmatrix} \omega_1 & \omega_{tpl} & \omega_2 & \omega_3 & \omega_{tpu} & \omega_4 \end{bmatrix}^T \tag{3.10}$$

where, ω_{tpl} and ω_{tpu} are the $N_1 - 1$ by 1 and $N_2 - 1$ by 1 row matrices containing the in-band turning points for the lower and upper passbands respectively. Note that the in-band turning points in these row matrices are arranged in ascending order of magnitude. Once the critical points matrix in (3.10) are known, the linear system of equations in (3.5) can be solved for the unknowns in x.

The reflection polynomial coefficients, ε and ω_d determined by solving (3.5) can be substituted into equation (3.1) to form the new characteristic function. The new in-band turning points can then be computed by setting the derivative of the characteristic function to zero.

$$\frac{d}{d\omega}\{T_{2N}(\omega)\} = \frac{d}{d\omega}\left\{ \frac{F_{2N}(\omega)}{P_{NTZ}(\omega)} \right\} = 0 \tag{3.11}$$

The in-band turning points for the lower passband are obtained by choosing the $N_1 - 1$ roots of (3.11) lying in the range (ω_1, ω_2) and those for the upper passband are obtained by choosing the $N_2 - 1$ roots in the range (ω_3, ω_4). The critical points matrix, ω_{cp} can then be formed as in (3.10).

3.3.3 Characteristic function value at the critical points

As illustrated in Fig. 3.2, the Chebyshev characteristic function oscillates between ± 1 in the intervals $[\omega_1, \omega_2]$ and $[\omega_3, \omega_4]$. Therefore, the value of the characteristic function at the critical points can be assigned to either $+1$ or -1. Using the degree of each passband and by setting the number of transmission zeros in the inner stopband, the characteristic function value at the critical points can be set. The assignment of the function value at two successive critical points in the same passband can be represented by $T_{2N}(\omega_{cp_i}) = -T_{2N}(\omega_{cp_{i+1}})$. In other words, if the function value at ω_1 is set to -1, the function value at the first in-band

turning point must be $+1$. Consequently, if the degree of the passband is even, the value of the characteristic function at the upper cut-off frequency of the passband is equal to that at the lower cut-off frequency of the same passband (as in Passband 2 of Fig. 3.2). If the degree of the passband is odd, the value of the characterstic function at the upper cut-off frequency of the passband is equal to (-1) times the value at the lower cut-off frequency of the same passband (as in Passband 1 of Fig. 3.2). Similarly, if the number of inner stopband transmission zeros is even, then $T_{2N}(\omega_3) = T_{2N}(\omega_2)$ and if it is odd, then $T_{2N}(\omega_3) = -T_{2N}(\omega_2)$.

Using this method, a $N+2$ by 1 column matrix comprising of the characteristic function value at the critical points can be formed. These are the expected values of the characteristic function, $T_{2N_{expected}}(\omega)$, that the optimisation routine will seek to achieve. Note that the polynomial $P_{rem}(\omega)$ can be easily formed using the NTZ prescribed transmission zeros:

$$P_{rem}(\omega) = \prod_{i=1}^{NTZ} (\omega - \omega_i) \tag{3.12}$$

The column matrix $P_{rem}(\omega_{cp})$ can be easily computed by evaluating the polynomial (3.12) at each critical point in (3.10).

3.3.4 Iterative procedure

The following steps describe the iterative procedure to be executed.

1. The initial $N+2$ by 1 critical points matrix can be generated as described in section 3.3.2. The expected characteristic function values at the critical points $\left(T_{2N_{expected}}(\omega_{cp})\right)$ and the $P_{rem}(\omega_{cp})$ column matrix can be obtained as described in section 3.3.3. Using these matrices, the system of linear independent equations in (3.5) is formed.

2. By solving the set of equations in (3.5), the N unknown reflection polynomial coefficients, the normalisation parameter ε and the dependent transmission zero ω_d are determined. These parameters are then substituted back into equation (3.1) to form the new characteristic function.

3. The new in-band turning points are computed by determining the roots of the derivative of the new characteristic function. The new critical points matrix ω_{cp} is then formed as described in section 3.3.2.

4. The $N+2$ by 1 column matrix $T_{2N_{optimised}}(\omega_{cp})$ is formed by evaluating the new characteristic function at each of the new critical points.

5. Steps 2-4 are repeated till the following convergence criterion is met: $|T_{2N_{expected}}(\omega_{cp}) - T_{2N_{optimised}}(\omega_{cp})| < \kappa \quad \forall \quad \omega_{cp}$. Here, κ is the maximum allowable error that can be chosen depending upon the accuracy desired.

Depending upon the accuracy required, the algorithm usually converges within a few iterations. The entire iterative procedure is amenable to computer programming, for example MATLAB.

The fact that the characteristic function contains a dependent transmission zero means that a satisfactory solution may not always be achievable. The solution to the linear optimisation routine may be such that the dependent transmission zero lies in one of the two passbands. This might be a correct solution mathematically. However, it is certainly not the desired solution for filter synthesis. One of the approaches to tackle this issue is to constrain the dependent transmission zero to lie in one of the three stopbands. In this case, the system of linear equations may not have a solution at all. This implies that the prescribed transmission zeros may only take certain positions which would force the dependent transmission zero to lie outside the passbands. While the position of the dependent transmission zero is not known a priori, it can be constrained to lie in one of the stopbands. This can be achieved by setting the number of transmission zeros in the inner-stopband, thus, making it a control parameter. Once the number of inner-stopband transmission zeros is fixed, it does not matter which one of the transmission zeros is considered dependent or prescribed. Interchanging any one of the prescribed transmission zeros with a dependent transmission zero yields the same transfer function. The dependent transmission zero position is affected by the relative bandwidths of the two passbands, the degree of the two passbands, the number of transmission zeros between the two passbands and the separation between the two passbands.

3.3.5 Synthesis example - Dual bandpass filter

Specifications

A synthesis example for a dual bandpass filter is presented to expound on the linear optimisation technique. The requirements for the two passbands of 1710 MHz - 1750 MHz and 1920 MHz - 1960 MHz are as follows: the passband return loss level > 20 dB, passband insertion loss level < 1 dB. A rejection of > 35 dB is desired in all three stopbands: 1625 MHz - 1675 MHz, 1800 MHz - 1875 MHz and 2025 MHz - 2050 MHz.

An 8th-degree dual bandpass filter with $N_1 = N_2 = 4$ was chosen to meet the desired specifications. Three transmission zeros were prescribed at 1685 MHz, 1800 MHz and 1875 MHz to achieve the necessary stopband attenuation level. The number of inner stopband transmission zeros was set to 2 so that the dependent transmission zero is constrained to one of the outer two stopbands.

Synthesis of Characteristic polynomials

The iterative procedure outlined in section 3.3.4 was carried out in the real distributed variable t. The electrical length of the distributed elements at the centre frequency was chosen to be $\pi/4$ radians. The cut-off frequencies can be converted to the distributed domain as $t_c = [0.9014, 0.9330, 1.0797, 1.1175]^T$. The prescribed transmission zeros map to 0.8822, 0.9740 and 1.0387 respectively, in the distributed domain. The $N+2$ by 1 matrices of initial critical points (t_{cp}) and the expected values of the characteristic function at these critical points can be formed as described in sections 3.3.2 and 3.3.3 respectively.

Table 3.1 Initial critical points and the expected value of the characteristic function at the critical points for a 8-4 dual bandpass filter

initial t_{cp} (rad/s)	$T_{2N_{expected}}(t_{cp})$
0.9014	-1
0.9109	$+1$
0.9172	-1
0.9235	$+1$
0.9330	-1
1.0797	-1
1.0910	$+1$
1.0986	-1
1.1062	$+1$
1.1175	-1

The prescribed transmission zero polynomial $P_{rem}(t)$ can be formed using the prescribed transmission zeros as:

$$P_{rem}(t) = t^7 - 2.8058t^5 + 2.6014t^3 - 0.7965t$$

Note that the $P_{rem}(t)$ polynomial is a purely odd monic polynomial with alternating positive and negative real coefficients. The linear system of independent equations of the form $Ax = B$ is solved to obtain the unknown parameters. The computed coefficients of $F_{2N}(t)$, ε and the dependent transmission zero t_d are substituted to form the new characteristic function $T_{2N}(t)$. Using the derivative of the new characteristic function, the in-band turning points are

computed to form the new critical points matrix t_{cp}. The new critical points matrix t_{cp} is used to calculate $T_{2N_{optimised}}(t_{cp})$. The iterative procedure was repeated till the system converged for $\kappa = 10^{-5}$ in 4 iterations.

The dependent transmission zero was computed to be at $t_d = 1.2011$ corresponding to 2043.1 MHz and the scalar normalisation parameter $\varepsilon = 1.8921 \times 10^{-6}$. The reflection polynomial in the real distributed domain was computed to be:

$$F_{2N}(t) = t^{16} - 8.1905t^{14} + 29.2120t^{12} - 59.2526t^{10} + 74.7570t^8 - 60.0742t^6$$
$$+ 30.0277t^4 - 8.5360t^2 + 1.0566$$

The transmission and reflection characteristic polynomials were converted to the complex distributed domain ρ using Richard's transformation $\rho = j\tan(\theta) = jt$. The Hurwitz polynomial in the complex distributed plane $E_{2N}(\rho)$ was calculated using the alternating pole technique [7]. The normalised characteristic polynomials and their corresponding singularities in the ρ-plane are given in Table 3.3.5. Note that there are 8 finite transmission zeros (at positive and negative frequencies) and one at dc, leaving $16 - 9 = 7$ transmission zeros at infinity. The transfer and reflection characteristics of the plot are displayed in Fig. 3.4.
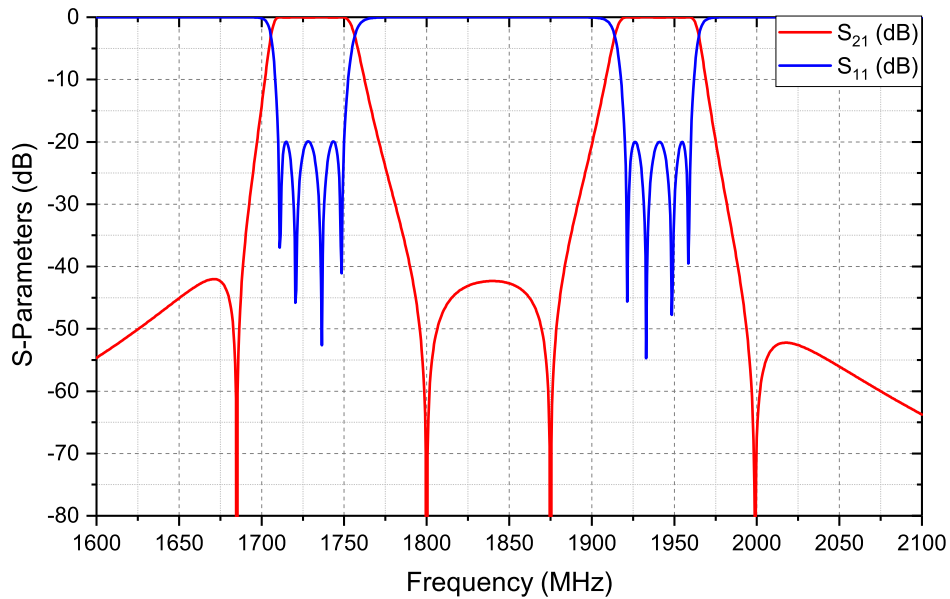
Fig. 3.4 An example of a 16th-degree dual bandpass filter response with four finite transmission zeros

Table 3.2 A 16th-degree dual bandpass Chebyshev filter function with four finite transmission zeros

(a) Normalised characteristic polynomials
$$\varepsilon_T = 5.3118 \times 10^4, \varepsilon_R = 1$$

$$
\begin{aligned}
P_{NTZ}(\rho) \quad &= \rho^9 + 4.2485\rho^7 + 6.6493\rho^5 + 4.5496\rho^3 + 1.1491\rho \\
F_{2N}(\rho) \quad &= \rho^{16} + 8.1905\rho^{14} + 29.2120\rho^{12} + 59.2526\rho^{10} + 74.7570\rho^8 + 60.0742\rho^6 \\
&\quad + 30.0277\rho^4 + 8.5360\rho^2 + 1.0566 \\
E_{2N}(\rho) \quad &= \rho^{16} + 0.1478\rho^{15} + 8.2014\rho^{14} + 1.0574\rho^{13} + 29.2787\rho^{12} + 3.2256\rho^{11} \\
&\quad + 59.4217\rho^{10} + 5.4393\rho^9 + 74.9845\rho^8 + 5.4760\rho^7 + 60.2456\rho^6 + 3.2913\rho^5 \\
&\quad + 30.0963\rho^4 + 1.0935\rho^3 + 8.5473\rho^2 + 0.1550\rho + 1.0566
\end{aligned}
$$

(b) Roots of the characteristic polynomials

Transmission zeros (Roots of $P_{NTZ}(\rho)$)	Reflection zeros (Roots of $F_{2N}(\rho)$)	Transmission/Reflection poles (Roots of $E_{2N}(\rho)$)
$\pm j0.8822$	$\pm j0.9024$	$-0.0142 \pm j1.1087$
$\pm j0.9740$	$\pm j0.9099$	$-0.0058 \pm j1.0759$
$\pm j1.0387$	$\pm j0.9222$	$-0.0036 \pm j0.8989$
$\pm j1.2011$	$\pm j0.9317$	$-0.0133 \pm j0.9237$
0	$\pm j1.0811$	$-0.0055 \pm j1.1211$
$j\infty$	$\pm j1.0915$	$-0.0148 \pm j1.0893$
$j\infty(\times 2)$	$\pm j1.1062$	$-0.0055 \pm j0.9365$
$j\infty(\times 4)$	$\pm j1.1162$	$-0.0111 \pm j0.9071$

3.4 Dual band synthesis and design example

Specifications

A synthesis example for two closely spaced bands at 1000 MHz - 1010 MHz and 1040 MHz - 1050 MHz is presented in this section. A minimum return loss level of 20 dB and a maximum insertion loss level of 1 dB are required in both passbands. Rejection levels of > 30 dB are desired in the two stopbands of interest: 1020 MHz - 1030 MHz and 1060 MHz - 1070 MHz.

A 7th-degree dual bandpass filter with $N_1 = 3$ and $N_2 = 4$ was chosen to meet the desired specifications. Three transmission zeros were placed at 1021.2 MHz, 1028.7 MHz and 1064 MHz to achieve the necessary stopband attenuation level. The number of inner stopband transmission zeros was set to 2 so that the dependent transmission zero is constrained to one of the outer two stopbands.

Synthesis of Characteristic polynomials

The iterative procedure in section 3.3.4 was carried out in the real distributed variable t. The electrical length of the distributed elements at the centre frequency was chosen to be $\pi/4$ radians. Using the transformation from ω-plane $\longrightarrow$ t-plane, the cut-off frequencies can be mapped to $t_c = [0.9624, 0.9773, 1.0233, 1.0391]^T$. Similarly, the prescribed transmission zeros at 1021.2 MHz, 1028.7 MHz and 1064 MHz map to 0.9947, 1.0062 and 1.0621 respectively. The first passband is divided into $N_1 + 1 = 4$ equal frequency intervals and the second passband is divided into $N_2 + 1 = 5$ equal frequency intervals. The mid-points of the inner $N_1 - 1 = 2$ intervals of the first passband and those of the inner $N_2 - 1 = 3$ intervals of the second passband constitute the initial set of in-band turning points. Using these in-band turning points, the $N + 2$ by 1 column matrix of the initial critical points can be formed as described in section 3.3.2. The expected value of the characteristic function at the critical points can be set as explained section 3.3.3.

Table 3.3 Initial critical points and the expected value of the characteristic function at the critical points for a 7-4 dual bandpass filter

initial t_{cp} (rad/s)	$T_{2N_{expected}}(t_{cp})$
0.9624	-1
0.9680	$+1$
0.9717	-1
0.9773	$+1$
1.0233	$+1$
1.0280	-1
1.0312	$+1$
1.0343	-1
1.0391	$+1$

The prescribed transmission zero polynomial can be formed by using the prescribed transmission zeros as its factors. Note that to realise a bandpass transfer function, at least one transmission zero has to be placed at dc. If the number of transmission zeros at dc is odd, P_{rem} is a purely odd polynomial.

$$P_{rem}(t) = t^7 - 3.1298t^5 + 3.2598t^3 - 1.1299t$$

The system of $N + 2$ linear independent equations of the form (3.5) is solved to obtain the unknown parameters in matrix x. The computed coefficients of the reflection polynomial $F_{2N}(t)$, the scalar normalisation parameter ε and the dependent transmission zero t_d are substituted into equation (3.1) to form the new characteristic function. By setting the

derivative of the new characteristic function to zero, the extremes of the function are computed. These extremes along with the cut-off frequency points form the new critical points column matrix t_{cp}. By evaluating the characteristic function at each of the new critical points, the $N+2$ by 1 column matrix $T_{2N_{optimised}}(t_{cp})$ can be computed. The above iterative procedure is repeated until the convergence criterion is met: $|T_{2N_{expected}}(t_{cp}) - T_{2N_{optimised}}(t_{cp})| < \kappa \quad \forall \quad t_{cp}$. The system converged for $\kappa = 10^{-7}$ in 10 iterations.

The final values for the unknown parameters were as follows:

$$F_{2N}(t) = t^{14} - 7.0885t^{12} + 21.5205t^{10} - 36.2749t^{8} + 36.6635t^{6}$$
$$- 22.2194t^{4} + 7.4762t^{2} - 1.0774$$

$\varepsilon = 1.8483 \times 10^{-6}$ and $t_d = 1.0478$ corresponding to 1055.2 MHz. The computed transmission and reflection polynomials can be exploited to determine the Hurwitz polynomial using the alternating pole technique. The normalised characteristic polynomials and their corresponding singularities in the complex distributed plane are listed in Table 3.4.

Table 3.4 A 14th-degree dual bandpass Chebyshev filter function with four finite transmission zeros

(a) Normalised characteristic polynomials
$\varepsilon_T = 5.4377 \times 10^4, \varepsilon_R = 1$

$$
\begin{aligned}
P_{NTZ}(\rho) &= \rho^9 + 4.2278\rho^7 + 6.6962\rho^5 + 4.7090\rho^3 + 1.2406\rho \\
F_{2N}(\rho) &= \rho^{14} + 7.0885\rho^{12} + 21.5205\rho^{10} + 36.2749\rho^8 + 36.6635\rho^6 + 22.2194\rho^4 \\
&\quad + 7.4762\rho^2 + 1.0774 \\
E_{2N}(\rho) &= \rho^{14} + 0.0667\rho^{13} + 7.0907\rho^{12} + 0.4059\rho^{11} \\
&\quad + 21.5318\rho^{10} + 1.0291\rho^9 + 36.2979\rho^8 + 1.3907\rho^7 + 36.6869\rho^6 + 1.0564\rho^5 \\
&\quad + 22.2313\rho^4 + 0.4277\rho^3 + 7.4786\rho^2 + 0.0721\rho + 1.0774
\end{aligned}
$$

(b) Roots of the characteristic polynomials

Transmission zeros	Reflection zeros	Transmission/Reflection poles
(Roots of $P_{NTZ}(\rho)$)	(Roots of $F_{2N}(\rho)$)	(Roots of $E_{2N}(\rho)$)
$\pm j0.9947$	$\pm j0.9640$	$-0.0048 \pm j1.0373$
$\pm j1.0062$	$\pm j0.9708$	$-0.0030 \pm j1.0220$
$\pm j1.0478$	$\pm j0.9769$	$-0.0089 \pm j0.9715$
$\pm j1.0621$	$\pm j1.0245$	$-0.0014 \pm j1.0405$
0	$\pm j1.0297$	$-0.0068 \pm j1.0294$
$j\infty$	$\pm j1.0358$	$-0.0034 \pm j0.9799$
$j\infty(\times 4)$	$\pm j1.0392$	$-0.0050 \pm j0.9601$
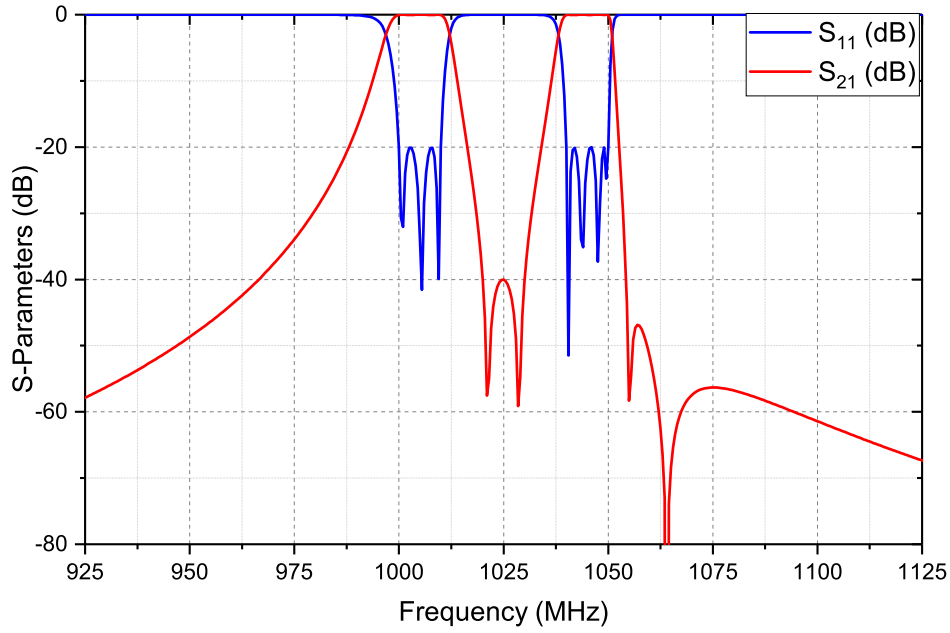
Fig. 3.5 An example of a 14th-degree dual bandpass filter response with four finite transmission zeros

Coupling matrix synthesis

The characteristic polynomials can be used to calculate the Y-parameters, from which the transversal coupling matrix can be computed using the method described in section 2.3.1. By performing similarity transformations on the transversal coupling matrix, it can be reconfigured into a practically suitable topology. In order to realise a 7th-order filter network with 4 finite transmission zero pairs, a folded topology had to be implemented.

The $N \times N$ bandpass distributed coupling matrix is represented by:

$$Y_{BP}(\rho) = M_{Ts} + \rho M_{Cs} + M_{Ls}/\rho \tag{3.13}$$

The $N \times N$ inductive coupling matrix M_{Ls} is given by equation (3.14).

$$M_{Ls} = \begin{bmatrix} +1.0007 & -0.0654 & 0 & 0 & 0 & 0 & 0 \\ -0.0654 & +1.0021 & -0.0264 & 0 & 0 & -0.0092 & -0.0040 \\ 0 & -0.0264 & +1.0100 & -0.0487 & -0.0249 & -0.0094 & 0 \\ 0 & 0 & -0.0487 & +1.0331 & -0.0312 & 0 & 0 \\ 0 & 0 & -0.0249 & -0.0312 & +1.0328 & -0.0240 & 0 \\ 0 & -0.0092 & -0.0094 & 0 & -0.0240 & +1.0032 & -0.0653 \\ 0 & -0.0040 & 0 & 0 & 0 & -0.0653 & +1.0007 \end{bmatrix} \tag{3.14}$$

M_{Ts} is the $N \times N$ termination matrix with all entries equal to zero, except for $M_{Ts}(1,1) = M_{Ts}(N,N) = 0.0341$. The capacitive coupling matrix M_{Cs} is a $N \times N$ identity matrix. As the coupling matrix is synthesised in the distributed domain, it can be realised using open and short-circuited stubs. Note that all the inter-resonator couplings in this example are inductive.

A combline filter
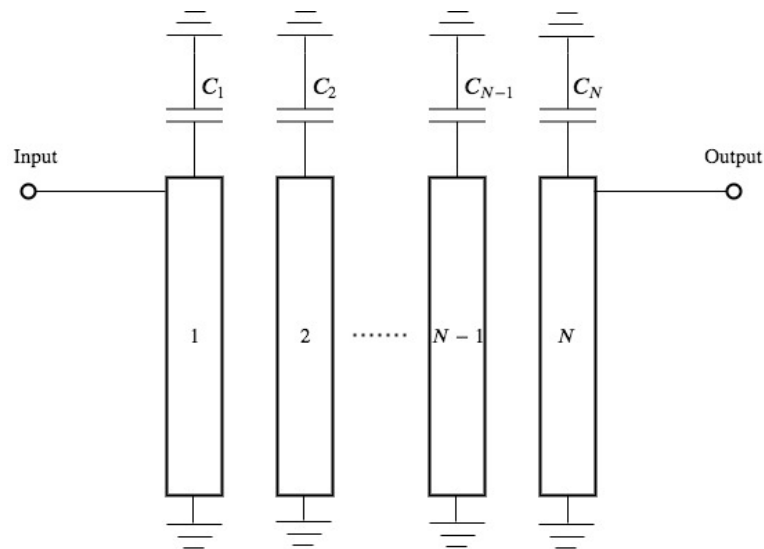
Fig. 3.6 An Nth-degree combline filter.

A combline filter is composed of an array of coupled TEM commensurate lines as illustrated in Fig. 3.6. The TEM lines are short-circuited at one end. The other end of the lines are loaded with lumped capacitors C_r, which are connected to ground. The TEM lines behave as inductors and resonate with the lumped capacitors at a frequency below the quarter-wavelength frequency [2]. For a given resonant frequency, increasing the loading capacitance decreases the length of the transmission line. In addition, the inter-resonator couplings are weak as compared to some of the other filter structures, such as interdigital filter, implying that the resonators are placed closer together. Thus, a combline realisation results in a fairly compact filter structure. Combline filters provide a large spurious window and are easy to implement in different topological configurations.

The equivalent network for a combline filter consists of shunt parallel-connected mixed lumped-distributed resonators coupled through distributed circuit elements. The shunt resonators consist of a short-circuited stub in parallel with a lumped capacitor, as depicted in Fig. 3.7c. The commensurate TEM lines can be realised using cylindrical rods between parallel ground planes. The spacing between the non short-circuited end of the cylindrical rod

and the lid provides the loading capacitance. This capacitance can be increased by decreasing the distance between the rod and the lid or by increasing the surface area between the two.

Conversion of purely distributed network to combline equivalent network

In order to realise the filter network using capacitively loaded coaxial resonators, the purely distributed circuit has to be converted into a combline equivalent circuit.

A purely distributed circuit represented by the coupling matrix Y_{BP} was converted to the equivalent combline network as illustrated in Fig. 3.7. The open-circuited stubs in the distributed network were converted to lumped capacitors by forcing the admittances of each of the resonators to be equal at the outer two band-edge frequencies [60].

$$
\begin{aligned}
t_1 Y_{oc_r} - \frac{1}{t_1 Y_{sc_r}} &= \omega_1 C_r - \frac{1}{t_1 Y_r} \\
t_4 Y_{oc_r} - \frac{1}{t_4 Y_{sc_r}} &= \omega_4 C_r - \frac{1}{t_4 Y_r}
\end{aligned}
\tag{3.15}
$$

where, $t_1 = tan(a\omega_1)$ and $t_4 = tan(a\omega_4)$. By solving the equations in (3.15), values for the capacitor and the short-circuited stub of the rth resonator can be calculated.

$$
\begin{aligned}
C_r &= \frac{t_1^2 - t_4^2}{\omega_1 t_1 - \omega_4 t_4} \\
\frac{1}{Y_r} &= \frac{1}{Y_{sc_r}} \omega_1 t_1 C_r - t_1^2 Y_{oc_r}
\end{aligned}
\tag{3.16}
$$

In order to obtain the optimum Q, the coupling matrix is scaled such that the coaxial resonator impedance is 75 Ω. The final element values for a combline filter network in a 50 Ω system are given in Table 3.4.

Table 3.5 Element values for combline realisation of a 14th-order dual band transfer function

Shunt short-circuited stubs	Lumped capacitors	Inter-resonator couplings
Z_r = 75 Ω	$C_1 = 2.0713$ pF $C_2 = 2.0689$ pF $C_3 = 2.0556$ pF $C_4 = 2.0178$ pF $C_5 = 2.0183$ pF $C_6 = 2.0670$ pF $C_7 = 2.0713$ pF	$K = 366.7290$ Ω $Z_{12} = 1403.3$ Ω, $Z_{26} = 9985.7$ Ω $Z_{23} = 3489.5$ Ω, $Z_{27} = 22944$ Ω $Z_{34} = 1915.4$ Ω, $Z_{35} = 3745.8$ Ω $Z_{45} = 3017.3$ Ω, $Z_{36} = 9804.3$ Ω $Z_{56} = 3875.5$ Ω $Z_{67} = 1406.1$ Ω
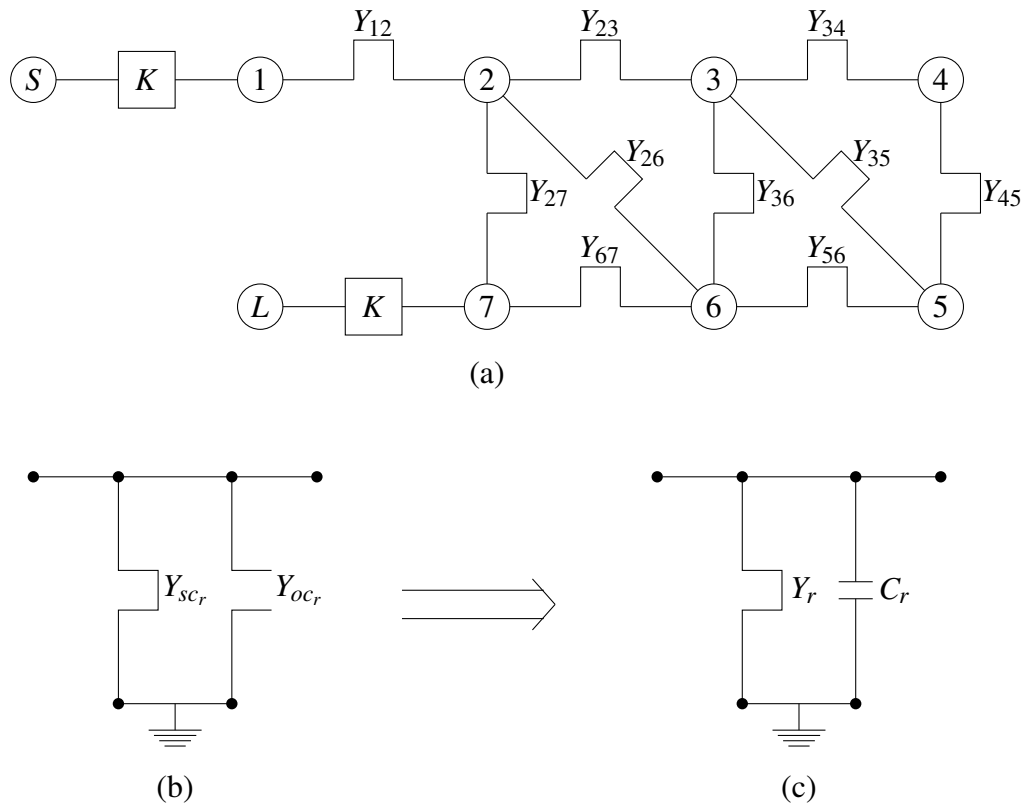
Fig. 3.7 (a) 7-4 Dual band filter topology (b) Distributed resonator at node r (c) Equivalent combline resonator at node r

Physical Realisation and Results

Initial dimensions for the filter prototype were determined using the practical procedures outlined in section 2.4. The filter was optimised on an EM software till a satisfactory performance was achieved. The fabricated filter without the tuning screws is displayed in Fig. 3.8.

The physical length of the coaxial resonators for an electrical length of $\theta_0 = 45°$ is $l = 36.6$ mm. The inter-resonator inductive couplings were realised by varying the rib heights between two resonators. An exception to this was the weak cross-coupling between resonators 3 and 6, which was realised by varying the iris width between them. Brass transformers were implemented to realise the external couplings. The physical dimensions of the final prototype filter are listed in Table 3.4. Note that the specified fabrication tolerance for the prototype was ± 0.1.

A comparison between the ideal circuit simulation and the measured response of the filter can be observed in Fig. 3.9. A minimum return loss level of 20 dB was achieved in both
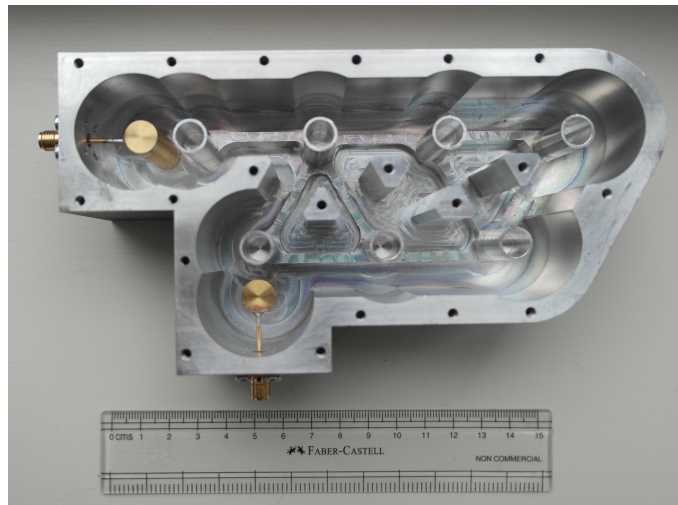
Fig. 3.8 A 7-4 dual bandpass prototype filter without lid and tuning screws

Table 3.6 Physical dimensions for the 7-4 dual bandpass filter prototype

Dimension	Value (mm)
Coaxial resonator length	36.6
Resonator outer diameter	10.0
Resonator inner diameter	8.0
Rib height 1-2	11.0
Rib height 2-3	4.1
Rib height 3-4	9.5
Rib height 4-5	8.5
Rib height 5-6	3.1
Rib height 6-7	10.6
Rib height 2-6	1.4
Rib height 2-7	1.0
Rib height 3-5	7.8
Iris thickness 3-6	11.8
Rib width	3.0
Distance between transformers and first (last) resonator	4.0
Tuning screw diameter	6.35

passbands. The measured insertion loss level ranged between 0.9 dB to 1.5 dB. These values are higher than the expected values. This can be attributed to the filter hardware not being plated and due to the inaccuracies arising during the fabrication process. An average Q-factor of about 1350 was measured at the centre of both passbands. The position of the transmission zeros for the measured response of the filter vary slightly as compared to those in the ideal
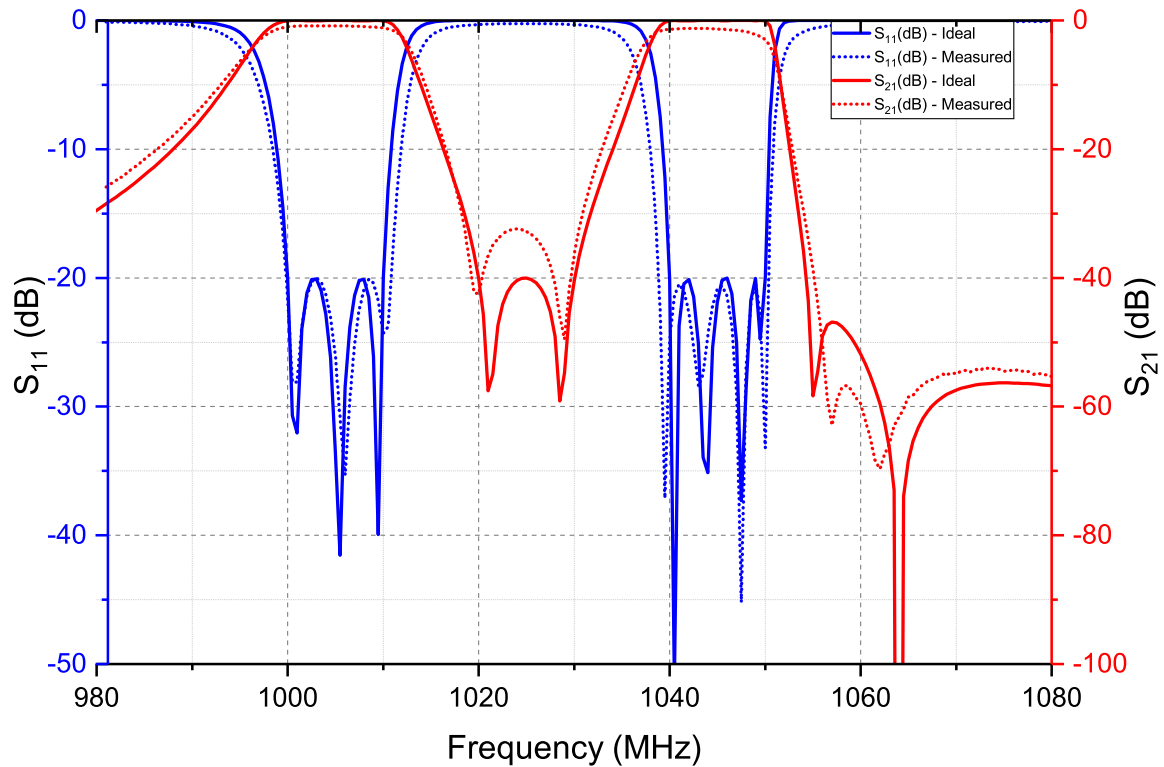
Fig. 3.9 A 7-4 dual bandpass prototype filter without lid and tuning screws

circuit simulation response. Although this has altered the stopband rejection levels for the measured response, the required stopband specifications are still satisfied.

3.5   Accuracy Issues

Depending upon the relative bandwidths of the passbands, the placement of transmission zeros and the level of accuracy desired (value of κ), it was found that the linear optimisation technique could synthesise filter networks upto degree 12 (transfer function 24). Note that the statement is pertinent to performing the entire procedure in the distributed domain. For complex or higher-order filter networks, the algorithm fails to converge due to numerical inaccuracies. These inaccuracies arise due to ill-conditioning in the intermediate steps of the synthesis procedure. Due to the loss of accuracy, determining the roots of the reflection polynomial becomes problematic, resulting in the algorithm not converging.

Loss of accuracy in the classical filter synthesis procedure is a well-known problem [61]. Every stage of the synthesis procedure incurs the loss of one significant digit. Therefore, for synthesis of complex and higher-order filters ($N > 12$), a precision of even 64 digits

may not be sufficient. Even the commercial filter and coupling matrix synthesis software (CMS) allows synthesis of filter networks only upto degree 14. This is a issue for dual and multi-bandpass filter synthesis as individual passbands of degree 6 or higher may be desired for certain applications. A comprehensive description of the numerical ill-conditioning encountered in the classical filter synthesis procedure can be found in [62].

One possible solution to the accuracy issue is to perform the entire synthesis procedure in the transformed frequency variable z [63]. The transformation maps the passband(s) (and inner stopband) to the entire imaginary axis and the outer stopbands to the entire real axis. This avoids the numerical inaccuracies encountered in the s or ρ-planes. The next chapter explains the transformation of the entire optimisation procedure to the z-plane.

3.6   Conclusion

A review of the existing techniques for the design and synthesis of dual and multi-bandpass filters has been presented. A new method for the direct synthesis of dual bandpass filters has been explained in detail in section 3.3. The presented technique is applicable to the synthesis of symmetric and asymmetric filter responses. As the synthesis procedure is carried out directly in the bandpass domain, filters with wide passbands and large band-to-band separation can be synthesised. To expound on the synthesis technique, a dual bandpass synthesis example has been presented in section 3.3.5. To demonstrate the practicality of the technique a dual bandpass filter has been synthesised and fabricated. The limitation of the synthesis process due to accuracy issues encountered for higher-order filters has been discussed in section 3.5. In order to deal with the accuracy issue, the linear optimisation technique is transformed to the z-plane. This transformation is presented in the next chapter.

Chapter 4

Synthesis of multi-band filters in transformed variable plane

Synthesis in the complex frequency plane results in numerical inaccuracies for higher-order filtering functions. In this chapter, the transformation applied to the filter synthesis procedure in order to improve its numerical accuracy is reviewed. A brief overview of the existing technique for the determination of the single-band generalised Chebyshev characteristic function in the transformed variable plane, as discussed extensively in [13], is presented. The linear optimisation method is formulated for the synthesis of generalised Chebyshev multi-band filters in the transformed variable plane, viz., the z-plane. The improved numerical accuracy arising from the transformation enables the synthesis of higher-order dual band and multi-band filters. In order to take full advantage of the transformed frequency plane, the process of generation of characteristic polynomials as well as that of element extraction must be carried out in the z-plane. A comprehensive description of various single band approximations in the transformed variable plane can be found in [61, 63, 13, 64].

4.1 Synthesis of single-band filters in the transformed variable plane

A synthesis technique for asymmetric, equal-ripple single bandpass filters in the z-plane is described in this section. Suppose N is the degree of the single bandpass filter network. For direct bandpass synthesis, the degree of the characteristic function, the reflection function, as well as the transmission function in the transformed variable plane is $2N$.

4.1.1 The transformed variable plane

The transformation of the complex frequency variable, s, to the transformed frequency variable, z, is represented mathematically by [62]:

$$z^2 = \frac{s^2 + \omega_2^2}{s^2 + \omega_1^2} \quad Re\{z\} > 0 \tag{4.1}$$

where, ω_1 and ω_2 are the lower and upper cut-off frequencies of the single bandpass filter. By dividing the numerator and the denominator of equation (4.1) by the upper cut-off frequency, the bilinear transformation can be simplified to:

$$z^2 = \frac{S^2 + 1}{S^2 + \alpha^2} \implies S^2 = \frac{1 - \alpha^2 z^2}{z^2 - 1} \tag{4.2}$$

where, $\alpha = \omega_1/\omega_2$ and $S = j(\omega/\omega_2)$. The transformation (4.1) maps the lower passband edge to $z = j\infty$ and the upper passband edge to $z = 0$. Thus, the passband is spread over the entire imaginary axis of the z-plane. Similarly, the lower and upper stopbands are mapped to the entire real axis of the z-plane. Consequently, the reflection zeros will only take imaginary values and the transmission zeros will only take real values in the transformed variable plane. Note that the transmission zeros at dc map to $z = 1/\alpha$ and those at infinity map to $z = 1$.

4.1.2 Determination of the characteristic function

The squared modulus of the characteristic function in the transformed variable plane is defined by the ratio of the transformed reflection function squared to that of the transformed transmission function squared [13].

$$|T(z)|^2 = \frac{F(z)^2}{P(z)^2} \tag{4.3}$$

The transformed transmission zeros z_i can be obtained by taking the positive roots of equation (4.1). These transformed roots include the transmission zeros at dc, at infinity and at finite frequencies. Note that the transmission zeros at finite frequencies always occur in pairs. By taking the product of the factors formed by these transformed roots, the transmission polynomial in the z-plane can be obtained.

$$P(z) = \prod_{i=1}^{2N}(z_i + z) \tag{4.4}$$

The transformed transmission polynomial can be represented by the summation of two sub-polynomials as:

$$e(z) + zf(z) = \prod_{i=1}^{2N}(z_i + z) \tag{4.5}$$

where, $e(z)$ and $f(z)$ are both even polynomials of z. Therefore, the even powers of the polynomial $P(z)$ constitute the polynomial $e(z)$ and its odd powers constitute $zf(z)$. The degree of $e(z)$ is, therefore, the same as the degree of the transformed transmission polynomial, i.e, $2N$. Similarly, the degree of the polynomial $f(z)$ is $2N-2$.

It can be proven [13] that, for a single bandpass filter, the roots of the monic polynomial $e(z)$ are, in fact, the N pairs of reflection zeros of the transfer function. Also, the roots of the polynomial $f(z)$ are the $N-1$ pairs of in-band turning points. The squared modulus of the transformed characteristic function can, thus, be represented in terms of the two sub-polynomials as:

$$|T(z)|^2 = \frac{\varepsilon^2 e(z)^2}{e(z)^2 - z^2 f(z)^2} \tag{4.6}$$

where, ε is the scalar factor that normalises the passband to a given equal-ripple level. Hence, $\varepsilon e(z)$ is the transformed reflection polynomial, also denoted by $F(z)$. Note that this is, however, not the case for a multi-bandpass characteristic function. Therefore, determination of the multi-bandpass reflection polynomial in the z-plane requires a more elaborate procedure.

The transformed reflection and transmission polynomials can be used to obtain the Hurwitz polynomial. Using the Feldtkeller equation, the squared modulus of the transfer function in the transformed variable plane can be represented as:

$$|H(z)|^2 = \frac{(1+\varepsilon^2)e(z)^2 - z^2 f(z)^2}{e(z)^2 - z^2 f(z)^2} \tag{4.7}$$

The roots of the numerator of (4.7) that lie in the left-half of the s-plane form the Hurwitz polynomial roots. These left-half plane roots transformed to the z-plane are used to form the transformed Hurwitz polynomial. A comprehensive description of the method used to determine the Hurwitz polynomial in the transformed variable plane is given in section 4.5. The procedure for the calculation of the $ABCD$-parameters and the Y-parameters in the z-plane is presented in section 4.6. The method is the same for the direct synthesis of single or multi-band coupling matrices.

4.2 The transformed frequency variable for multi-band filters

Consider a multi-bandpass filter with N_B passbands. The degree of such a filter can be represented by the summation of the degrees of the individual passbands.

$$N = \sum_{i=1}^{N_B} N_i \tag{4.8}$$

where, N is the degree of the multi-band filter network and N_i is the degree of the ith passband. For a filter with N_B passbands, there exists $N_B - 1$ inner stopbands (ISB), two outer stopbands
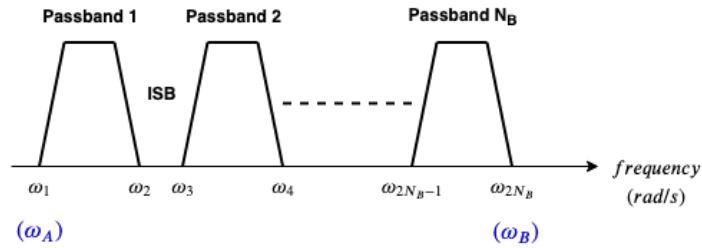
Fig. 4.1 Illustration of a multi-bandpass filter with N_B passbands

and $2N_B$ cut-off frequencies (two for each passband). Suppose ω_A is the lower cut-off frequency of the first passband and ω_B is the upper cut-off frequency of the upper-most passband, as illustrated in Fig. 4.1.

The transformation from the complex frequency plane to the transformed variable plane can be expressed in terms of these outermost cut-off frequencies as:

$$z^2 = \frac{s^2 + \omega_B^2}{s^2 + \omega_A^2} \quad \mathrm{Re}\{z\} \geq 0 \tag{4.9}$$

The transformation maps the frequencies in the range $\omega_A \leq \omega \leq \omega_B$ to the entire imaginary axis. The frequencies $\omega < \omega_A$ and $\omega > \omega_B$ are mapped to the entire real axis. Thus, the transformation maps the passbands and the inner stopbands to the imaginary axis and the outer two stopbands to the real axis. The condition $\mathrm{Re}\{z\} \geq 0$ implies that only the positive roots of z are used.
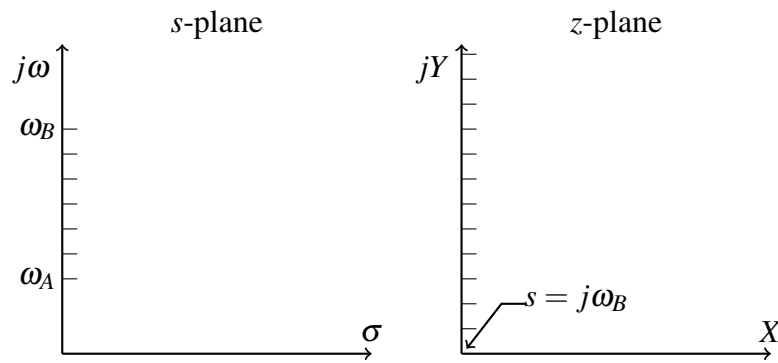
(a) Mapping of the passbands and inner stopbands
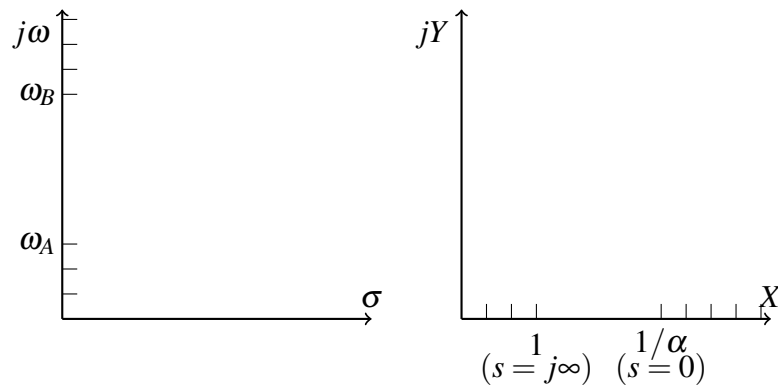
(b) Mapping of the outer two stopbands

Fig. 4.2 Transformation from the complex frequency plane (s-plane) to the transformed variable plane (z-plane)

In order to facilitate the mathematics, the right-hand side of equation (4.9) can be normalised to the uppermost cut-off frequency, ω_B, such that

$$z^2 = \frac{S^2 + 1}{S^2 + \alpha^2} \tag{4.10}$$

where, the constant $\alpha = (\omega_A/\omega_B)$ and $S = j(\omega/\omega_B) = j\Omega$. By the definition of α, for bandpass filters, $0 < \alpha < 1$. Normalising the frequencies to ω_B maps the lowermost cut-off frequency to $\Omega = \alpha$ and the uppermost cut-off frequency to $\Omega = 1$. In the z-plane, the lowermost and uppermost cut-off frequencies are mapped to $z = \infty$ and $z = 0$, respectively. The roots of the transmission polynomial at dc, i.e, at $s = 0$ are mapped to $z = 1/\alpha$ and those at $s = j\infty$ are mapped to $z = 1$. The mappings can be summarised by Table 4.1

Table 4.1 Mapping between s, Ω and z planes

	s-plane	Ω-plane	z-plane
Transformation	$s = j\omega$	$\Omega = \omega/\omega_B$	$z = \left(\frac{s^2+\omega_B^2}{s^2+\omega_A^2}\right)^{1/2}$
Lowermost band-edge	$s_A = j\omega_A$	$\Omega = \alpha$	$z = j\infty$
Uppermost band-edge	$s_B = j\omega_B$	$\Omega = 1$	$z = 0$
Passbands and inner stopbands	$s_A \leq s \leq s_B$	$\alpha \leq \Omega \leq 1$	jY-axis
Outer stopbands	$s < s_A, s > s_B$	$\Omega < \alpha, \Omega > 1$	X-axis
dc	$s = 0$	$\Omega = 0$	$z = \frac{1}{\alpha}$
Infinity	$s = j\infty$	$\Omega = \infty$	$z = 1$

The bilinear transformation in (4.9) can be re-arranged to obtain:

$$s^2 = \frac{\omega_B^2 - z^2\omega_A^2}{z^2 - 1} \implies S^2 = \frac{1 - \alpha^2 z^2}{z^2 - 1} \tag{4.11}$$

An example of the transformation of the roots of a 7-4 dual band characteristic function is demonstrated in Fig. 4.3. The passband reflection zeros and the inner stopband transmission zeros are spread across the entire imaginary axis. The transmission zeros in the outer two stopbands and those at dc and infinity are mapped to the real axis. It is the roots near the passband edges (i.e., the roots of the reflection and Hurwitz polynomials) that result in the numerical inaccuracies. Therefore, the applied transformation improves the conditioning of the matrices in the intermediate steps of the synthesis procedure by spreading the roots of the characteristic polynomials. This results in a significant improvement in the overall numerical accuracy.

The transformation in (4.9) is a ratio of the distance of a frequency point from the uppermost band-edge to that of its distance from the lowermost band-edge. Thus, the roots closer to ω_A will result in transformed roots that are better separated from each other than those closer to the ω_B band-edge. It is evident in Fig. 4.3 that the reflection zeros of the second passband are located closer together than the those of the first passband. Hence, it is important to note that as the number of passbands increases, the improvement in the numerical accuracy of the z-plane decreases. Nonetheless, the overall accuracy of the synthesis procedure in the transformed variable plane will always be better than that in the s-plane.
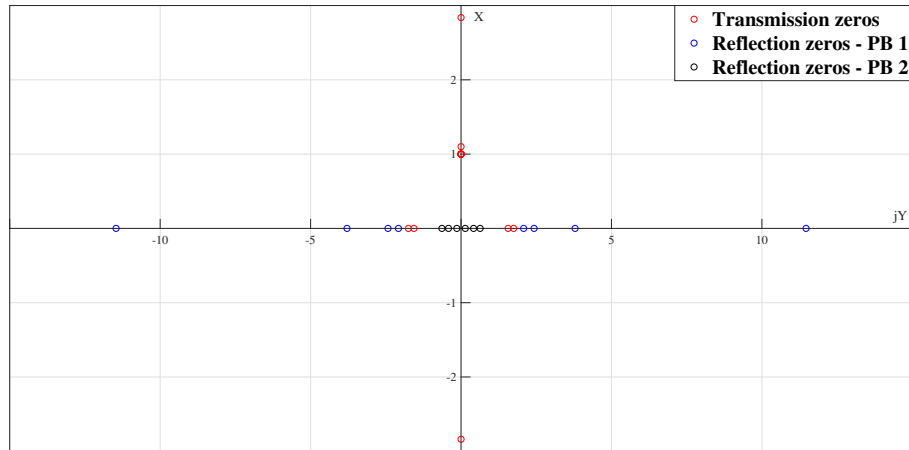
Fig. 4.3 Roots of a 7-4 dual bandpass characteristic function in the z-plane

4.3 Multi-band characteristic function

4.3.1 Introduction of dependent parameters

For a linear system of equations, the number of equations (or the number of knowns) and the number of unknowns must be equal so as to obtain a unique solution to the problem. If the number of unknowns exceeds the number of equations, or if the equations are degenerate, the solution to the linear system is either not unique or does not exist at all. On the other hand, if the number of equations exceeds the number of unknowns, a solution to the problem does not exist.

An Nth-degree single bandpass filter has N unknown coefficients for the monic reflection polynomial and the unknown scalar normalisation parameter, accounting for the $N+1$ unknowns. The $N+1$ critical points form the known parameters. Therefore, number of known and unknown parameters for a single bandpass filter are equal implying that a unique solution can be obtained. As the number of passbands is increased to N_B, the number of knowns, i.e., the critical points for an Nth degree filter increases to $N + N_B$ (as will be explained in section 4.4). However, the number of unknowns, viz., the N reflection polynomial coefficients and the normalisation parameter, remains constant at $N+1$. In order to match the number of knowns, some of the parameters have to be made dependent. For example, to obtain $N + N_B$ unknowns, $N_B - 1$ pairs of finite transmission zeros have to be dependent. Hence, moving to direct synthesis of multi-bandpass filters reduces the available degree of freedom in terms of the characteristic function specifications. Note that the above discussion is not pertinent to multiple single band filters connected in parallel. In that case,

the filters are synthesised as single band filters, where the number of knowns and unknowns is the same.

4.3.2 Characteristic function

For a multi-bandpass filter of degree N and with N_B passbands, the reflection polynomial can be expressed in terms of its constituent factors:

$$F(s) = \prod_{i=1}^{N}(s^2 + \omega_{r_i}^2) \tag{4.12}$$

where, ω_{r_i} is the ith reflection zero.

Suppose the transmission polynomial has N_{oz} prescribed transmission zeros at dc, N_{fz} pairs of prescribed transmission zeros at finite frequencies and $N_B - 1$ pairs of dependent transmission zeros at unknown finite frequencies. Such a polynomial can be expressed mathematically as:

$$P(s) = s^{N_{oz}} \prod_{m=1}^{N_{fz}}(s^2 + \omega_{f_m}^2) \prod_{n=1}^{N_B-1}(s^2 + \omega_{d_n}^2) \tag{4.13}$$

where, ω_{f_m} is the mth prescribed transmission zero position and ω_{d_n} is the nth dependent transmission zero position. Note that the subscript indicating the degree of the two polynomials is ignored so as to avoid confusion during the their transformation to the z-plane. The remaining transmission zeros are at located infinity and are denoted by N_{iz}, where

$$N_{iz} = 2N - N_{oz} - 2N_{fz} - 2(N_B - 1)$$
$$\text{so that} \quad 2N = N_{oz} + N_{iz} + 2N_{fz} + 2(N_B - 1) \tag{4.14}$$

In order for the above equation to be true, it is necessary that for a bandpass filter, the sum of the transmission zeros at dc and infinity must always be even.

Substituting the transformation (4.11) in equation (4.12) yields an expression for the reflection polynomial in the transformed variable plane.

$$F(z) = \prod_{i=1}^{N}\left[\left(\frac{1-\alpha^2 z^2}{z^2-1}\right) - \left(\frac{1-\alpha^2 z_{r_i}^2}{z_{r_i}^2-1}\right)\right]$$
$$= \frac{C_f}{(z^2-1)^N}\prod_{i=1}^{N}(z_{r_i}^2 - z^2) \tag{4.15}$$

where, z_{r_i} is the ith reflection zero mapped to the z-plane using equation (4.9) and C_f is a constant given by the expression:

$$C_f = \frac{(1-\alpha^2)^N}{\omega_B^N} \prod_{i=1}^{N} \frac{1}{(z_{r_i}^2 - 1)} \tag{4.16}$$

The transmission polynomial has N_{oz} transmission zeros at dc and hence, will yield a different form as that to the transformed reflection function in (4.15). The factor accounting for the transmission zeros at dc can be transformed to the z-plane as:

$$s^{N_{oz}} = \frac{1}{j\omega_B} \left(\frac{1-\alpha^2 z^2}{z^2 - 1} \right)^{N_{oz}/2} \tag{4.17}$$

Hence, for odd values of N_{oz} the factor accounting for transmission zeros at dc in the transformed variable plane will be a square-rooted term. Transforming the transmission zeros at finite frequencies yields factors of the form:

$$(s^2 + \omega_i^2) = \frac{1}{\omega_B} \left[\frac{(z_i^2 - z^2)(1-\alpha^2)}{(z^2 - 1)(z_i^2 - 1)} \right] \tag{4.18}$$

where, ω_i is the ith transmission zero at a finite frequency and z_i is its transformed position in the z-plane. Using the results in equations (4.17) and (4.18), the z-plane transmission function can be written as:

$$\begin{aligned}
P(z) &= \varepsilon C_t \left(\frac{1-\alpha^2 z^2}{z^2 - 1} \right)^{N_{oz}/2} \prod_{m=1}^{N_{fz}} \left[\frac{(z_{f_m}^2 - z^2)}{(z^2 - 1)} \right] \prod_{n=1}^{N_B - 1} \left[\frac{(z_{d_n}^2 - z^2)}{(z^2 - 1)} \right] \\
&= \varepsilon C_t \frac{(1-\alpha^2 z^2)^{N_{oz}/2}}{(z^2 - 1)^{N_{oz}/2 + N_{fz} + (N_B - 1)}} \prod_{m=1}^{N_{fz}} (z_{f_m}^2 - z^2) \prod_{n=1}^{N_B - 1} (z_{d_n}^2 - z^2)
\end{aligned} \tag{4.19}$$

where, the constant C_t can be given by:

$$C_t = \frac{(1-\alpha^2)^{N_{fz} + (N_B - 1)}}{\omega_B^{N_{fz} + (N_B - 1)} \prod_{m=1}^{N_{fz}} (z_{f_m}^2 - 1) \prod_{n=1}^{N_B - 1} (z_{d_n}^2 - 1)} \tag{4.20}$$

Taking the ratio of the two functions,

$$T(z)T(-z) = \frac{F(z)F(-z)}{P(z)P(-z)}$$

$$|T|^2 = \frac{C_f^2 \prod_{i=1}^{N}(z_{r_i}^2 - z^2)^2}{\varepsilon^2 C_t^2 (1 - \alpha^2 z^2)^{N_{oz}}(z^2 - 1)^{2(N - (N_{oz}/2 + N_{fz} + N_B - 1))} \prod_{m=1}^{N_{fz}}(z_{f_m}^2 - z^2)^2 \prod_{n=1}^{N_B - 1}(z_{d_n}^2 - z^2)^2}$$

$$= \frac{C_f^2 \prod_{i=1}^{N}(z_{r_i}^2 - z^2)^2}{\varepsilon^2 C_t^2 (1 - \alpha^2 z^2)^{N_{oz}}(z^2 - 1)^{N_{iz}} \prod_{m=1}^{N_{fz}}(z_{f_m}^2 - z^2)^2 \prod_{n=1}^{N_B - 1}(z_{d_n}^2 - z^2)^2}$$

(4.21)

Equation (4.21) demonstrates that the zeros of the characteristic function in the transformed frequency plane are the reflection zeros transformed to the z-plane. The denominator of the transformed characteristic function has factors accounting for the transmission zeros at dc, infinity and at finite frequencies. Notice that, unlike in the complex frequency plane, the factor accounting for the attenuation poles at infinity contributes to the degree of the transmission function in the transformed variable plane.

Evaluating the characteristic function in (4.21) at the lower band-edge yields

$$|T|^2 \bigg|_{z \to \infty} = \frac{C_f^2}{\varepsilon^2 C_t^2}$$

(4.22)

As explained in section 3.3.3, the value of the characteristic function at the critical points is set to ± 1. Assuming the characteristic function value at the lower band-edge is always set to (-1),

$$|T|^2 \bigg|_{z \to \infty} = \frac{C_f^2}{\varepsilon^2 C_t^2} = (-1)^2$$

(4.23)

Hence, by evaluating the characteristic function at the lowermost band-edge frequency, the constants and unknown scalar parameter are eliminated. This simplifies the characteristic function expression to:

$$|T|^2 = \frac{\prod_{i=1}^{N}(z_{r_i}^2 - z^2)^2}{(1 - \alpha^2 z^2)^{N_{oz}}(z^2 - 1)^{N_{iz}} \prod_{m=1}^{N_{fz}}(z_{f_m}^2 - z^2)^2 \prod_{n=1}^{N_B - 1}(z_{d_n}^2 - z^2)^2}$$

(4.24)

The denominator of the function in (4.24) is purely even and can be expressed in the form of $e(z)^2 - z^2 f(z)^2$, where $e(z)$ and $f(z)$ are both even polynomials in z. Therefore, the above

equation can be re-written as:

$$|T|^2 = \frac{F(z)^2}{e(z)^2 - z^2 f(z)^2}$$
$$= \frac{F(z)F(-z)}{[e(z) + zf(z)][e(z) - zf(z)]}$$

(4.25)

Equating the denominators of equations (4.24) and (4.25) yields

$$[e(z) + zf(z)][e(z) - zf(z)] = (1 - \alpha^2 z^2)^{N_{oz}} (z^2 - 1)^{N_{iz}} \prod_{m=1}^{N_{fz}} (z_{f_m}^2 - z^2)^2 \prod_{n=1}^{N_B - 1} (z_{d_n}^2 - z^2)^2$$

$$= \left[(1 + \alpha z)^{N_{oz}} (z + 1)^{N_{iz}} \prod_{m=1}^{N_{fz}} (z_{f_m} + z)^2 \prod_{n=1}^{N_B - 1} (z_{d_n} + z)^2 \right]$$

$$\times \left[(1 - \alpha z)^{N_{oz}} (z - 1)^{N_{iz}} \prod_{m=1}^{N_{fz}} (z_{f_m} - z)^2 \prod_{n=1}^{N_B - 1} (z_{d_n} - z)^2 \right]$$

(4.26)

The roots of the function $[e(z) + zf(z)]$ are located in the left-half plane and those of the function $[e(z) - zf(z)]$ are located in the right-half plane. Therefore,

$$[e(z) + zf(z)] = (1 + \alpha z)^{N_{oz}} (z + 1)^{N_{iz}} \prod_{m=1}^{2N_{fz}} (z_{f_m} + z) \prod_{n=1}^{2(N_B - 1)} (z_{d_n} + z)$$

$$\therefore [e(z) + zf(z)] = \prod_{m=1}^{2N - 2(N_B - 1)} (z_m + z) \prod_{n=1}^{2(N_B - 1)} (z_{d_n} + z)$$

(4.27)

where, z_m is the position of the mth prescribed transmission zero. This includes the transmission zeros at dc and infinity. By taking the square-root of the denominator of equation (4.24), an alternative expression for the transmission polynomial in the transformed plane can be obtained. For an odd value of N_{oz}, the transformed transmission function has square-rooted terms accounting for transmission zeros at dc and infinity.

$$P(z) = (1 - \alpha^2 z^2)^{N_{oz}/2} (z^2 - 1)^{N_{iz}/2} \prod_{m=1}^{N_{fz}} (z_{f_m}^2 - z^2) \prod_{n=1}^{N_B - 1} (z_{d_n}^2 - z^2)$$

$$= U(z) \sqrt{1 - \alpha^2 z^2} \sqrt{z^2 - 1} \quad \text{(for } N_{oz} \text{ odd)}$$

(4.28)

where, $U(z)$ is an even polynomial of degree $2N - 2$.

The new expression for the characteristic function contains N unknown reflection zeros (or N coefficients of the reflection zero polynomial) and $N_B - 1$ unknown dependent transmission zero positions accounting for $N + N_B - 1$ unknown parameters. By evaluating the characteristic function at the lower band-edge, the constants C_f, C_t and the normalisation scalar parameter ε can be eliminated. Therefore, the function has to be evaluated at the remaining $N + N_B - 1$ critical points that form the known parameters of the linear system. A linear system of $N + N_B - 1$ independent equations is, thus, to be solved in the transformed variable plane to obtain the solution for the multi-band synthesis problem.

4.4 Formulation of the linear system of equations

As derived in section 4.3.2, the generalised Chebyshev function for a multi-bandpass filter can be written as:

$$T(z) = \frac{-F(z)}{P_{rem}(z)P_d(z)} \tag{4.29}$$

where, $P_{rem}(z)$ is the function whose roots are the prescribed transmission zeros of the multi-band transfer function and $P_d(z)$ is the function whose roots are the dependent transmission zeros to be determined. It is important to note that the transmission zeros at infinity contribute to the degree of $P_{rem}(z)$. The negative sign in the numerator arises from the evaluation of the constants at the lowermost band-edge frequency (equation (4.23)). Re-arranging equation (4.29) gives,

$$
\begin{aligned}
T(z)P_{rem}(z)P_d(z) &= -F(z) \\
T(z)P_{rem}(z)(z^{2N_B-2} + d_{N_B-2}z^{2N_B-4} + \cdots + d_1 z^2 + d_0) \\
&= -(z^{2N} + f_{N-1}z^{2N-2} + f_{N-2}z^{2N-4} + \cdots + f_1 z^2 + f_0)
\end{aligned}
\tag{4.30}
$$

Here, $f_{N-1}, f_{N-2}, \cdots, f_1, f_0$ are the N unknown coefficients of the reflection function in the z-plane. Similarly, $d_{N_B-2}, d_{N_B-4}, \cdots, d_1, d_0$ are the $N_B - 1$ unknown coefficients of the dependent transmission function.

The critical points for an ith passband ($i \in 1 : N_B$) of a multi-band filter are comprised of the $N_i - 1$ in-band turning points and two cut-off frequency points. Hence, N_B passbands will have $\prod_{i=1}^{N_B}(N_i - 1) = N - N_B$ in-band turning points and $2N_B$ cut-off frequency points, resulting in $N + N_B$ critical points. However, as illustrated earlier, the function evaluates to (-1) at the lowermost band-edge frequency. Hence, equation (4.30) can be expressed as a

function of the remaining $N + N_B - 1$ critical points, so that

$$
\begin{aligned}
(f_{N-1} z_{cp}^{2N-2} &+ f_{N-2} z_{cp}^{2N-4} + \cdots + f_1 z_{cp}^2 + f_0) \\
&+ T(z_{cp}) P_{rem}(z_{cp})(d_{N_B-2} z_{cp}^{2N_B-4} + \cdots + d_1 z_{cp}^2 + d_0) = -z_{cp}^{2N} - T(z_{cp}) P_{rem}(z_{cp}) z_{cp}^{2N_B-2}
\end{aligned}
\tag{4.31}
$$

where, z_{cp} is an $N + N_B - 1$ by 1 column matrix of critical points. The above equation represents a linear system of $N + N_B - 1$ independent equations of the form:

$$
Ax = B
$$

where, A is an $N + N_B - 1$ by $N + N_B - 1$ square matrix defined by:

$$
A = \left[z_{cp}^{2N-2} \quad z_{cp}^{2N-4} \quad \cdots \quad z_{cp}^2 \quad 1 \quad T(z_{cp})P_{rem}(z_{cp})z_{cp}^{2N_B-4} \quad \cdots \right.
$$
$$
\left. T(z_{cp})P_{rem}(z_{cp})z_{cp}^2 \quad T(z_{cp})P_{rem}(z_{cp}) \right]
\tag{4.32}
$$

The $N + N_B - 1$ by 1 column matrix B is given by:

$$
B = \left[-z_{cp}^{2N} - T(z_{cp})P_{rem}(z_{cp})z_{cp}^{2N_B-2} \right]
\tag{4.33}
$$

The unknown matrix x is an $N + N_B - 1$ by 1 column matrix defined as:

$$
x = \left[f_{N-1} \quad f_{N-2} \quad \cdots \quad f_1 \quad f_0 \quad d_{N_B-2} \quad d_{N_B-1} \quad \cdots \quad d_1 \quad d_0 \right]^T
\tag{4.34}
$$

The system of linear dependent equations in the transformed variable plane can be solved iteratively as in the s-plane. The dependent transmission zero positions can be obtained by finding the roots of the purely even monic polynomial formed using the dependent transmission coefficients in (4.34).

4.4.1 Determination of the critical points

The initial critical points of a multi-bandpass filter are determined using the same process as in the complex frequency plane. The calculation of the initial in-band turning points is carried out in the ω-plane before transforming them to the z-plane. This step can not be carried out in the z-plane as the lowermost band-edge is mapped to $z = j\infty$.

To determine the initial turning points for a multi-bandpass filter, the ith passband ($i \in 1 : N_B$) must be divided into $N_i + 1$ equal frequency intervals in the range $[\omega_{li}, \omega_{ui}]$. Here, ω_{li} and ω_{ui} are the lower and upper cut-off frequencies of the ith passband, respectively. The $N_i - 1$ mid-points of these frequency intervals form the initial set of in-band turning points for the ith passband. These in-band turning points (stored in a row matrix ω_{tpi}) and the cut-off frequency points form the critical points for the ith passband. An $N + N_B$ by 1 column matrix of the initial critical points can be formed using

$$
\omega_{cp} = \left[\sum_{i=1}^{N_B} \left\{ zeros\left(1, \left(\sum_{m=1}^{i-1} N_m \right) + i - 1 \right), \omega_{li}, \omega_{tpi}, \right. \right.
$$
$$
\left. \left. \omega_{ui}, zeros\left(1, N + N_B - \left(\sum_{m=1}^{i} N_m \right) - i \right) \right\} \right]^T
$$

(4.35)

which can then be converted to the transformed frequency plane using (4.9). The lowermost band-edge at $z = j\infty$ can be excluded to form the desired $N + N_B - 1$ by 1 column matrix of the initial critical points in the z-plane. Note that the transformed critical points will be in descending order of magnitude.

If all the coefficients in matrix x are known, the in-band turning points can be obtained from the differential of the function in (4.29), i.e., the solution of:

$$
\frac{d}{dz} T(z) = \frac{d}{dz} \left\{ \frac{-F(z)}{P_{rem}(z) P_d(z)} \right\} = 0
$$

(4.36)

The in-band turning points are obtained by choosing the $N_i - 1$ roots of (4.36) in the range $[z_{ui}, z_{li}]$. These in-band turning points matrices, along with the cut-off frequency points can be combined to form the critical points matrix z_{cp} (as in 4.35).

The expected value of the characteristic function at the critical points must be set as explained in section 3.3.3. The iterative procedure in section 3.3.4 is followed till the algorithm converges.

4.5 Calculation of $E(z)$

The procedure for calculating the Hurwitz polynomial for a multi-bandpass filter in the transformed variable plane is significantly different to that in the s-plane. The reflection and transmission polynomials are related to the Hurwitz polynomial by the conservation of

energy equation, as alluded to in section 2.2. It can be shown that the three characteristic polynomials are related to their corresponding z-plane equivalents by an unimportant factor $(s^2 + \omega_A^2)^N$ [13].

$$F(z) \frac{F(s)}{(s^2 + \omega_A^2)^N}$$
$$P(z) \frac{P(s)}{(s^2 + \omega_A^2)^N} \tag{4.37}$$
$$E(z) \frac{E(s)}{(s^2 + \omega_A^2)^N}$$

where, $E(z)$ is the transformed Hurwitz polynomial. Subtituting the above expressions into the conservation of energy equation yields,

$$E(z)E^*(z) = F(z)F^*(z) + P(z)P^*(z)$$
$$= F(z)^2 + P(z)^2 \tag{4.38}$$

The reflection and transmission polynomials, $F(s)$ and $P(s)$ respectively, are either purely even or purely odd polynomials, Hence, in the transformed plane, the product of these polynomials with their corresponding conjugates can be represented by $F(z)^2$ and $P(z)^2$, respectively. On the contrary, $E(s)$ is neither purely even nor purely odd and hence, $E(z)E^*(z) \neq E(z)^2$. Substituting $e(z)^2 - z^2 f(z)^2$ for $P(z^2)$ yields,

$$E(z)E^*(z) = F(z)^2 + (e(z)^2 - z^2 f(z)^2) \tag{4.39}$$

As $F(z)^2$, $e(z)^2$ and $z^2 f(z)^2$ are all even functions, $E(z)E^*(z)$ must also be a purely even function of degree $4N$. It can, therefore, be represented by the product of quadratic factors of the form:

$$E(z)E^*(z) = \prod_{i=1}^{N}(z^2 + m_i z + n_i)(z^2 - m_i z + n_i)$$
$$= \prod_{i=1}^{N}(z^4 + M_i z^2 + N_1) \tag{4.40}$$

where, $M_i = 2n_i - m_i^2$ and $N_i = n_i^2$. By substituting the transformation (4.9) in equation (4.40), the s-plane quadratic roots can be obtained. These roots are of the form:

$$
\begin{aligned}
E(z)E^*(z) &= \prod_{i=1}^{N} \left[\left(\frac{s^2 + \omega_B^2}{s^2 + \omega_A^2} \right)^2 + M_i \left(\frac{s^2 + \omega_B^2}{s^2 + \omega_A^2} \right) + N_i \right] \\
&= \prod_{i=1}^{N} \left[\frac{R_i^2 s^4 + (2N_i \omega_A^2 + M_i(\omega_A^2 + \omega_B^2) + 2\omega_B^2)s^2 + T_i^2}{(s^2 + \omega_A^2)^2} \right] \\
&= \prod_{i=1}^{N} \left[\left(\frac{R_i s^2 + A_i s + T_i}{s^2 + \omega_A^2} \right) \left(\frac{R_i s^2 - A_i s + T_i}{s^2 + \omega_A^2} \right) \right] \\
&= \prod_{i=1}^{N} \left[\frac{R_i^2 s^4 + (2R_i T_i - A_i^2)s^2 + T_i^2}{(s^2 + \omega_A^2)^2} \right]
\end{aligned}
\tag{4.41}
$$

where, $R_i^2 = (1 + M_i + N_i)$,
$T_i^2 = (\omega_B^4 + M_i \omega_A^2 \omega_B^2 + N_i \omega_A^4)$, and
$2R_i T_i - A_i^2 = 2N_i \omega_A^2 + M_i(\omega_A^2 + \omega_B^2) + 2\omega_B^2 \Longrightarrow A_i^2 = 2R_i T_i - (2N_i \omega_A^2 + M_i(\omega_A^2 + \omega_B^2) + 2\omega_B^2)$.
The first quadratic term in equation (4.41) contains the required left-half plane roots. Once these roots are identified, the function can be converted back to the z-plane. This can be achieved by substituting the transformation in (4.11) into the final expression in (4.41). The quadratic factors in the z-plane can be represented by:

$$
E(z)E^*(z) = \prod_{i=1}^{N} (p_i z^2 + q_i \sqrt{(z^2 - 1)(\omega_B^2 - \omega_A^2 z^2)} + r_i)
\tag{4.42}
$$

where, $p_i = (T_i - R_i \omega_A^2)/(\omega_B^2 - \omega_A^2)$,
$q_i = (\sqrt{A_i} * \omega_B)/(\omega_B^2 - \omega_A^2)$ and
$r_i = (R_i \omega_B^2 - T_i)/(\omega_B^2 - \omega_A^2)$.

The quadratic factors can be multiplied to obtain the transformed Hurwitz function of the form $E(z) = E_A(z) + E_B(z) \sqrt{(z^2 - 1)(\omega_B^2 - \omega_A^2 z^2)} = E_A(z) + E_B(z) \sqrt{(z^2 - 1)(1 - \alpha^2 z^2)}$. The polynomials $E_A(z)$ and $E_B(z)$ are purely even polynomials of degrees $2N$ and $2N - 2$, respectively. The forward transmission and reflection coefficients can then be represented by the equations:

$$
\begin{aligned}
S_{11}(z) &= \frac{F(z)}{E_A(z) + E_B(z) \sqrt{(z^2 - 1)(1 - \alpha^2 z^2)}} \\
S_{21}(z) &= \frac{P(z)}{E_A(z) + E_B(z) \sqrt{(z^2 - 1)(1 - \alpha^2 z^2)}}
\end{aligned}
\tag{4.43}
$$

4.6 Coupling matrix synthesis

For a two-port reciprocal network, the *ABCD*-parameters must satisfy the following condition:

$$AD - BC = 1 \tag{4.44}$$

In order for the above condition to hold true in the transformed variable plane, a constant l must be computed such that the function $E_A(z) - lF(z)$ contains the factor $(z^2 - 1)$ [63, 65]. Thus,

$$l = \left. \frac{E_A(z)}{F(z)} \right|_{z=1} \tag{4.45}$$

In addition, the function $E_A(z) - lF(z)$ will also contain the factor $(1 - \alpha^2 z^2)$ [63]. The equations relating the *ABCD*-parameters and the characteristic polynomials for a two-port lossless symmetrical network are given in section 2.3. Using the relationships in equation (2.19) and the above results, the $[Y]$-parameters in the transformed frequency plane can be given by:

$$
\begin{aligned}
Y_{11n}(z) &= E_B(z)\sqrt{(z^2-1)(1-\alpha^2 z^2)} \\
Y_{12n}(z) &= P(z) = U(z)\sqrt{(z^2-1)(1-\alpha^2 z^2)} \\
Y_{21n}(z) &= P(z) = U(z)\sqrt{(z^2-1)(1-\alpha^2 z^2)} \\
Y_{22n}(z) &= E_B(z)\sqrt{(z^2-1)(1-\alpha^2 z^2)} \\
Y_d(z) &= E_A(z) + lF(z)
\end{aligned}
\tag{4.46}
$$

where, $P(z)$ can be represented by the equation (4.28). The $[ABCD]$-parameters in the transformed plane can then be computed using the standard $[Y]$- to $[ABCD]$ transformation [36]:

$$
\begin{bmatrix} A & B \\ C & D \end{bmatrix} = \frac{1}{2P(z)} \begin{bmatrix} E_B(z)\sqrt{(z^2-1)(1-\alpha^2 z^2)} & E_A(z)+lF(z) \\ E_A(z)-lF(z) & E_B(z)\sqrt{(z^2-1)(1-\alpha^2 z^2)} \end{bmatrix} \tag{4.47}
$$

As described in section 2.3.1, the *s*-plane admittance parameters of a bandpass filter can be expressed in terms of their residues and eigenvalues as:

$$
\frac{1}{y_d} \begin{bmatrix} y_{11n} & y_{12n} \\ y_{21n} & y_{22n} \end{bmatrix} = \begin{bmatrix} \sum_{k=1}^{N} \frac{2r_{11k}s}{s^2-p_k^2} & \sum_{k=1}^{N} \frac{2r_{12k}s}{s^2-p_k^2} \\ \sum_{k=1}^{N} \frac{2r_{21k}s}{s^2-p_k^2} & \sum_{k=1}^{N} \frac{2r_{22k}s}{s^2-p_k^2} \end{bmatrix} \tag{4.48}
$$

The eigenvalues in the transformed variable plane can be obtained by taking the roots of the denominator of the admittance function. By exploiting the transformation in (4.9), the eigenvalues can be transformed to the z-plane. Consider the kth term of the short-circuited admittance function $y_{11}(z)$ expressed in terms of its poles and residues. Substitute the transformation in (4.9) in this expression yields,

$$
\frac{2r_{11k}s}{s^2 - p_k^2} = \frac{2r_{11k}\sqrt{\frac{1-\alpha^2 z^2}{z^2-1}}}{\left(\frac{1-\alpha^2 z^2}{z^2-1}\right) - \left(\frac{1-\alpha^2 z_{p_k}^2}{z_{p_k}^2-1}\right)}
$$
$$
= \frac{2r_{11k}(z_{p_k}^2 - 1)\sqrt{(z^2-1)(1-\alpha^2 z^2)}}{(z_{p_k}^2 - z^2)(1-\alpha^2)}
$$

(4.49)

Hence, to determine the kth residue of the short-circuited admittance function $y_{11}(z)$, the following expression is evaluated at the kth eigenvalue.

$$
2r_{11k} = \left[\frac{y_{11n}}{y_d} \cdot \frac{(z_{p_k}^2 - z^2)(1-\alpha^2)}{(z_{p_k}^2 - 1)\sqrt{(z^2-1)(1-\alpha^2 z^2)}} \right]\Bigg|_{z=z_{p_k}}
$$
$$
= \left[\frac{E_B(z)\sqrt{(z^2-1)(1-\alpha^2 z^2)}}{y_d'(z)(z_{p_k}^2 - z^2)} \cdot \frac{(1-\alpha^2)(z_{p_k}^2 - z^2)}{(z_{p_k}^2 - 1)\sqrt{(z^2-1)(1-\alpha^2 z^2)}} \right]\Bigg|_{z=z_{p_k}}
$$

(4.50)

Cancelling the common factors yields,

$$
\therefore r_{11k} = \frac{1}{2}\left[\frac{E_B(z)(1-\alpha^2)}{y_d'(z)(z_{p_k}^2 - 1)} \right]\Bigg|_{z=z_{p_k}}
$$

(4.51)

Similarly, the kth residue of the short-circuited admittance function $y_{21}(z)$ can be calculated by evaluating the following expression at the kth eigenvalue.

$$
r_{21k} = \frac{1}{2}\left[\frac{U(z)(1-\alpha^2)}{y_d'(z)(z_{p_k}^2 - 1)} \right]\Bigg|_{z=z_{p_k}}
$$

(4.52)

Note that it is in the derivation of the above equation that the transmission function of the form $P(z) = U(z)\sqrt{(z^2-1)(1-\alpha^2 z^2)}$ is useful. Once the residues and eigenvalues of the transfer function are determined, the transversal coupling matrix can be obtained. By performing similarity transformations on the coupling matrix, a practically suitable topology can be obtained.

4.7   Triple band synthesis and design example

A triple bandpass filter for cellular base station specifications is to be synthesised in the tranformed frequency domain to validate the procedure presented in this chapter.

Specifications

Three passbands are specified at 1700 MHz - 1750 MHz, 1830 MHz - 1850 MHz and 1910 MHz - 1935 MHz. A minimum return loss level of 20 dB and a maximum insertion loss level of 1 dB are required in the three passbands. Rejection levels of > 30 dB are desired in the two stopbands of interest: 1770 MHz - 1790 MHz and 1860 MHz - 1880 MHz.

A 10th-degree triple bandpass filter with $N_1 = 4$, $N_2 = 3$ and $N_3 = 3$ was chosen to meet the desired specifications. As explained in section 4.3.1, for a triple bandpass filter ($N_B = 3$), two pairs of transmission zeros have to be dependent. To satisfy the desired stopband rejection levels, four finite transmission zero pairs were required with two pairs prescribed at 1788 MHz and 1873 MHz, respectively. The number of transmission zeros in both the inner stopbands was set to 2 so that one pair of dependent transmission zero is constrained in each of the inner stopbands.

Synthesis of Characteristic polynomials

The initial critical points are calculated in the ω-plane using the procedure explained in section 4.4.1. The transformation in equation (4.9) is used to map these critical points to the z-plane. The lowermost cut-off frequency, mapped to $z = j\infty$, is excluded to obtain the $N + N_B - 1$ by 1 matrix of initial critical points (z_{cp}). The expected value of the characteristic function at these critical points $\left(T_{expected}(z_{cp})\right)$ is set using the method described in section 3.3.3. The initial critical points in the transformed variable plane and the expected characteristic function values at these points are listed in Table 4.2. The cut-off frequency points mapped to the z-plane are given by $z_c = [j\infty, j1.9880, j0.9281, j0.7773, j0.3561, 0]^T$. The prescribed transmission zeros at 1788 MHz and 1873 MHz are mapped to $j1.3353$ and $j0.6180$ respectively.

The polynomial $P_{rem}(z)$, as defined in equation (4.29), can be formed using the prescribed transmission zeros. These include the transformed poles at $z = 1/\alpha$ corresponding to $s = 0$ and $z = 1$ corresponding to $s \to j\infty$. The prescribed transmission polynomial is given by:

$$
\begin{aligned}
P_{rem}(z) = {} & z^{16} + 12.1382z^{15} + 69.6855z^{14} + 253.8816z^{13} + 664.6687z^{12} + 1338.6z^{11} \\
& + 2154.9z^{10} + 2824.3z^9 + 3031.9z^8 + 2666.2z^7 + 1916.8z^6 + 1122.1z^5 \\
& + 528.6572z^4 + 194.6294z^3 + 52.5894z^2 + 9.2078z + 0.7752
\end{aligned}
$$

$$(4.53)$$

Table 4.2 Initial critical points and the expected value of the characteristic function at the critical points for a 10-4 triple bandpass filter

initial z_{cp} (rad/s)	$T_{expected}(z_{cp})$
$j3.9593$	$+1$
$j2.9961$	-1
$j2.4709$	$+1$
$j1.9880$	-1
$j0.9281$	-1
$j0.8696$	$+1$
$j0.8320$	-1
$j0.7773$	$+1$
$j0.3561$	$+1$
$j0.2754$	-1
$j0.2103$	$+1$
$j0.0000$	-1

Note that the prescribed transmission polynomial has purely real positive coefficients. By evaluating the above polynomial at the $N + N_B - 1$ critical points, the column matrix $P_{rem}(z_{cp})$ can be obtained. A linear system of $N + N_B - 1$ independent equations is be formed as explained in section 4.4. By solving the system of linear equations, a solution for the unknown parameters, viz., the N reflection polynomial coefficients and the $N_B - 1$ dependent transmission zeros is obtained. These computed parameters are then be used to form the new characteristic function of the form (4.29). By setting the derivative of the new characteristic function to zero, the new in-band turning points are determined, which are used to form the new critical points matrix z_{cp}. By evaluating the characteristic function at each of the new critical points, a column matrix $T_{optimised}(z_{cp})$ is obtained. The procedure was repeated till the algorithm converged for $\kappa = 10^{-8}$ in 4 iterations.

The dependent transmission zeros in the transformed domain were computed to be at $z_{d_1} = j0.6582$ and $z_{d_2} = j1.4882$ corresponding to 1867.1 MHz and 1776.4 MHz respectively. The final values for the transformed reflection polynomial are:

$$F(z) = z^{20} + 1.4765 \times 10^3 z^{18} + 3.4232 \times 10^3 + 2.7790 \times 10^4 z^{14} + 9.4798 \times 10^4 z^{12}$$
$$+ 13.8070 \times 10^4 z^{10} + 9.3944 \times 10^4 z^8 + 2.9008 \times 10^4 z^6 + 3.3292 \times 10^3 z^4 \qquad (4.54)$$
$$+ 125.3440 z^2 + 0.7438$$

The Hurwitz function $E(z)$ is calculated using the method described in section 4.5. The coefficients of the transformed characteristic polynomials are presented in Table 4.3. The singularities of the reflection and transmission polynomial and the factors of the $E(z)$ poly-

nomial of the form $(p_i z^2 + q_i \sqrt{(z^2-1)(\omega_B^2 - \omega_A^2 z^2)} + r_i)$ are also listed in Table 4.3. The normalisation parameters ε_R and ε_T are calculated using the same method as that in the s-plane. The transmission and reflection characteristics of the filter are plotted in Fig. 4.4.

Table 4.3 A 20th-degree triple bandpass Chebyshev filter function with four finite transmission zeros

(a) Transformed characteristic polynomials
$$\varepsilon_T = 0.1005, \varepsilon_R = 1$$

$P(z)$ $\quad = z^{20} + 12.1382 z^{19} + 72.3336 z^{18} + 2.8602 \times 10^2 z^{17} + 8.5016 \times 10^2 z^{16}$
$\quad\quad 2.0226 \times 10^3 z^{15} + 3.9818 \times 10^3 z^{14} + 6.6127 \times 10^3 z^{13} + 9.3760 \times 10^3 z^{12}$
$\quad\quad 1.1429 \times 10^4 z^{11} + 1.2013 \times 10^4 z^{10} + 1.0892 \times 10^4 z^9 + 8.5135 \times 10^3 z^8$
$\quad\quad 5.7241 \times 10^3 z^7 + 3.2916 \times 10^3 z^6 + 1.6012 \times 10^3 z^5 + 6.4728 \times 10^2 z^4$
$\quad\quad 2.1113 \times 10^2 z^3 + 52.5116 z^2 + 8.8348 z + 0.7438$

$F(z)$ $\quad = z^{20} + 1.4765 \times 10^3 z^{18} + 3.4232 \times 10^3 + 2.7790 \times 10^4 z^{14} + 9.4798 \times 10^4 z^{12}$
$\quad\quad + 13.8070 \times 10^4 z^{10} + 9.3944 \times 10^4 z^8 + 2.9008 \times 10^4 z^6 + 3.3292 \times 10^3 z^4$
$\quad\quad + 125.3440 z^2 + 0.7438$

$E_A(z)$ $\quad = z^{20} + 27.8061 z^{18} - 1.9922 \times 10^2 z^{16} - 3.6917 \times 10^3 z^{14} - 1.4265 \times 10^4 z^{12}$
$\quad\quad - 2.0895 \times 10^4 z^{10} - 1.3427 \times 10^4 z^8 - 3.5299 \times 10^3 z^6 - 1.9810 \times 10^2 z^4$
$\quad\quad 20.4802 z^2 + 0.8041$

$E_B(z)$ $\quad = -0.6970 z^{18} + 30.4121 z^{16} + 6.1781 \times 10^2 z^{14} + 3.2442 \times 10^3 z^{12}$
$\quad\quad + 6.6947 \times 10^3 z^{10} + 6.2644 \times 10^3 z^8 + 2.7101 \times 10^3 z^6 + 4.8329 \times 10^2 z^4$
$\quad\quad + 23.1329 z^2 - 0.3860$

(b) Transformed roots of the characteristic polynomials

Transmission zeros (Roots of $P(z)$)	Reflection zeros (Roots of $F(z)$)	Transmission/Reflection poles		
		p_i	q_i	r_i
$\pm j1.4882$	$\pm j11.0118$	0.4966	0.9880	27.6166
$\pm j1.3353$	$\pm j3.7517$	0.5921	0.9172	9.8367
$\pm j0.6582$	$\pm j2.4208$	0.9188	0.4492	4.7494
$\pm j0.6180$	$\pm j2.0278$	0.9997	0.0285	0.0158
$+1.1382$	$\pm j0.9156$	0.9983	0.0669	0.0557
$+1$	$\pm j0.8420$	0.9950	0.1137	3.5868
±1	$\pm j0.7846$	0.9970	0.0879	0.6870
±1	$\pm j0.3422$	0.9987	0.0580	0.9130
±1	$\pm j0.2415$	0.9995	0.0369	0.1490
$\pm1(\times2)$	$\pm j0.0851$	0.9997	0.0261	0.5769
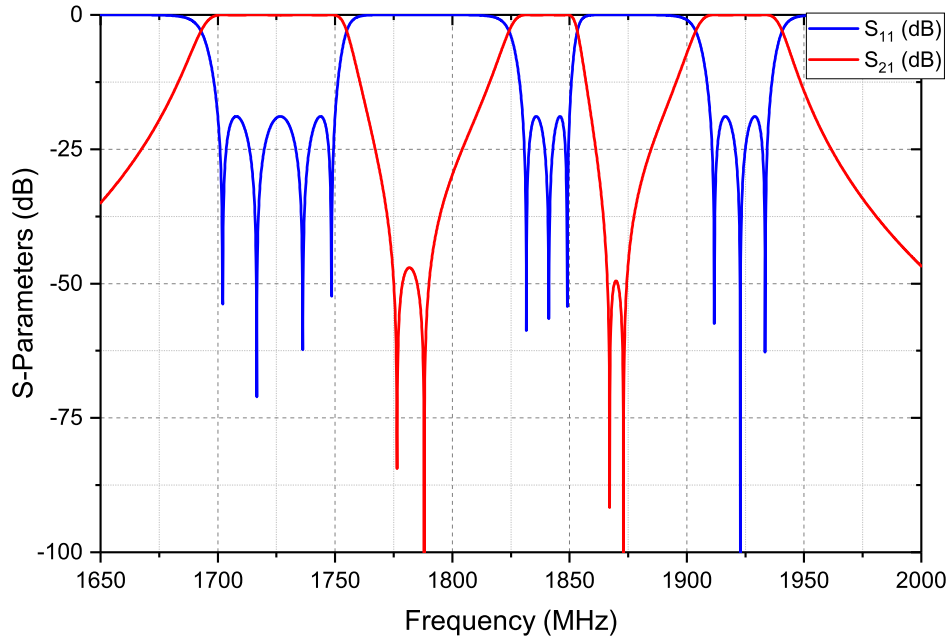
Fig. 4.4 An example of a 20th-degree triple bandpass filter response with four finite transmission zeros

Coupling matrix synthesis

The triple bandpass filter is to be realised as a coaxial cavity structure. A network composed of distributed elements yields a better approximation for such prototypes. Thus, the singularities of the characteristic polynomials in the transformed plane can be converted to the complex frequency plane using (4.11) and further to the complex distributed plane using Richard's transformation [20]. The characteristic polynomials in the ρ-plane can then be formed using the mapped roots.

The characteristic polynomials can be used to obtain the short-circuited admittance parameters, from which the transversal coupling matrix of the form $Y_{BP} = M_{Ts} + \rho M_{Cs} + M_{Ls}/\rho$ can be obtained. By performing similarity transformations, the transversal coupling matrix can be reconfigured into the desired topology. In order to realise a 10-4 filter transfer function, a topology comprising of two triplets and a quartet was implemented. The first triplet was used to generate the transmission zero at 1876 MHz and the second triplet was used to generate the dependent transmission zero at 1776.4 MHz. The remaining tow finite transmission zeros were generated using a quartet. The distributed network topology is displayed in Fig. 4.5, where each resonant node represents a shunt parallel-connected resonator composed of a short and an open-circuited stub. The $N \times N$ inductive and capacitive distributed coupling matrices, M_{Ls} and M_{Cs}, are given by the equations (4.55) and (4.56) respectively. The termination matrix M_{Ts} is an $N \times N$ matrix with all entries zero except $M_{Ts}(1,1) = M_{Ts}(N,N) = 0.0906$.

In the formulation of the coupling matrix it is assumed that all the inter-resonator couplings are inductive. In some cases, however, one or more of the inductive inter-resonator couplings may be negative. These can be converted to capacitive couplings by performing appropriate matrix operations that eliminate the entry from the M_{Ls} matrix and introduce it into the M_{Cs} matrix.
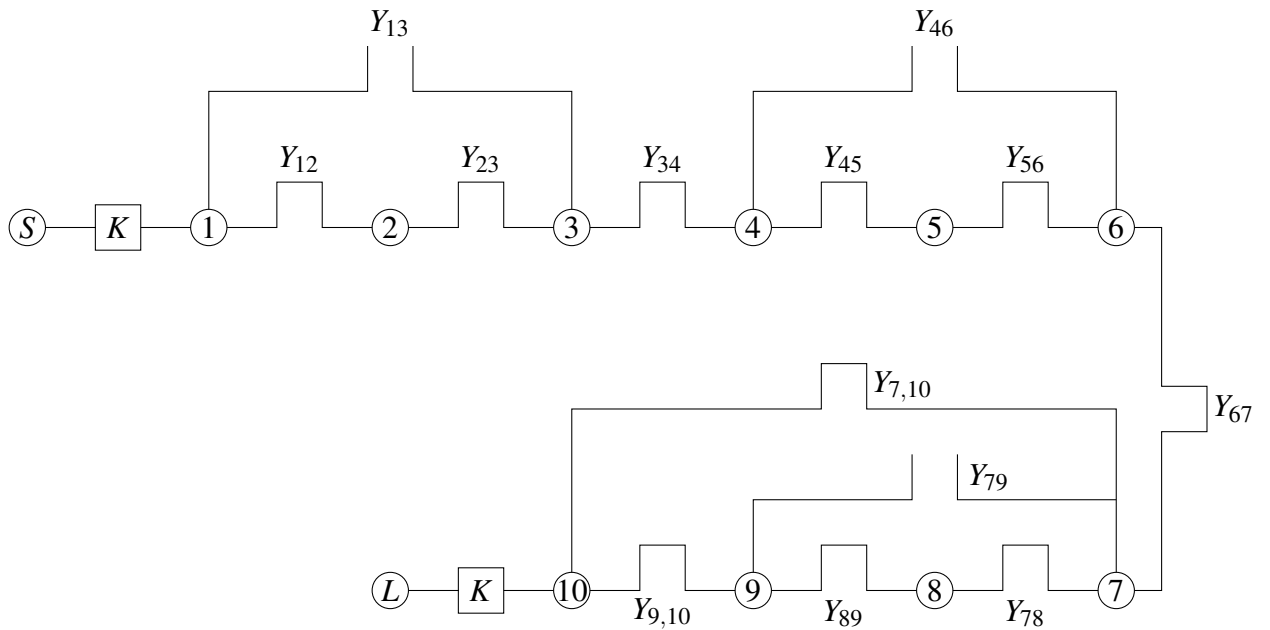
Fig. 4.5 A schematic of the network topology for the 10-4 triple bandpass filter

$$M_{Ls} = \begin{bmatrix} 0.9675 & -0.0727 & 0 & 0 & 0 & 0 & 0 & 0 & 0 & 0 \\ -0.0727 & 1.1269 & -0.0285 & 0 & 0 & 0 & 0 & 0 & 0 & 0 \\ 0 & -0.0285 & 0.9746 & -0.0761 & 0 & 0 & 0 & 0 & 0 & 0 \\ 0 & 0 & -0.0761 & 1.0208 & -0.1084 & 0 & 0 & 0 & 0 & 0 \\ 0 & 0 & 0 & -0.1084 & 0.9681 & -0.0361 & 0 & 0 & 0 & 0 \\ 0 & 0 & 0 & 0 & -0.0361 & 0.9749 & -0.1175 & 0 & 0 & 0 \\ 0 & 0 & 0 & 0 & 0 & -0.1175 & 1.0071 & -0.0260 & 0 & -0.0921 \\ 0 & 0 & 0 & 0 & 0 & 0 & -0.0260 & 1.0654 & -0.0741 & 0 \\ 0 & 0 & 0 & 0 & 0 & 0 & 0 & -0.0741 & 1.0258 & -0.1312 \\ 0 & 0 & 0 & 0 & 0 & 0 & -0.0921 & 0 & -0.1312 & 1.0090 \end{bmatrix}$$

$$(4.55)$$

$$
M_{Cs} =
\begin{bmatrix}
1 & 0 & -0.1450 & 0 & 0 & 0 & 0 & 0 & 0 & 0 \\
0 & 1 & 0 & 0 & 0 & 0 & 0 & 0 & 0 & 0 \\
-0.1450 & 0 & 1 & 0 & 0 & 0 & 0 & 0 & 0 & 0 \\
0 & 0 & 0 & 1 & 0 & -0.1084 & 0 & 0 & 0 & 0 \\
0 & 0 & 0 & 0 & 1 & 0 & 0 & 0 & 0 & 0 \\
0 & 0 & 0 & -0.1084 & 0 & 1 & 0 & 0 & 0 & 0 \\
0 & 0 & 0 & 0 & 0 & 0 & 1 & 0 & -0.0224 & 0 \\
0 & 0 & 0 & 0 & 0 & 0 & 0 & 1 & 0 & 0 \\
0 & 0 & 0 & 0 & 0 & 0 & -0.0224 & 0 & 1 & 0 \\
0 & 0 & 0 & 0 & 0 & 0 & 0 & 0 & 0 & 1
\end{bmatrix}
\tag{4.56}
$$

Physical Implementation

The purely distributed coupling matrix Y_{BP} was converted into the combline equivalent circuit using the method described in section 3.4. The $N \times N$ coupling matrix was scaled such that the shunt short-circuited stub impedance is 75 Ω. The final element values for the combline equivalent circuit in a 50 Ω system are presented in Table 4.7.

Table 4.4 Element values for combline realisation of a 20th-order triple band transfer function

Shunt short-circuited stubs	Lumped capacitors	Inter-resonator couplings
$Z_r = 75\ \Omega$	$C_1 = 1.173$ pF $C_2 = 1.06287$ pF $C_3 = 1.18154$ pF $C_4 = 1.13028$ pF $C_5 = 1.21192$ pF $C_6 = 1.16843$ pF $C_7 = 1.18548$ pF $C_8 = 1.10752$ pF $C_9 = 1.15189$ pF $C_{10} = 1.16967$ pF	$K_{in} = 223.731\ \Omega,\ K_{out} = 225.258\ \Omega$ $Z_{12} = 1414.84\ \Omega,\ Z_{13} = 623.971\ \Omega$ $Z_{23} = 2647.54\ \Omega,\ Z_{46} = 899.238\ \Omega$ $Z_{34} = 1217.78\Omega,\ Z_{79} = 2970.29\ \Omega$ $Z_{45} = 821.915\ \Omega,\ Z_{7,10} = 958.016\ \Omega$ $Z_{56} = 2951.42\Omega$ $Z_{67} = 756.461\ \Omega$ $Z_{78} = 3365.54\ \Omega$ $Z_{89} = 1345.35\ \Omega$ $Z_{9,10} = 713.555\ \Omega$

Using the practical procedures outlined in section 2.4, initial dimensions for the coaxial prototype were determined. The filter was modelled on an EM software and the physical parameters were optimised until a satisfactory response was achieved. The final values for the physical dimensions of the triple band prototype are listed in Table 4.7. Fabrication tolerances of ± 0.1 were specified for the prototype filter. The coaxial triple band prototype with lid and tuning screws is diplayed in Fig. 4.6.

The inductive couplings were realized by varying the height of ribs between two resonators. The capacitive cross-couplings were realized using suspended copper strips. The capacitance on the open-circuited end of the resonators was achieved using tuning screws. The height

Table 4.5 Physical dimensions for the 10-4 triple bandpass filter prototype

Dimension	Value (mm)
Coaxial resonator length	20.7
Resonator outer diameter	10.0
Resonator inner diameter	8.0
Cavity height	31.0
Rib height 2-3	6.0
Rib height 3-4	5.5
Rib height 4-5	7.0
Rib height 5-6	5.7
Rib height 6-7	10.2
Rib height 8-9	5.2
Rib height 9-10	10.8
Copper strip 1-3	11.0 (height), 16.5 (length)
Copper strip 4-6	7.0 (height), 17.0 (length)
Copper strip 7-9	10.2 (height), 12.6 (length)
Tuning screw diameter	6.35
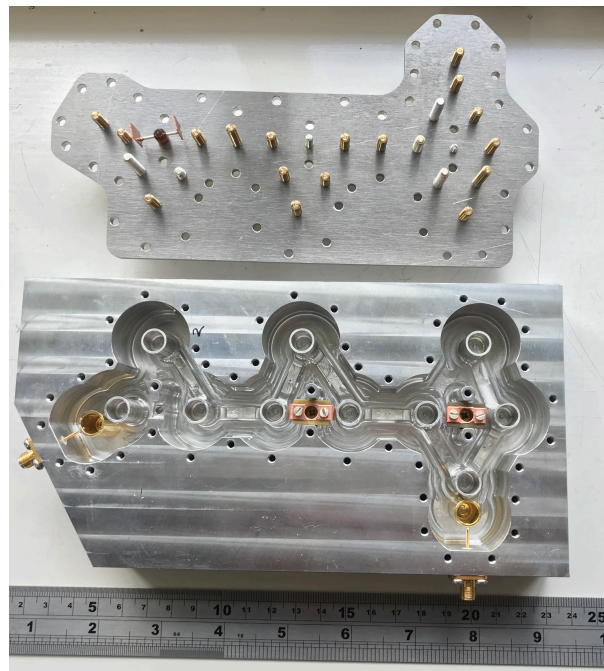
Fig. 4.6 A fabricated triple bandpass filter hardware for the 10-4 triple bandpass filter

and the distance of these copper strips from the corresponding resonator surfaces determined the coupling achieved between two resonators. Both coupling mechanisms were designed with tuning screws on the lid to aid fine-tuning post-fabrication. Brass transformers were utilized to realize the external coupling.
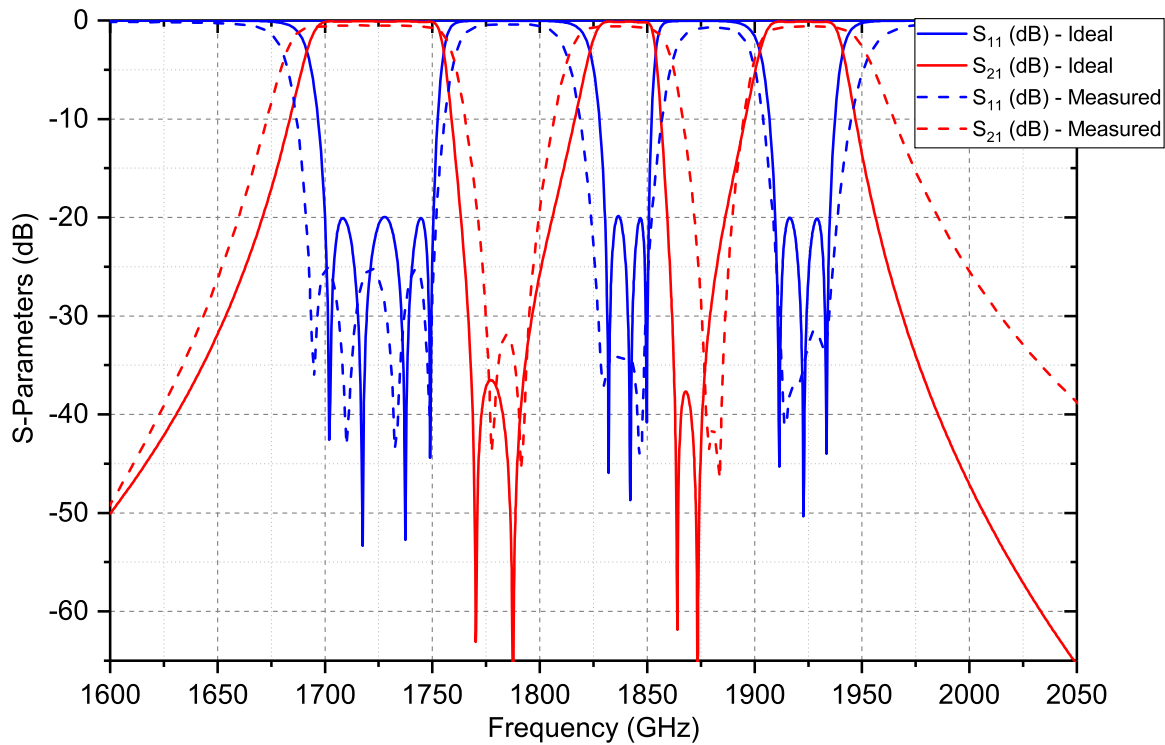
Fig. 4.7 Ideal and measured responses for the 10-4 triple bandpass filter

A comparison between the ideal circuit simulation and the measured response of the triple band filter can be seen in Fig. 4.7. The filter was designed for a return loss of > 20 dB in all three passbands. From the measured response, it can be seen that the passband return loss levels are > 25 dB in all passbands, thus, satisfying the corresponding specification. The measured passband insertion loss was in the range of about 0.5 dB to 0.85 dB. On an average, the measured Q-factor at the centre of each passband is about 1090. The bandwidth of the first and second passbands is slightly wider than the required specifications. A small frequency shift in the position of finite transmission zeros is also observed. This frequency shift in the transmission zero positions can be attributed to the errors arising due to the partial manual fabrication of the suspended copper strips and due to the filter hardware not being completely optimized on the electromagnetic software pre-fabrication. The bandwidth expansion could be a result of the frequency shift in the position of transmission zeros. These issues can be easily rectified by complete optimization of the hardware on the electromagnetic software pre-fabrication. Note that as the number of passbands increases, the sensitivity to the element values also increases. Overall, the measured response achieved was satisfactory and is in reasonably good agreement with the circuit simulation response.

4.8   Conclusion

The transformation from the complex frequency variable to the transformed frequency variable has been discussed in detail in section 4.2. A multi-band characteristic function for a generalised Chebyshev response has been defined in the new variable plane. The linear optimisation technique, introduced in Chapter 3, has been re-formulated for multi-band synthesis in the z-plane. A synthesis and design example of a triple bandpass filter realised using a coaxial prototype has been presented in section 4.7. The following chapter uses the linear optimisation technique in the z-plane to synthesise various network topologies for a given transfer function. A pattern recognition algorithm is applied to these topologies in order to establish certain guidelines for predicting the optimum network topology for power handling for a given transfer function.

Chapter 5

Investigation of the optimum topology for single band transfer functions

5.1 Motivation

The typical filtering specifications for multiplexers employed at the cellular base station require low passband insertion loss (typically < 0.5 dB), high rejection levels on one side of the passband and comparatively low rejection levels on the other side. Such high performance filters require estimation of their power handling capacity to avoid multipaction (for space applications) or ionisation breakdown (for terrestrial communications).

Ionisation breakdown [66] occurs when a non-conductive medium, such as air, is subjected to high electric fields to the point where the air molecules become ionised and the medium becomes conductive. Multipaction [67] is an electron resonance phenomenon where electrons accelerated by the applied RF fields impact with the surfaces to continuously create secondary electrons. Thus, the peak internal electric fields generated in the cavity can lead to breakdown of the filter. This is an important factor in determining the power handling capacity of the filter. The various factors influencing the power handling capability of the RF filters, viz. the geometry and dielectric material of the filter, the atmospheric pressure and temperature have been covered extensively in [36, 68–71].

An accurate estimation of the power handling capacity of a microwave filter involves modelling and fine-tuning of 3-dimensional resonant cavities in an electromagnetic (EM) software. Such EM packages employ computationally intensive numerical techniques such as Finite Element Method or Finite Difference Time Domain method. Even with the available effi-

cient software packages, the entire process is cumbersome and inefficient to make initial predictions about the power handling capacity of the filter.

An alternative approach for estimating the power handling capacity of the cavity filter is by predicting the peak internal electric fields using the equivalent circuit model [72, 73]. Ernst [73] derived explicit formulae relating the peak internal electric fields of a Chebyshev direct-coupled cavity waveguide filter to its group delay. In [74], he derived expressions to prove that the time-averaged stored energy (t.a.s.e) of a two-port filter is directly proportional to its group delay. As the t.a.s.e of the filter is related to the power handling of the filter, his work proved that the power handling capacity and the group delay of a two-port filter network are directly proportional to each other. A method to calculate the peak nodal voltages of a cross-coupled lumped element equivalent filter network, which are related to the peak internal electric fields of the filter prototype by an appropriate scaling factor has been presented in [75]. A similar approach that exploits the t.a.s.e of the bandpass lumped element prototype and relates it to the peak internal electric fields of the filter prototype to determine the power handling capacity of a filter has been proposed in [76]. All of the above methods are concerned with estimating the power handling capacity of a filter by exploiting the equivalent circuit model of the filter prototype.

It is well-known that for any given lumped two-port linear network with an excitation applied at the input, a response is obtained at the output [24]. The problem of determining such a network (Fig. 5.1), given the excitation and the response is known as synthesis. The solution to the problem of synthesis is typically not unique. In other words, a given transfer function can be realised using multiple filter networks, i.e., filter topologies. Depending upon the chosen filter topology, the peak nodal voltages or the t.a.s.e distribution in the network varies. Hence, the power handling capacity of a filter is strongly influenced by the topology used to realise it. This research has focused on prediction and improvement of the power handling capacity of the filter by choosing the topology giving the minimum peak t.a.s.e for a given transfer function.
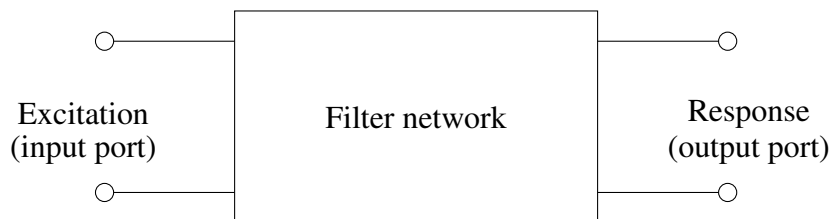
Fig. 5.1 Schematic of a two-port filter network with an excitation applied at the input and a response observed at the output

A comparison between the t.a.s.e distribution within cascaded triplet and cascaded quartet topologies realising a 6th-degree power transfer function with a pair of symmetric finite transmission zeros has been presented in [77]. It was concluded that the cascaded quartet topology demonstrated a much lower peak t.a.s.e than the cascaded triplet topology. Ernst [78] used a stochastic search method to find the optimum topology for a given transfer function by minimising the peak t.a.s.e. However, this method can result in topologies that are practically unrealisable. A similar approach to finding an optimum power handling topology for a given power transfer function by minimising the peak nodal voltages was proposed in [79]. It is important to understand that the t.a.s.e distribution in filter topologies is influenced by the power transfer function in consideration. Hence, investigating the t.a.s.e distribution in various topologies for a single transfer function is insufficient to make concrete conclusions about the prediction of an optimum topology for any randomly chosen transfer function.

In this chapter, an unsupervised clustering algorithm, called the k-means clustering algorithm has been implemented to discover patterns in the stored energy distribution of bandpass filter networks. With the aid of this algorithm, key characteristics of the stored energy distribution within various network topologies realising the same power transfer function can be discovered. Therefore, by finding regularities in large stored energy data sets comprising of numerous transfer functions and their network topologies, predictions about the optimum topology for power handling can be made. A large set of specifications have been investigated to provide generalized "rules" to predict the optimum topology. The study has been limited to practically realisable and widely used topologies comprising of cascaded triplets (CT) and cascaded quartets (CQ).

5.2 K-Means clustering algorithm

The k-means clustering algorithm [80] is an iterative algorithm that partitions a given data set into K homogeneous groups (i.e., clusters) based on a similarity (or dissimilarity) measure. The algorithm groups the objects (also referred to as data points) in the data set such that objects belonging to the same cluster are more similar to each other than the objects belonging to different clusters. Each object is a multi-dimensional varible, i.e, it is defined by multiple variables or attributes. The k-means algorithm is classed as an unsupervised learning algorithm, meaning that the underlying structure of the data is unknown. Hence, there are no pre-existing labels associated with the input data. A comprehensive description of unsupervised learning algorithms can be found in [81].

5.2.1   Method

Suppose $X^T = \{x_1, x_2, \cdots, x_{n-1}, x_n\}$ represents a data set with n objects, where each object x_i is described by m attributes, i.e, $x_i{}^T = \{x_{i,1}, x_{i,2}, \cdots, x_{i,m-1}, x_{i,m}\}$. Consequently, X is an $n \times m$ matrix, where the rows represent the objects and the columns represent the attributes that define each object, as in equation (5.1).

$$
X = \begin{bmatrix}
x_{1,1} & x_{1,2} & x_{1,3} & \cdots & x_{1,m-1} & x_{1,m} \\
x_{2,1} & x_{2,2} & x_{2,3} & \cdots & x_{2,m-1} & x_{2,m} \\
\vdots & \vdots & \vdots & \vdots & \vdots & \vdots \\
x_{i,1} & x_{i,2} & x_{i,3} & \cdots & x_{i,m-1} & x_{i,m} \\
\vdots & \vdots & \vdots & \vdots & \vdots & \vdots \\
x_{n-1,1} & x_{n-1,2} & x_{n-1,3} & \cdots & x_{n-1,m-1} & x_{n-1,m} \\
x_{n,1} & x_{n,2} & x_{n,3} & \cdots & x_{n,m-1} & x_{n,m}
\end{bmatrix}
\tag{5.1}
$$

The algorithm commences by randomly choosing K objects from the data set that form the initial set of centroids represented by the vector μ_k, where $k = 1, 2, \cdots, K$. Here, μ_k is an m-dimensional vector that represents the centroid, i.e. the mean, of the kth cluster. By computing the distance between the objects and each centroid, the objects are assigned to the nearest centroid. In each iteration the centroids are updated by taking the mean of the objects assigned to that cluster. The objects are re-allocated to the nearest cluster and the algorithm continues to iterate until either the cost function is minimized or the assignment of data points stops changing. The cost function to be minimised can be represented mathematically as:

$$
E = \sum_{k=1}^{K} \sum_{i=1}^{n} y_{ik} \cdot d\{x_i, \mu_k\}
\tag{5.2}
$$

where, $y_{ik} = 1$ if the object i belongs to the cluster k and $y_{ik} = 0$, otherwise. $d\{x_i, \mu_k\}$ is the squared Euclidean distance between the ith object and the kth centroid. Thus, the function to be minimised is the sum of the squared Euclidean distances between a centroid and the objects assigned to the corresponding cluster. By minimising this distance, the objects belonging to the same cluster must be closer together than the objects belonging to a different cluster. Note that the initial centroids are chosen from the objects in the data set, but the updated centroids usually are not members of the data set.

The k-means algorithm usually converges within a few iterations. The computational complexity of each iteration of the k-means algorithm is $K \times n \times t$, where t is the time taken to compute each squared Euclidean distance. Therefore, k-means is a fast clustering algorithm

that can be effectively used on a large set of data. It is one of the most commonly used pattern recognition algorithms owing to its simplicity and efficiency in clustering large data sets [82]. A visual representation of the clusters generated by implementing the k-means algorithm on a synthetically generated two-dimensional data set is presented in Fig. 5.2. The centroids represent an average of the objects within each cluster.
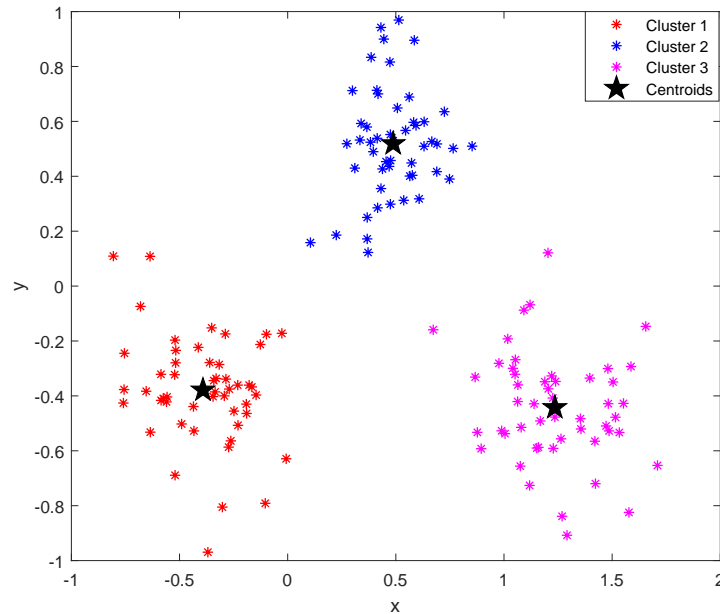
Fig. 5.2 K-means clustering results for synthetically generated data, $K = 3$

As k-means is a distance-based clustering algorithm, it can only be applied to numerical data or sequential categorical data [83]. Numeric attributes can take continuous values within a finite range of values. On the contrary, categorical attributes only take discrete values or represent characteristics, for example, the gender or occupation of a person. An apparent issue with clustering numerical values is that it will be dominated by the attributes with the largest variance and mean. To alleviate this issue, weighting the numeric values appropriately may be necessary. Alternatively, all the numeric attributes can be standardised to have a mean of zero and a variance of unity. The latter technique is used more commonly and is an important step in pre-processing the data.

5.2.2   Limitations

As alluded to in the previous section, the k-means clustering algorithm can only be applied to numeric attributes or sequential categorical attributes. It can, however, be extended to k-

prototypes algorithm which is capable of dealing with mixed data sets [83, 84]. Alternatively, each categorical attribute can be represented by binary attributes (0 or 1) which can be treated as numeric values. However, this method is not suitable for clustering large or high-dimensional data sets.

The k-means algorithm is a non-deterministic, greedy algorithm. This means that the clustering results are dependent on the randomly chosen initial centroids. Different initial centroids yield different clustering results. As it is a greedy algorithm, the solution obtained may be a locally optimal solution but not a globally optimal one. The simplest approach to mitigate these issues is to run the algorithm with multiple sets of randomly chosen initial centroids and choose the best run. This simplistic clustering algorithm is also susceptible to outliers. These must be identified and preferably filtered out before the analysis process.

A major concern with using the k-means algorithm is choosing the value of K correctly. There are various methods available to address this issue. The elbow method and the silhouette method, as described in section 5.2.3, are some of the most frequently used techniques in the determination of the value of K. Another approach is to perform hierarchical clustering on a subset of the data set to get familiarised with it. Based on these results and on the understanding of the data set, an appropriate value of K can then be chosen. The prior two methods are used in this work and are described in the following section.

5.2.3   Choosing the value of K

The most commonly adopted approach for determining the appropriate value of K involves running the algorithm for various values of K and then choosing the optimum value based on a designated metric. The two methods used in this work are described below.

The Elbow Method

The elbow method is one of the techniques used to find the optimal number of clusters for a data set. The procedure involves performing k-means clustering for various values of K. For each value of K, the within cluster sum of squares (WCSS) of the distances of the objects to the closest centroid is calculated. Note that this is just the cost function for each K. If there are clear, well-separated clusters within the data set, by plotting the cost function for each K against the number of clusters, an "arm-shaped" plot is obtained. The optimal number of clusters is then chosen to be the "elbow-point" of this arm-shaped plot. As the number of clusters starts increasing, the sum of squares of distances of the objects from the centroid for

each cluster starts decreasing. However, the optimal number of clusters is chosen to be the one where the reduction in the value of this sum starts diminishing.

To illustrate, the elbow method was applied to the two-dimensional synthetically generated data in section 5.2.1. The plot obtained is displayed in Fig. 5.3. It is evident that the elbow point is obtained at $K = 3$ meaning that the optimal number of clusters for the given data set is 3. If the data set does not comprise of well-separated or clear clusters, then the elbow
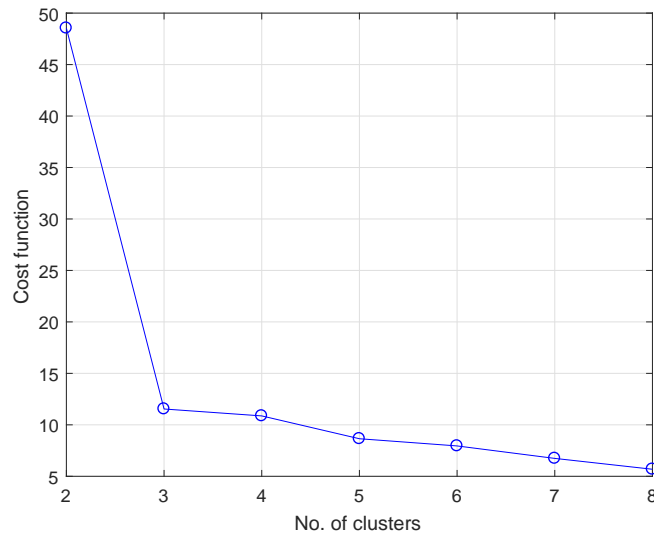
Fig. 5.3 The elbow method applied to the synthetically generated data in Fig. 5.2, the elbow point obtained at $K = 3$.

method may fail to give an accurate answer. In this case, the elbow point of the plot may not be clear. The silhouette method may provide a more accurate solution for such data sets.

The Silhouette Method

The silhouette method is one of the techniques used to validate the clusters for a given data set. The silhouette coefficient is a measure of the quality of each cluster. It lies within the range $[-1, +1]$. A high value of the silhouette coefficient indicates good clustering, i.e., the objects within that cluster are far away from the objects in the neighbouring cluster. On the contrary, a negative value of the silhouette coefficient indicates bad clustering, i.e., the object is nearer to the neighbouring cluster than the one it is assigned to. A silhouette coefficient of 0 indicates that the object lies at the decision boundary of the two clusters. The optimal value of K is chosen to be the one that maximises the average silhouette coefficient for different

values of K [85]. An in-depth description of the procedure to calculate the average silhouette coefficients can be obtained in [85].

The average silhouette coefficients for the synthetically generated data in Fig. 5.2 for $K = \{2,3,4,5,6,7,8\}$ are given in Table 5.1. From the obtained values it can be observed that the average silhouette coefficient is highest for $K = 3$. Hence, $K = 3$ is the optimum number of clusters for the two-dimensional synthetically generated data, as is clearly visible in Fig. 5.2. The silhouette plot for the example with $K = 3$ is displayed in Fig. 5.4. It can be seen that the silhouette coefficient values for each cluster are greater than 0.8, meaning that the clusters are well-separated.

Table 5.1 Silhouette coefficients (S.C) for the example in Fig. 5.2.

K	2	3	4	5	6	7	8
S.C	0.6839	0.8893	0.7841	0.6638	0.6665	0.5412	0.5129
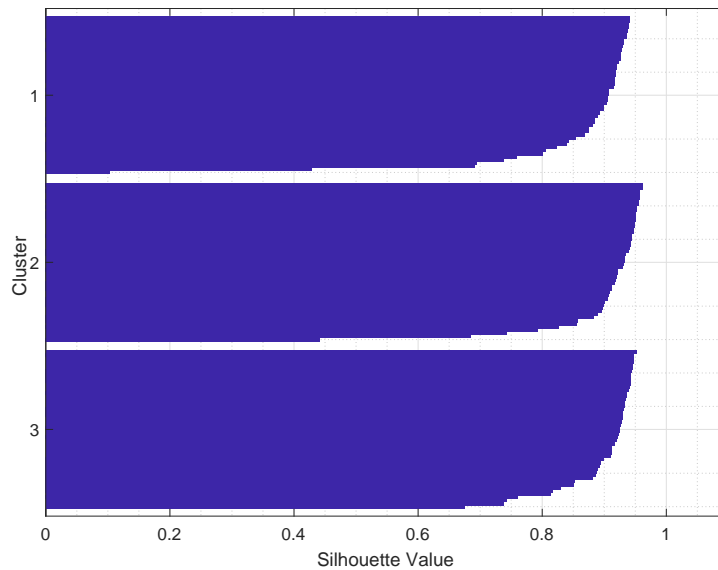
Fig. 5.4 Silhouette values for the two-dimensional synthetically generated data, $K = 3$

The entire algorithm was implemented on MATLAB. The input to the algorithm comprises of the input data matrix of the form X, the number of clusters that the data has to be partitioned into, the maximum number of iterations allowed for the algorithm to converge and the number of random centroid initialisations. The output of the clustering algorithm comprised of an $n \times 1$ vector matrix of clustering indices for each object and the K centroid positions.

5.3 Stored energy in two-port filter networks

The total time-averaged stored energy for any given filter network is the sum of the electric and magnetic energies stored in each resonator. This total t.a.s.e is constant for all networks realising the same power transfer function. The distribution of this energy within the network, however, is dependent on the topology used to realise it.
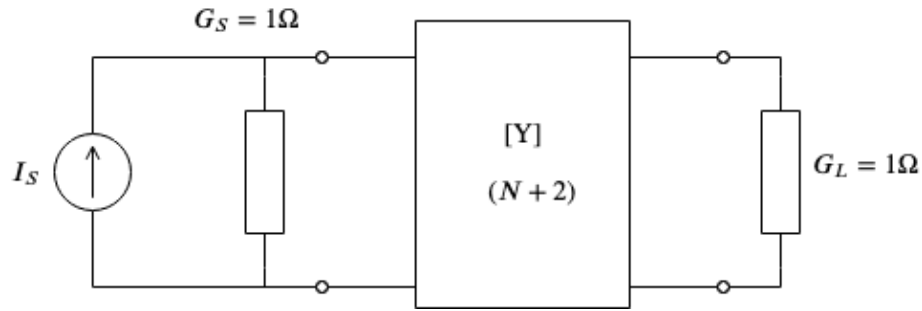
Fig. 5.5 A multi-coupled two-port network represented by an $(N+2)$ admittance matrix [7].

For a general multi-coupled two-port lossless bandpass filter network represented by Fig. 5.5, the complex nodal voltages are given by the equation

$$V = Y^{-1}I \tag{5.3}$$

Here, Y is equal to the $(N+2) \times (N+2)$ bandpass admittance matrix defined by equation (2.34). The nodal voltages and currents are given by the $(N+2) \times 1$ column matrices $V = [V_0, V_1, \cdots, V_N, V_{N+1}]^T$ and $I = I_S \cdot [1, 0, \cdots, 0, 0]^T$. I_S is the excitation current for an input power of 1 W.

The time averaged energies stored in a capacitor and a inductor are given by equations (5.4a) and (5.4b), respectively.

$$W_C(\omega) = \frac{1}{4}|V(\omega)|^2 C \tag{5.4a}$$

$$W_L(\omega) = \frac{1}{4}|I(\omega)|^2 L = \frac{1}{4}\frac{|V(\omega)|^2}{\omega^2 L} \tag{5.4b}$$

Therefore, the total t.a.s.e in the kth resonator is given by the sum of the time-averaged stored energies in the shunt inductor and shunt capacitor at the kth node.

$$W_k(\omega) = \frac{1}{4}|V_k(\omega)|^2 \left(C_k + \frac{1}{\omega^2 L_k}\right) \tag{5.5}$$

Typically, the t.a.s.e plot has a minima at the centre of the passband, rising to sharp peak(s) in the transition region just outside the passband. A high value of the peak t.a.s.e implies high peak internal electric fields, implying that the chances of a breakdown occuring are higher. Thus, by choosing a topology that lowers the peak t.a.s.e for a given transfer function the power handling capacity of a filter can be significantly improved.

5.4   T.a.s.e distribution in filter networks for 6-2 single band-pass transfer functions

The clustering algorithm was implemented on various cascaded triplet (CT) and cascaded quartet (CQ) topologies generated for 240 different single bandpass specifications. The order of the filter network was set to 6 ($N = 6$) and the number of finite transmission zero pairs was set to 2. This would enable realisation of each transfer function using networks comprising of two triplets or a single quartet. As proven in [86], the total t.a.s.e of a power transfer function is strongly influenced by its selectivity. Selectivity of a filter is determined by the bandwidth and degree of the filter and by the postion of the transmission zeros. Thus, to simplify the analysis process, the passband frequencies and the degree of the filter can be fixed whilst varying the position of the finite transmission zeros. By doing so, the selectivity of the power transfer function is effectively altered.

5.4.1   Generation of input data

The passband frequencies were set to 1000 MHz - 1030 MHz. The finite transmission zeros (t.z) frequencies were generated randomly within a reasonable frequency range on either side of the passband. The transmission zeros in the lower stopband were constrained to frequencies ranging from 900 MHz (f_1 - 0.1 $\times f_1$) - 995 MHz (f_1 - 0.005 $\times f_1$). Similarly, the transmission zeros in the upper stopband were constrained to frequencies from 1035.2 MHz (f_2 + 0.005 $\times f_2$) to 1133 MHz (f_2 + 0.1 $\times f_2$). The generated specifications can be such that both transmission zeros lie in the lower stopband, or both transmission zeros lie in the upper stopband, or one transmission zero lies in the lower stopband and the other one lies in the upper stopband. Sixty specifications were generated to account for each of these transmission zero cases, resulting in a total of 240 specifications.

The various n-tuplet arrangements that can be synthesised for a 6-2 transfer function are displayed in Fig. 5.6 and Fig. 5.7, respectively. Note that the quartets in Fig. 5.7 are

displayed with a forward asymmetric cross-coupling (for example, 1-3 cross-coupling for network (a)). By changing the direction of the asymmetric cross-coupling for each network
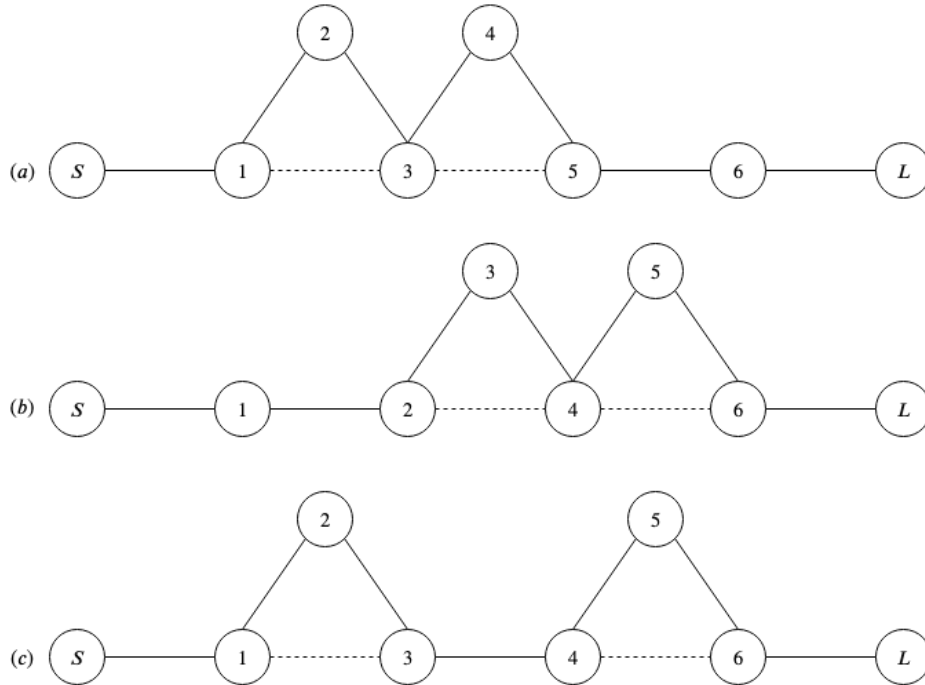
Fig. 5.6 Cascaded triplet networks for a 6-2 transfer function

in Fig. 5.7, six CQ topologies can be obtained for each specification. Similarly, by changing the sequence of transmission zero extraction, six CT topologies can be obtained for each specification. Thus, a total of twelve topologies are synthesised per power transfer function.

As the objective is to discover patterns that aid in predicting the optimum topology for power handling, two CT topologies and two CQ topologies with the lowest peak t.a.s.e were extracted for each transfer function. In order to facilitate the comparison of the topologies and to comprehend the factors that influence the t.a.s.e distribution, two worst case CT and CQ topologies were also extracted for each transfer function. As a result, the problem was reduced to clustering 1920 topologies for 240 different single bandpass filtering specifications.

The single bandpass Chebyshev polynomials were generated using the multi-band linear optimisation technique in Chapter 4. The single bandpass characteristic function accounts for the simplest case for the algorithm with $N_B = 1$ and $P_d(z) = 1$. The lumped element networks for the twelve topologies were synthesised using the method described in section 4.6.
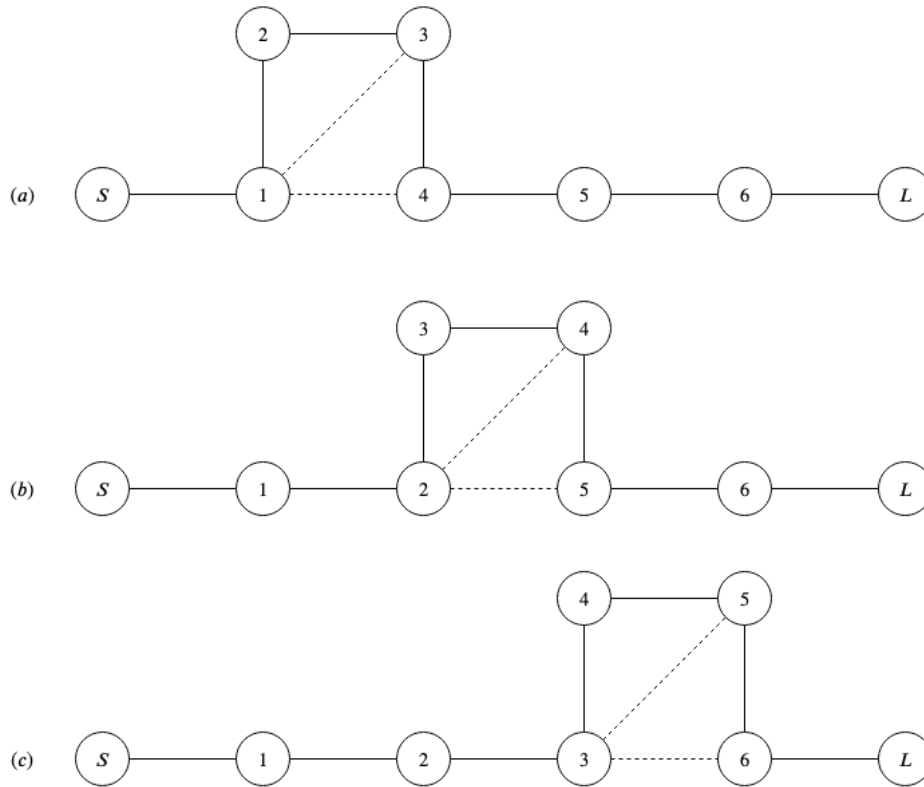
Fig. 5.7 Cascaded quartet networks for a 6-2 transfer function

5.4.2   Modelling input data

The filter topology and the t.a.s.e distribution within the network determine the power handling capacity of that network. A CQ topology can be defined by the following attributes:

1. the position of the quartet in the network,

2. the relative position of the finite transmission zeros (from the closest band-edge) generated by the quartet, and

3. the direction of the asymmetric cross-coupling of the quartet.

Similarly, a CT topology can be defined by the attributes listed below:

1. positions of the triplets in the network, and

2. the relative transmission zero positions (from the closest band-edge) in the appropriate sequence.

The calculated peak t.a.s.e for any given topology serves as an indicator of the power handling capacity of the filter network. A higher peak t.a.s.e value implies that the power handling capacity of that filter network is worse than the network with a lower peak t.a.s.e value. These attributes are used to form the input data set for k-means clustering.

As the CQ and CT topologies are described by dissimilar attributes, individual input data sets have to be modelled for the two types of networks. Clustering can then be performed on the two data sets separately. The CT topologies were used to form a data set denoted by X_t and the CQ topologies formed a data set denoted by X_q. Each data set consisted of two lowest peak t.a.s.e and two highest peak t.a.s.e topologies for each transfer function. This accounted for a total of 960 topologies in each data set. Therefore, the X_t and the X_q data sets consist of 960 objects each, described by the various attributes listed above.

The peak t.a.s.e was expressed in nJ for all objects in both data sets. The relative positions of the two finite transmission zeros from the closest band-edges was expressed in MHz. As only a single quartet is required to realise the desired transfer functions, the sequence of the relative transmission zero positions in the input data set is irrelevant. In the case of the CT topologies, however, the transmission zero positions must correspond to the triplet that is used to generate them. Note that the relative transmission zero positions take positive values for transmission zeros in the lower stopband (as $f_{n_i} < f_1$) and negative values for those in the upper stopband (as $f_{n_i} > f_2$). The position of the triplet or the quartet is represented by their last resonator. The direction of the asymmetric cross-coupling in the quartet can be represented using binary attributes, i.e., '1' represents forward asymmetric cross-coupling and '0' represents backward asymmetric cross-coupling. For the simple single quartet case in consideration, the asymmetric cross-coupling direction was not used as an attribute in the input data set, as better clustering results were obtained by excluding it. It was, however, used in the analysis of the obtained clusters. Likewise, the resonator demonstrating the maximum peak t.a.s.e for each topology was also used in the analysis process. These variables can be stored in an additional vector matrix that is used solely for the purpose of cluster analysis.

To illustrate, consider an example specification with two finite transmission zeros placed at 980 MHz and 1040 MHz. Suppose topologies (a) in Figures 5.6 and 5.7 account for the worst case topologies. These topologies can be entered into the X_t and X_q data sets, respectively, as follows:

The entries x_{t_1} and x_{q_1} in Tables 5.2 and 5.3 represent the objects for the CT and CQ topologies in consideration, respectively. The attributes of the objects are represented the columns of the respective tables. From the object entry in the X_t data set, it can be inferred that the first triplet (resonators 1-2-3) produces the transmission zero positioned at 10 MHz

Table 5.2 Object entry for the CT data set

	Peak t.a.s.e (nJ)	Relative t.z position (1)	Relative t.z position (2)	Triplet position (1)	Triplet position (2)
x_{t_1}	72.5	-10	20	3	5
	$x_{t_{11}}$	$x_{t_{12}}$	$x_{t_{13}}$	$x_{t_{14}}$	$x_{t_{15}}$

Attributes

Table 5.3 Object entry for the CQ data set

	Peak t.a.s.e (nJ)	Relative t.z position (1)	Relative t.z position (2)	Quartet position
x_{q_1}	52.8	20	-10	4
	$x_{q_{11}}$	$x_{q_{12}}$	$x_{q_{13}}$	$x_{q_{14}}$

Attributes

from the upper band-edge, i.e., at 1040 MHz. Similarly, the second triplet (resonators 3-4-5) generates a transmission zero positioned at 20 MHz from the lower band-edge, i.e., at 980 MHz. The object entry for the X_q data set represents a quartet positioned at resonators 1-2-3-4. By cascading rows of such objects, each representing a distinct topology, the two input data sets, viz., X_t and X_q can be developed.

Note that, although the resonator numbers are discrete values, they are sequential categorical attributes and hence, can be treated as numeric values for k-means clustering. As alluded to in section 5.2.1, the input data sets have to be standardised such that each attribute has a mean of zero and a standard deviation of unity. The standardised data set forms the first input to the clustering algorithm.

5.4.3   Optimum value of K

The second input to the clustering algorithm is the number of clusters that the data set has to be partitioned into. The elbow method, described in section 5.2.3, was used to determine the optimum value of K for both data sets. The k-means clustering algorithm was implemented on both data sets X_t and X_q separately. The value of K was varied from 2 to 15 in steps of unity. The within cluster sum of squares of distances from the objects to the corresponding cluster centroids was computed for each value of K. In order to improve the chances of

finding a globally optimal solution for each K, the algorithm was run with 10 sets of randomly chosen initial centroids. A maximum of 30 iterations were allowed for the convergence of each run. For each value of K, the run that minimised that cost function the most was chosen as the best run. By plotting the WCSS for different values of K, the elbow point was determined for both data sets. From Figures 5.8a and 5.8b, it is evident that the elbow point occurs at $K = 11$ for X_t data set and at $K = 8$ for X_q data set. Thus, the optimum number of clusters that the X_t and X_q data sets are to be partitioned into is $K = 11$ and $K = 8$, respectively.
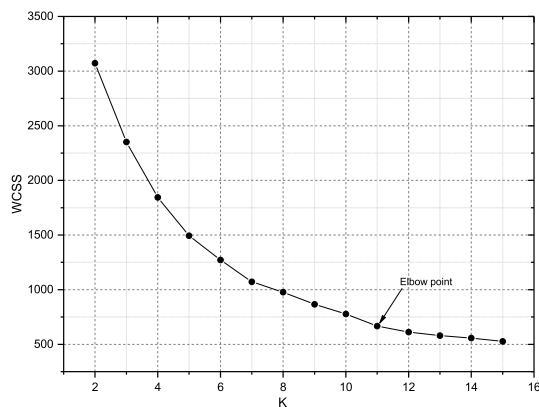
(a) The elbow method applied to the X_t data set; the elbow point obtained at $K = 11$.
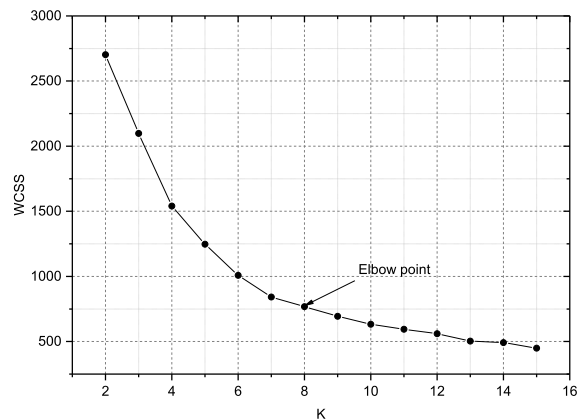
(b) The elbow method applied to the X_q data set; the elbow point obtained at $K = 8$.

Fig. 5.8 The elbow method applied to the X_t and X_q data sets.

5.4.4   Clustering Results and Analysis

Graphical representations of the means of the peak t.a.s.e and the relative transmission zero positions for each cluster of the X_t and X_q data sets are displayed in Fig. 5.9 and Fig. 5.14 respectively. The number of objects with the various CT network arrangements (displayed in Fig. 5.6) grouped in each cluster is represented by the bar graph in Fig. 5.10. Category A in the graph implies that the transmission zero closest to band-edge is created using the triplet positioned closest to the source. Likewise, category B implies that the transmission zero closest to the band-edge is created using the triplet positioned closest to the load. The number of objects with the various CQ network arrangements (displayed in Fig. 5.7) grouped in each cluster is represented by the bar graph in Fig. 5.15. The number of clustered objects with forward and backward asymmetric cross-coupling is also indicated in the graph. The

statistics on the resonator demonstrating the peak t.a.s.e are exhibited using the bar graphs in Fig. 5.11 and Fig. 5.16.

Cascaded triplet data set

Clusters 1, 2 and 7 account for the topologies representing transfer functions that are highly selective and/or extremely asymmetric. The total t.a.s.e, and consequently the average peak t.a.s.e of the power transfer functions included in these three clusters is higher than all other clusters. Cluster 1 consists of the best case topologies, whereas cluster 2 consists of the second best and at least one of the worst case topologies. Cluster 7 accounts for objects with the worst case topologies for the transfer functions that are most selective. The objects grouped in cluster 1 are such that the transmission zero closest to the band-edge is generated using the triplet closest to the load (category B). On the contrary, the objects in clusters 2 and 7 belong to category A. All objects in cluster 7 have network arrangement (a) implying that the two triplets are positioned close to the source. Approximately 95% of the objects in cluster 2 meaning that the two triplets have a shared resonator between them. For all objects in clusters 2 and 7, the resonator demonstrating the peak t.a.s.e is the one opposite to the cross-coupling of the first triplet. In cluster 1, the resonator giving the peak t.a.s.e is dependent upon the position of the two transmission zeros. If both transmission zeros lie in the same stopband, the resonator giving the maximum peak t.a.s.e is the one opposite to the cross-coupling of the triplet closest to the source. If the transmission zeros lie on either side of the passband and if the triplets are positioned closer to the load, then the resonator giving the peak t.a.s.e is the one opposite to the cross-coupling of the triplet closest to the load (object x_{t_1}). If the first triplet is shifted closer to the source and if the transmission zero generated by it is sufficiently close to the band-edge, then the resonator demonstrating the peak t.a.s.e s the one opposite opposite to its cross-coupling (object x_{t_2}). Consider the topology and transfer function represented by object x_{t_3}. The transmission zero generated by the first triplet (resonators 2-3-4) is located very close to the lower band-edge. In this case, the resonator demonstrating the peak t.a.s.e will be the one opposite to the first cross-coupling, i.e., resonator 3. On the contrary, if the first triplet produced a transmission zero far away from the band-edge, as in object x_{t_4}, the peak t.a.s.e resonator is always the one opposite to the second cross-coupling.

The objects in clusters 3 and 4 represent topologies for transfer functions with both transmission zeros placed in the upper stopband (USB). The transfer functions have relatively low selectivity, i.e., the transmission zeros are positioned considerably away from the upper band-edge. Cluster 3 comprises of the second best and the worst case CT topologies for
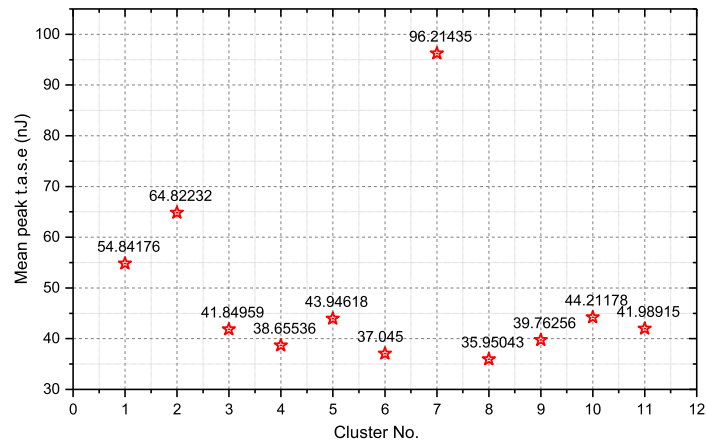
(a) Mean peak t.a.s.e for each cluster - X_t data set
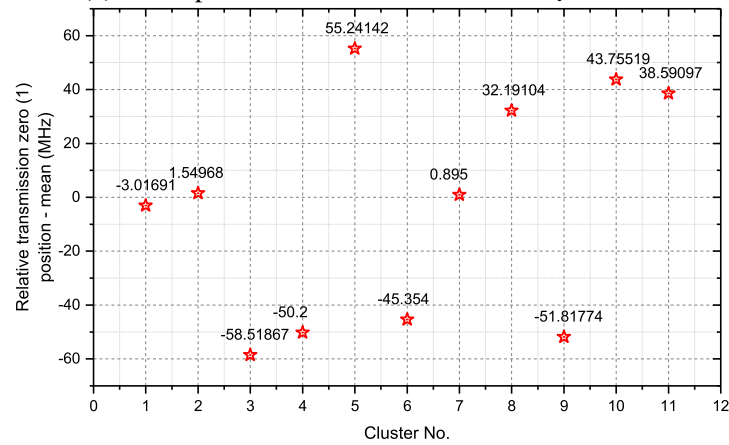
(b) Mean t.z (1) position for each cluster - X_t data set
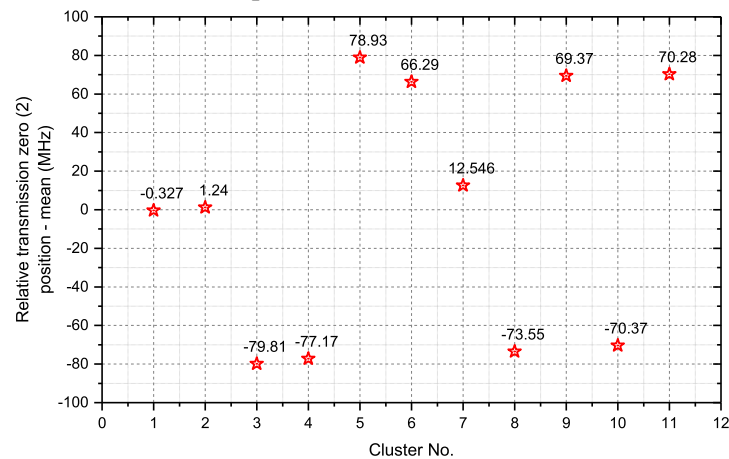
(c) Mean t.z (2) position for each cluster - X_t data set

Fig. 5.9 Means of the peak t.a.se and relative transmission zero positions for each cluster of the X_t data set.
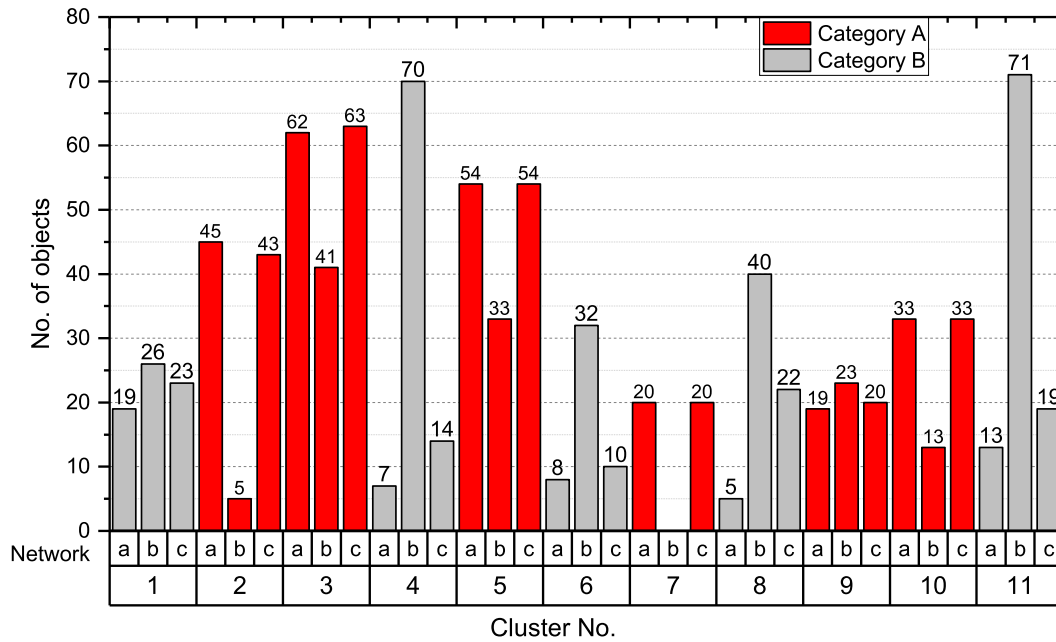
Fig. 5.10 CT network topologies grouped in each cluster for the 6-2 single band specifications: Category A implies that the t.z closest to the band-edge is generated by the triplet closest to the source. Category B implies that the t.z closest to the band-edge is generated by the triplet closest to the load.
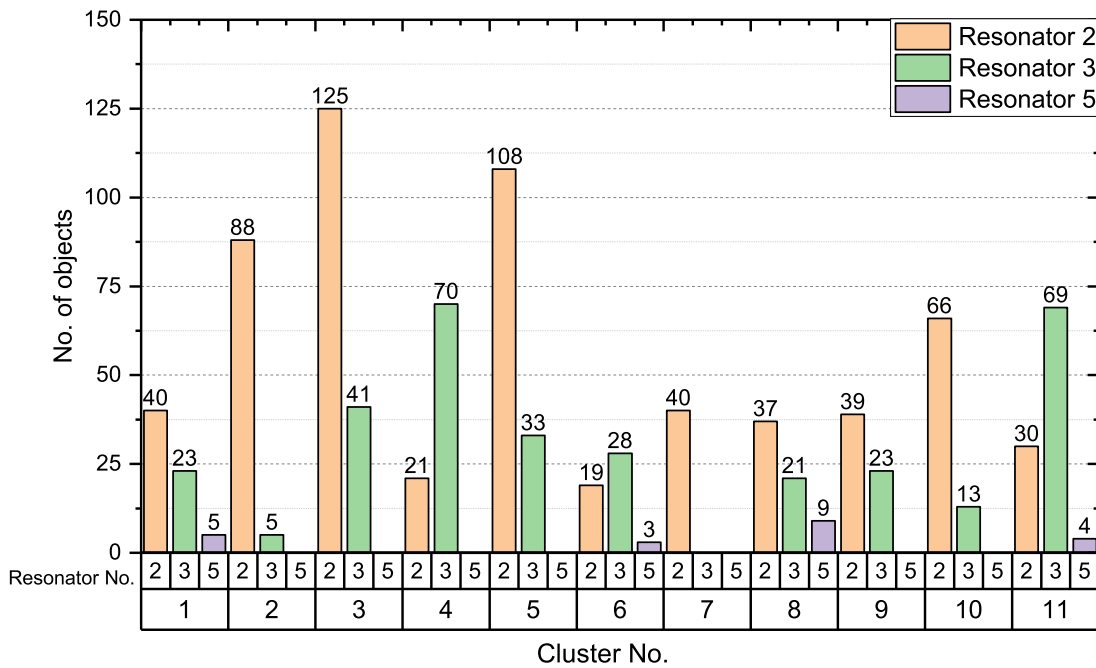
Fig. 5.11 Statistics for the peak t.a.s.e resonators in each cluster for the 6-2 single band CT network topologies.

Table 5.4 Examples of objects clustered in Cluster 1 of the X_t data set and the corresponding peak t.a.s.e resonator

	Peak t.a.s.e (nJ)	Relative t.z position (1)	Relative t.z position (2)	Triplet position (1)	Triplet position (2)	Peak t.a.s.e resonator
x_{t_1}	44.42	7.64	-21.7	6	4	5
x_{t_2}	49.4	7.64	-21.7	6	3	2
x_{t_3}	69.08	-6.4	7.7	6	4	3
x_{t_4}	53.73	-5.5	56.5	6	3	5
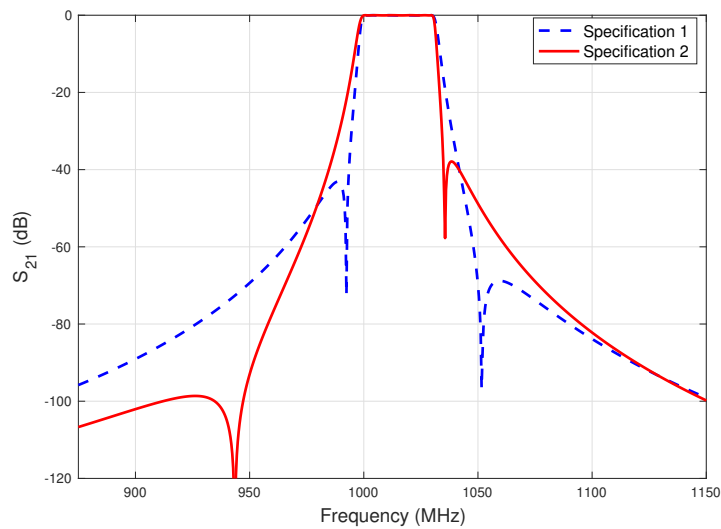
Fig. 5.12 Examples of amplitude responses for the objects clustered in cluster 1: highly selective and/or asymmetric transfer functions.

transfer functions of this type. Cluster 4 consists of the optimum CT topology for transfer functions of this type. From Fig. 5.10, it is evident that all objects in cluster 3 belong to category A. On the contrary, the objects in cluster 4 belong to category B. The resonator giving the maximum peak t.a.s.e for topologies in both clusters is the one opposite to the cross-coupling of the triplet closest to the source. Note that the peak t.a.s.e values for the second best and the worst case topologies do not differ significantly and hence, are grouped in the same cluster.

Clusters 5 and 11 represent topologies for transfer funcions with both transmission zeros lying in the lower stopband (LSB). Both transmission zeros are located considerably away from the lower band-edge as is evident from the t.z. means in Fig.5.9. Cluster 5 comprises of the second best and the worst case CT topologies, whereas cluster 11 comprises of the

optimum CT topologies for transfer functions of this type. The objects in cluster 5 belong to category A and those in cluster 11 belong to category B. Therefore, for the optimum CT topology, the triplet closest to the load is used to create the transmission zero closest to the band-edge. For all topologies in both clusters, the resonator demonstrating the peak t.a.s.e is the one opposite to the cross-coupling of the triplet closest to the source.

The objects in clusters 6 and 9 represent the best and worst case CT topologies, respectively, for transfer functions with a single transmission zero in each stopband (LSB and USB). In about 85% of the objects, the relative transmission zero positions are at approximately equal distances from the respective band-edges, with the transmission zero on the upper side being slightly closer than that on the lower side. In the remaining cases, the transfer function is more selective on the upper side of the passband than the lower side. From Fig. 5.10, it can be observed that the lowest peak t.a.s.e topologies, i.e., objects in cluster 6 belong to category B. The highest peak t.a.s.e topologies, i.e., objects in cluster 9 belong to category A. The resonator giving the peak t.a.s.e is the one opposite to the first cross-coupling for objects in both clusters. Examples of the transfer functions and the corresponding stored energy distribution plots are displayed in Fig. 5.13.

The objects clustered in cluster 8 represent the best case CT topologies for transfer functions that are more selective on the lower side of the passband than the upper side. Approximately 92% of the objects in this cluster represent topologies (b) or (c) in Fig. 5.10. All the topologies in this cluster belong to category B. Cluster 10 represents the worst case topologies for transfer functions of this type. The topologies in cluster 10 belong to category A and the resonator opposite to the first cross-coupling demonstrates the peak t.a.s.e.

Cascaded quartet data set

Clusters 1 and 6 comprise topologies representing transfer functions with both transmission zeros located in the LSB. The transmission zeros are positioned away from the lower band-edge. The objects in cluster 6 constitute the best case CQ topologies for transfer functions of this type, whereas, those in cluster 1 constitute the worst cases. Cluster 1 is entirely composed of topologies with CQ arrangement (a), implying that the quartet is placed next to the source for these topologies. The number of objects with forward asymmetric cross-coupling is exactly twice the number of objects with backward cross-coupling. In almost all cases, the resonator demonstrating the peak t.a.s.e is the one opposite to the asymmetric cross-coupling of the quartet. The objects in cluster 6 have CQ arrangements (b) or (c), implying that the quartet is placed away from the source. A larger number of topologies have backward
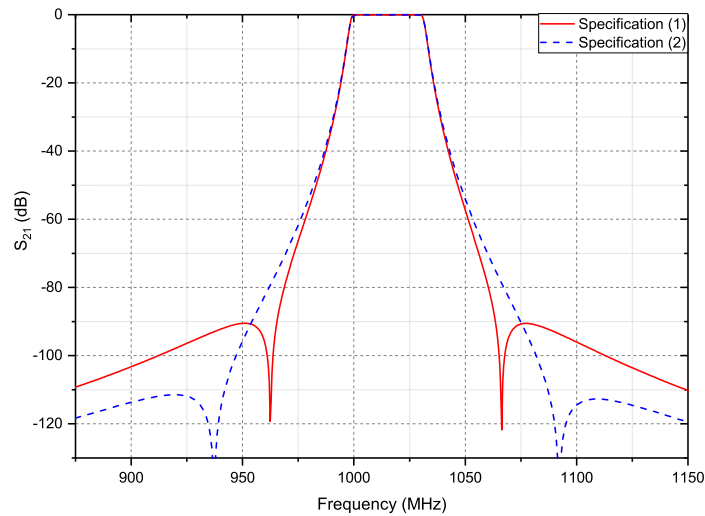
(a) Examples of amplitude responses for the objects clustered in cluster 6: transmission zeros at approximately similar distances from the respective band-edges.
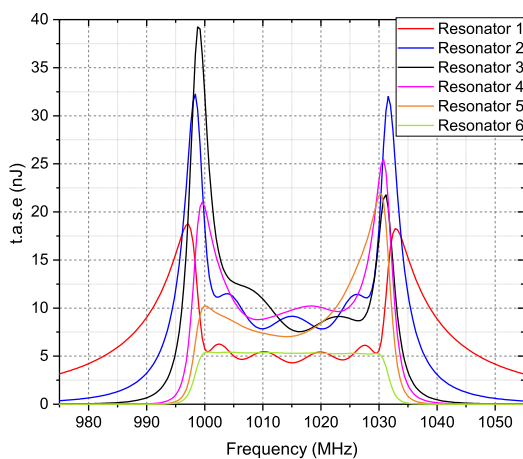
(b) T.a.s.e in (nJ) for example specification (1): triplet positioned at resonators 2-3-4 generates a t.z at 1066.6 MHz and triplet at resonators 4-5-6 generates a t.z at 962.5 MHz.
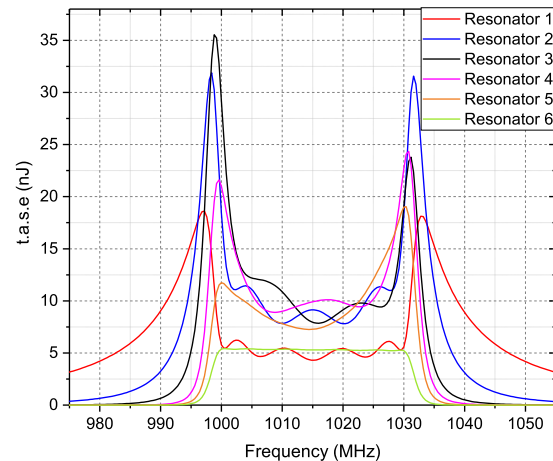
(c) T.a.s.e in (nJ) for example specification (1): triplet positioned at resonators 2-3-4 generates a t.z at 1092.2 MHz and triplet at resonators 4-5-6 generates a t.z at 937.8 MHz.

Fig. 5.13 Examples of objects grouped in cluster 6.

asymmetric cross-coupling as compared to those with forward cross-coupling. An example of the t.a.s.e distribution in two optimum case topologies for transfer functions of this type are displayed in Fig. 5.17. The objects in clusters 3 and 8 constitute the best and the worst case topologies, respectively, for transfer functions with both transmission zeros in the USB. The transmission zeros are located considerably away from the upper band-edge. The topologies in cluster 3 have the quartet placed away from the source, whereas those in cluster 8 have the
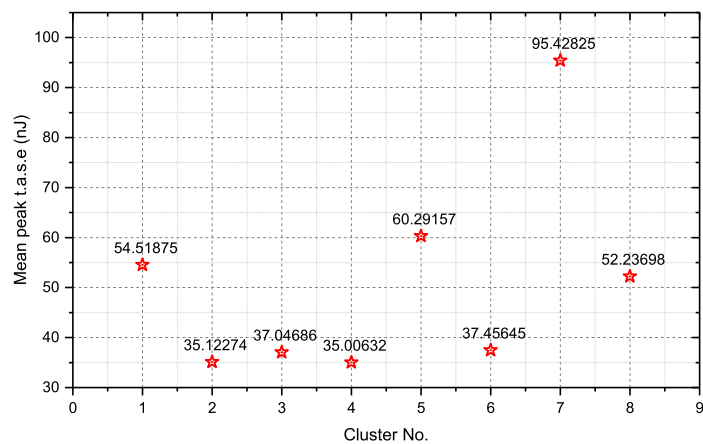
(a) Mean peak t.a.s.e for each cluster - X_q data set
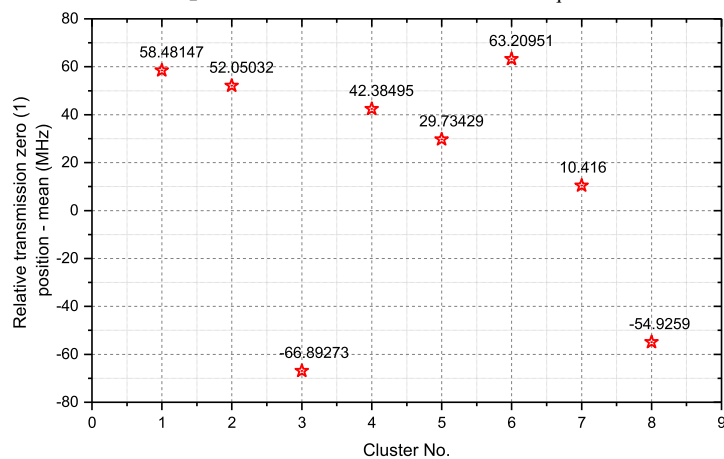
(b) Mean t.z (1) position for each cluster - X_q data set
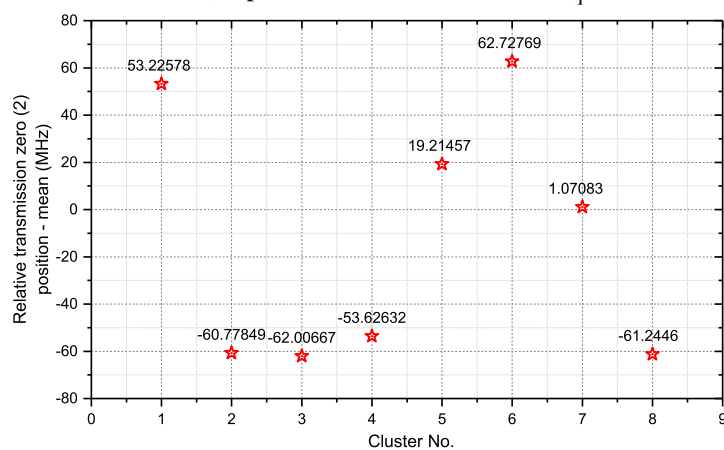
(c) Mean t.z (2) position for each cluster - X_q data set

Fig. 5.14 Means of the peak t.a.s.e and relative transmission zero positions for each cluster of the X_q data set.
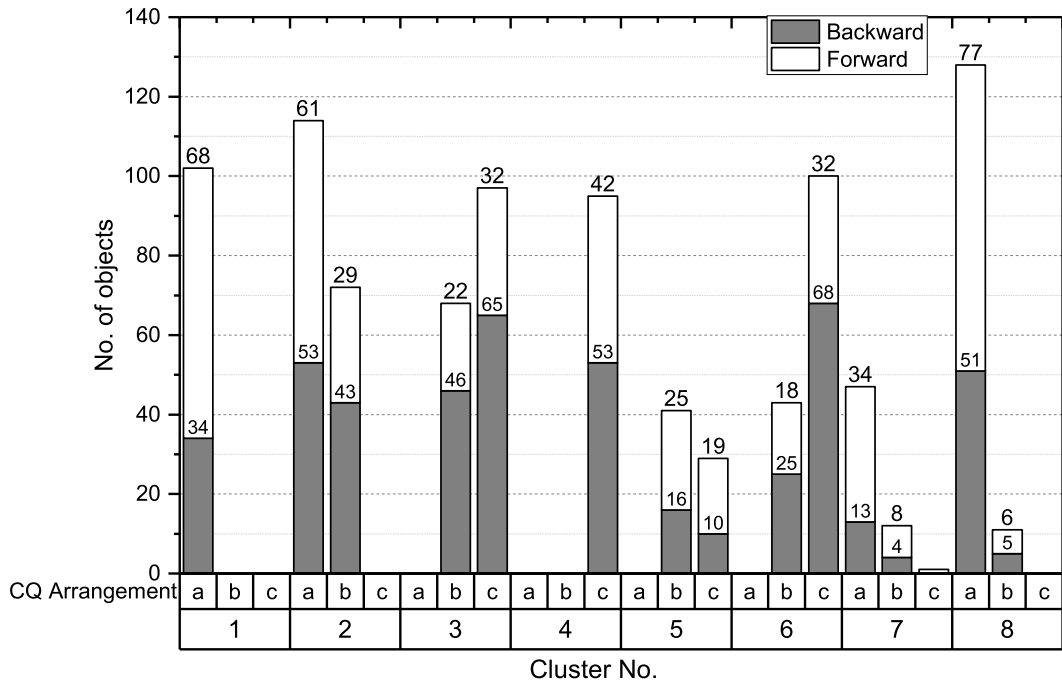
Fig. 5.15 CQ network topologies grouped in each cluster for the 6-2 single band specifications
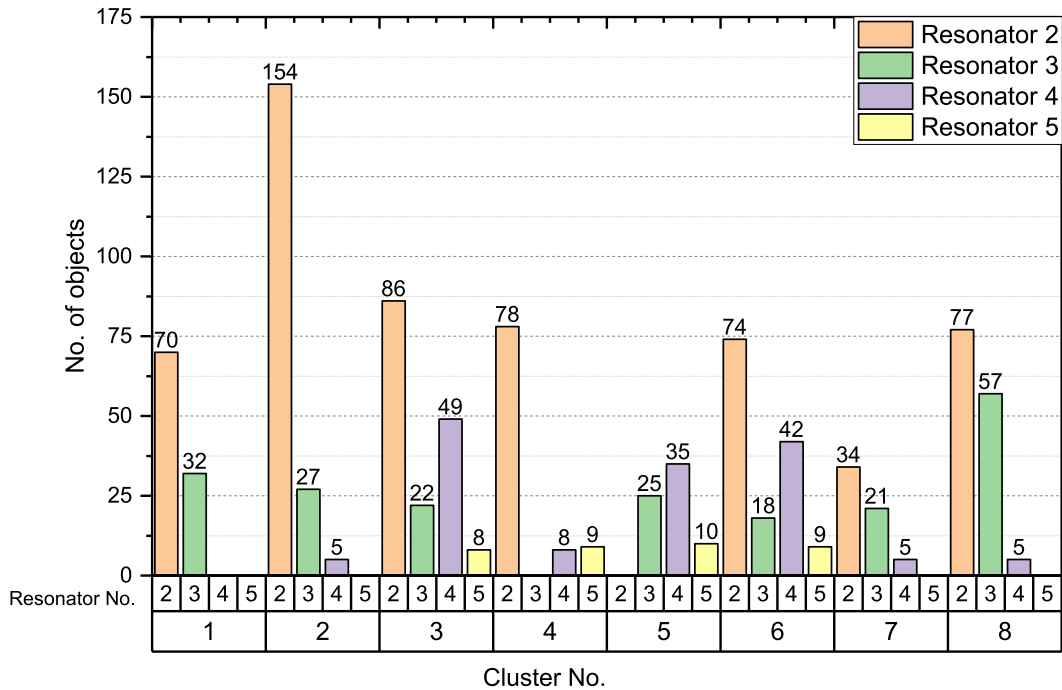
Fig. 5.16 Statistics for peak t.a.s.e resonator in each cluster.

quartet placed next to the source. The resonator demonstrating the peak t.a.s.e for topologies in cluster 8 is the one opposite to the asymmetric cross-coupling of the quartet.
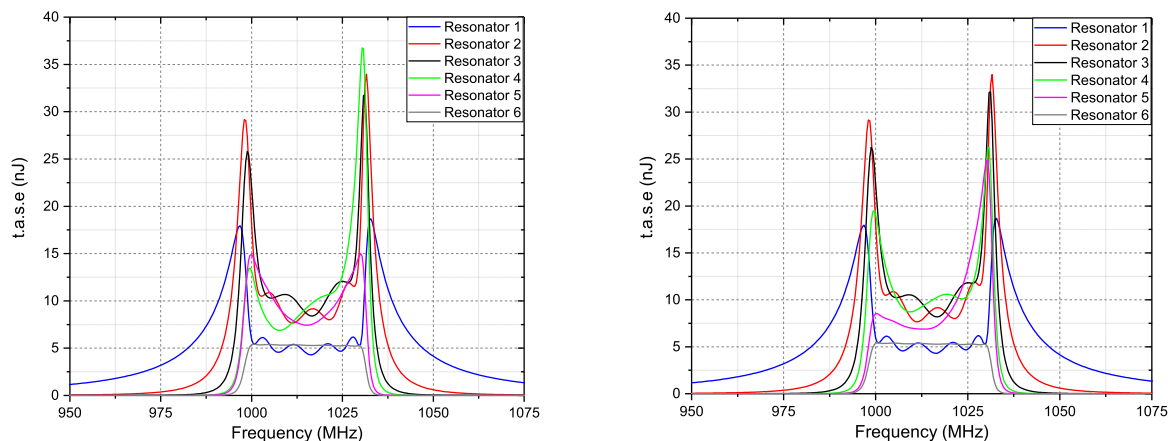
(a) T.a.s.e distribution for an object in cluster 1. The quartet is positioned at resonators 2-3-4-5 and employs a backward asymmetric cross-coupling.

(b) T.a.s.e distribution for an object in cluster 1. The quartet is positioned at resonators 3-4-5-6 and employs a backward asymmetric cross-coupling.

Fig. 5.17 T.a.s.e plots for transfer functions with transmission zeros located away from the band-edge in USB. The transmission zeros are located at 1081.3 MHz and at 1093.5 MHz.

The objects in clusters 2 and 4 represent topologies for transfer functions with a single transmission zero in each stopband. For a large percentage of the objects in these clusters, the transmission zeros lie at similar distances from the respective band-edges. The objects in cluster 2 account for the highest peak t.a.s.e topologies, and in some cases the second best case topologies, for transfer functions of this type. As in all of the worst case clusters, the topologies in this cluster have CQ arrangements (a) or (b). The topologies in cluster 4 constitute the lowest peak t.a.s.e topologies and have CQ arrangement (c). The number of objects with forward and backward asymmetric cross-couplings is comparable in both clusters. For most topologies in both clusters, the resonator giving the maximum peak t.a.s.e is resonator 2. Clusters 5 and 7 represent transfer functions that are extremely selective. The transmission zeros may or may not lie in separate stopbands. The lowest peak t.a.s.e topologies, and in some cases one of the highest peak t.a.s.e topologies are included in cluster 5. Cluster 7 contains the worst case topologies for transfer functions of this type. Approximately 83% of the topologies in this cluster have a quartet placed next to the source and 70% have forward asymmetric cross-coupling. For all topologies in this cluster, the resonator giving the peak t.a.s.e is the one opposite to the asymmetric cross-coupling.

Consider an example of the transfer function represented by objects in clusters 2 and 4. Suppose the two finite transmission zeros are located at frequencies 48.4 MHz from the lower band-edge and 44.4 MHz from the upper band-edge, i.e., at 951.6 MHz and at 1074.4

MHz. The four topologies that account for the best and the worst CQ topologies for the given specification are:

Table 5.5 Object entry for the CQ data set

	Peak t.a.s.e (nJ)	Relative t.z position (1)	Relative t.z position (2)	Quartet position	Asymmetric cross-coupling direction
x_{q_1}	31.97	48.4	-44.4	6	1
x_{q_2}	31.97	48.4	-44.4	5	1
x_{q_3}	32.93	48.4	-44.4	4	1
x_{q_4}	32.96	48.4	-44.4	4	0

Objects x_{q_1} and x_{q_2} account for the best CQ topologies, whereas objects x_{q_3} and x_{q_4} account for the worst CQ topologies. Object x_{q_1} is clustered in cluster 4 and the remaining objects are grouped in cluster 2. The t.a.s.e plots for each resonator in the best and the worst case CQ topologies are displayed in Figures 5.18a and 5.18b. It can be seen that the difference in the t.a.s.e distribution for both cases is insignificant. An interesting point to note is that the t.a.s.e plots are symmetric about the geometric mean frequency. Such a symmetric distribution of t.a.s.e within the resonators yields a low peak t.a.s.e for CQ topologies.
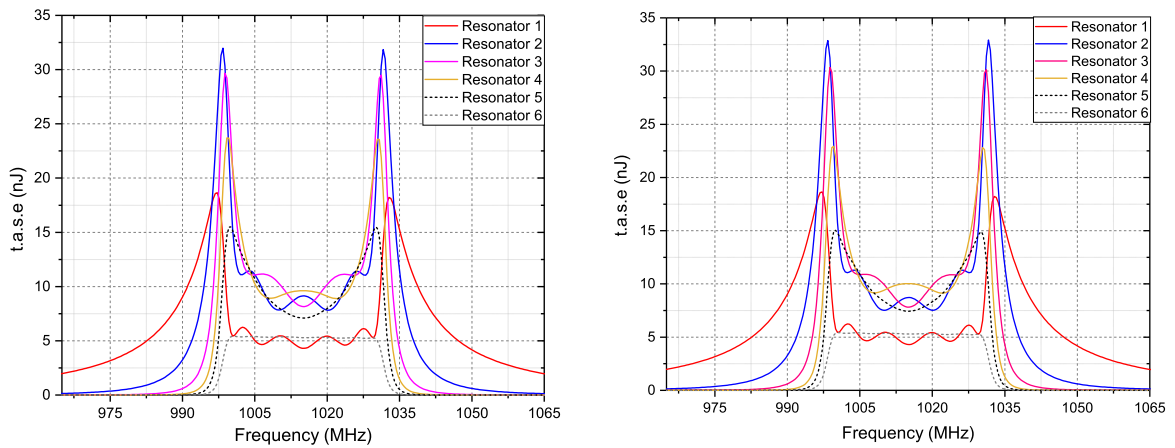
(a) Best case CQ topology represented by object x_{q_1}

(b) Worst case CQ topology represented by object x_{q_4}

Fig. 5.18 T.a.s.e plots for transfer functions with transmission zeros at similar distances from the band-edges.

5.4.5 General patterns

Cascaded triplets

From the results presented in the above section, it is apparent that clusters 1, 4, 6, 8 and 11 comprise of topologies belonging to category B in Fig. 5.10. These are the clusters that contain the best case topologies for various transfer functions. Thus, it can be concluded that the peak t.a.s.e of a given topology can be reduced by using the triplet closest to the load to create the transmission zero located closest to the band-edge. About 86.25% of the objects grouped in these clusters have CT arrangements (b) or (c) (refer to Fig. 5.6 and Fig. 5.10). In most of these clusters, the number of objects with CT arrangement (b) is greater than twice the number of objects with CT arrangement (c). Therefore, it can be deduced that placing the triplets away from the source decreases the peak t.a.s.e of a topology. For the clusters
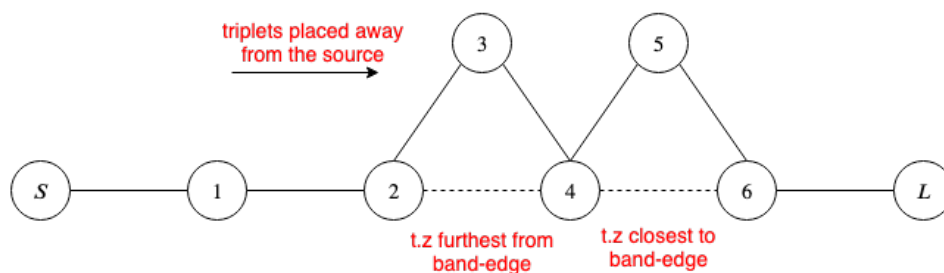
Fig. 5.19 Optimum CT topology for 6-2 single band transfer functions.

comprising of the highest peak t.a.s.e topologies, the resonator giving the peak t.a.s.e is always the one opposite to the cross-coupling of the triplet closest to the source. Likewise, for all CT topologies realising a transfer function where both transmission zeros lie in the same stopband, the resonator giving the peak t.a.s.e is the one opposite to the first cross-coupling. In general, given that the total t.a.s.e of the transfer function is sufficiently high to reach the first triplet in the network, the peak t.a.s.e resonator is always the one opposite to one of the triplet cross-couplings. This phenomenon can be explained by considering the admittances of the couplings in a triplet. The cross-coupling admittance in a triplet is always lower than the admittance of the mainline coupling. In other words, the mainline couplings are generally much stronger than the cross-couplings. Hence, for a signal travelling from resonator $k-1$ to $k+1$ in the triplet (refer to Fig. 5.20) a larger amount of energy is coupled between resonators $k-1$ and k than between resonators $k-1$ and $k+1$, resulting in a peak at the centre resonator k.
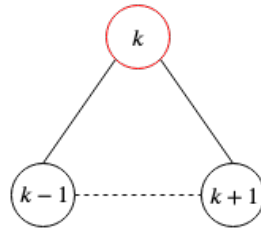
Fig. 5.20 Peak t.a.s.e resonator in a CT network is always the one opposite to one of the cross-couplings.

Cascaded quartets

The objects in clusters 3, 4, 5 and 6 have CQ arrangements (b) or (c) (refer to Fig. 5.7 and Fig. 5.15). These are the clusters that contain the lowest peak t.a.s.e topologies for various transfer functions. Therefore, it can be concluded that the quartet must be placed away from the source to decrease the peak t.a.s.e and consequently, improve the power handling capacity of the filter network. If both transmission zeros are located in the same stopband, the optimum CQ topology is the one where the quartet is placed next to the source and has a backward asymmetric cross-coupling direction. If the transmission zeros are placed on either side of the passband, the quartet must be placed either next to the load. In this case, the direction of the asymmetric cross-coupling for the optimum topology may be forward or backward. If
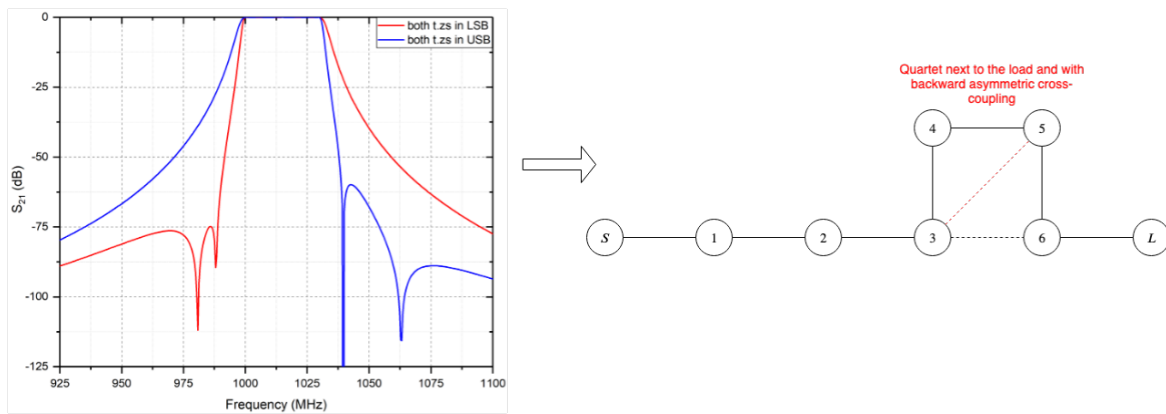
Fig. 5.21 The optimum CQ topology for 6-2 single bandpass transfer functions with both transmission zeros in the same stopband.

the transfer function is almost symmetric, the quartet must be placed in the middle of the network so that the network elements are also almost symmetric. The t.a.s.e plots for such transfer functions are almost symmetric about their geometric mean frequency resulting in a lower peak t.a.s.e value. For transfer functions where both transmission zeros are located in

the same stopband, the resonator giving the peak t.a.s.e in all topologies is always the one opposite to the asymmetric cross-coupling.
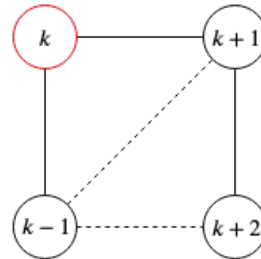
Fig. 5.22 Peak t.a.s.e resonator in a CQ network is the one opposite to the asymmetric cross-coupling.

Comparison between CT and CQ topologies

It was found that for transfer functions with both transmission zeros lying in the same stopband and placed sufficiently close together, CQ topologies provided a better t.a.s.e distribution. For a given transfer function, the CQ topology in Fig 5.21 is the optimum choice provided that equation (5.6) is satisfied.

$$\frac{|f_c - f_{n1}|}{|f_{n1} - f_{n2}|} > 0.2 \tag{5.6}$$

where, f_c is the appropriate cut-off frequency (lower cut-off frequency if both t.zs lie in the LSB and upper cut-off frequency if both t.zs lie in the USB), f_{n1} is the transmission zero closest to f_c and f_{n2} is the transmission zero furthest from f_c.

For transfer functions that are close to being symmetric, the CQ topology provides a uniform t.a.s.e distribution, yielding a lower peak t.a.s.e than the corresponding CT topology. In about 96.5% of the power transfer functions, the peak t.a.s.e value of the optimum CQ topology was either lower than or equal to the optimum CT topology.

5.5   T.a.s.e distribution in filter networks for 9-5 single bandpass transfer functions

5.5.1   Generation and modelling of input data

The clustering algorithm was applied to cascaded n-tuplet topologies generated for 50 different single bandpass specifications. The degree of the filter network, the passband frequencies and the number of finite transmission zeros were fixed to 9, 1805 MHz - 1880 MHz and 5 respectively. The position of the finite transmission zeros, however, was chosen at random from a reasonable range of values.

Two quartets and a triplet are required to realise a 9th-order bandpass transfer function with 5 finite transmission zero pairs. This can be achieved only if each pair of consecutive n-tuplets share a resonator between them. The three different n-tuplet arrangements considered are presented in Fig. 5.23. Note that the quartets are displayed with a forward asymmetric cross-coupling. By changing the direction of cross-coupling for the two quartets and by changing the sequence of transmission zero extraction, 360 topologies can be generated for each specification. Hence, 18000 topologies can be obtained for 50 different specifications.

As the objective is to discover patterns that aid in predicting the optimum topology for power handling, 10 best topologies and 10 worst topologies were extracted. Thus, a total of 1000 topologies were to be clustered. The input vector matrix was composed of rows representing the objects and columns respresenting the attributes that describe each object. The factors influencing the t.a.s.e distribution within these n-tuplet networks and that determine the power handling capability of the filter are:

- the n-tuplet arrangement in the network,

- the relative transmission zero positions,

- the sequence of extraction of transmission zeros,

- the peak t.a.s.e, and

- the direction of asymmetric cross-coupling for the quartets.

The relative transmission zero positions from the closest band-edges were calculated as in the previous example in section 5.4.1. These relative transmission zero positions were used as attributes for a given topology in the sequence of their extraction. The direction
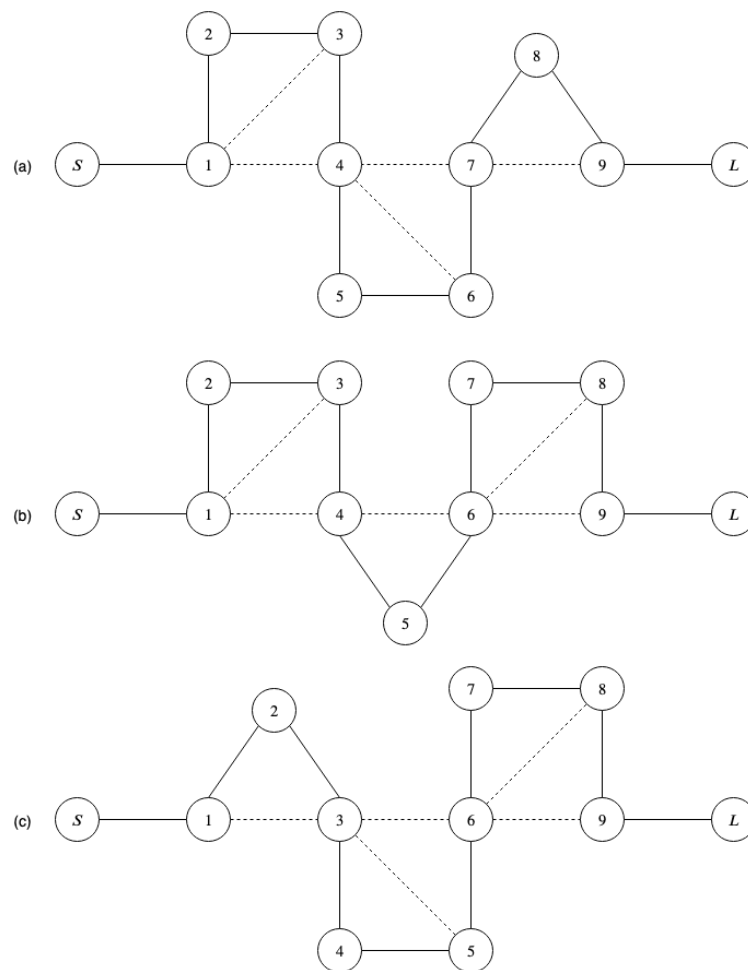
Fig. 5.23 Cascaded n-tuplet networks for a 9th-degree filter with 5 finite transmission zeros. Note: each quartet is drawn with a forward cross-coupling direction.

of the asymmetric cross-coupling of the quartet was represented by binary values, viz., '1' representing a forward asymmetric cross-coupling and '0' representing a backward asymmetric cross-coupling. As the n-tuplet arrangement is a categorical attribute, it had to be converted into sequential numerical attributes. Therefore, '1' ,'2' and '3' represented topologies (a), (b) and (c) in Fig. 5.23, respectively. By a method of trial and error, the attributes that provide the best clustering for the given data set were chosen. These include: the peak t.a.s.e in nJ, the relative transmission zeros in the sequence of their extraction, the n-tuplet arrangement and the direction of the asymmetric cross-coupling for the first quartet.

5.5.2   Optimum value of K

The optimum number of clusters that the data has to be partitioned into is determined using the methods described in section 5.2.3. The elbow method, as well as the silhouette method were used to determine the optimum value of K for the data set. The value of K was varied from 2 to 15 in steps of unity. The WCSS for each K is plotted in Fig. 5.24 to determine the optimum K. From the plot it is evident that the elbow point occurs at $K = 8$. The optimum
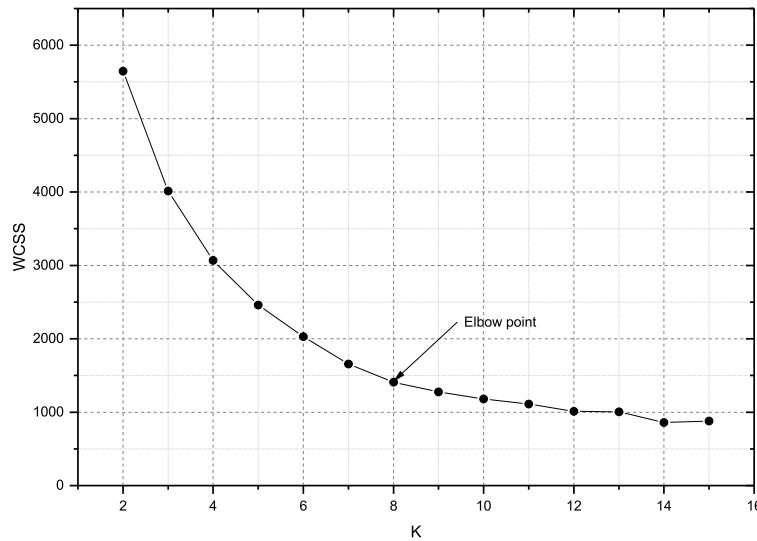
Fig. 5.24 The elbow method applied to the 9-5 n-tuplet data set; the elbow point obtained at $K = 8$.

choice for K can also be validated using the silhouette method described in section 5.2.3. Table 5.6 provides the silhouette coefficients for different values of K. It can be observed that the maximum value occurs for $K = 8$.

Table 5.6 The silhouette coefficients (S.C) for various values of K for a data set comprising of topologies for various 9-5 single bandpass specifications

K	2	3	4	5	6	7	8	9	10
S.C	0.4315	0.5487	0.5612	0.5739	0.6227	0.6575	0.6613	0.6577	0.5382
K	11	12	13	14	15				
S.C	0.6344	0.6299	0.6372	0.6414	0.5522				

5.5.3   Clustering results and analysis

A graphical representation of the means of the peak t.a.s.e and the transmission zero positions is displayed in Fig. 5.25. The number of objects with various n-tuplet arrangements, viz., (a), (b) and (c) in fig. 5.23 grouped in each cluster is represented by the grouped bar graph in Fig. 5.26. It also represents the statistics for the cross-coupling direction of the first quartet in the various n-tuplet topologies.

Worst peak t.a.s.e clusters

Clusters 3, 4, 6 and 7 comprise of objects with the highest peak t.a.s.e values. It is evident from Fig. 5.26 that approximately 98.5% of the objects in these clusters have n-tuplet arrangements (a) or (b). This implies that a quartet is placed next to the source in these topologies. The finite transmission zeros generated by this quartet always lie in the same stopband, as can be deduced from Figures 5.25b and 5.25c. At least one of these transmission zeros was also located close to the band-edge. From the graphical representations in Figures 5.25b-5.25e, it can be observed that at least one of the transmission zeros generated by the first quartet in these clusters has a mean of about ±30 MHz (relative position from the band-edge), i.e, approximately 1.6% of the geometric mean frequency. In about 96% of the topologies grouped in these clusters, the quartet closest to the source has a backward asymmetric cross-coupling. Note that this introduces an additional energy path to the resonator shared between the quartet and the adjacent n-tuplet. In all of the objects grouped in clusters 3, 4, 6 and 7, the resonator demonstrating the peak t.a.s.e is always the one opposite to the asymmetric cross-coupling of the first quartet. Thus, for about 96% of the topologies in these clusters have resonator 3 giving the peak t.a.s.e.

As proven in section 5.4.5, a quartet is better suited to generating transmision zeros lying on either side of the passband. If the transmission zeros are located in the same stopband, the asymmetry in the quartet element values increases. This results in an asymmetric stored energy response for a resonator (usually the one opposite to the asymmetric cross-coupling of the quartet), which in turn implies a higher peak t.a.s.e. This is illustrated with the aid of an example. Consider a 9th-order bandpass filter with 5 finite transmission zero pairs at 1745 MHz, 1760 MHz, 1780 MHz, 1925 MHz and 1970 MHz realised using n-tuplet arrangement (b). Suppose the quartet closest to the source is used to produce transmission zeros at 1760 MHz and 1780 MHz. The succeeding triplet generates a transmission zero at 1925 MHz followed by a quartet generating the ones at 1745 MHz and 1970 MHz. The t.a.s.e distribution plots for resonators 1-4 forming the first quartet are displayed in Fig. 5.29.
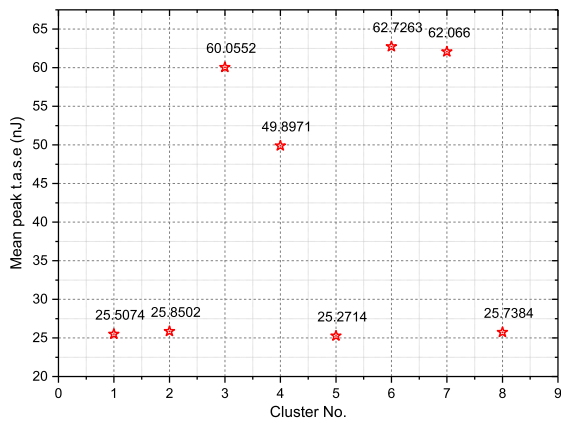
(a) Mean peak t.a.s.e values for each cluster
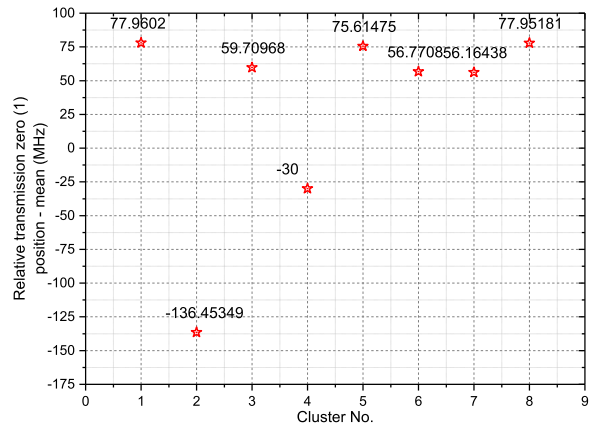
(b) Mean t.z (1) values for each cluster
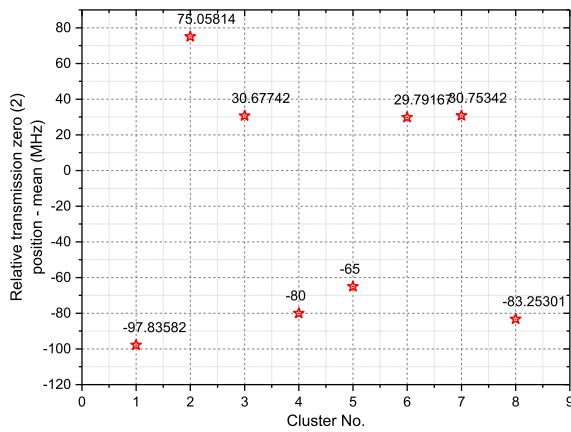
(c) Mean t.z (2) values for each cluster
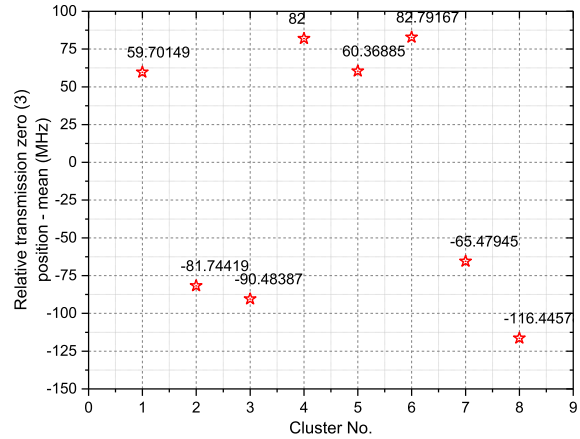
(d) Mean t.z (3) values for each cluster
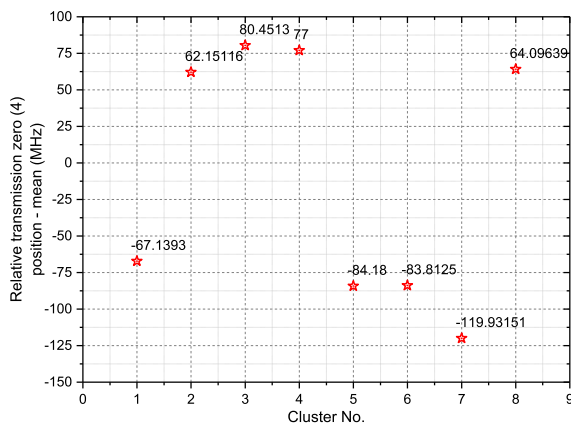
(e) Mean t.z (4) values for each cluster
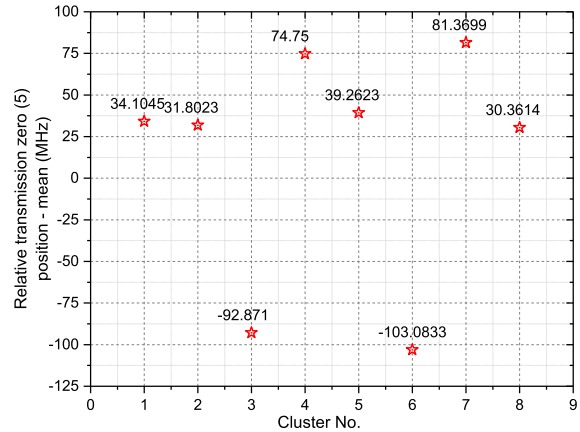
(f) Mean t.z (5) values for each cluster

Fig. 5.25 Graphical representations of the peak t.a.s.e and t.z mean values for the $K = 8$ clusters that the given data set has been partitioned into.

It is evident from this plot that the t.a.s.e distribution is almost symmetric about the geometric mean frequency for all resonators except resonator 3. The stored energy plot for resonator 3 is highly asymmetric with a sharp peak occuring just below the lower cut-off frequency.
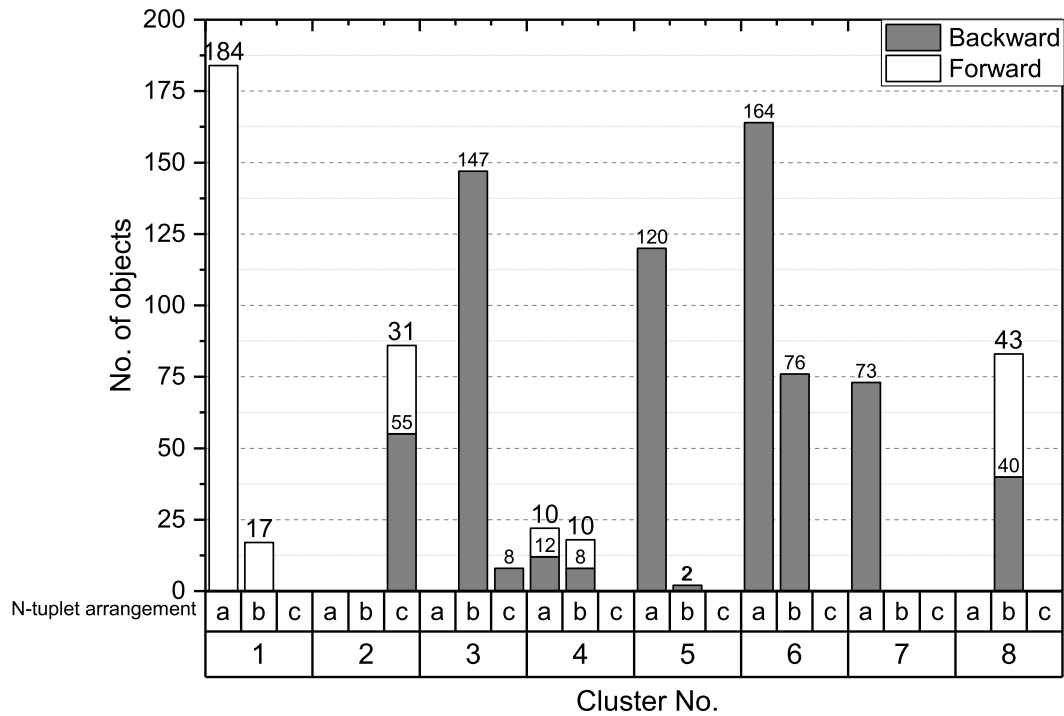
Fig. 5.26 The number of objects in each cluster with n-tuplet arrangements (a),(b) and (c) from Fig. 5.23. The number of objects with forward and backward asymmetric cross-coupling directions for the first quartet in the n-tuplet topologies is indicated.

Lowest peak t.a.s.e clusters

The clusters representing the objects with the lowest peak t.a.s.e, and thus, the optimum power handling topologies are clusters 1, 2, 5 and 8. Clusters 1, 5 and 8 are composed entirely of objects with n-tuplet arrangements (a) or (b) from Fig. 5.23, implying that a quartet is positioned next to the source for these topologies. On the contrary, cluster 2 is composed of objects with n-tuplet arrangement (c), implying that a triplet is placed next to the source. From the means of the relative transmission zero positions for clusters 1,5 and 8, it is evident that in all topologies, the quartet closest to the source is used to produce transmission zeros lying on either side of the passband. These transmission zeros are either the ones that lie furthest away from the passband or the ones that lie at similar distances from the respective band-edges. If latter is the case, then the t.a.s.e gets distributed more uniformly within the quartet resulting in a lower peak t.a.s.e. The direction of the asymmetric cross-coupling of the first quartet in topologies giving the lowest peak t.a.s.e is determined by the sequence of transmission zeros generated by the quartet and the subsequent n-tuplet. For cluster 1, the sequence of transmission zero extraction is: furthest away from the band-edges on either side to closest to the band-edge. Note that a quartet is always used to generate transmission
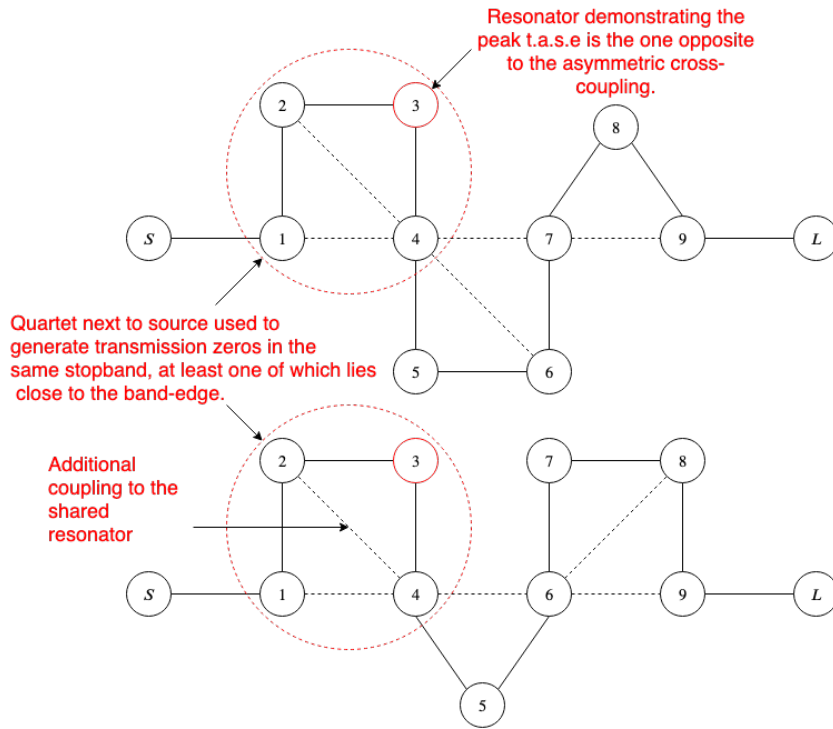
Fig. 5.27 Representation of the worst case n-tuplet toplogies realising various 9-5 single bandpass transfer functions.
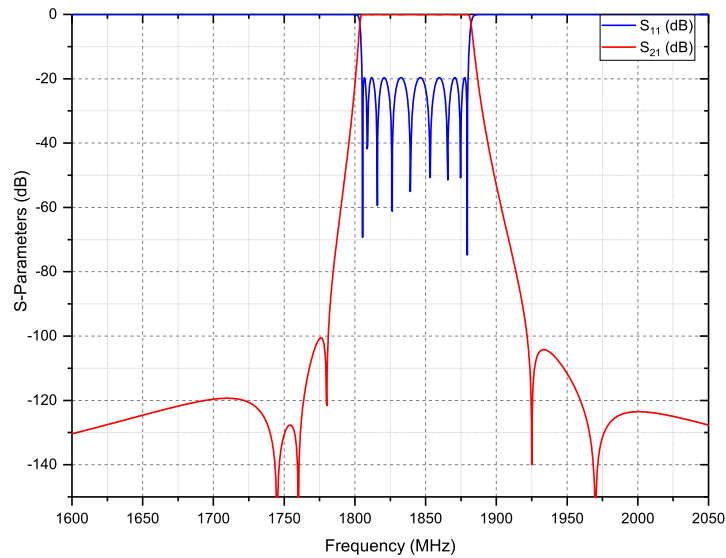
Fig. 5.28 An example specification of a 9-5 bandpass filter.

zeros on either side of the passband. In such cases, the quartet closest to the source always has forward asymmetric cross-coupling. A representation of the sequence of generation of
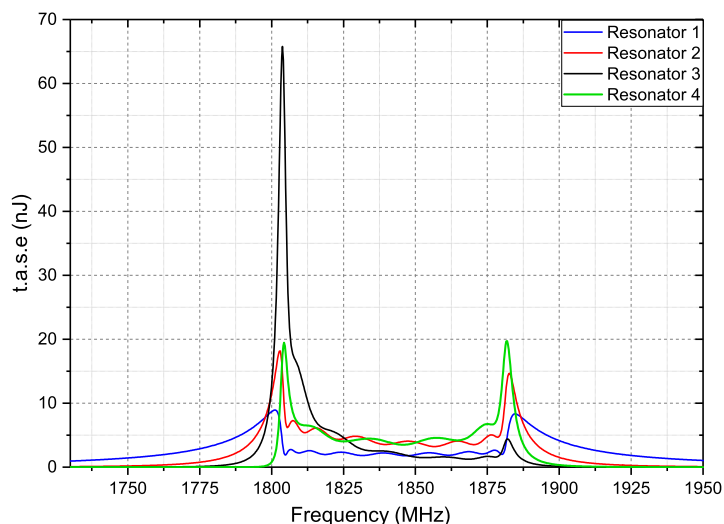
Fig. 5.29 The t.a.s.e plots for resonators in a quartet producing transmission zeros at frequencies 1780 MHz and 1760 MHz. The remaining network consists of a triplet producing a transmission zero at 1925 MHz followed by a quartet producing transmission zeros at 1745 MHz and 1970 MHz.

transmission zeros for objects in cluster 1 using the n-tuplet topology (a) is presented in Fig. 5.32.
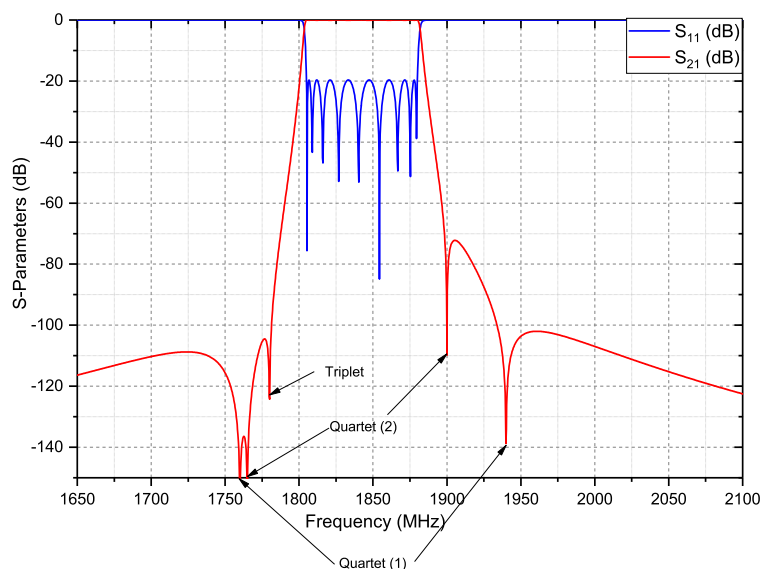
Fig. 5.30 The sequence of transmission zero extraction for objects in cluster 1 is from furthest out to closest in (with respect to the band-edges).

The choice of transmission zeros to be generated by the first quartet is between the ones that lie furthest away from the band-edges on either side (as in cluster 1) or the ones that yield a

more uniform t.a.s.e distribution within the quartet. The latter is the case for objects grouped in cluster 5. In such cases, the first quartet always has backward asymmetric cross-coupling. The transmission zeros generated by this quartet usually lie at similar distances from the respective band-edges so that the nodal admittances are similar in value. The transfer function in Fig. 5.28 realised using n-tuplet arrangement (a) represents an object belonging to cluster 5. Here, the first quartet is used to produce the transmission zeros at 1745 MHz and 1925 MHz. The consecutive quartet is used to generate the transmission zeros at 1760 MHz and 1970 MHz, followed by a triplet producing a transmission zero at 1780 MHz. The t.a.s.e distribution for resonators 1-4 forming the first quartet is displayed in Fig. 5.31. The t.a.s.e distribution is even and almost symmetric about the geometric mean frequency for these resonators.
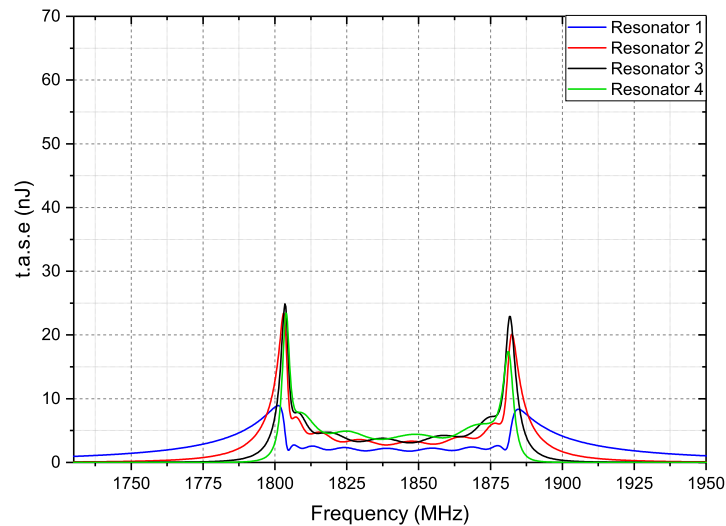
Fig. 5.31 The t.a.s.e plots for resonators (1-4) in a quartet producing transmission zeros at 1745 MHz and 1925 MHz. The remaining network comprises of a second quartet producing transmission zeros at 1760 MHz and 1970 MHz followed by a triplet producing a transmission zero at 1780 MHz.

By comparing the t.a.s.e distribution plots in Figures 5.29 and 5.31, it can be seen that the peak t.a.s.e can be reduced to less than half the value by extracting appropriate transmission zeros with the first quartet.

Cluster 2 is comprised of objects with n-tuplet arrangement (c), i.e., a triplet is placed next to the source for these topologies. Here, the transmission zero furthest away from the band-edge is generated using the triplet. The subsequent quartet is used to produce transmission zeros lying on either side of the passband and that are located away from the band-edge. The remaining transmission zeros are generated using the last quartet. The
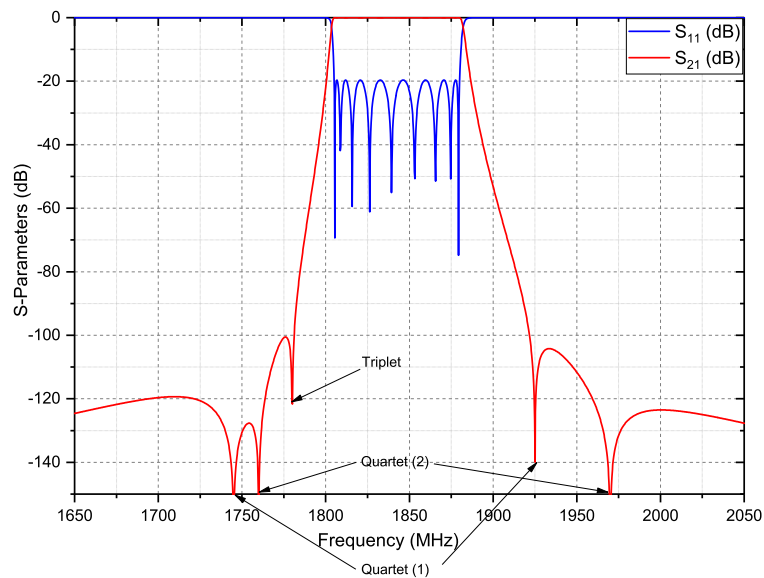
Fig. 5.32 The sequence of transmission zero extraction for objects in cluster 5.

resonator demonstrating the peak t.a.s.e for these topologies is the one opposite to the asymmetric cross-coupling of the first or the second quartet.

5.5.4   General patterns

1. A quartet must always be used to generate transmission zeros located on either side of the passband.

2. The transmission zeros generated by the quartet placed closest to the source must either lie furthest away or at similar distances from the respective band-edges. If latter is the case, a more uniform t.a.s.e distribution is obtained resulting in reduced peak t.a.s.e.

3. If a triplet is placed next to the source, it must be used to generate the transmission zero that lies furthest away from the band-edge.

4. The transmission zero/s lying closest to the band-edge must be produced by the n-tuplet lying furthest away from the source.

5. For n-tuplets with a shared resonator between them, the direction of asymmetric cross-coupling should be such that the number of energy paths going to the common resonator is minimum. An exception to this rule is when the first quartet in the n-tuplet arrangement is used to generate transmission zeros that are positioned at

similar distances from the band-edges. In this case, the direction of the asymmetric cross-coupling is such that an additional energy path goes to the shared resonator.

6. In general, an n-tuplet arrangement commencing with a quartet provides a better t.a.s.e distribution that the one commencing with a triplet.

7. The resonator demonstrating the peak t.a.s.e for the worst case topologies is always the one opposite to the asymmetric cross-coupling of the first quartet.

8. The resonator demonstrating the peak t.a.s.e for the best case topologies is usually the one opposite to the asymmetric cross-coupling in one of the quartets.

5.6   Conclusion

An overview of the methods reported in the literature for predicting and improving the power handling capacity of microwave filters has been presented in section 5.1. The k-means clustering method, described in section 5.2, has been implemented to find regularities in the stored energy distribution for various networks realising the same single bandpass transfer function. Large data sets comprising of CQ and CT topologies realising various transfer functions have been generated and analysed to obtain generalised rules that aid prediction of the optimum power handling topology for a given transfer function. The general patterns obtained using the clustering results of n-tuplet topologies realising various 6th-order and 9th-order single bandpass transfer functions have been presented in section 5.4.5 and section 5.5.4, respectively. In the next chapter, the k-means algorithm has been implemented to find patterns in the t.a.s.e distribution of networks realising various dual bandpass transfer functions.

Chapter 6

Investigation of the optimum topology for dual band transfer functions

In this chapter, the k-means clustering algorithm has been implemented to find patterns in the stored energy distribution of various generalised Chebyshev dual bandpass transfer functions. Data sets comprising of cascaded triplet and cascaded quartet network topologies realising various 6-2 and 9-5 dual bandpass transfer functions have been generated. By performing clustering on these data sets, regularities in the t.a.s.e distribution of dual bandpass transfer functions have been discovered and analysed. These regularities aid in establishing generalised rules that enable prediction of the optimum power handling topology for generalised Chebyshev dual bandpass transfer functions. The characteristic polynomials and the cascaded n-tuplet network topologies for the generalised Chebyshev dual bandpass transfer functions were generated using the multi-bandpass linear optimisation technique described in chapter 4.

6.1 T.a.s.e distribution in filter networks for 6-2 dual bandpass transfer functions

The k-means algorithm was applied to data sets comprising of CT and CQ filter topologies realising seventy different 6-2 dual bandpass transfer functions. The degree of each passband was set to 3, i.e, $N_1 = N_2 = 3$. For each specification, a single transmission zero was prescribed in the inner stopband. The second transmission zero, i.e., the dependent transmission zero, was constrained to the inner stopband. The lower cut-off frequency of

the lower passband, denoted by f_1, was set to 1000 MHz. The upper cut-off frequency of the lower passband and the two cut-off frequencies of the upper passband (denoted by f_2, f_3 and f_4, respectively) were randomly chosen for each specification. By altering these frequencies, the ratio of the bandwidths of the two passbands and the separation between the two passbands were effectively altered. These two parameters influence the placement of the transmission zeros in the inner stopband, and consequently, influence the selectivity of the transfer function. The passband ratio, defined by the ratio of the bandwidth of the lower passband to that of the upper passband, ranged from about 0.3333 to 3. The inner stopband ratio, defined by the ratio of the inner stopband to the bandwidth of the entire dual band, ranged from about 0.3333 to about 0.8825.

The various CT and CQ network arrangements that can be used to realise the 6-2 dual band transfer functions are depicted in Figures 5.6 and 5.7, respectively. As explained in section 5.4.1, by changing the direction of asymmetric cross-coupling in the quartets, 6 distinct CQ filter topologies can be obtained. Similarly, by changing the sequence in which the transmission zeros are generated, 6 distinct CT topologies can be obtained. Therefore, 12 different topologies are generated for each specification, resulting in a total of 840 topologies for 70 specifications. The t.a.s.e was calculated using equation (5.5). For each specification, the two topologies giving the lowest peak t.a.s.e and the two giving the high peak t.a.s.e were extracted. The clustering was, thus, performed on 280 topologies representing the 70 different specifications.

6.1.1   Modelling input data

The input data set must comprise of objects whose attributes represent the transfer function, as well as the topology used to realise it. As an indictor of the power handling capacity of the filter, the attributes must also include the peak t.a.s.e observed in the equivalent filter network. The following attributes were used to represent the various 6-2 dual bandpass power transfer functions:

1. The passband ratio (PBR) - ratio of the bandwidth of the lower passband to that of the upper passband: $(f_2 - f_1)/(f_4 - f_3)$.

2. The inner stopband ratio (ISBR) - ratio of the bandwidth of the inner stopband to the total bandwidth of the entire dual band: $(f_3 - f_2)/(f_4 - f_1)$

3. The relative transmission zero position ratio (RTZR) - ratio of the position of the inner stopband transmission zeros (f_n) from f_2, to the bandwidth of the inner stopband: $(f_n - f_2)/(f_3 - f_2)$.

If PBR < 1, then the bandwidth of the lower passband is smaller than that of the upper passband. Similarly, if PBR > 1, then the bandwidth of the upper passband is smaller than that of the lower passband. If PBR is unity, it implies that the bandwidths of the two passbands are equal. A small value of the relative transmission zero ratio implies that the transmission zero is located closer to f_2 and a high value indicates otherwise.

As in section 5.4.2, the CT and the CQ network topologies were modelled using separate data sets, viz., X_t and X_q, respectively. The positions of the two triplets within the filter network were represented by their last resonators. Similarly, the position of the quartet was represented by its last resonator. The direction of the asymmetric cross-coupling in the quartet was represented by binary values, i.e., '1' represented forward asymmetric cross-coupling and '0' represented backward asymmetric cross-coupling.

Consider an example specification with two passbands located at 1000 MHz - 1010 MHz and 1070 MHz - 1090 MHz. A transmission zero was prescribed at 1030 MHz, yielding a dependent transmission zero at 1019.6 MHz. Suppose the transfer function was realised using two triplets positioned at resonators 2-3-4 and resonators 4-5-6, respectively. The first triplet was used to generate the transmission zero at 1030 MHz and the second triplet was used to generate the transmission zero at 1019.6 MHz. The object entry for this topology in the X_t data set is given in Table 6.1.

Table 6.1 An example of an object entry for a CT topology realising a 6-2 dual band transfer function.

	Peak t.a.s.e (nJ)	PBR	ISBR	Relative t.z position ratio - (1)	Relative t.z position ratio - (2)	Triplet position (1)	Triplet position (2)
x_{t_1}	22.4570	0.5	0.6667	0.1600	0.3333	6	4

The transmission zeros at 1019.6 MHz and 1030 MHz are represented by the relative transmission zero position ratios 0.1600 and 0.3333, respectively. Suppose a CQ network with the quartet positioned at resonators 3-4-5-6 and with a forward asymmeric cross-coupling was used to realise the same power transfer function. The object entry for this topology in the X_q data set is displayed in Table 6.2.
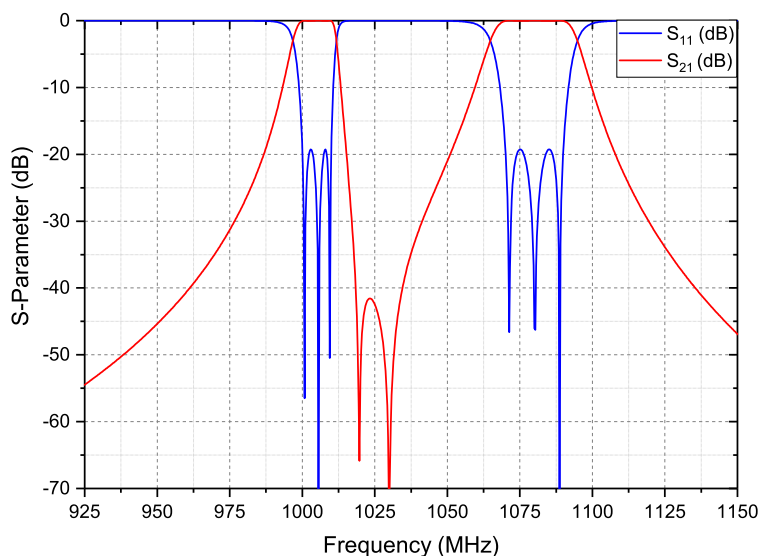
Fig. 6.1 An example specification for a 6-2 dual bandpass transfer function.

Table 6.2 An example of an object entry for a CQ topology realising a 6-2 dual band transfer function.

	Peak t.a.s.e (nJ)	PBR	ISBR	Relative t.z position ratio - (1)	Relative t.z position ratio - (2)	Quartet position (1)	Asymmetric cross-coupling direction
x_{q_1}	62.3610	0.5	0.6667	0.1600	0.3333	6	1

By cascading rows of such objects, each representing a distinct topology, the two input data sets, viz., X_t and X_q can be developed.

6.1.2   Optimum value of K

The optimum number of clusters that the X_t and X_q data sets have to be partitioned into were chosen using the elbow method described in section 5.2.3. The k-means algorithm was applied to the two data sets separately. The value of K was varied from 2 to 15 in steps of unity. The within cluster sum of squares of distances from the objects to the corresponding cluster centroids for the two data sets are displayed in Fig. 6.2. It is evident that the elbow points occur at $K = 6$ for both data sets.

The results can be verified using the silhouette method described in section 5.2.3. The silhouette coefficients for values of K varying from 2 to 15 are provided in Table 6.3. The highest value of the silhouette coefficient occurs at $K = 6$ for both data sets. Thus, it can be

concluded that the optimal number of clusters that the data sets are to be partitioned into is $K = 6$.
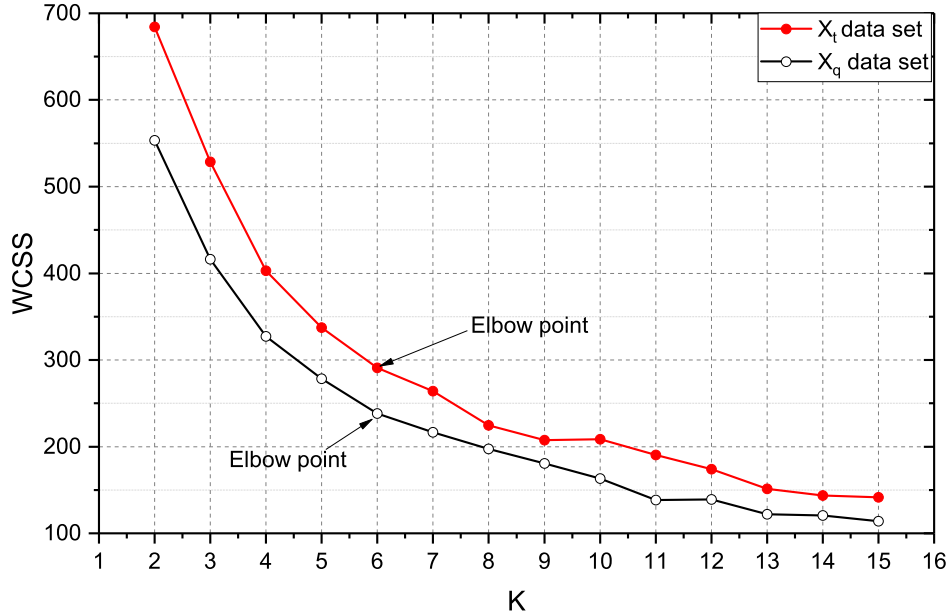
Fig. 6.2 The elbow method applied to X_t and X_q data sets. Elbow points occur at $K = 6$ for both data sets.

Table 6.3 The silhouette coefficients (S.C) for various values of K for a data set comprising of CT topologies for various 6-2 dual bandpass specifications

$X_t : K$	2	3	4	5	6	7	8	9	10
S.C	0.5210	0.5430	0.5216	0.5332	0.5530	0.5408	0.4918	0.4675	0.4650
$X_t : K$	11	12	13	14	15				
S.C	0.4506	0.4799	0.4598	0.4756	0.4312				
$X_q : K$	2	3	4	5	6	7	8	9	10
S.C	0.4442	0.4733	0.5078	0.4955	0.5333	0.4833	0.4925	0.4456	0.4371
$X_q : K$	11	12	13	14	15				
S.C	0.5215	0.4097	0.4902	0.4441	0.4716				

6.1.3   Clustering results and analysis

Graphical representations of the various attributes describing the transfer functions and the corresponding n-tuplet topologies are presented in Fig. 6.3 - Fig. 6.5 for the X_t data set and in Fig. 6.10 - Fig. 6.12 for the X_q data set. Note that the CT and CQ arrangements that can

be used to realise the 6-2 dual bandpass transfer functions are represented by Fig. 5.6 and Fig. 5.7, respectively.

Cascaded triplet data set

Clusters 1 and 2 comprise of the worst case topologies for transfer functions that, collectively, have passband ratios ranging from 0.5 to 1.6. For cluster 1, where the PBR lies in the upper part of the aforementioned range, the ISBR lies in the lower range, i.e., from ≈ 0.3333 to ≈ 0.6316. In contrast, for cluster 2 where $0.5 \leq \text{PBR} \leq 1$, the ISBR values lie in the range from ≈ 0.5333 to ≈ 0.8824. The two transmission zeros are biased towards the upper passband for high values of PBR and towards the lower passband for low values of PBR. Examples of transfer functions grouped in these clusters are displayed in Fig. 6.6. The objects in cluster 1 are split equally between the three CT arrangements, whereas those in cluster 2 are predominantly of type (b). By inspecting the two clusters, it was evident that the triplet placed close to the source was used to produce the transmission zero whose distance from the closest band-edge was a minimum. In addition, the resonator exhibiting the peak t.a.s.e for all topologies was the one opposite to the cross-coupling of the triplet positioned closest to the source. The latter two observations are consistent with those obtained for single band CT topologies.

Clusters 3 and 4 comprise of the best case topologies for transfer functions that are highly asymmetric. In the present context, highly asymmetric transfer functions refer to those whose PBR is either less than 0.7 or greater than 1.6. In order to achieve the desired selectivity, the two transmission zeros are located close to the lower passband for low values of PBR. Similarly, for high values of PBR, the transmission zeros are positioned closer to the upper passband. Examples of transfer functions grouped in this cluster are displayed in Fig. 6.7. Approximately 95% of the filter topologies grouped in these two clusters employ CT arrangements (b) or (c). In all topologies grouped in these clusters, the triplet placed closest to the source was used to generate the transmission zero positioned furthest away from either band-edges. The resonator demonstrating the peak t.a.s.e in most cases, however not all, is the one opposite to the cross-coupling of the triplet placed closest to the source.

Cluster 5 comprises of a mixture of the best and the worst case topologies for transfer functions with $1 \leq \text{PBR} \leq 1.6667$. The ISBR for these transfer functions is in the range $0.3333 \leq \text{ISBR} \leq 0.6$. Approximately 53% of the objects grouped in this cluster constitute the worst case topologies. Interestingly, all of these topologies represented transfer functions with PBR = 1. In such cases, the two transmission zeros are located at similar distances
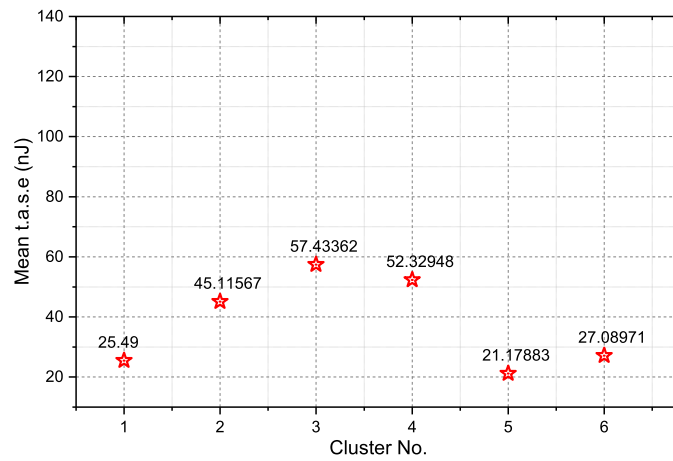
(a) Mean peak t.a.s.e for each cluster - X_t data set
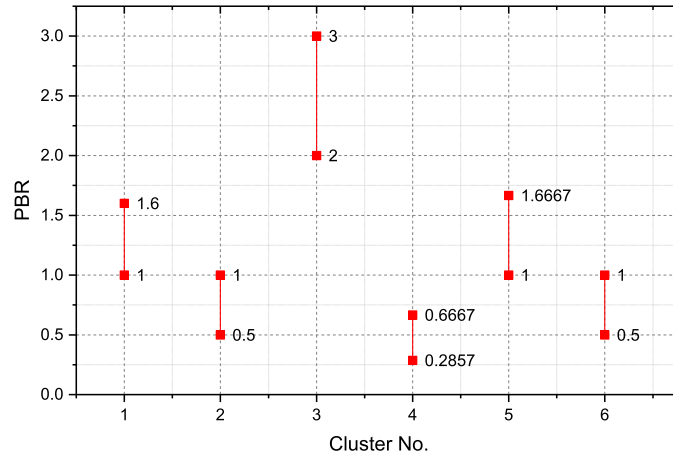
(b) Range of passband ratio for each cluster - X_t data set
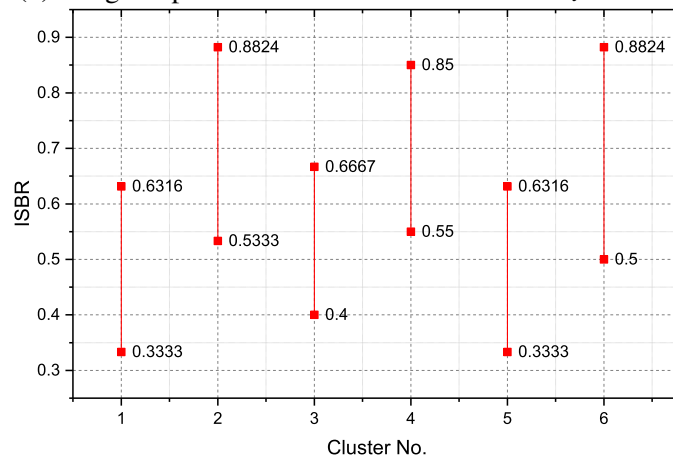
(c) Range of inner stopband to total bandwidth ratio for each cluster - X_t data set

Fig. 6.3 Statistics for mean t.a.s.e, PBR and ISBR for each cluster of the X_t data set.
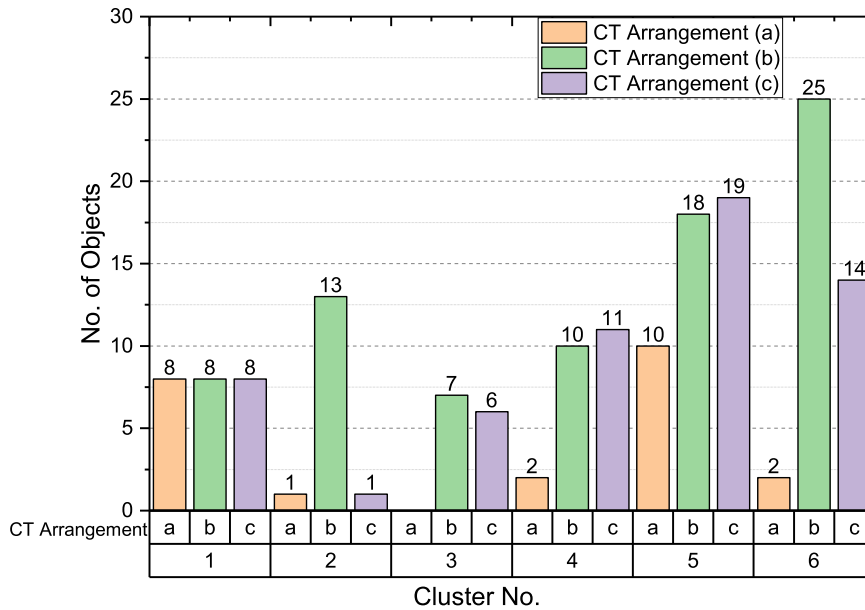
Fig. 6.4 The number of objects with the various CT arrangements from Fig. 5.6 that are grouped in each cluster.
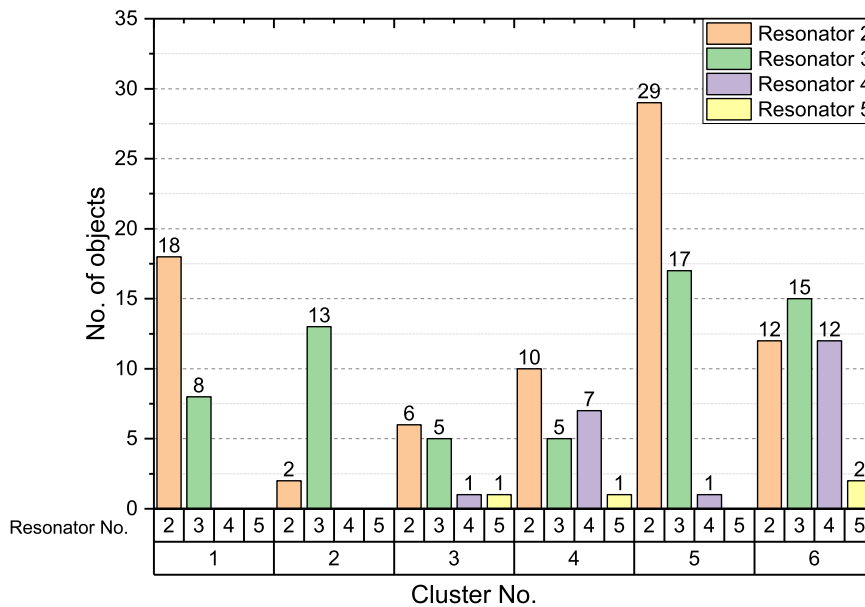
Fig. 6.5 Statistics for the peak t.a.s.e resonators in each cluster for the 6-2 dual band CT network topologies.

from the respective band-edges, thus, yielding an almost symmetric response. The resonator demonstrating the peak t.a.s.e for these objects is always the one opposite to the cross-coupling of the triplet placed closest to the source. In contrast, the topologies representing transfer functions whose PBR $\neq$ 1 constituted the best case topologies. These topologies
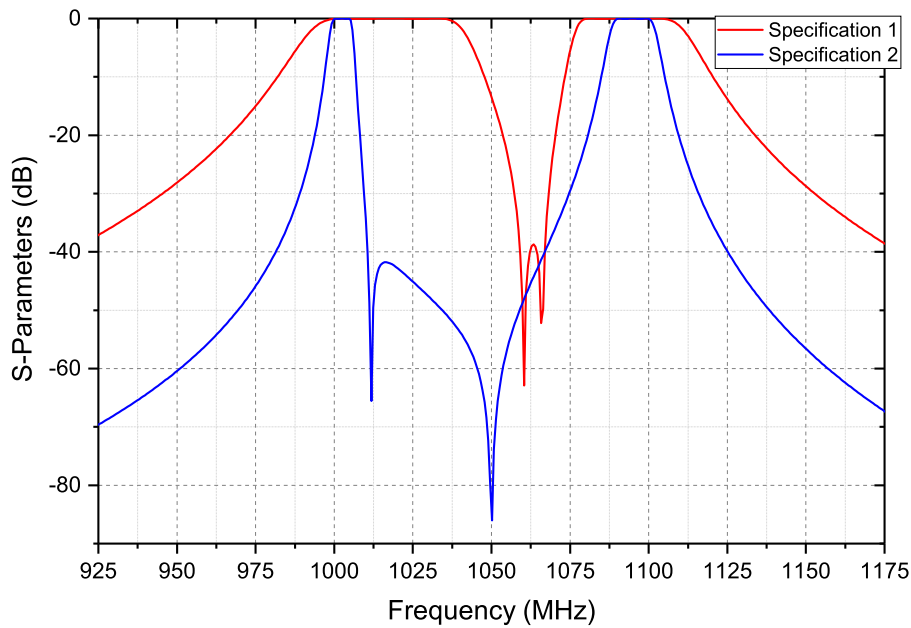
Fig. 6.6 Examples of transfer functions grouped in clusters 1 and 2. Specification 1 represents an object from cluster 1 whose PBR = 1.4. Similarly, specification 2 represents an object from cluster 2 whose PBR = 0.5.
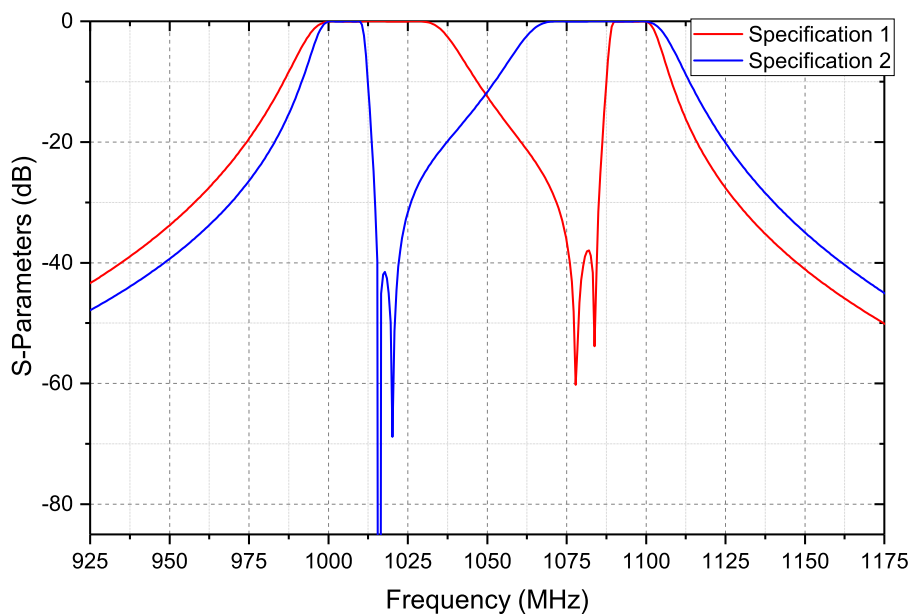
Fig. 6.7 Examples of transfer functions grouped in clusters 3 and 4. Specification 1 represents an object from cluster 3 whose PBR = 3. Similarly, specification 2 represents an object from cluster 4 whose PBR = 0.3333.

employed CT arrangements (b) or (c). As in clusters 3 and 4, the the triplet placed closest to the source was used to generate the transmission zero positioned furthest away from either

band-edges. Furthermore, in most cases, the resonator exhibiting the peak t.a.s.e was the one opposite to the cross-coupling of the triplet placed closest to the source. Examples of transfer functions and the corresponding topologies grouped in cluster 5 are represented by Fig. 6.8 and the Table 6.4. The object x_{t_1} represents the worst case topology for a transfer function with PBR = 1, whereas x_{t_2} represents the best case topology for a transfer function with PBR = 1.25.

Table 6.4 Examples of objects grouped in cluster 5 - X_t data set for 6-2 dual band transfer functions.

	Peak t.a.s.e (nJ)	PBR	ISBR	Relative t.z position ratio - (1)	Relative t.z position ratio - (2)	Triplet position (1)	Triplet position (2)
x_{t_1}	25.5890	1	0.5000	0.3750	0.6075	4	6
x_{t_2}	14.4620	1.25	0.5500	0.5236	0.6327	4	6
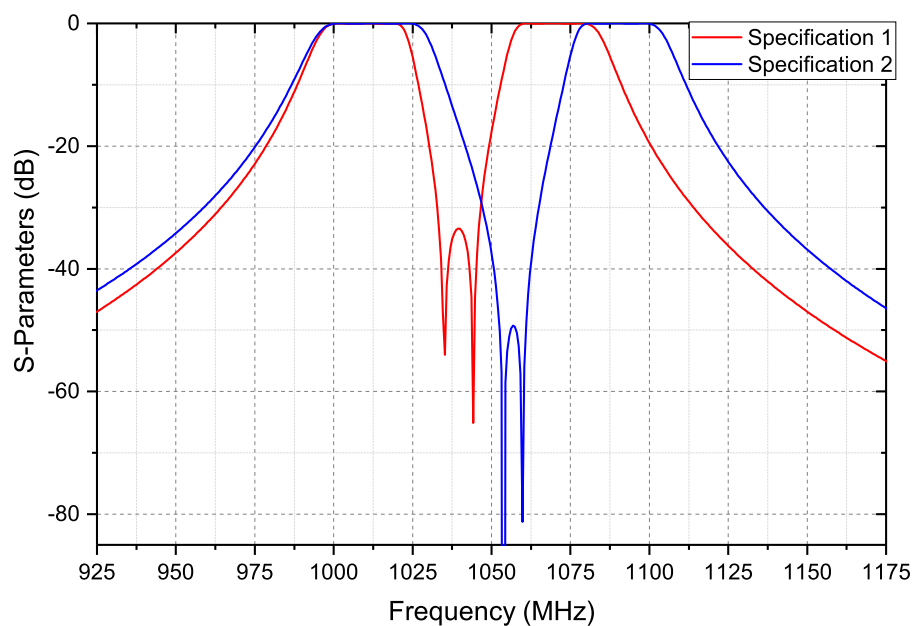
Fig. 6.8 Examples of transfer functions grouped in cluster 5. Specifications 1 and 2 represent the objects x_{t_1} and x_{t_2}, respectively, from Table 6.4.

Approximately 85% of the objects in cluster 6 constitute the best case topologies for transfer functions with $0.5 \leq$ PBR ≤ 1. The ISBR of these transfer functions is in the range $0.5 \leq$ ISBR ≤ 0.8824. The objects that constitute the worst case topologies represent transfer functions with PBR = 1. Hence, from the results obtained for clusters 5 and 6, it can be

concluded that CT topologies are not a suitable choice for realisation of transfer functions that are close to being symmetric. The objects representing the optimum topologies are composed of CT arrangements (b) or (c). The resonator giving the peak t.a.s.e in most, but not all, cases is the one opposite to the cross-coupling of the triplet placed closest to the source. Figure 6.9 and Table 6.5 represent the transfer functions and the corresponding network topologies, respectively, grouped in cluster 6. The object x_{t_1} represents the worst case topology for a transfer function with PBR = 1, whereas x_{t_2} represents the best case topology for a transfer function with PBR = 0.75.

Table 6.5 Examples of objects grouped in cluster 6 - X_t data set for 6-2 dual band transfer functions.

	Peak t.a.s.e (nJ)	PBR	ISBR	Relative t.z position ratio - (1)	Relative t.z position ratio - (2)	Triplet position (1)	Triplet position (2)
x_{t_1}	35.5990	1	0.7500	0.3333	0.6483	6	4
x_{t_2}	20.5740	0.75	0.5625	0.2222	0.5489	6	4
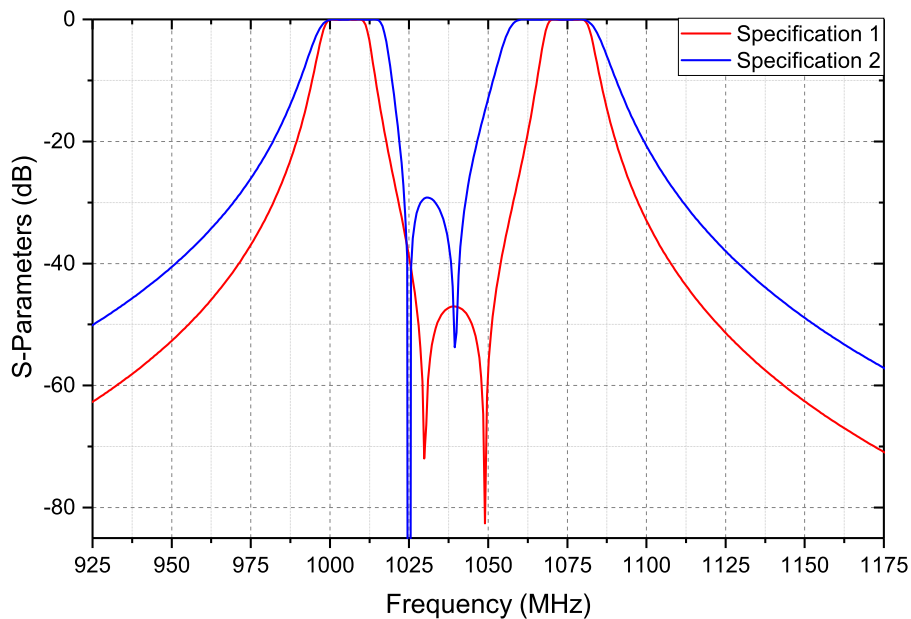
Fig. 6.9 Examples of transfer functions grouped in cluster 6. Specifications 1 and 2 represent the objects x_{t_1} and x_{t_2}, respectively, from Table 6.5.

Cascaded quartet data set

The objects representing the worst case filter topologies for highly asymmetric transfer functions are grouped in clusters 1 and 2. Highly asymmetric, in this context, refers to transfer functions with $0.2857 \leq PBR \leq 0.75$ or $2 \leq PBR \leq 3$. In order to achieve the desired selectivity, the two transmission zeros are located close to the lower passband for low values of PBR. Similarly, the transmission zeros are biased towards the upper passband for high values of PBR. Collectively, the ISBR for clusters 1 and 2 is in the range $0.4 \leq ISBR \leq 0.85$. The objects employ CQ arrangement (c) with a forward asymmetric cross-coupling or CQ arrangement (b) with a backward asymmetric cross-coupling. In both of the aforementioned topologies, the resonator opposite to the asymmetric cross-coupling is resonator 4. It is this resonator that demonstrates the peak t.a.s.e for all topologies in these clusters. Tables 6.6 and 6.7 present examples of objects grouped in clusters 1 and 2, respectively.

Table 6.6 Examples of objects grouped in cluster 1 - X_q data set for 6-2 dual band transfer functions.

	Peak t.a.s.e (nJ)	PBR	ISBR	Relative t.z position ratio - (1)	Relative t.z position ratio - (2)	Quartet position (1)	Asymmetric cross-coupling direction
x_{q_1}	65.5750	0.5000	0.6250	0.2000	0.2780	6	1
x_{q_2}	31.6080	0.75	0.6500	0.2308	0.5385	6	1

Table 6.7 Examples of objects grouped in cluster 2 - X_q data set for 6-2 dual band transfer functions.

	Peak t.a.s.e (nJ)	PBR	ISBR	Relative t.z position ratio - (1)	Relative t.z position ratio - (2)	Quartet position (1)	Asymmetric cross-coupling direction
x_{q_1}	91.6420	3	0.6000	0.8000	0.8983	6	1
x_{q_2}	111.7300	2	0.6667	0.6933	0.8000	5	0

Clusters 3 and 6 comprise of the best case topologies for transfer functions that have passband ratios in the range $1 \leq PBR \leq 1.6667$ and $0.6667 \leq PBR \leq 1$, respectively. The ISBR for the two clusters is such that $0.3333 \leq ISBR \leq 0.8824$. The objects in cluster 3 employ CQ arrangement (b) or (c) with a forward asymmetric cross-coupling. Cascaded quartet arrangement (b), however, provides a slightly lower peak t.a.s.e for such transfer functions than CQ arrangement (c). In contrast, cluster 6 comprises of objects employing CQ arrangement (a)
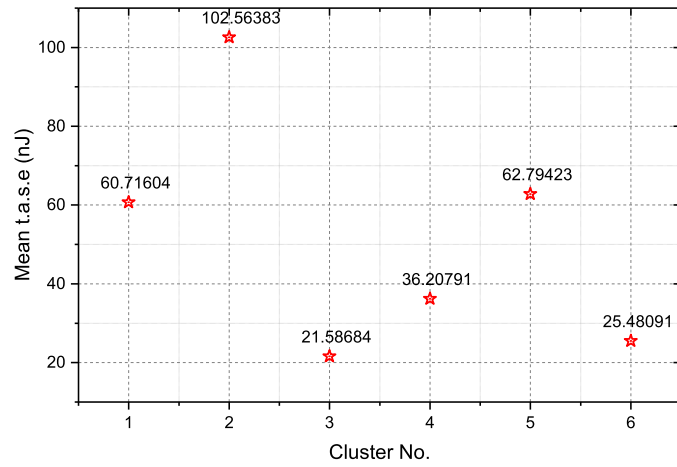
(a) Mean peak t.a.s.e for each cluster - X_q data set
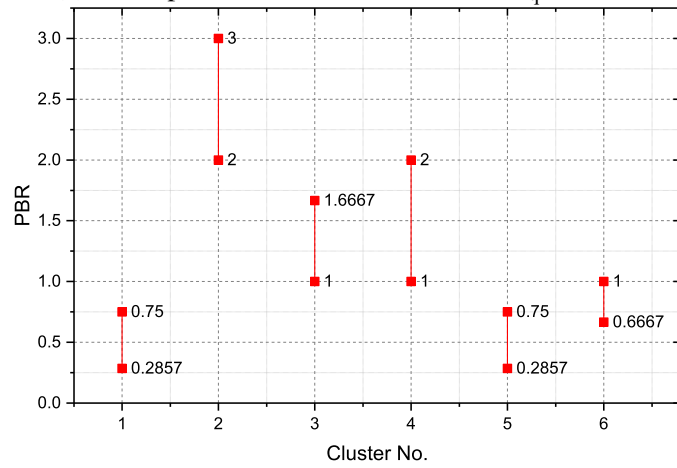
(b) Range of passband ratio for each cluster - X_q data set
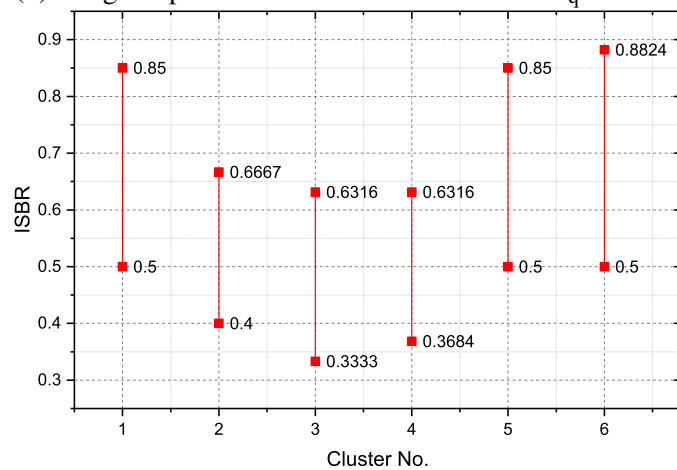
(c) Range of inner stopband to total bandwidth ratio for each cluster - X_q data set

Fig. 6.10 Statistics for mean t.a.s.e, PBR and ISBR for each cluster of the X_q data set.
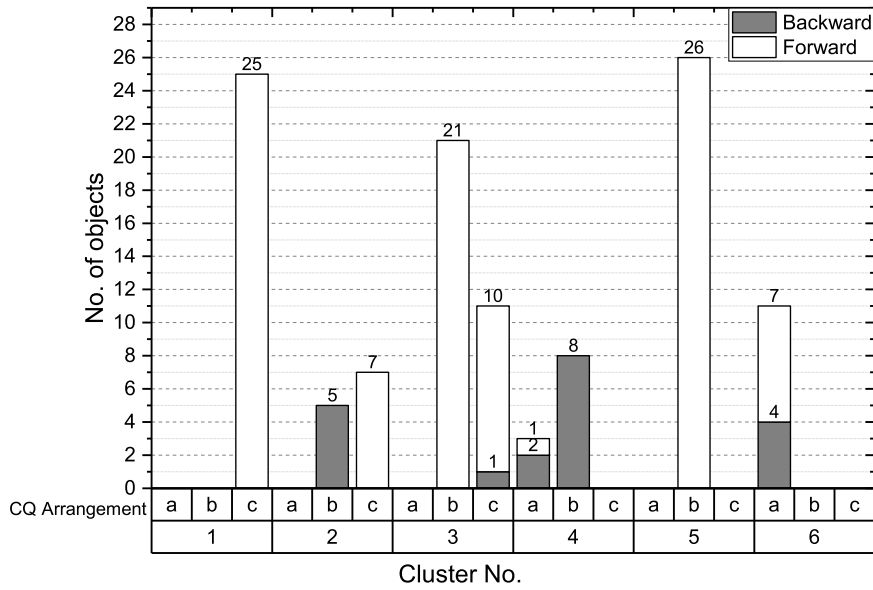
Fig. 6.11 The number of objects with the various CQ arrangements from Fig. 5.6 that are grouped in each cluster.
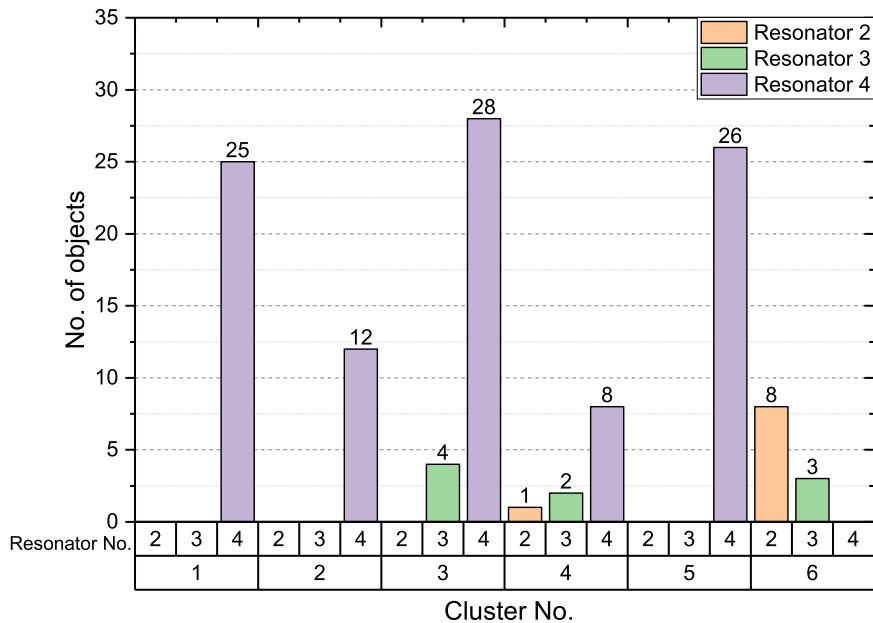
Fig. 6.12 Statistics for the peak t.a.s.e resonators in each cluster for the 6-2 dual band CQ network topologies.

with a forward and backward cross-coupling constituting the two optimum topologies for the transfer function. Note that approximately 82% of the filter topologies grouped in cluster 6 represent transfer functions with PBR = 1. Examples of objects grouped in the clusters 3 and 6 are presented in Table 6.8 and Table 6.9, respectively.

Table 6.8 Examples of objects grouped in cluster 3 - X_q data set for 6-2 dual band transfer functions.

	Peak t.a.s.e (nJ)	PBR	ISBR	Relative t.z position ratio - (1)	Relative t.z position ratio - (2)	Quartet position (1)	Asymmetric cross-coupling direction
x_{q_1}	20.6610	1	0.6000	0.3333	0.6489	5	1
x_{q_2}	16.8250	1.25	0.5500	0.5236	0.6327	5	1

Table 6.9 Examples of objects grouped in cluster 6 - X_q data set for 6-2 dual band transfer functions.

	Peak t.a.s.e (nJ)	PBR	ISBR	Relative t.z position ratio - (1)	Relative t.z position ratio - (2)	Quartet position (1)	Asymmetric cross-coupling direction
x_{q_1}	23.9590	1	0.7500	0.3333	0.6489	4	0
x_{q_2}	26.1870	0.75	0.5625	0.3333	0.4178	4	1

Cluster 4 contains a mixture of the best and the worst case topologies realising transfer functions with passband ratio in the range $1 \leq PBR \leq 1.6667$. The ISBR value range from ≈ 0.3210 to ≈ 0.6316. The objects employing CQ arrangement (a) exhibit lower peak t.a.s.e, thus, representing the best case topologies for such transfer functions. On the contrary, the objects in this cluster that employ CQ arrangement (b) represent the worst case topologies. In addition, the resonator exhibiting the peak t.a.s.e is the one opposite to the asymmetric cross-coupling of the quartet. Examples of objects included in this cluster are presented in Table 6.10. Object x_{q_1} represents the best case topology, whereas object x_{q_2} represents the worst case topology for the same transfer function.

Table 6.10 Examples of objects grouped in cluster 4 - X_q data set for 6-2 dual band transfer functions.

	Peak t.a.s.e (nJ)	PBR	ISBR	Relative t.z position ratio - (1)	Relative t.z position ratio - (2)	Quartet position (1)	Asymmetric cross-coupling direction
x_{q_1}	19.6010	1.5	0.4000	0.6020	0.7040	4	0
x_{q_2}	27.3830	1.5	0.4000	0.6020	0.7040	5	0

Cluster 5 comprises of objects constituting the worst case topologies for transfer functions with low values of PBR, i.e, $0.3333 \leq PBR \leq 0.75$. The ISBR ranges from 0.5 to 0.85. The

CQ network topologies included in this cluster are such that a quartet employing backward asymmetric cross-coupling is placed at resonators 2-3-4-5. The resonator exhibiting the peak t.a.s.e is always the one opposite to the asymmetric cross-coupling of the quartet. Examples of objects grouped in cluster 5 are presented in Table 6.11.

Table 6.11 Examples of objects grouped in cluster 5 - X_q data set for 6-2 dual band transfer functions.

	Peak t.a.s.e (nJ)	PBR	ISBR	Relative t.z position ratio - (1)	Relative t.z position ratio - (2)	Quartet position (1)	Asymmetric cross-coupling direction
x_{q_1}	34.3960	0.75	0.5625	0.3333	0.4178	5	0
x_{q_2}	97.1680	0.3333	0.6000	0.1000	0.1717	5	0

6.1.4 General patterns

The clustering results presented in the previous section can be exploited to establish certain patterns that aid understanding of the stored energy distribution within 6-2 dual bandpass transfer functions. The following patterns can be utilised to predict the optimum power handling topologies for the various transfer functions.

Consider the highly asymmetric transfer functions represented by the passband ratios satisfying either of the following two conditions:

1. $0.2857 \leq PBR \leq 0.6667$, or

2. $2 \leq PBR \leq 3$

In order to achieve the required selectivity, the two inner stopband transmission zeros are located very close to the upper band-edge of the lower passband for low values of PBR. Similarly, for high values of PBR, the transmission zeros are positioned close to the lower band-edge of the upper passband. These transfer functions are best realised using the CT arrangements illustrated in Fig.5.6 (b) or (c). In either of these two topologies, the transmission zero located closest to the respective band-edge is to be generated using the triplet placed next to the load. Note that the admittance of the cross-coupling generating the triplet closest to a band-edge is always higher than the admittance of the cross-coupling generating a transmission zero further from the same band-edge. By choosing such a topology, the amount of energy transferred to the triplet with the highest cross-coupling admittance

is minimum. Subsequently, a lower peak t.a.s.e is achieved for a given transfer function. Consider an example where the CT arrangement (b) in Fig. 6.13 was used to realise a dual band transfer function with passbands at 1000 MHz - 1010 MHz and 1060 MHz - 1080 MHz. For PBR = 0.5, a transmission zero was prescribed at 1020 MHz so that a dependent transmission zero was obtained at 1023.9 MHz. The triplet closest to the load was used to generate the transmission zero at 1020 MHz. This constituted the best case topology for the given transfer function. The t.a.s.e distribution within the filter network is depicted in Fig. 6.14. A quartet placed next to the load and employing a forward asymmetric cross-coupling constituted the worst case topology for the same power transfer function. The t.a.s.e distribution for this topology is displayed in Fig. 6.15. By comparing the two plots, it can be seen that the peak t.a.s.e can be reduced to almost half the value by choosing the appropriate topology for realisation.
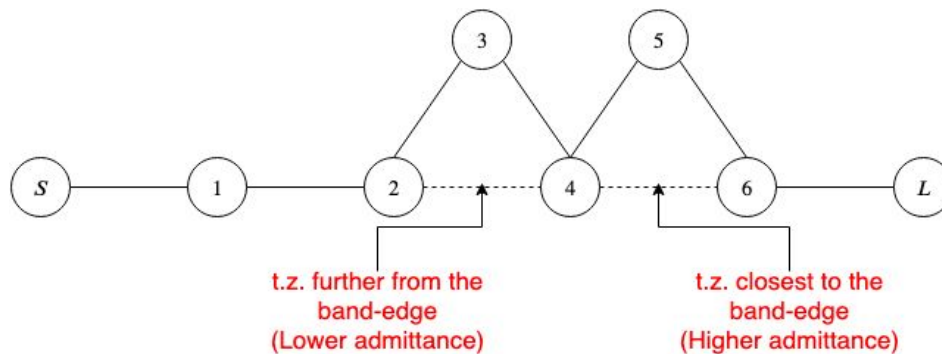
Fig. 6.13 A triplet close to the load is used to generate a transmission zero closest to the band-edge.

The dual band transfer functions with PBR = 1 are usually best realised using a CQ topology. The two inner stopband transmission zeros for such transfer functions are located at similar distances from the inner band-edges (i.e., f_2 and f_3). The optimum choice of CQ arrangement is influenced by the ISBR value and by the relative position of transmission zeros from the band-edges. Typically, it was found that for higher values of ISBR, i.e., for large band-to-band separation, a quartet positioned next to the source provides the optimum t.a.s.e distribution (refer to cluster 6 of the X_q data set). In contrast, for lower values of ISBR (typically, < 0.5), CQ arrangements (b) or (c), and employing forward asymmetric cross-coupling provide a lower peak t.a.s.e. This can be illustrated using Table 6.12. The optimum CQ arrangement for $0.5 \leq \text{ISBR} \leq 0.65$ may be either (a) or (b) depending upon the transmission zero positions. The t.a.s.e distribution graphs for the topologies represented by objects x_{q_1} and x_{q_2} are displayed in Figures 6.17, respectively. It can be observed that the t.a.s.e is almost symmetric
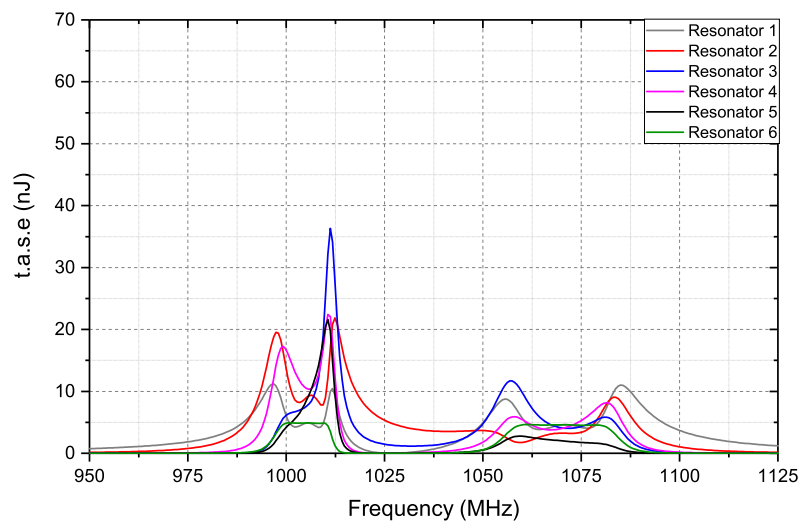
Fig. 6.14 The t.a.s.e distribution for the best case CT topology realising a transfer function with PBR = 0.5.
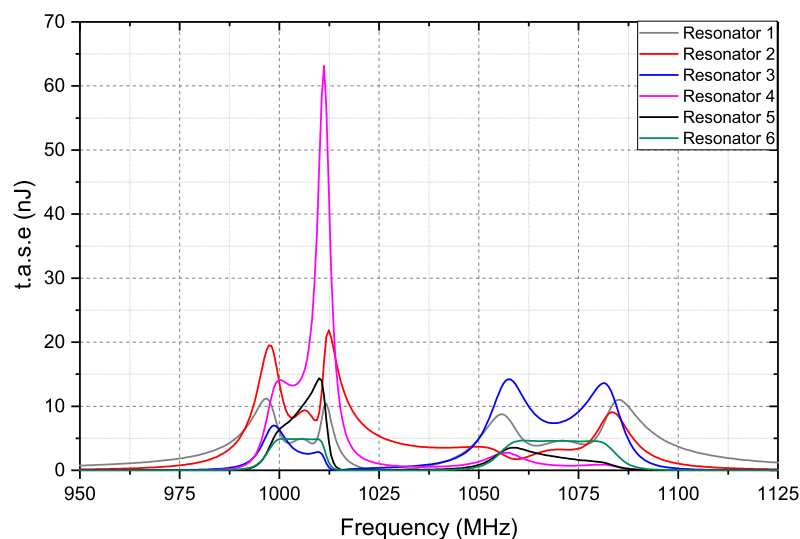
Fig. 6.15 The t.a.s.e distribution for the worst case CQ topology realising a transfer function with PBR = 0.5.

about the geometric mean frequency for CQ topologies realising a dual transfer function with PBR = 1.

Consider the transfer functions whose PBR satisfies one of the following two conditions:

1. $0.5 \leq \text{PBR} < 1$, or

2. $1 < \text{PBR} \leq 1.6667$

Table 6.12 Examples of objects grouped in cluster 5 - X_q data set for 6-2 dual band transfer functions.

	Peak t.a.s.e (nJ)	PBR	ISBR	Relative t.z position ratio - (1)	Relative t.z position ratio - (2)	Quartet position (1)	Asymmetric cross-coupling direction
x_{q_1}	23.9590	1	0.75	0.3333	0.6483	4	1
x_{q_2}	16.9380	1	0.3333	0.3475	0.6250	5	1
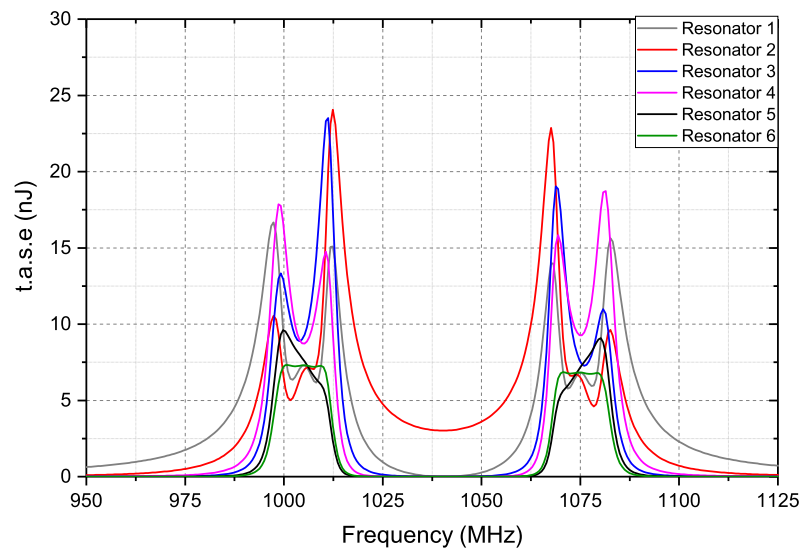
Fig. 6.16 The t.a.s.e distribution for the CQ topology represented by object x_{q_1} in Table 6.12.
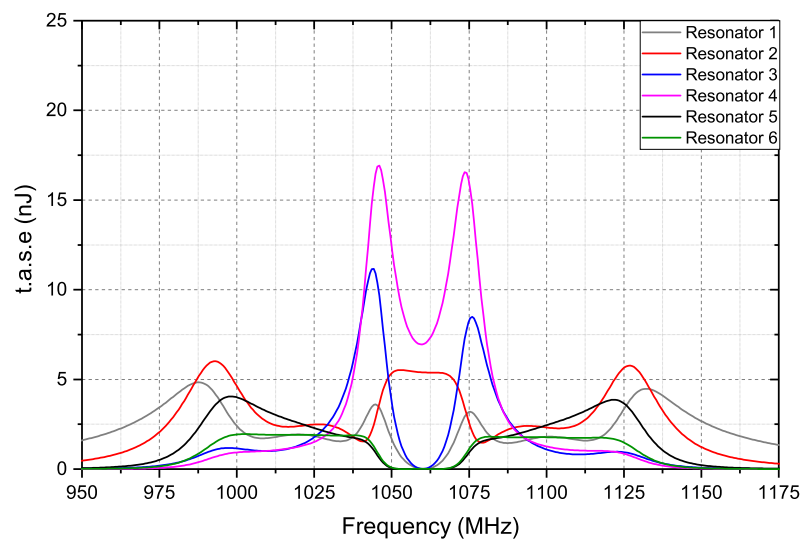
Fig. 6.17 The t.a.s.e distribution for the CQ topology represented by object x_{q_2} in Table 6.12.

For a large percentage of such transfer functions, CT topologies provide a lower peak t.a.s.e as compared to the CQ topologies. This can be verified using the objects grouped in clusters 5 and 6 for the X_t data set. However, it was observed that for certain transfer functions with sufficiently low values of ISBR, topologies employing CQ arrangement (b) with a forward cross-coupling can give a lower peak t.a.s.e value. Clusters 3, 4 and 6 comprise of topologies of this type.

In general, the optimum CT topologies are such that the triplet placed next to the load generates the transmission zero located furthest from any of the band-edges. The resonator exhibiting the peak t.a.s.e in such topologies is typically the one opposite to the cross-coupling of the triplet closest to the source. The optimum CQ topologies typically employ a forward asymmetric cross-coupling. The resonator giving the peak t.a.s.e in these topologies is one of resonators opposite to the symmetric cross-coupling. In all of the worst case CQ topologies, however, it is always the resonator opposite to the asymmetric cross-coupling that demonstrates the peak t.a.s.e.

6.1.5   Example using EM simulations

The patterns established in the previous section have been exploited to predict the optimum power handling topology for an example specification. Combline realisations of an optimum topology and a topology that would typically be implemented by a filter design engineer to realise the given specification have been implemented on CST Studio. The peak electric fields observed in both filter prototypes have been compared to validate the guidelines determined in section 6.1.4.

Specification (1):

Two passbands are specified at 1000 MHz - 1020 MHz and 1070 MHz - 1100 MHz. The degree of each passband is set to 3, i.e, $N_1 = N_2 = 3$ and thus, $N = 6$. A finite transmission zero is prescribed at 1032 MHz, yielding a dependent transmission zero at 1041 MHz. A minimum return loss level of 20 dB is required in each passband. The ideal circuit simulation response is displayed in Fig. 6.18.

The above specifications represent a transfer function with PBR = 0.6667, ISBR = 0.5 and relative transmission zero ratios of 0.2400 and 0.4200. The optimum filter topology for such an asymmetric transfer function is such that:
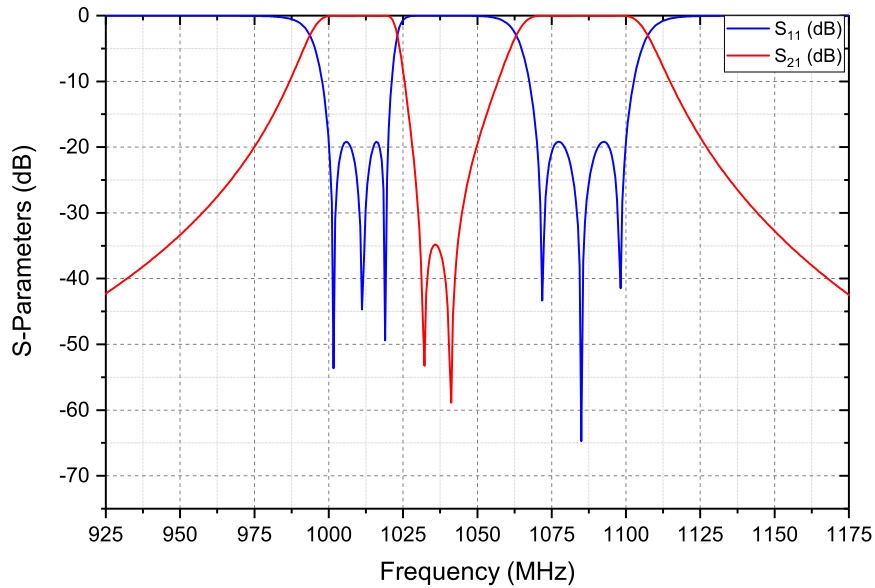
Fig. 6.18 A circuit simulation response for example specification (1).

1. the two triplets are placed as far away from the source as possible (as in CT arrangement (b)), and

2. the triplet closest to the load is used to generate the transmission zero located furthest from the band-edges.
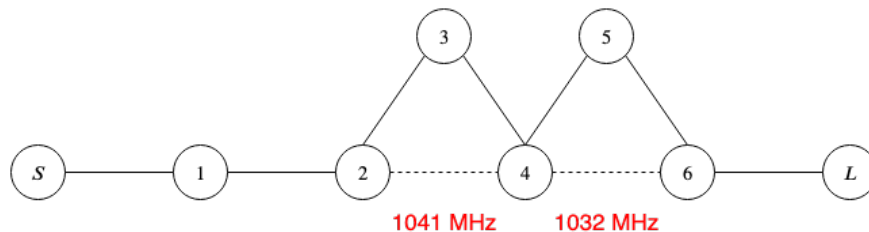
Fig. 6.19 A schematic of the optimum topology for the dual transfer function given by specification (1).

Typically, a 6th-degree transfer function with two finite zeros would be realised using a quartet. Using the patterns obtained for 6-2 single band transfer functions in section 5.4.5, the quartet would be positioned next to the load to obtain a lower peak t.a.s.e. Thus, for the purposes of comparison, the 6-2 dual band transfer function in Fig. 6.18 was realised using the CQ topology illustrated in Fig. 6.20. The t.a.s.e distribution plots for the synthesised filter networks represented by the schematics in Fig. 6.19 and Fig. 6.20, respectively, are displayed in Fig. 6.21. It was observed that resonator 3 exhibits the peak t.a.s.e of approximately 18.85
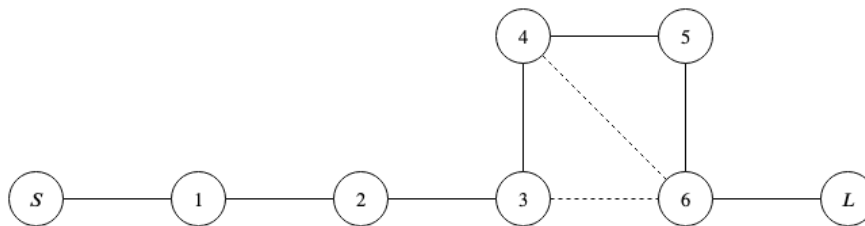
Fig. 6.20 A schematic of a CQ topology used to realise the dual transfer function given by specification (1).
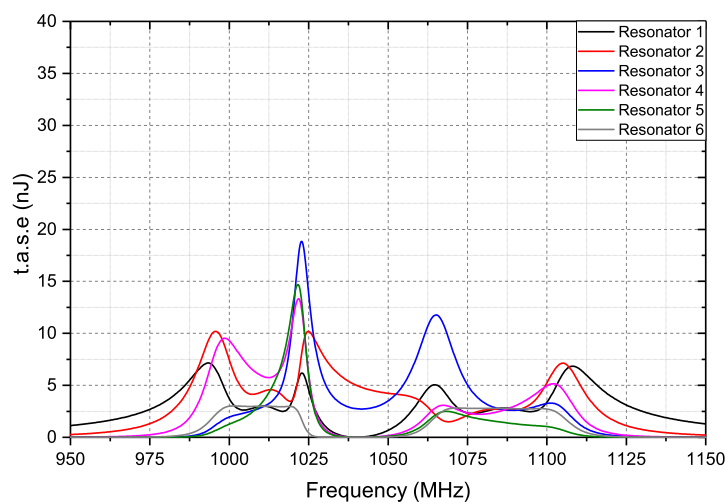
(a) T.a.s.e distribution plots for the optimum CT filter network.
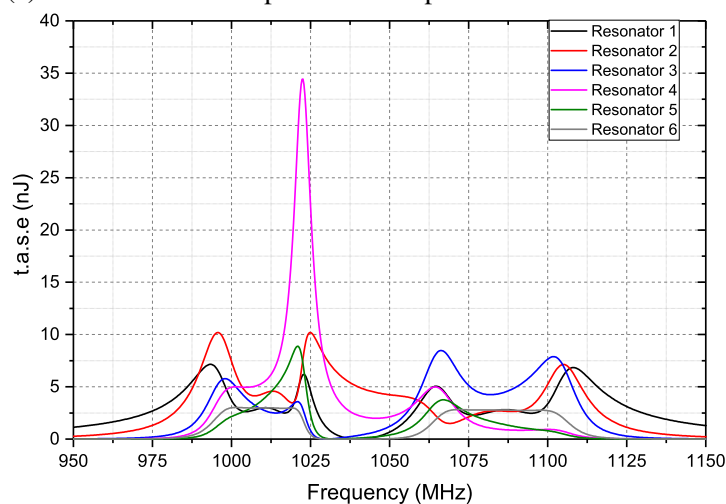
(b) T.a.s.e distribution plots for the CQ filter network - worse case topology.

Fig. 6.21 T.a.s.e distribution plots for synthesised filter networks represented by the schematics in Fig. 6.19 and Fig. 6.20, respectively.

(a) A top hat resonator   (b) Sideview   (c) Top view
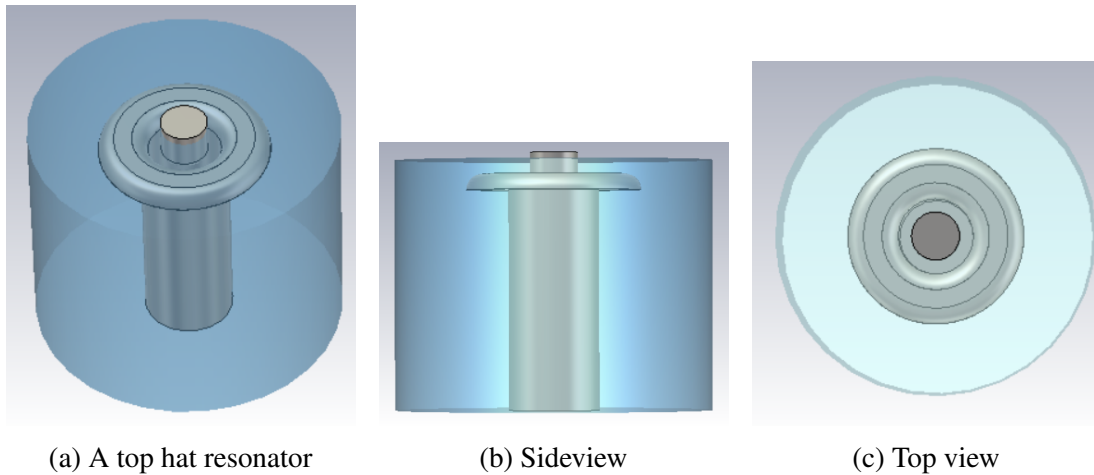
Fig. 6.22 A top hat resonator modelled in CST

nJ in the CT topology. A peak t.a.s.e of approximately 34.44 nJ was observed at resonator 4 of the CQ topology. Therefore, the peak t.a.s.e observed in the CQ filter network is almost 1.8 times the peak t.a.s.e observed in the optimum topology.

It is known that increasing the size of the filter increases its power handling capacity [2]. However, there are size constraints imposed on all commercial coaxial filters. Hence, the two prototypes were constrained to similar physical dimensions to enable a valid comparison. The length of the resonators was reduced by introducing top hat structures. These offer a larger capacitance at the top-end of each resonator, thus, shifting the resonant frequency to a higher frequency. Hence, for a given resonant frequency the length of the resonator can be reduced by introducing a top hat at its top-end. A CST model of a top hat resonator with a tuning screw is displayed in Fig. 6.22. The practical procedures outlined in section 2.4 were used to obtain the initial dimensions for the two prototypes. The inductive couplings were realised using irises and ribs. The capacitive cross-couplings were realised using suspended copper strips. Subsequently, the prototypes were modelled on CST and their physical parameters were optimised until satisfactory responses were achieved. The CST models of the 6th-degree CT and CQ combline filter prototypes are displayed in Fig 6.23 and Fig. 6.24, respectively. The optimised EM simulation responses for the optimum CT topology and the CQ topology are displayed in Fig. 6.25 and Fig. 6.26, respectively.

A return loss level of ≈ 18 dB to ≈ 22.4 dB was obtained in the two passbands for the optimum filter prototype. Similarly, the passband return loss level for the CQ topology ranged between ≈ 18.5 dB to ≈ 22.5 dB. The final physical dimensions for the two prototypes are listed in Table 6.1.5 and Table 6.1.5. The summation of the peak electric fields obtained by exciting ports 1 and 2 of the optimum CT topology at the upper cut-off frequency of
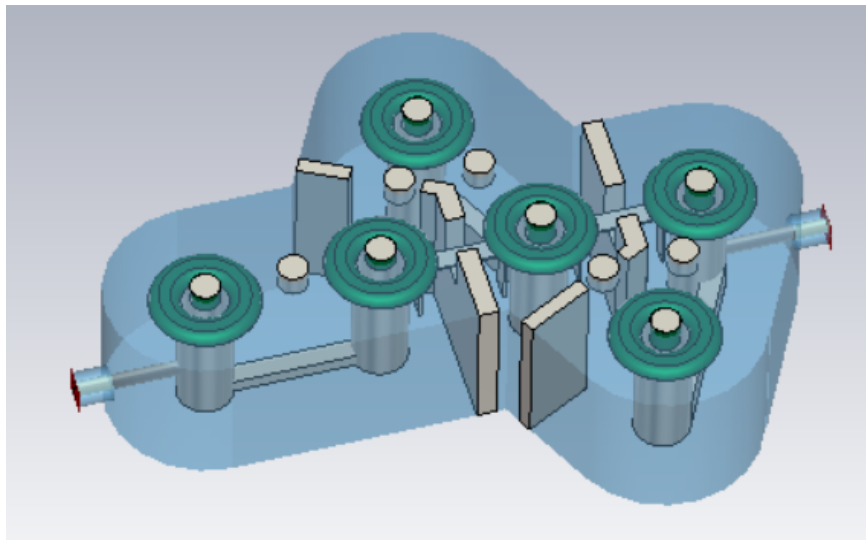
Fig. 6.23 A combline filter prototype of the optimum CT topology for 6th-degree dual bandpass transfer function as modelled on CST.
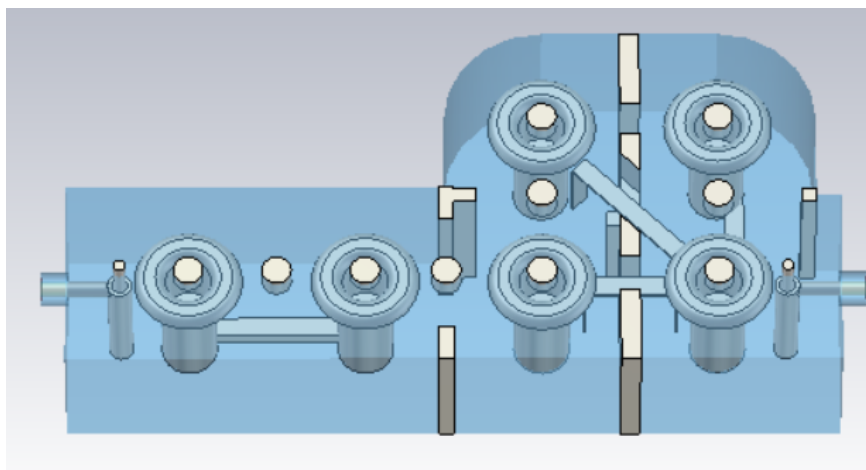
Fig. 6.24 A combline filter prototype of the CQ topology for 6th-degree dual bandpass transfer function as modelled on CST.

the lower stopband is illustrated in Fig. 6.27. A maximum of 110307 V/m is observed at resonator 3. Similarly, the summation of the peak electric fields at 1020 MHz for the CQ topology is displayed in Fig. 6.28. A maximum electric field of 159199 V/m is observed at resonator 4 for the CQ topology. Hence, the maximum electric field observed in the CQ topology is approximately 1.5 times the maximum electric field value observed in the CT topology.

The EM simulation results are, therefore, in good agreement with the theoretical results. Hence, it can be concluded that the patterns obtained using the k-means clustering method in
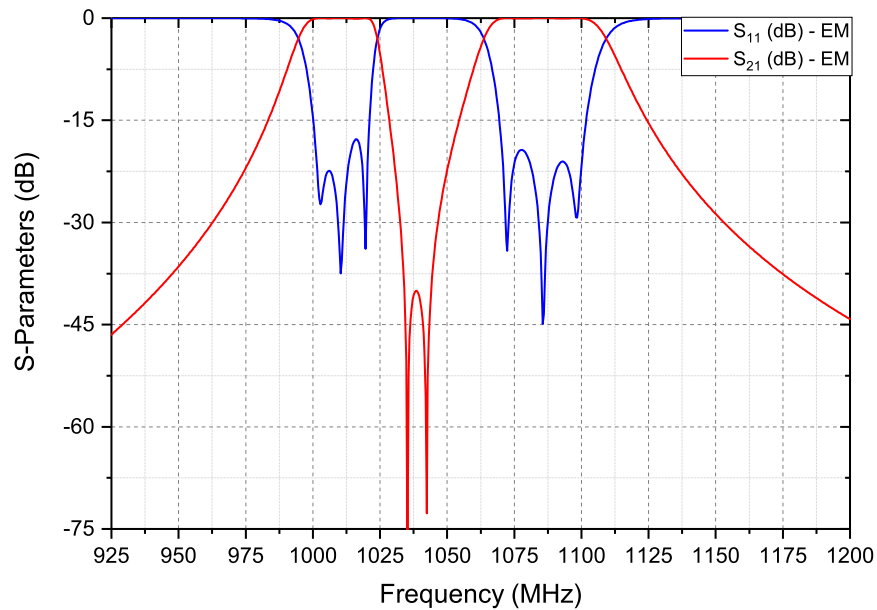
Fig. 6.25 An optimised EM simulation for 6-2 dual bandpass specification (1) realised using the CT topology in Fig. 6.19.
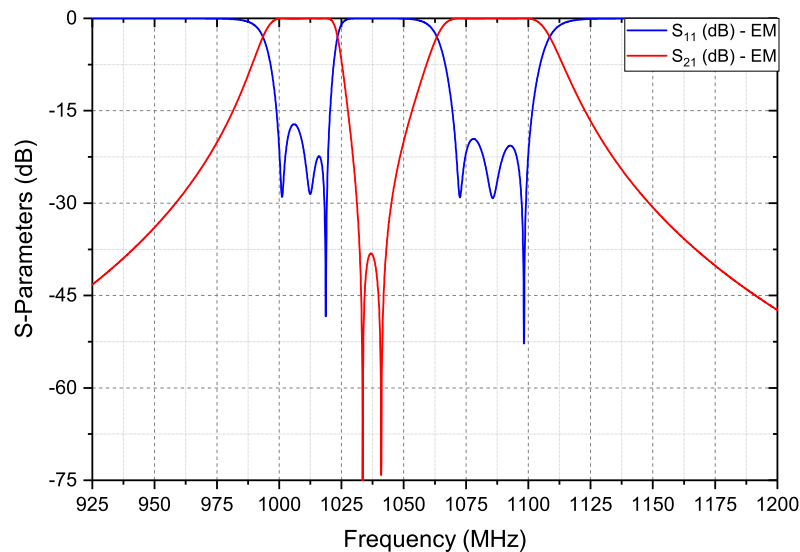
Fig. 6.26 An optimised EM simulation for 6-2 dual bandpass specification (1) realised using the CQ topology in Fig. 6.20.

section 6.1.4 can be exploited to predict the optimum power handling topology for a given transfer function and given size constraints.

Table 6.13 Physical dimensions for the combline realisation of the CT topology realising a 6-2 dual bandpass transfer function.

Dimension	Value (mm)
Coaxial resonator length	28.6
Resonator outer diameter	11.4
Resonator inner diameter	9.4
Top hat outer diameter	22
Cavity height	31.3
Input tap height	8.5
Input tap height	9.5
Rib height 1-2	2.8
Iris width 2-3	14.2
Rib height 3-4	7
Iris width 4-5	10.3
Rib height 5-6	7.3
Copper strip 2-4	13.6 (height), 16.9 (length)
Copper strip 4-6	14 (height), 16.8 (length)
Tuning screw diameter	6.35

Table 6.14 Physical dimensions for the combline realisation of the CQ topology realising a 6-2 dual bandpass transfer function.

Dimension	Value (mm)
Coaxial resonator length	28.6
Resonator outer diameter	11.4
Resonator inner diameter	9.4
Top hat outer diameter	22
Cavity height	31.3
Transformer outer diameter	5
Transformer to resonator distance (input and output)	6.3
Rib height 1-2	2.6
Iris width 2-3	25.3
Iris width 3-4	26.7
Iris width 4-5	7
Rib height 5-6	0.8
Copper strip 3-6	15.5 (height), 18.3 (length)
Copper strip 4-6	15 (height), 20.4 (length)
Tuning screw diameter	6.35
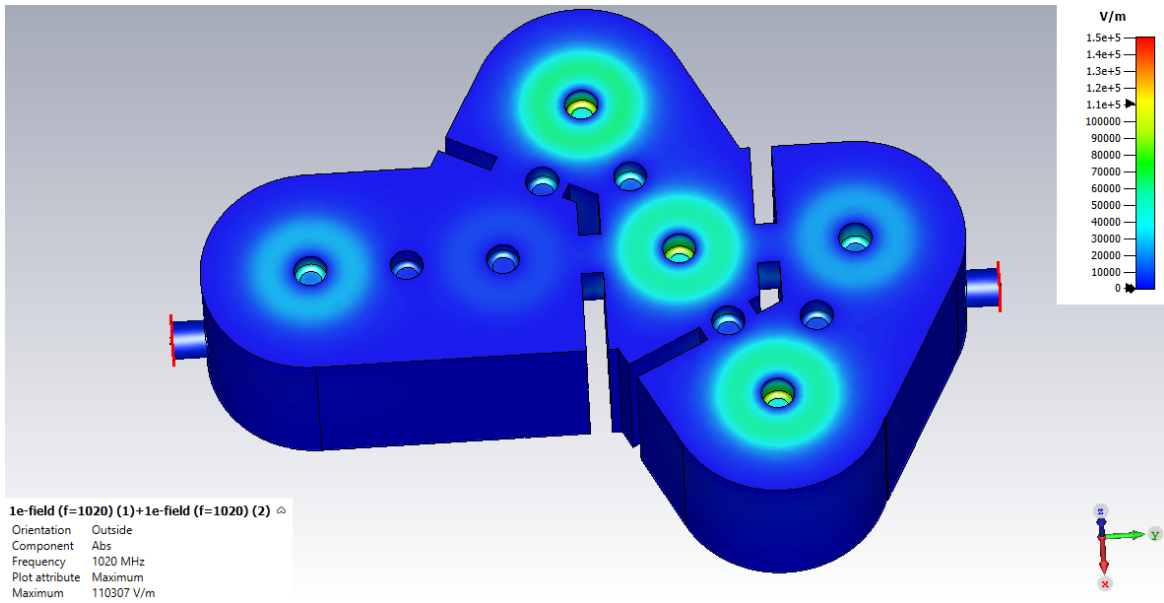
Fig. 6.27 Peak electric fields observed for the 6-2 CT topology at 1020 MHz.
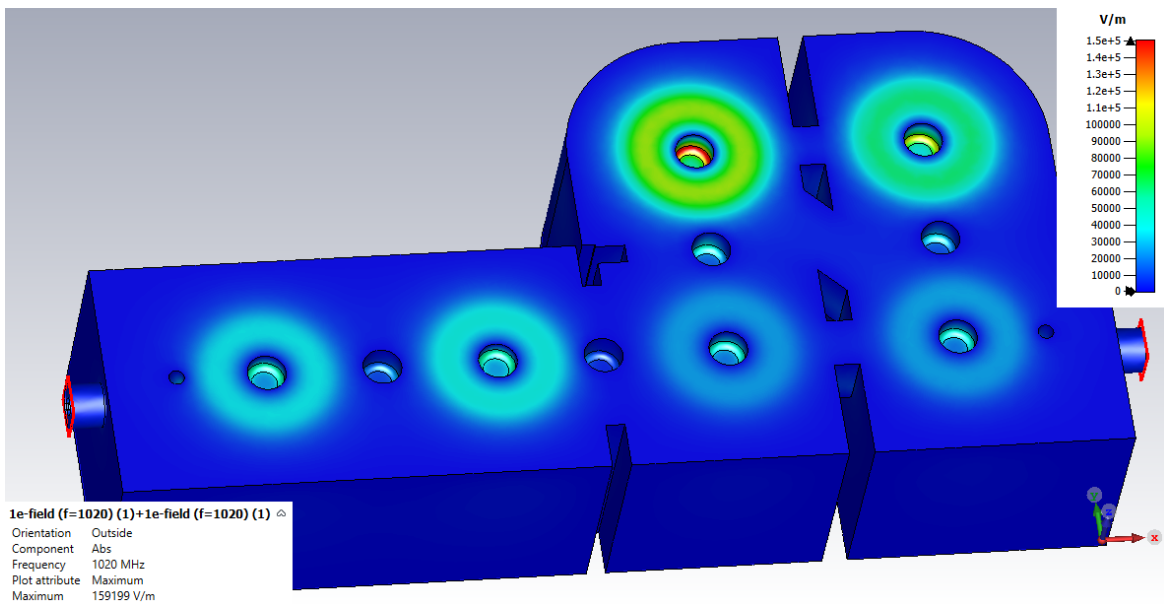
Fig. 6.28 Peak electric fields observed for the 6-2 CQ topology at 1020 MHz.

6.2   T.a.s.e distribution in filter networks for 8-4 dual band-pass transfer functions

The k-means clustering algorithm was applied to a data set consisting of more complex dual bandpass filter topologies. Cascaded n-tuplet topologies realising sixty distinct 8-4 dual bandpass transfer functions were generated using the direct coupling matrix synthesis method explained in section 2.3.1. For each specification, the degree of each passband was set to $N_1 = N_2 = 4$. The number of inner stopband transmission zeros were set to 2, 3 or 4. The lowermost cut-off frequency was fixed at 1000 MHz and the remaining three cut-off frequencies were varied so as to achieve different passband ratios and inner stopband to total bandwidth ratios.

An 8th-degree transfer function with four finite transmission zero pairs can be realised using either two cascaded quartets or a single quartet in cascade with two triplets. The possible CQ and cascaded n-tuplet topologies are depicted in Fig. 6.29 and Fig. 6.30, respectively. The quartets are displayed with a forward asymmetric cross-coupling in all topological arrangements. By changing the sequence of transmission zero generation and the asymmetric cross-coupling direction for the quartets, 72 CQ topologies and 72 cascaded n-tuplet topologies are obtained for each specification. This yields a total of 8640 cascaded filter topologies for 60 different dual band specifications. Five topologies exhibiting the minimum and the maximum peak t.a.s.e, each, were extracted for clustering.

6.2.1   Modelling input data

The five topologies exhibiting the lowest peak t.a.s.e for each transfer function were assigned a flag ranging from 1 to 5, 1 being the topology with the lowest peak t.a.s.e. Similarly, the five topologies with the highest peak t.a.s.e were assigned flags ranging from -1 to -5, -5 being the one with the highest peak t.a.s.e. These topologies were then separated into two distinct data sets, viz. the cascaded quartet data set X_q and the cascaded n-tuplet data set X_n. The CQ arrangements (a), (b) and (c) in Fig. 6.29 were represented using values '0', '1' and '2', respectively. Similarly, the cascaded n-tuplet arrangements in Fig. 6.30 were represented by '0', '1' and '2', respectively. The direction of the asymmetric cross-coupling in the quartets was represented by binary values. A value of '0' implied that the quartet employed backward asymmetric cross-coupling and '1' implied a forward asymmetric cross-coupling. The peak t.a.s.e was used as an indicator of the power handling capacity of the filter network.
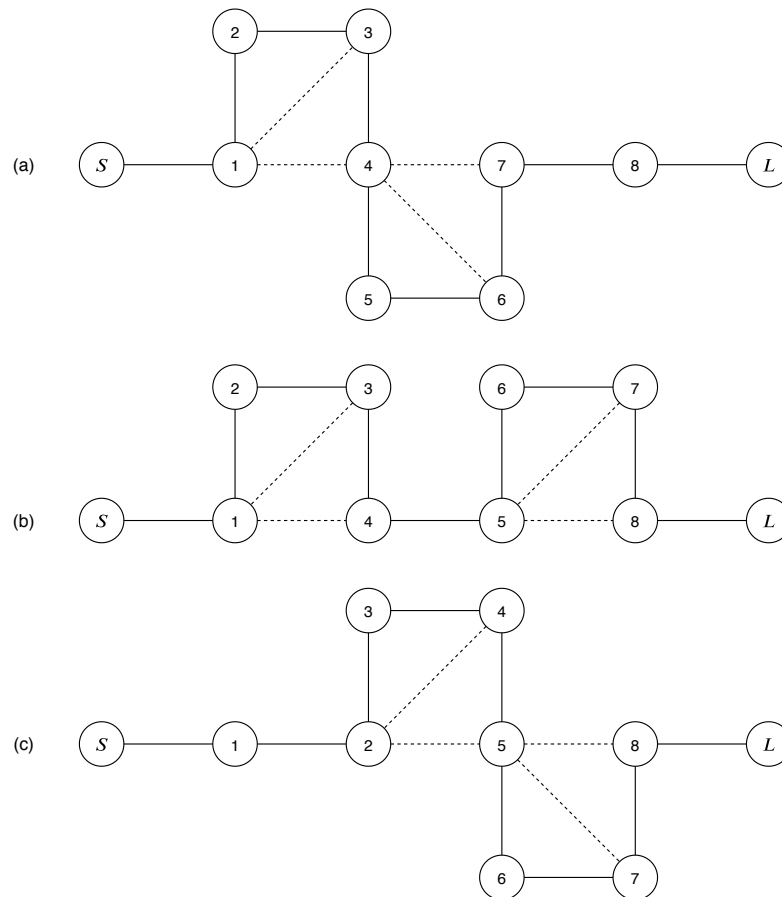
Fig. 6.29 Purely cascaded quartet topologies used to realise 8-4 dual band transfer functions.

The following two attributes were used to represent the dual band transfer functions in both data sets:

1. The passband ratio (PBR) - ratio of the bandwidth of the lower passband to that of the upper passband: $(f_2 - f_1)/(f_4 - f_3)$.

2. The inner stopband ratio (ISBR) - ratio of the bandwidth of the inner stopband to the total bandwidth of the entire dual band: $(f_3 - f_2)/(f_4 - f_1)$.

The attributes used to describe the transmission zero positions for each data set were, however, non-identical. In case of the purely CQ topologies, it was realised that the transmission zeros produced by the quartet closest to the source affected the peak t.a.s.e the most. It is the position of these two transmission zeros from the closest band-edge/s and the separation between the two that determines the admittances of the cross-couplings. This, in turn, affects the peak t.a.s.e observed at the nodes in the quartet. Hence, the attributes describing the
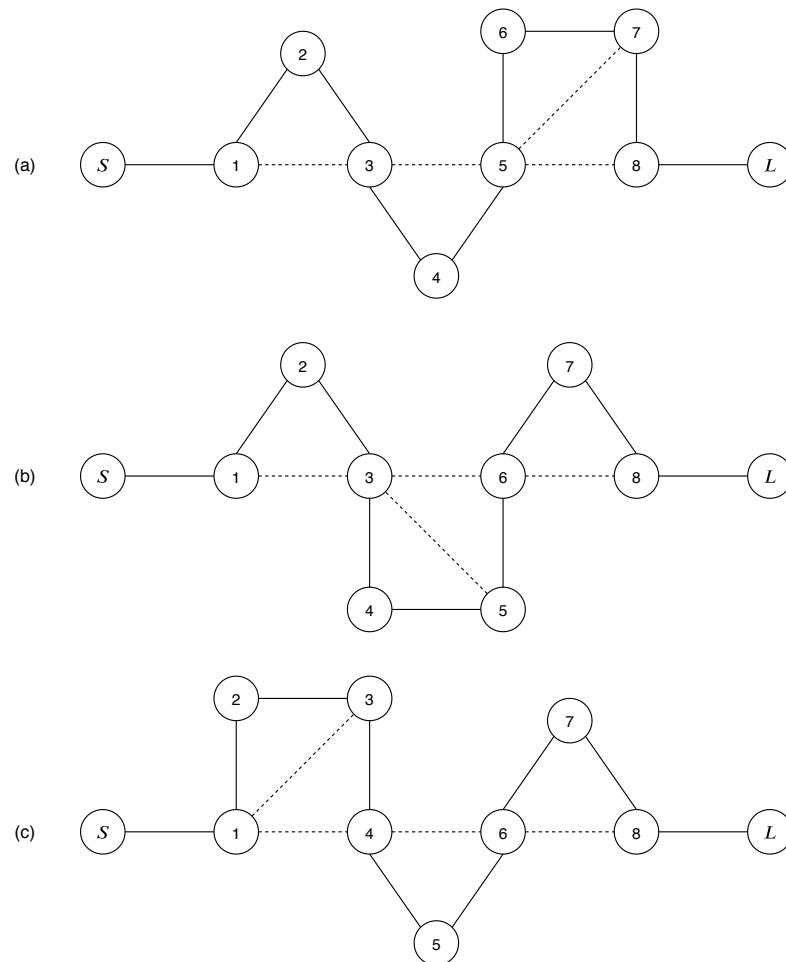
Fig. 6.30 Cascaded n-tuplet topologies used to realise 8-4 dual band transfer functions.

positions of the transmission zeros generated by the quartet closest to the source are as follows:

1. The transmission zero separation ratio (TSR) - the ratio of the separation between the two transmission zeros produced by the quartet closest to the source to the bandwidth of the entire dual band, i.e., $|f_{n1} - f_{n2}|/(f_4 - f_1)$.

2. The relative transmission zero position ratio (RTR) -
   For outer stopband transmission zeros, this ratio is defined as the ratio of the relative position of the transmission zero from its closest band-edge (f_{cbe}) to the bandwidth of the entire dual band, i.e, $|f_{n1} - f_{cbe}|/(f_4 - f_1)$.
   For inner stopband transmission zeros, this ratio is defined as the negative ratio of the relative position of the transmission zero from its closest band-edge (f_{cbe}) to the bandwidth of the inner stopband, i.e, $-|f_{n1} - f_{cbe}|/(f_3 - f_2)$.

In case of the cascaded n-tuplet data set, the relative transmission zero position ratio defined above was used as an attribute to describe all four finite transmission zeros.

Consider an example specification with two passbands located at 1000 MHz-1010 MHz and 1040 MHz - 1050 MHz. Three transmission zeros were prescribed at 1020 MHz, 1070 MHz and 1081 MHz. The number of inner stopband transmission zeros was constrained to 2. Subsequently, a dependent transmission was obtained at 1015 MHz. Suppose the CQ arrangement (b) in Fig. 6.29 was used to realise the desired transfer function in Fig. The quartet positioned at resonators 1-2-3-4 was used to produce the transmission zeros at 1020 MHz and 1070 MHz. The object entry for such a topology in the X_q data set is given in Table 6.15. The transmission zero at 1020 MHz is represented by: $- \mid 1010 - 1020 \mid /(1040 - 1010) = -0.3333$ and that at 1070 MHz is represented by: $\mid 1050 - 1070 \mid /(1050 - 1000) = 0.4$. The transmission zero separation ratio is given by: $\mid 1020 - 1070 \mid /(1050 - 1000) = 1$. Suppose cascaded n-tuplet arrangement (c) was used to realise the above transfer function.

Table 6.15 An example of an object entry for the X_q data set for 8-4 dual bandpass transfer functions.

	Peak t.a.s.e (nJ)	PBR	ISBR	TSR	RTR - (1)	RTR - (2)	CQ arrange-ment	cross-coupling direc-tion	Flag
x_q	45.2240	1	0.6	1	-0.3333	0.4	1	0	1

The quartet was used to produce the transmission zeros at 1015 MHz and 1020 MHz, followed by two triplets generating the transmission zeros at 1081 MHz and 1075 MHz. The object entry for this topology in the X_n data set is presented in Table 6.16. This topology constitutes the second worst topology for the given transfer function.

Table 6.16 An example of an object entry for the X_n data set for 8-4 dual bandpass transfer functions.

	Peak t.a.s.e (nJ)	PBR	ISBR	RTR - (1)	RTR - (2)	RTR - (3)	RTR - (4)	CQ arrange-ment	cross-coupling direc-tion	Flag
x_n	142.94	1	0.6	-0.1667	-0.3333	0.62	0.4	2	0	-4

6.2.2 Optimum value of K

Cascaded quartet data set

The elbow method was used to obtain the optimum number of clusters for the X_q data set to be partitioned into. The plot for the WCSS against the number of clusters is displayed in Fig 6.31. From the displayed plot, a clear elbow point could not be determined. Therefore, the silhouette method was applied to the data set to obtain the optimal number of clusters. The silhouette coefficients for various values of K are presented in Table 6.17.
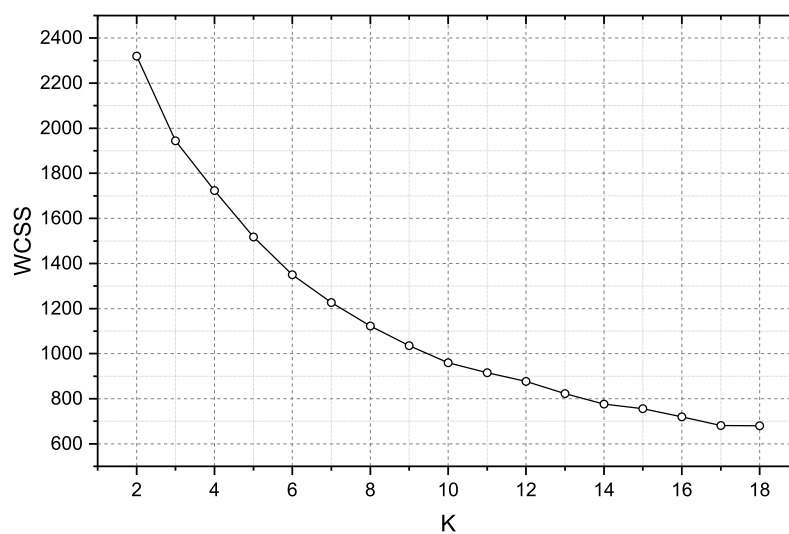
Fig. 6.31 The elbow method applied to the X_q data set for 8-4 dual band transfer functions. A definitive elbow point not achieved.

Table 6.17 The silhouette coefficients (S.C) for various values of K for a data set comprising of CQ topologies for various 8-4 dual bandpass specifications

$X_q : K$	2	3	4	5	6	7	8	9	10
S.C	0.2864	0.3139	0.3194	0.3656	0.3452	0.3559	0.3788	0.3940	0.4068
$X_q : K$	11	12	13	14	15				
S.C	0.3975	0.3868	0.3961	0.3953	0.4008				

A maximum value of the silhouette coefficient is observed for $K = 10$. Thus, the optimal number of clusters for the X_q data set is 10.

Cascaded n-tuplet data set

Th silhouette method was applied to the X_n data set to achieve a maximum value of silhouette coefficient at $K = 4$. Thus, the cascaded n-tuplet data set was partitioned into $K = 4$ clusters.

Table 6.18 The silhouette coefficients (S.C) for various values of K for a data set comprising of cascaded n-tuplet topologies for various 8-4 dual bandpass specifications

$X_n : K$	2	3	4	5	6	7	8	9	10
S.C	0.2723	0.2873	0.3354	0.2566	0.2898	0.2668	0.2554	0.3134	0.2831
$X_n : K$	11	12	13	14	15				
S.C	0.3210	0.3002	0.2760	0.3108	0.3192				

6.2.3   Clustering results and analysis

Graphical representations of the means of various attributes describing the transfer functions and topologies grouped in each cluster of the X_q data set are presented in Fig. 6.32 - Fig. 6.33. Figure 6.33 represents the transmission zero separation ratio and the relative transmission zero position ratios for the transmission zeros produced by the quartet closest to the source. Figure 6.39 illustrates the mean values of the peak t.a.s.e, the passband ratio and the inner stopband ratio for the X_n data set. The mean transmission zero position ratios for each cluster of the X_n data set are displayed in Fig. 6.40.

Cascaded quartet data set

The five topologies yielding the lowest peak t.a.s.e values, or a subset of these topologies for the various transfer functions are grouped in clusters 3, 4, 6 and 9. Clusters 3 and 9 comprise of topologies representing transfer functions with a wide range of passband ratios and inner stopband ratios ranging from about 0.4091 to 0.75. Approximately 84 % of the objects in these clusters represent transfer functions with only 2 finite transmission zeros constrained to the inner stopband. CQ arrangement (c) was employed to realise such transfer functions whilst achieving an optimum stored energy distribution. In the optimum topologies, the quartet at resonators 2-3-4-5 was used to generate an inner and an outer stopband transmission zero. Therefore, a high mean transmission zero separation ratio was achieved for both clusters (refer to Fig. 6.33).
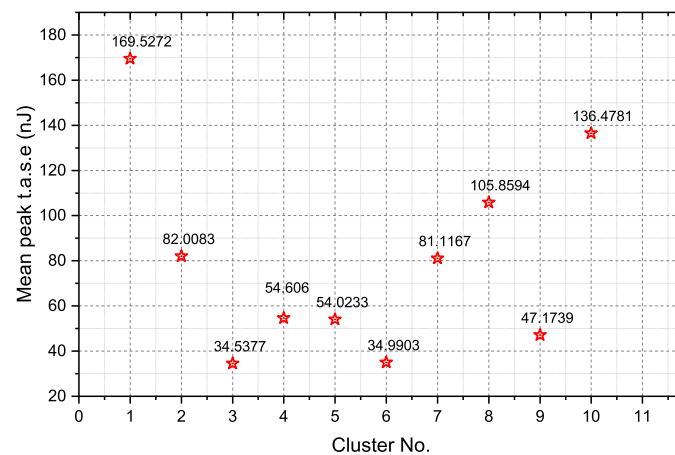
(a) Mean peak t.a.s.e for each cluster - X_q data set
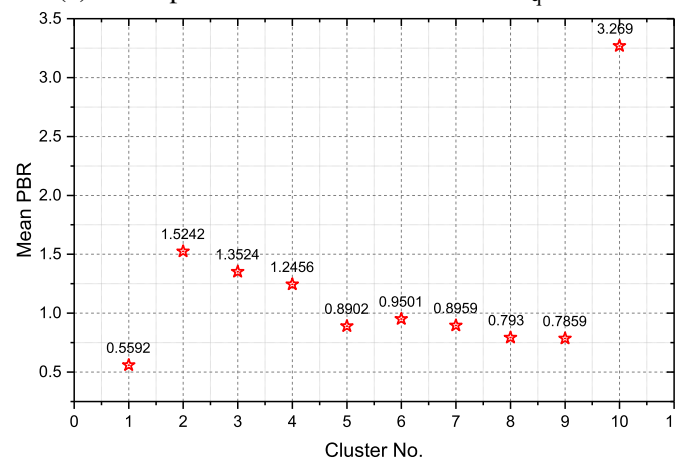
(b) Mean PBR value for each cluster - X_q data set
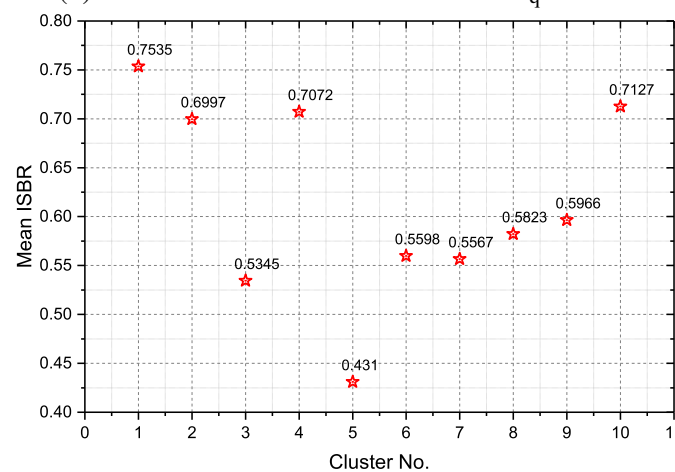
(c) Mean ISBR value for each cluster - X_q data set

Fig. 6.32 Mean peak t.a.s.e, PBR and ISBR for each cluster of the X_q data set comprising of 8-4 dual bandpass topologies.
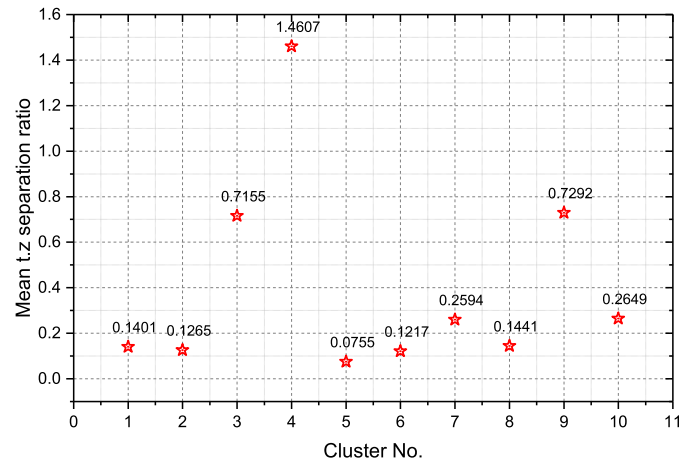
(a) Mean t.z separation ratio for each cluster - X_q data set
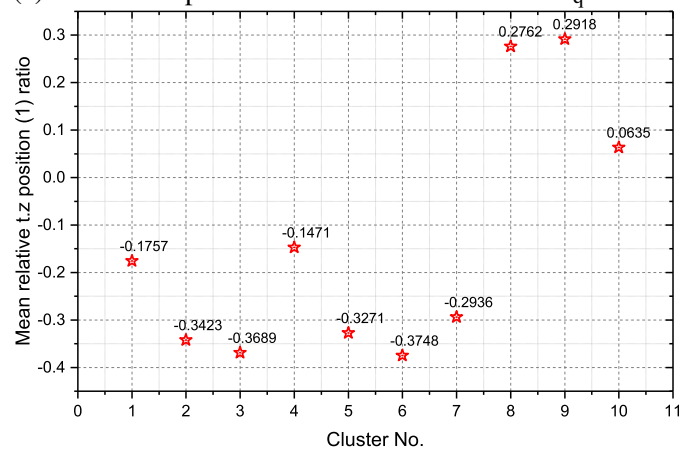
(b) Mean relative t.z position (1) ratio for each cluster - X_q data set
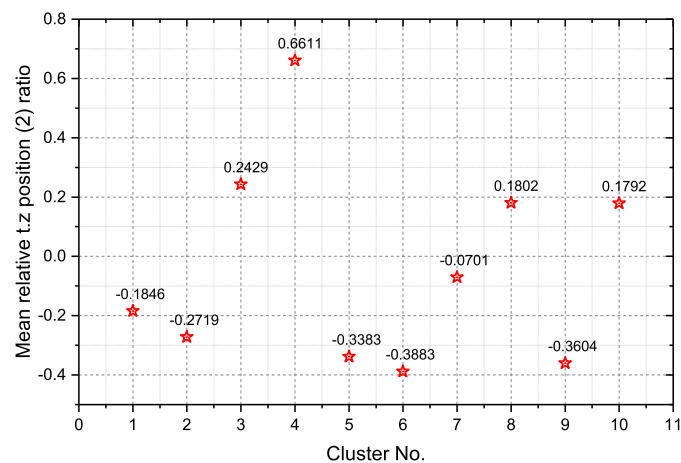
(c) Mean relative t.z position (2) ratio for each cluster - X_q data set

Fig. 6.33 Mean t.z separation ratio and relative t.z position ratios for transmission zeros generated by the quartet closest to the source - X_q data set comprising of 8-4 dual bandpass topologies.

The quartet employed forward asymmetric cross-coupling for topologies in which it was used to generate transmission zeros in the lower and inner stopbands. Conversely, it employed backward asymmetric cross-coupling when used to generate transmission zeros in the inner and upper stopbands. Examples of transfer functions grouped in these clusters are presented in Fig. 6.34. The two transmission zeros produced by the quartet closest to the source for each optimum topology are highlighted in the plots. The corresponding object entries are presented in Table 6.19 and Table 6.20, respectively. The t.a.s.e distribution plots for two objects are presented in Fig. 6.35 and Fig. 6.35. In both topologies, resonator 4 exhibited the peak t.a.s.e.
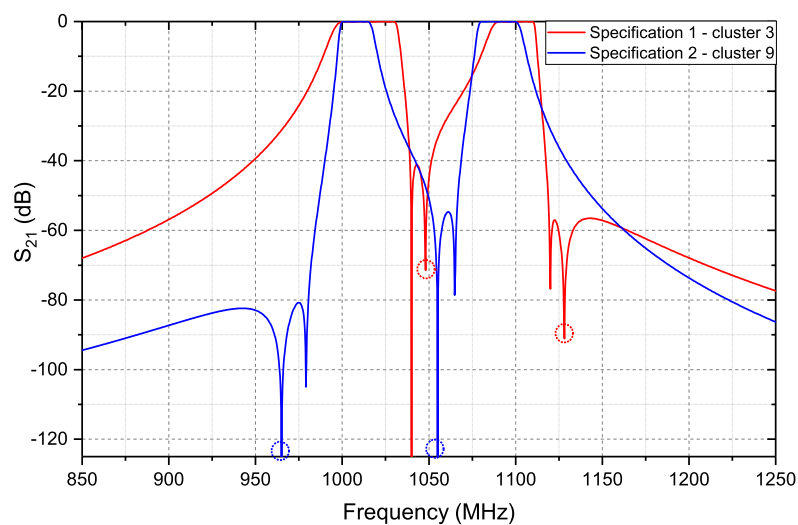
Fig. 6.34 Examples of transfer functions grouped in clusters 3 and 9. Specifications 1 and 2 represent objects x_{q1} from Table 6.19 and Table 6.21, respectively.

Table 6.19 Examples of objects grouped in cluster 3 - X_q data set for 8-4 dual band transfer functions.

	Peak t.a.s.e (nJ)	PBR	ISBR	TSR	RTR - (1)	RTR - (2)	CQ arrange-ment	cross-coupling direc-tion	Flag
x_{q1}	28.4640	1.5	0.5455	0.7282	-0.3	0.1645	2	0	1

It can be concluded that the optimum choice of the transmission zeros to be produced by the quartet closest to the source depends on the separation between the two transmission zero positions and on their distance from the closest band-edges. It is preferred that the two transmission zeros are further away from the band-edges and have a large separation between them.

Table 6.20 Examples of objects grouped in cluster 9 - X_q data set for 8-4 dual band transfer functions.

	Peak t.a.s.e (nJ)	PBR	ISBR	TSR	RTR - (1)	RTR - (2)	CQ arrange-ment	cross-coupling direc-tion	Flag
x_{q1}	28.5050	0.75	0.65	0.9	0.35	-0.3846	2	1	1
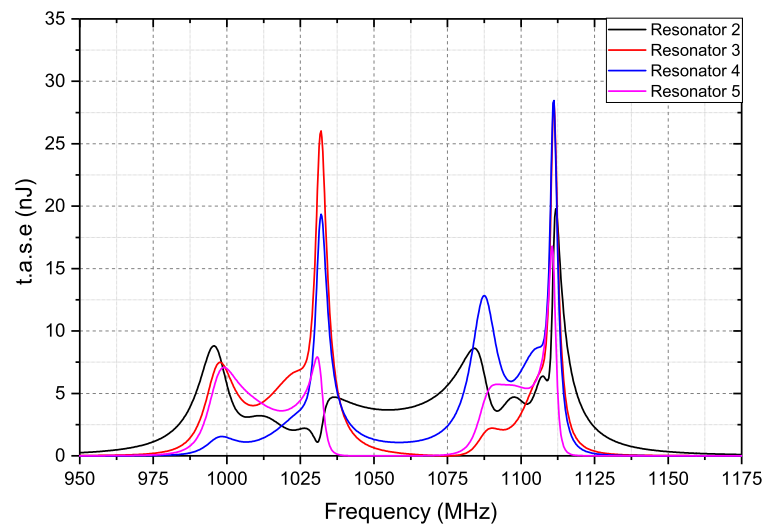
Fig. 6.35 T.a.s.e distribution plot for resonators 2-3-4-5 in the CQ topology represented by object x_{q1} in Table 6.19. Peak t.a.s.e was observed at resonator 4.
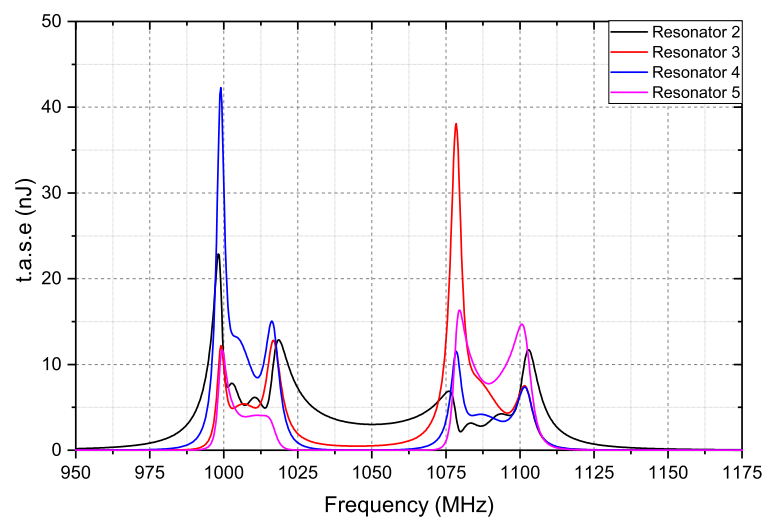
Fig. 6.36 T.a.s.e distribution plot for resonators 2-3-4-5 in the CQ topology represented by object x_{q1} in Table 6.20. Peak t.a.s.e was observed at resonator 4.

Cluster 4 comprises of objects constituting the best case topologies for transfer functions with $1 \leq$ PBR ≤ 2 and a band-to-band separation of $0.5882 \leq$ ISBR ≤ 0.8333. In this cluster, all transfer functions but one have PBR $= 1$. The objects with PBR $= 2$ constitute the outliers and hence, are excluded from further analysis. The remaining objects in this cluster represent transfer functions that are almost symmetric about the geometric mean frequency and have two transmission zeros constrained to the inner stopband. CQ arrangement (c) demonstrates the optimum t.a.s.e distribution for such transfer functions if the outer stopband transmission zeros are located far away from the band-edges. In this case, the quartet at resonators 2-3-4-5 is utilised to generate the outer stopband transmission zeros. It was observed that the quartet always employed backward asymmetric cross-coupling. On the contrary, CQ arrangements (a) and (b) provide the optimum t.a.s.e distribution for almost symmetric transfer functions where the outer stopband transmission zeros are located close to the band-edge. Here, the quartet at resonators 1-2-3-4 is used to generate the inner stopband transmission zeros. This quartet always employed forward asymmetric cross-coupling. An example of a transfer function grouped in this cluster and the corresponding object entry are presented in Fig. 6.37 and Table 6.21, respectively.

Cluster 6 consists of the best case topologies for transfer functions with $0.25 \leq$ PBR ≤ 1.5 and $0.36 \leq$ ISBR ≤ 0.85. Although most objects in this cluster represent topologies that are included in the five lowest peak t.a.s.e topologies, they may or may not constitute the optimum topology for transfer functions of this type. For some transfer functions grouped in this cluster, the optimum topology is a cascaded n-tuplet topology included in the X_n data set. The difference in the peak t.a.s.e values of the best and the second best topologies, however, is inconsiderable. Both transmission zeros generated by the quartet closest to the source are located in the inner stopband and at similar distances from the respective band-edges. Thus, the mean transmission zero separation ratio is low for this cluster. The CQ topology exhibiting the lowest peak t.a.s.e employs CQ arrangement (a) or (c). For transmission zero separation ratio < 0.1 and for number of inner stopband transmission zeros equal to 2, it was observed that the quartet closest to the source employed forward asymmetric cross-coupling. In contrast, for transmission zero separation ratio ≥ 0.1 and for number of inner stopband transmission zeros greater than 2, the quartet was realised with a backward asymmetric cross-coupling direction. Examples of objects grouped in this cluster are presented in Table 6.22. The corresponding transfer functions are displayed in Fig. 6.38. In example specification 1, the quartet closest to the source is used to produce the transmission zeros at 1050 MHz and 1060 MHz. Similarly, in specification 2, the quartet is used to produce the transmission zeros at 1052 MHz and 1066 MHz.
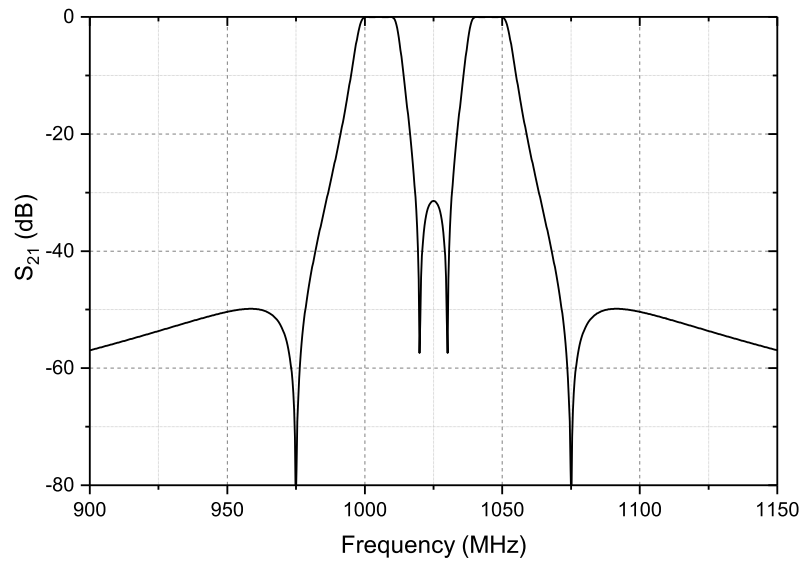
Fig. 6.37 An example of a transfer function grouped in cluster 4. The transfer function is almost symmetric about the geometric mean frequency.

Table 6.21 An example of an object grouped in cluster 4 - X_q data set for 8-4 dual band transfer functions.

	Peak t.a.s.e (nJ)	PBR	ISBR	TSR	RTR - (1)	RTR - (2)	CQ arrange-ment	cross-coupling direc-tion	Flag
x_{q1}	35.8730	1	0.6	1.9616	0.5	0.46	2	0	1

Table 6.22 Examples of objects grouped in cluster 6 - X_q data set for 8-4 dual band transfer functions.

	Peak t.a.s.e (nJ)	PBR	ISBR	TSR	RTR - (1)	RTR - (2)	CQ arrange-ment	cross-coupling direc-tion	Flag
x_{q1}	16.5840	1	0.5455	0.0909	-0.4169	-0.4169	0	1	1
x_{q2}	22.4090	1.1667	0.4091	0.1273	-0.3778	-0.3111	0	0	2

Clusters 1, 2, and 5 include the worst case topologies for transfer functions with at least 3 transmission zeros constrained to the inner stopband. In all topologies, the quartet closest to the source is used to generate transmission zeros located in the inner stopband. These transmission zeros are located close together, thus, giving a low transmission zero separation ratio. The transmission zeros are also the ones closest to the band-edge, thus resulting in low relative transmission zero position ratios. In most cases, the CQ arrangement employed does
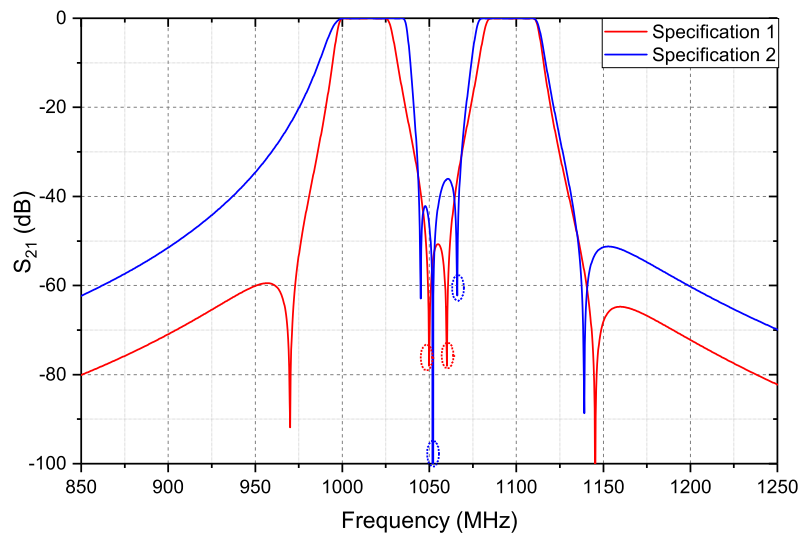
Fig. 6.38 Examples of transfer functions grouped in cluster 6. Specifications 1 and 2 represent objects x_{q1} and x_{q2} from Table 6.22 and Table 6.21, respectively.

not affect the peak t.a.s.e significantly. This can be illustrated with the aid of an example. Consider a transfer function with passbands at 1000 MHz - 1005 MHz and 1090 MHz - 1100 MHz. Three transmission zeros are prescribed at 1030 MHz, 1040 MHz and 1050 MHz. The number of inner stopband transmission zeros is set to 4 so that a dependent transmission zero is obtained at 1017.2 MHz. The first quartet in all of the five worst case topologies is used to generate the transmission zeros at 1017.2 MHz and 1030 MHz. The object entries for these worst case topologies are listed in Table 6.23. The difference in objects x_{q1} and x_{q5} (and x_{q2} and x_{q4}) is simply the direction of asymmetric cross-coupling in the second quartet. Resonator 3 demonstrates the peak t.a.s.e in all of the listed topologies.

Table 6.23 Examples of objects grouped in cluster 1 - X_q data set for 8-4 dual band transfer functions.

	Peak t.a.s.e (nJ)	PBR	ISBR	TSR	RTR - (1)	RTR - (2)	CQ ar-range-ment	cross-coupling direc-tion	Flag
x_{q1}	143.32	0.5	0.85	0.1280	-0.2941	-0.1435	0	0	-5
x_{q2}	143.32	0.5	0.85	0.1280	-0.2941	-0.1435	1	0	-4
x_{q3}	143.32	0.5	0.85	0.1280	-0.2941	-0.1435	2	1	-3
x_{q4}	143.32	0.5	0.85	0.1280	-0.2941	-0.1435	1	0	-2
x_{q5}	143.32	0.5	0.85	0.1280	-0.2941	-0.1435	0	0	-1

Clusters 8 and 10 comprise of objects representing the worst case topologies for highly asymmetric transfer functions with only two transmission zeros constrained to the inner stopband. The remaining two transmission zeros are located close to the lowermost band-edge (f_1) for cluster 8 and the uppermost band-edge (f_4) for cluster 10. The two outer stopband transmission zeros are located close together and are generated using the quartet positioned closest to the source. In such cases, the choice of CQ arrangement becomes irrelevant. Cluster 7 consists of topologies employing CQ arrangement (a), where the quartet closest to the source is used to produce at least one transmission zero located closest to the band-edge. A quartet with forward cross-coupling is used to produce transmission zeros in the inner and upper stopband. On the contrary, a quartet with backward asymmetric cross-coupling is used to generate transmission zeros in the inner and lower stopband.

Cascaded n-tuplet data set

Clusters 1 and 4 comprise of the topologies demonstrating the lowest peak t.a.s.e values for transfer functions with $0.25 \leq PBR \leq 2$ and $1 \leq PBR \leq 4$, respectively. Cluster 4 contains transfer functions with only 2 transmission zeros constrained to the inner stopband. It was observed that cascaded n-tuplet arrangement (c) demonstrated the optimum t.a.s.e distribution for transfer functions in this cluster. The quartet closest to the source is used to generate transmission zeros located in separate stopbands. It was observed that if these transmission zeros were located in the inner and upper stopbands, the quartet employed forward asymmetric cross-coupling. The triplet closest to the load was used to generate the transmission zero with the lowest RTR value. This implies that this transmission zero was located closest to the band-edge. Examples of objects grouped in cluster 4 are listed in Table 6.24. The corresponding transfer functions, highlighting the transmission zeros generated by the quartet next to the source are presented in Fig. 6.41.

The dual band topologies exhibiting the lowest peak t.a.s.e for transfer functions with at least 3 inner stopband transmission zeros are grouped in cluster 1. For transfer functions with 3 inner stopband transmission zeros, cascaded n-tuplet arrangement (c) is exploited where the two transmission zeros giving the largest separation are located far away from the band-edges. The triplet at resonators 6-7-8 is used to produce the transmission zero closest to the band-edge. If one of the transmission zeros giving the maximum separation was located close to a band-edge, n-tuplet arrangements (a) or (b) were exploited to realise the transfer function. The n-tuplet closest to the load was used to produce the transmission zero/s closest to the band-edge. Example of such a transfer function and the corresponding optimum topology is displayed in Fig. 6.42.
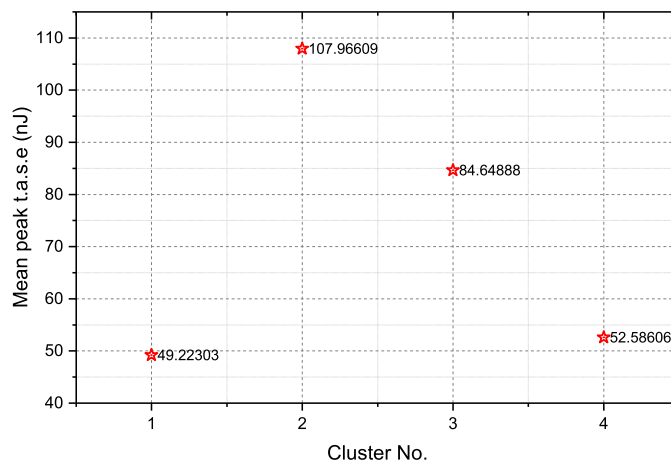
(a) Mean peak t.a.s.e for each cluster - X_n data set
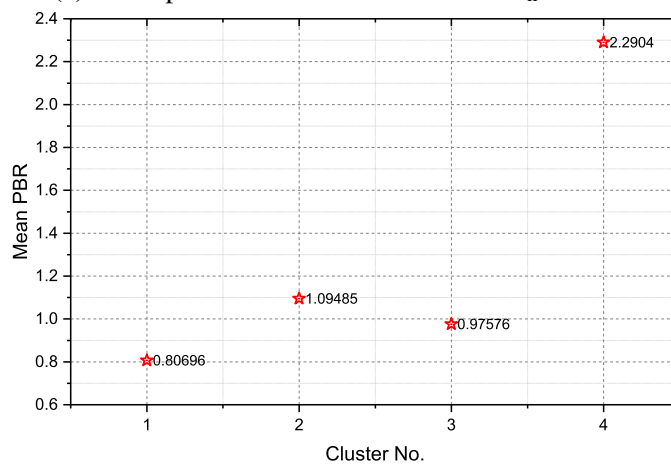
(b) Mean PBR value for each cluster - X_n data set
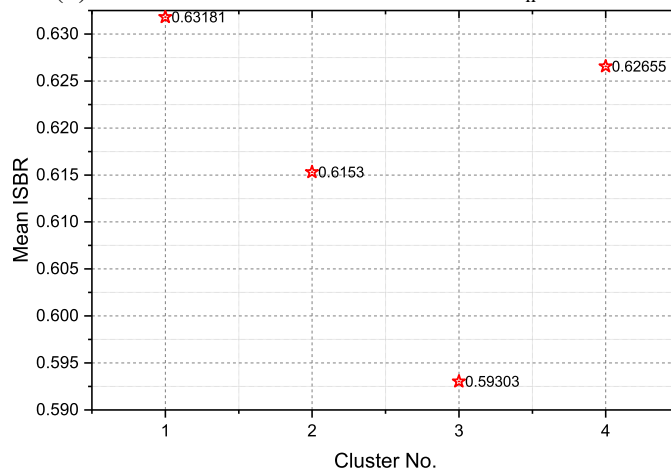
(c) Mean ISBR value for each cluster - X_n data set

Fig. 6.39 Mean peak t.a.s.e, PBR and ISBR for each cluster of the X_n data set comprising of 8-4 dual bandpass topologies.
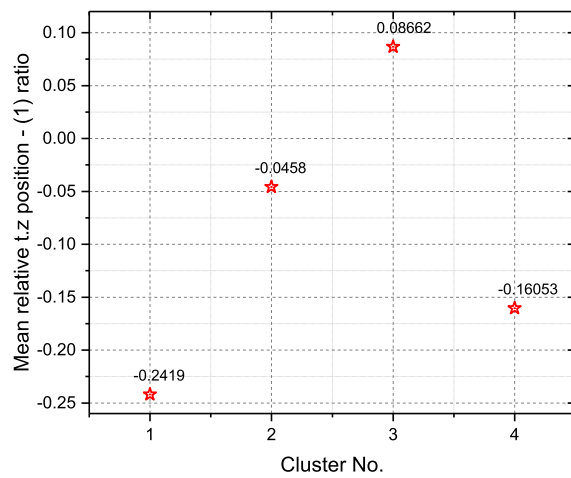
(a) Relative transmission zero position (1) ratio - X_n data set
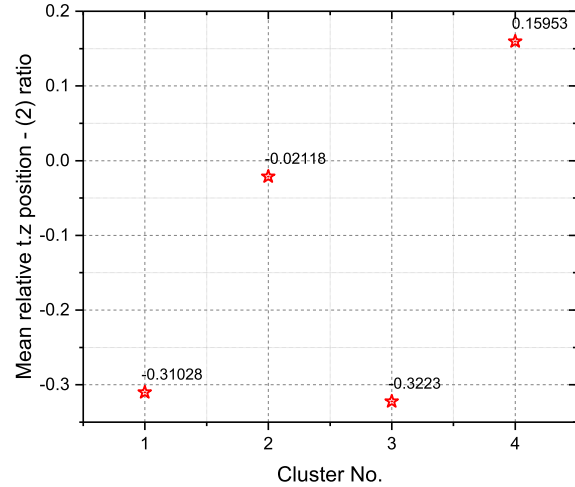
(b) Relative transmission zero position (2) ratio - X_n data set
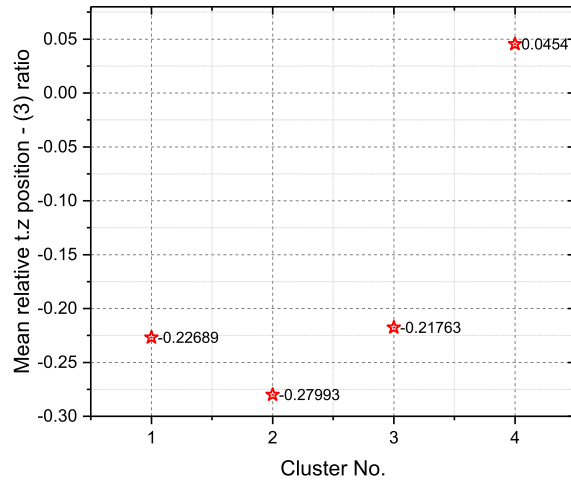
(c) Relative transmission zero position (3) ratio - X_n data set
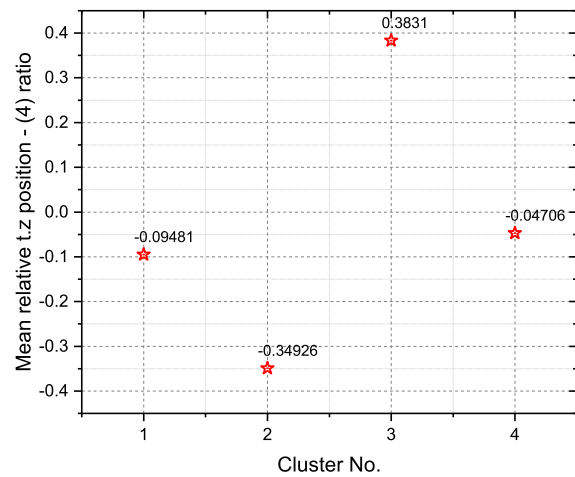
(d) Relative transmission zero position (4) ratio - X_n data set

Fig. 6.40 Relative transmission zero position ratio for the X_n data set comprising of 8-4 dual bandpass topologies.

In all optimum cascaded n-tuplet topologies, it was observed that the quartet employed forward asymmetric cross-coupling when generating a lower and an inner stopband transmission zero. Similarly, it employed backward cross-coupling when used to generate an inner and an upper stopband transmission zero. Dual bandpass transfer functions with four inner stopband transmission zeros and PBR $\neq$ 1 are grouped in cluster 1. The optimum cascade n-tuplet topology choice depends upon the position of the transmission zeros from the band-edges and the separation between them. Consider the dual band response displayed in Fig. 6.43 as an example. The two outermost inner stopband transmission zeros have the largest separation

between them and are located away from the band-edges. Cascaded n-tuplet arrangement (c), where the quartet at resonators 1-2-3-4 is used to produce the outermost transmission zeros, provides the optimum t.a.s.e distribution for such transfer functions. If one (or both) of the outermost transmission zeros giving the maximum separation are located very close to the band-edge, as in Fig. 6.44a, cascaded n-tuplet arrangement (a) proves to be the optimum topology choice. The triplets close to the source are exploited to produce the transmission zeros positioned furthest from the band-edges. On the contrary, cascaded n-tuplet arrangement (b) exhibited the lowest peak t.a.s.e for transfer functions such as the one in Fig. 6.44b. Here, the transmission zero furthest from the band-edges is generated by the triplet closest to the source, followed by the quartet generating well-separated transmission zeros that are not positioned close to the band-edges. Finally, the triplet next to the load generates the transmission zero closest to the band-edge.
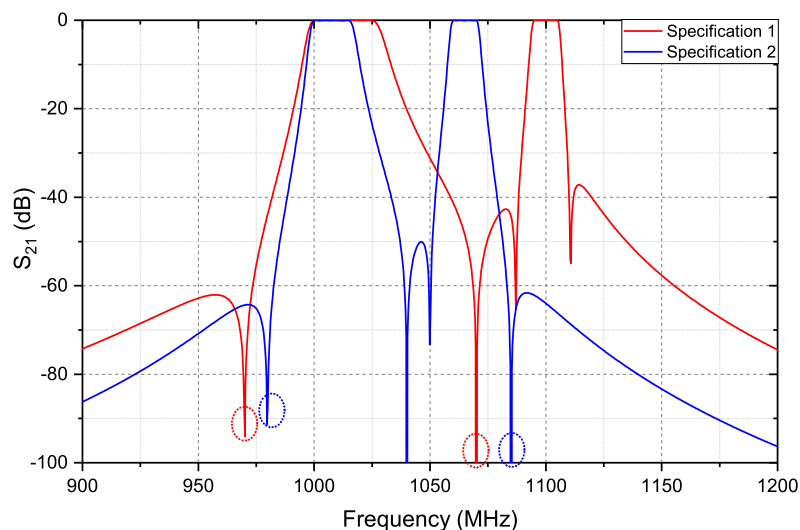
Fig. 6.41 Examples of transfer functions grouped in cluster 4. Specifications 1 and 2 represent objects x_{n1} and x_{n2} from Table 6.22, respectively.

Table 6.24 Examples of objects grouped in cluster 4 - X_n data set for 8-4 dual band transfer functions.

	Peak t.a.s.e (nJ)	PBR	ISBR	RTR - (1)	RTR - (2)	RTR - (3)	RTR - (4)	n-tuplet ar-range-ment	cross-coupling direc-tion	Flag
x_{n1}	47.359	2.5	0.6667	0.2857	-0.3571	-0.1143	0.0533	2	1	1
x_{n2}	39.978	1.5	0.6429	0.2143	0.2883	-0.4444	-0.2222	2	0	1
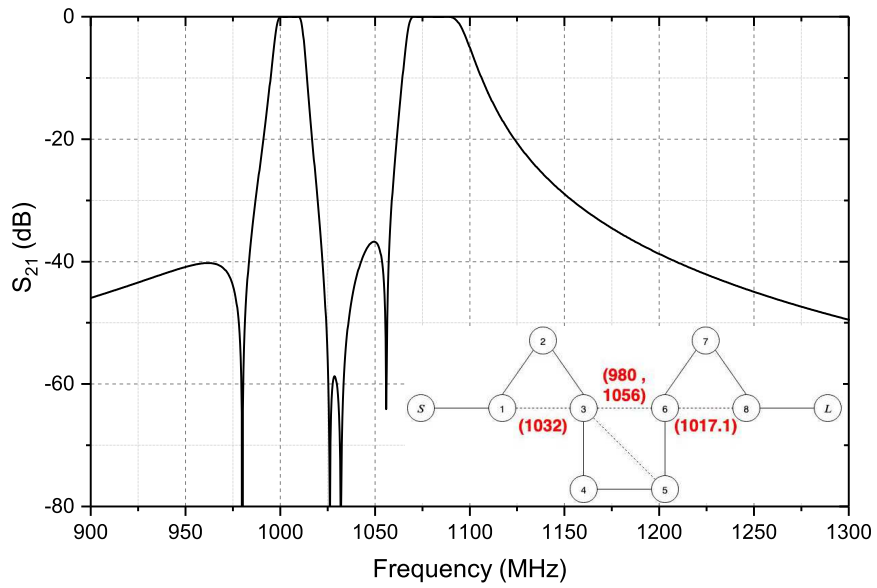
Fig. 6.42 A 16th-degree dual band transfer function with 3 inner stopband transmission zeros and the corresponding optimum topology.
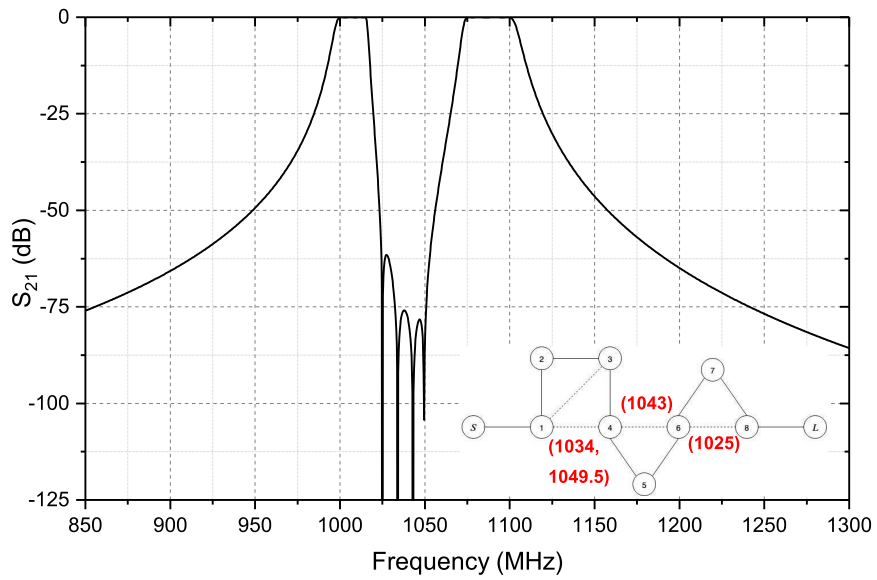
Fig. 6.43 A 16th-degree dual band transfer function with 4 inner stopband transmission zeros and the corresponding optimum topology.
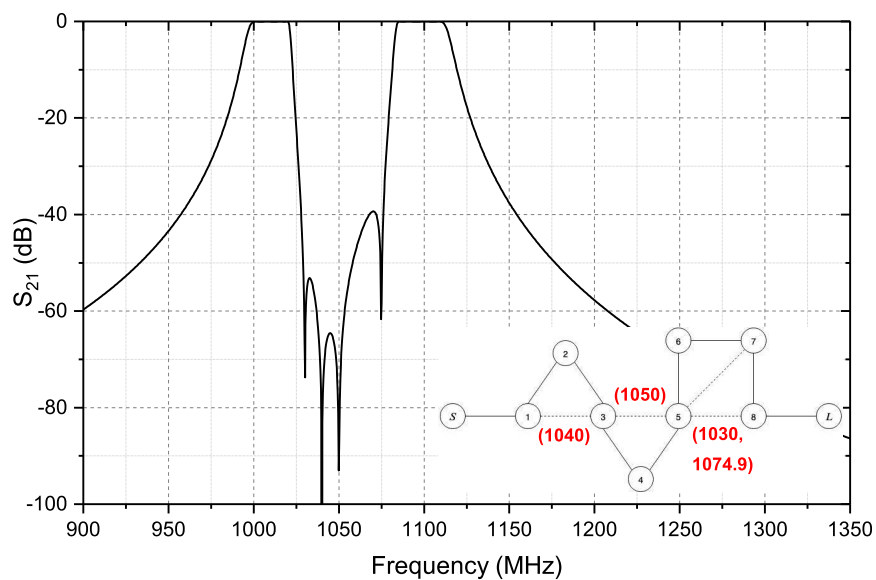
(a)
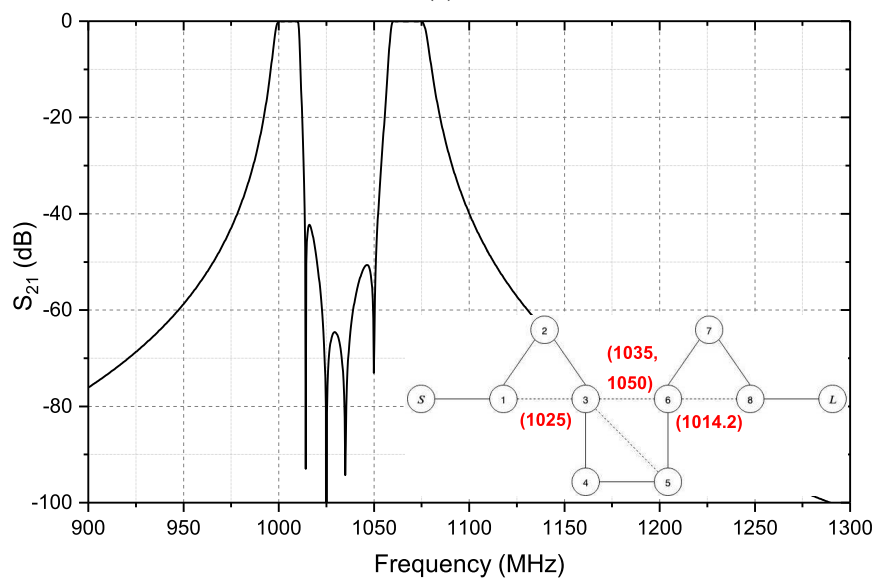
(b)

Fig. 6.44 Examples of transfer functions with 4 inner stopband transmission zeros and the corresponding optimum topologies grouped in cluster 1 of the X_n data set comprising of 8-4 dual band transfer functions.

6.2.4 General patterns

General patterns that will aid in predicting the optimum power handling topology for dual bandpass filters are presented in this section. The patterns have been determined from the clustering analysis presented in section 6.2.3.

Consider a dual bandpass transfer function with a single finite transmission zero in each of the outer two stopbands and two inner stopband transmission zeros. If the transfer function is almost symmetric about the geometric mean frequency and the RTR for the inner stopband transmission zeros is greater than that for the outer stopband transmission zeros, CQ arrangement (a) provides the lowest peak t.a.s.e. Here, the quartet closest to the source must be used to generate the inner stopband transmission zeros. The asymmetric cross-coupling directions of the quartets must be such that the number of energy paths going into the shared resonator is a minimum. In contrast, if the RTR for the inner stopband transmission zeros is lower than that for the outer stopband transmission zeros, CQ arrangement (c) yields the lowest peak t.a.s.e. In this case, the quartet closest to the source must be used to generate the outer stopband transmission zeros. Both quartets must employ backward asymmetric cross-coupling. These guidelines are illustrated in Fig. 6.45.

Suppose the two outer stopband transmission zeros are constrained to the same stopband, viz., the lower or the upper stopband. Typically, these outer stopband transmission zeros are constrained to the lower stopband for PBR < 1 and to the upper stopband for PBR > 1. If the passband ratio is equal to unity, CQ arrangement (b) yields the lowest peak t.a.s.e. For transfer functions where PBR $\neq$ 1, CQ arrangement (c) or cascaded n-tuplet arrangement (c) provide the lowest peak t.a.s.e. In general, it was observed that if the difference between the outer stopband transmission zero and the inner stopband transmission zero that were furthest from the band-edges was similar to the difference between the remaining two transmission zeros $\left(\mid f_{n1} - f_{n3} \mid \simeq \mid f_{n2} - f_{n4} \mid\right)$, then CQ arrangement (c) provides the lowest peak t.a.s.e. Alternatively, if the transfer function does not conform to either of the aforementioned characteristics, cascaded n-tuplet arrangement (c) should be used to realise it. In all cases, the quartet closest to the source must be used to generate the transmission zeros that have the largest separation between them and/or are located furthest from the corresponding band-edges. The triplet at resonators 6-7-8 in the cascaded n-tuplet topology must be exploited to produce the transmission zero located closest to the band-edge. The quartet closest to the source in the CQ arrangements must employ forward asymmetric cross-coupling when generating a lower and an inner stopband transmission zero. In contrast, it must employ backward asymmetric cross-coupling when generating an inner and an upper stopband
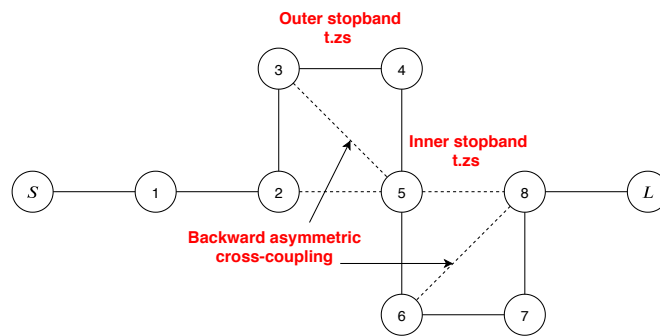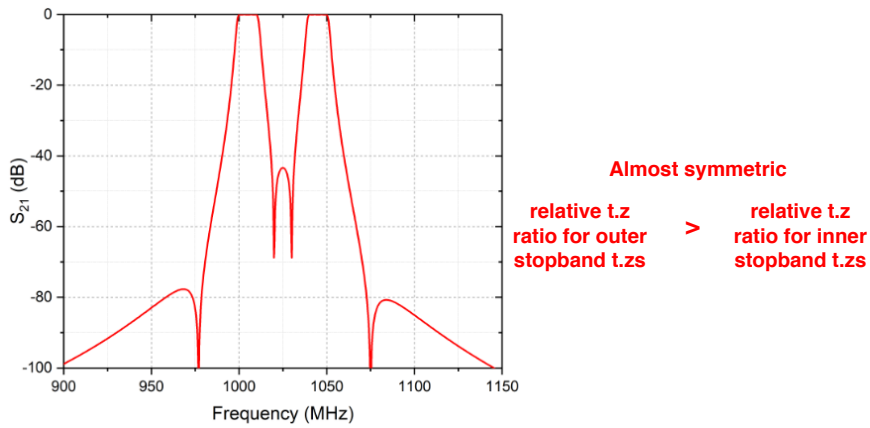
(a) If the RTR for the outer stopband t.zs is greater than that for the inner stopband t.zs.
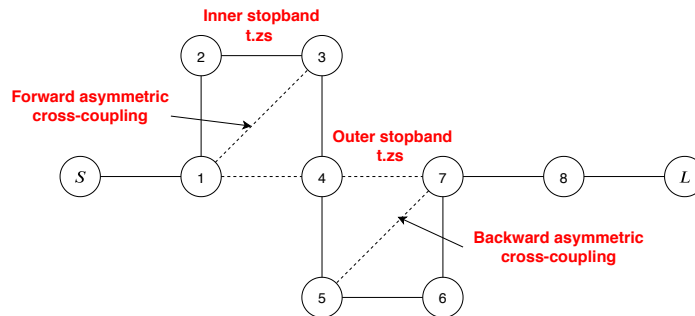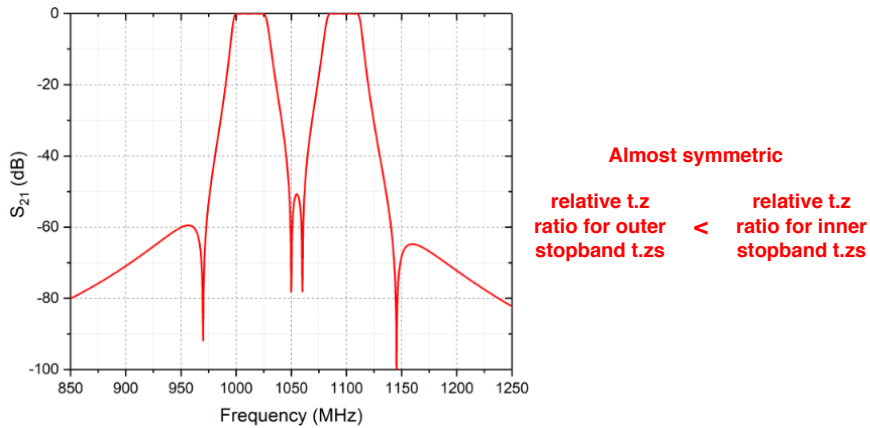
(b) If the RTR for the inner stopband t.zs is greater than that for the outer stopband t.zs.

Fig. 6.45 Generalised guidelines to predict the optimum topology for almost symmetric dual bandpass transfer functions.

transmission zero. The asymmetric cross-coupling direction employed by the second quartet must be such that the number of energy paths going into the shared resonator is a minimum.

Suppose three finite transmission zeros are constrained to the inner stopband so that a single transmission zero is obtained in the lower or the upper stopband. The optimum topology for such transfer functions depends upon the separation between the different transmission zero pairs and on their distance from the closest band-edge. In most cases, a cascaded n-tuplet topology proved to be an optimum topology choice for such transfer functions. Using the observations from the clusters, a procedure was developed to enable prediction of the optimum topology for such transfer functions. The described procedure should allow prediction of at least one of the five topologies yielding the lowest peak t.a.s.e, if not the optimum. It is assumed that for PBR < 1, a transmision zero is located in the lower stopband and for PBR > 1, a transmission zero is located in the upper stopband. The procedure for predicting the optimum cascaded n-tuplet topology is illustrated in Fig. 6.47 with the aid of a decision tree. One of the transmission zeros giving the maximum separation is always located in the outer stopband. Note that for the first decision in the decision tree, close refers to $|$ RTR$|$ < 0.28. In all cascaded n-tuplet arrangements, if the quartet is used to generate a transmission zero in the lower stopband, it must employ forward asymmetric cross-coupling direction. On the contrary, the quartet must employ backward asymmetric cross-coupling direction if it is used to generate an upper stopband transmission zero. For certain transfer functions where the relative transmission zero position ratio of the outer stopband transmission zero is less than 0.1, CQ arrangements (a) or (c) may provide the lowest peak t.a.s.e. In this case, the quartet closest to the source must be used to generate inner stopband transmission zeros located at similar distances from the band-edges or the pair of transmission zeros with the maximum separation between them.

Consider the transfer functions with all four finite transmission zeros constrained to the inner stopband. If the transfer function has a passband ratio of unity, CQ arrangements (a) or (b) must be used to obtain the lowest peak t.a.s.e. The quartet closest to the source must be used to generate the two transmission zeros that are at equal distances and are furthest away from the inner band-edges (f_2 and f_3). These are typically the inner two transmission zeros. The outer two transmission zeros must be generated using the quartet closest to the load. The quartet closest to the source must employ backward asymmetric cross-coupling. An example of the t.a.s.e distribution plots for resonators 1-4 of a CQ topology realising such a transfer function is demonstrated in Fig. 6.46. It can be seen that the t.a.s.e distribution is almost symmetric about the geometric mean frequency. As explained previously, this lowers the observed peak t.a.s.e. Transfer functions that are highly asymmetric, i.e., 0.5 > PBR and PBR > 2 must be realised using cascaded n-tuplet arrangements (a) or (c). Transmission

zeros with a large separation between them and that are away from the band-edges must be realised using the quartet in arrangement (c). The triplets close to the load should be exploited to produce the transmission zeros closest to the band-edge.
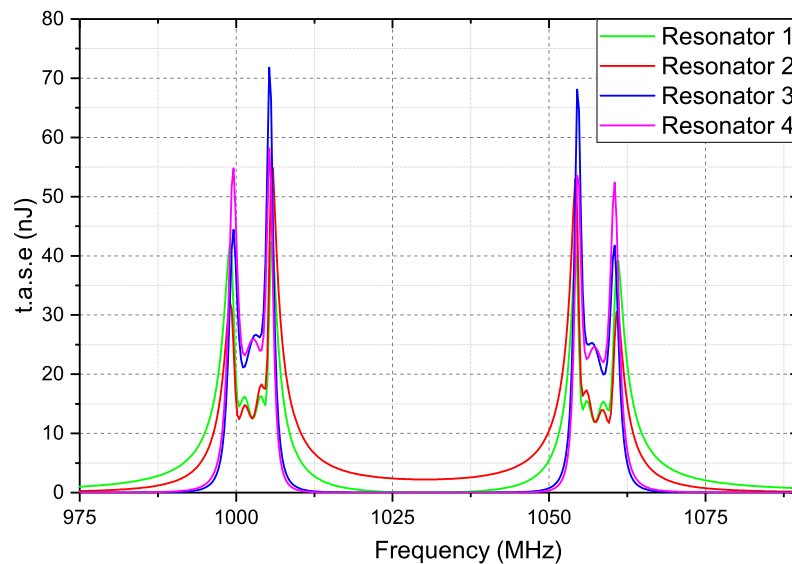
Fig. 6.46 The t.a.s.e distribution in resonators 1-4 of a quartet producing transmission zeros at 1025 MHz and 1035 MHz. The remaining network consists of a quartet at resonators 5-6-7-8 producing transmission zeros at 1015 MHz and 1044.5 MHz. The transfer function has a PBR = 1. Resonator 3 exhibits peak t.a.s.e for the topology.

In general, a quartet must be used to generate transmission zeros with maximum separation between them. An n-tuplet closest to the load must be used to generate the transmission zero closest to the band-edge. Transfer functions that exhibit almost symmetric characteristics are always best realised using cascaded quartet topologies. Usually, cascaded n-tuplets are better realisations for highly asymmetric characteristics. If the quartet in a cascaded n-tuplet topology is used to generate transmission zeros in the lower and the inner stopbands, it must employ forward asymmetric cross-coupling. Similarly, if it used to generate transmission zeros in the inner and the upper stopbands, it must employ backward asymmetric cross-coupling. In purely cascaded quartet topologies, if the quartet closest to the source is used to generate transmission zeros in the lower and the upper stopband, it must employ backward asymmetric cross-coupling.
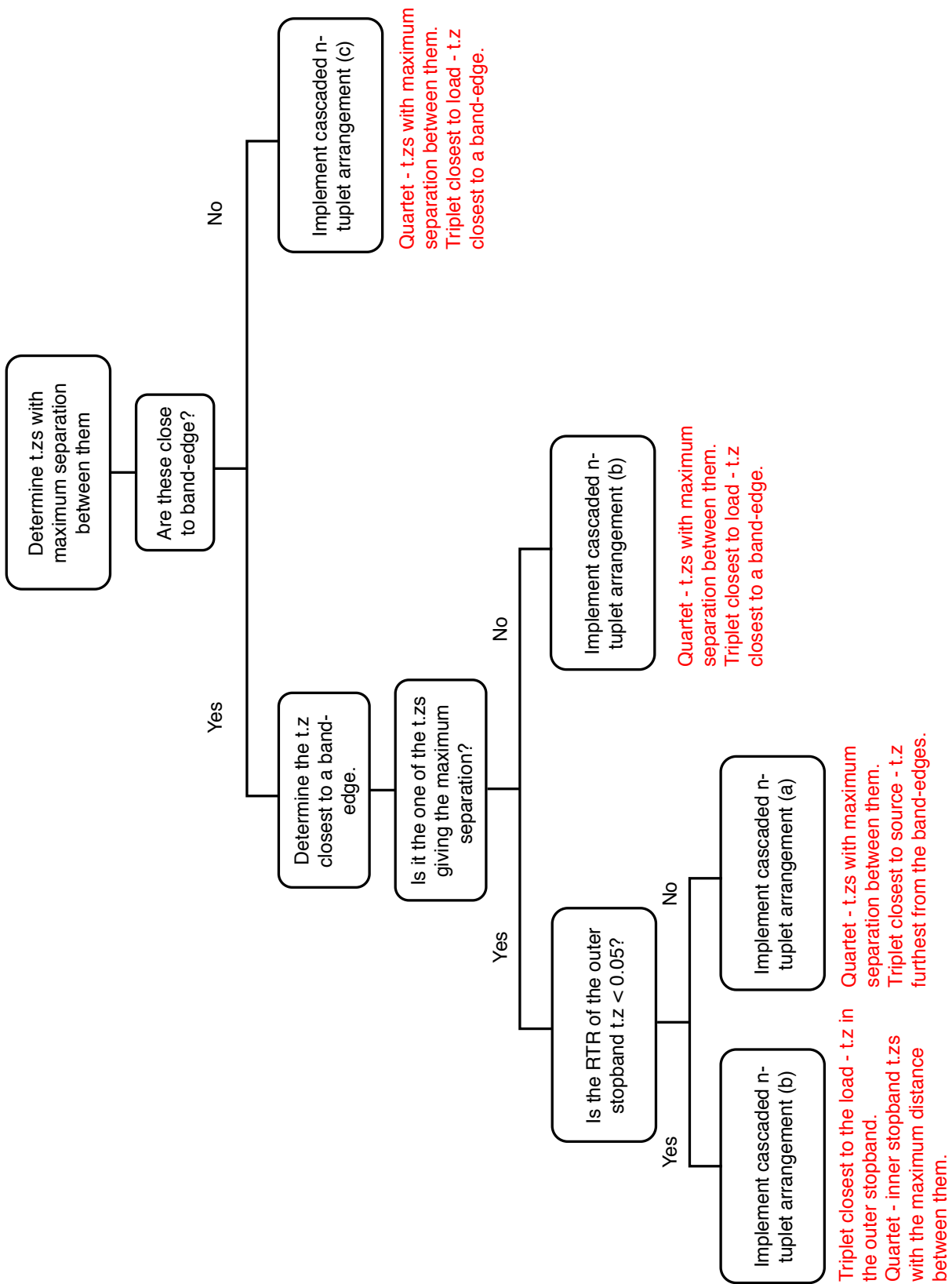
Fig. 6.47 A decision tree illustrating the procedure to predict the optimum cascaded n-tuplet topology for 8-4 dual bandpass transfer functions with 3 inner stopband transmission zeros.

6.3 Conclusion

The k-means clustering algorithm has been implemented to find patterns in the stored energy distribution within cascaded filter topologies realising various dual bandpass transfer functions. The generation and modelling of the input data sets comprising of 6-2 and 8-4 dual band transfer functions has been described. The clustering results and analysis for the data sets have been presented in section 6.1.3 and section 6.2.3, respectively. The general patterns obtained from the analysis of the clusters are presented in section 6.1.4 and section 6.2.4, respectively. These patterns aid in the prediction of the optimum power handling topology for various dual band transfer functions. Combline realisations of two distinct filter topologies realising the same 6th-order transfer function have been modelled on CST. The peak electric fields in the prototypes have been investigated to validate the guidelines obtained using the clustering approach. Finally, a thesis conclusion is presented in the following chapter.

Chapter 7

Conclusion and Future Work

The new generation of wireless communications systems demands a significant increase in the number of microwave filters required at the cellular base station. The conventional approach of employing parallel-connected single band filters results in increased size, cost, power consumption and complexity of the base station RF front-end. New methods for mitigating these issues involve incorporation of multiple passbands into a single filter unit.

A novel technique for the synthesis of multi-band filters has been presented in this thesis. The technique has been transformed to the transformed variable plane to offer improved numerical accuracy. The latter part of the thesis focuses on employing a pattern recognition algorithm to improve the power handling capacity of single and dual bandpass filters by choosing an appropriate network topology for a given transfer function.

An overview of the filter synthesis and design theory has been presented in Chapter 2. The theoretical background presented in this chapter forms the prerequisite for the remaining chapters. The motivation and literature review for each part of the research has been outlined at the beginning of the respective chapter.

A linear optimisation technique for the synthesis of dual bandpass filters in the complex frequency plane has been presented in Chapter 3. In this technique, a system of $N + 2$ linear independent equations is solved iteratively to optimise the in-band critical point positions such that the absolute value of the characteristic function at these points is approximately equal to unity (with a specified level of accuracy). The technique is applicable to the direct synthesis of symmetric and asymmetric single or dual bandpass generalised Chebyshev characteristic functions in the lumped or distributed bandpass domain. It allows arbitrary placement of transmission zeros implying full control over the stopband rejection. The technique is applicable to transfer functions with large band-to-band separation owing to the

frequency-variant nature of the inter-resonator couplings. A 7th-degree combline prototype synthesised using the presented technique has been fabricated and tested successfully for validation.

Depending upon the relative bandwidths and placement of the transmission zeros, it was found that the optimisation technique could synthesise filter networks upto degree 12 (degree of the transfer function is 24) with a good level of accuracy. For the synthesis of higher-order filters, numerical inaccuracies were encountered due to which the algorithm may fail to converge. Hence, the entire technique was re-devised in the transformed variable plane (z-plane) in Chapter 4. The technique was also generalised to allow for the synthesis of filters with multiple passbands. Re-formulation in the z-plane reduced the problem to solving a system of $N + N_B - 1$ linear independent equations (instead of $N + N_B$ in the s-plane; $N_B = 2$ for two passbands). A 10th-degree combline prototype synthesised using the multi-bandpass synthesis technique in the z-plane was fabricated and tested successfully to validate the theory. The future work for the multi-bandpass synthesis technique could include devising a methodical approach to the tuning of such prototype filters.

In Chapter 5, an unsupervised pattern recognition algorithm, called the k-means clustering algorithm, has been implemented to find patterns in the time-averaged stored energy distribution within various cascaded networks realising the same single bandpass power transfer function. The peak time-averaged stored energy in a filter network was used as an indictor of its power handling capacity. Seventy different 6th-degree single bandpass transfer functions with two finite transmission zeros were generated using the z-plane linear optimisation technique introduced in Chapter 4. Data sets comprising of simple cascaded triplet and cascaded quartet topologies realising these 6-2 single band transfer functions were generated. The clustering algorithm was applied to discover key characteristics of the data sets.

The algorithm was also applied to a data set comprising of more complex filter topologies realising 9th-degree transfer functions with five finite transmission zeros. Using the regularities discovered from the data set, guidelines for predicting the optimum power handling topology for a given single bandpass transfer function were determined. It is shown that by exploiting the established guidelines to choose a filter topology for a given transfer function, the peak time-averaged stored energy can be reduced significantly.

In general, it was observed that the choice of transmission zeros produced by the quartet must be such that: 1) they are located in separate stopbands (lower and upper), 2) they are located at similar distances from the respective band-edges and/or are located far away from the band-edges. A cascaded triplet topology is better suited for realisation of highly asymmetric

and selective transfer functions. In such topologies, it is always the resonator opposite to the cross-coupling in a triplet that demonstrates the peak time-averaged stored energy. The n-tuplet closest to the source must be used to produce the transmission zero located furthest away from the band-edges. Similarly, the n-tuplet producing the transmission zeros closest to the band-edge/s must be placed closest to the load. Typically, it was observed that n-tuplet arrangements commencing with a quartet provide a lower peak time-averaged stored energy.

Future research work could involve investigating larger data sets with a variablility in the parameters such as degree and bandwith of the passband. Doing so could potentially allow quantitative analysis of the data set and enable discovery of patterns that can be deemed completely general for choosing an optimum network topology.

In Chapter 6, the k-means clustering algorithm has been applied to data sets comprising of cascaded n-tuplet topologies realising 12th- and 16th-degree dual bandpass transfer functions. Using the key regularities in the data sets, guidelines for predicting the optimum power handling topology for a given dual bandpass transfer function were established. The observed patterns can be briefly summarised as follows:

- The dual band transfer functions that are almost symmetric about their geometric mean frequencies are best realised using cascaded quartet topologies.

- Transfer functions that are highly asymmetric and/or selective should be realised using purely cascaded triplet or cascaded n-tuplet (composed of both, triplets and quartets) topologies. The triplet must be exploited to generate the transmission zero providing the highest asymmetry to the filter response.

- The n-tuplet closest to the load should be used to produce transmission zero/s located closest to the band-edge/s.

- In general, the choice of transmission zeros to be produced by the quartet closest to the source is such that: 1) the separation between the two transmission zeros is large, if not maximum, 2) the transmission zeros are located far, if not furthest, from the band-edges, and 3) if possible, the relative positions of the transmission zeros from the closest band-edges are similar.

- For topologies where two n-tuplets (at least one of which is a quartet) share a common resonator, the direction of the asymmetric cross-coupling/s of the quartet/s is such that the number of energy paths going into the common node is a minimum.

The peak electric fields in the EM models of two topologies, an optimum topology and a typically implemented topology, realising the same 6-2 dual bandpass transfer function were compared to prove the theoretical results.

Again, future work could involve investigation of larger data sets comprising of a wider range of transfer functions. The algorithm could be applied to triple bandpass data sets to explore if the patterns obtained for dual bandpass filters are applicable to multi-band filters in general. In addition, the peak electric fields in the EM models of higher-order dual or multi-bandpass filter topologies realising the same power transfer function can be investigated. In addition, the stored energy distribution in diplexers could be investigated to establish general patterns for the prediction of the optimum power handling topology. These patterns could be compred to those obtained for dual bandpass transfer functions in Chapter 7.

Finally, a list of publications is presented in the following chapter.

Chapter 8

Published Work

8.1   Journal Paper

Abstract:

In this article, a new synthesis method for the generation of multiband generalized Chebyshev polynomials with prescribed transmission zeros is presented. The proposed linear optimization technique is applicable to symmetric and asymmetric filter responses. To demonstrate its general application, the technique has been applied to the direct synthesis of dual- and triple-bandpass filters. A 7th-degree dual-band prototype and a 10th-degree triple-band prototype, synthesized using the proposed technique, have been fabricated and tested to validate the practicality of the method.

8.2   Conference Paper

Abstract:

The k-means clustering algorithm has been implemented to find patterns in the time-averaged stored energy distribution in various filter networks. A large data set comprising of numerous

topologies for 50 different single band specifications has been investigated. By finding key characteristics within this data set, general guidelines for predicting the optimum topology for power handling have been established.

References

[1] Richard I Cameron and Ming Yu. Design of manifold-coupled multiplexers. *IEEE microwave magazine*, 8(5):46–59, 2007.

[2] Ian Hunter. *Theory and design of microwave filters*. Number 48. Iet, 2001.

[3] Meng Meng. *Design and synthesis of lossy microwave filters*. PhD thesis, University of Leeds, 2014.

[4] Jia-Sheng Hong and Michael J Lancaster. *Microstrip filters for RF/microwave applications*, volume 167. John Wiley & Sons, 2001.

[5] Richard J Cameron. Advanced coupling matrix synthesis techniques for microwave filters. *IEEE Transactions on Microwave Theory and Techniques*, 51(1):1–10, 2003.

[6] Robert E Collin. *Foundations for microwave engineering*. John Wiley & Sons, 2007.

[7] Richard J Cameron, Chandra M Kudsia, and Raafat R Mansour. *Microwave Filters for Communication Systems: Fundamentals, Design, and Applications*. John Wiley & Sons, 2018.

[8] Ian C Hunter, Laurent Billonet, Bernard Jarry, and Pierre Guillon. Microwave filters-applications and technology. *IEEE Transactions on Microwave Theory and Techniques*, 50(3):794–805, 2002.

[9] Giuseppe Macchiarella and Stefano Tamiazzo. Synthesis of star-junction multiplexers. *IEEE Transactions on Microwave Theory and Techniques*, 58(12):3732–3741, 2010.

[10] Jorge A Ruiz-Cruz, Chi Wang, and Kawthar A Zaki. Advances in microwave filter design techniques. *Microwave Journal*, 2008.

[11] Wai Kai Chen. *The electrical engineering handbook*. Elsevier, 2004.

[12] John D Rhodes and SA Alseyab. The generalized chebyshev low-pass prototype filter. *International Journal of Circuit Theory and Applications*, 8(2):113–125, 1980.

[13] Richard W Daniels. *Approximation methods for electronic filter design: with applications to passive, active, and digital networks*. McGraw-Hill New York, NY, USA:, 1974.

[14] John David Rhodes. *Theory of electrical filters*. Wiley, 1976.

[15] Richard J Cameron. General coupling matrix synthesis methods for chebyshev filtering functions. *IEEE Transactions on Microwave Theory and Techniques*, 47(4):433–442, 1999.

[16] Ian Hunter, Richard Ranson, Andrew Guyette, and Alaa Abunjaileh. Microwave filter design from a systems perspective. *Ieee microwave magazine*, 8(5):71–77, 2007.

[17] John Oliver Scanlan and Ralph Levy. *Circuit theory*, volume 2. Oliver & Boyd, 1973.

[18] J David Rhodes. The design and synthesis of a class of microwave bandpass linear phase filters. *IEEE Transactions on Microwave Theory and Techniques*, 17(4):189–204, 1969.

[19] John David Rhodes. The generalized direct-coupled cavity linear phase filter. *IEEE Transactions on Microwave Theory and Techniques*, 18(6):308–313, 1970.

[20] Paul I Richards. Resistor-transmission-line circuits. *Proceedings of the IRE*, 36(2):217–220, 1948.

[21] Evaristo Musonda. *Synthesis of filters for digital wireless communications*. PhD thesis, University of Leeds, 2015.

[22] R Levy. A new class of distributed prototype filters with applications to mixed lumped/distributed component design. *IEEE Transactions on Microwave Theory and Techniques*, 18(12):1064–1071, 1970.

[23] Evaristo Musonda and Ian C Hunter. Exact design of a new class of generalized chebyshev low-pass filters using coupled line/stub sections. *IEEE Transactions on Microwave Theory and Techniques*, 63(12):4355–4365, 2015.

[24] ME Van Valkenburg. *Modern network synthesis*. Wiley, 1964.

[25] Franklin Kuo. *Network analysis and synthesis*. John Wiley & Sons, 2006.

[26] Ernst A Guillemin. Synthesis of passive networks: theory and methods appropriate to the realization and approximation problems. 1957.

[27] Nevzat Yildirim, Ozlem A Sen, Yakup Sen, Mehmet Karaaslan, and Dieter Pelz. A revision of cascade synthesis theory covering cross-coupled filters. *IEEE transactions on microwave theory and techniques*, 50(6):1536–1543, 2002.

[28] A Atia and A Williams. New types of waveguide bandpass filters for satellite transponders. *Comsat Tech. Review*, 1(1):20–43, 1971.

[29] R Baum. Design of unsymmetrical band-pass filters. *IRE Transactions on Circuit Theory*, 4(2):33–40, 1957.

[30] Richard J Cameron. Advanced filter synthesis. *IEEE Microwave Magazine*, 12(6):42–61, 2011.

[31] H Clark Bell. Canonical asymmetric coupled-resonator filters. *IEEE Transactions on Microwave Theory and Techniques*, 30(9):1335–1340, 1982.

[32] Erwin Kreyszig. Advanced engineering mathematics, 8-th edition, 1999.

[33] David M Pozar. *Microwave engineering*. John Wiley & Sons, 2009.

[34] Stefano Tamiazzo and Giuseppe Macchiarella. An analytical technique for the synthesis of cascaded n-tuplets cross-coupled resonators microwave filters using matrix rotations. *IEEE transactions on microwave theory and techniques*, 53(5):1693–1698, 2005.

[35] Giuseppe Macchiarella. Accurate synthesis of inline prototype filters using cascaded triplet and quadruplet sections. *IEEE transactions on microwave theory and techniques*, 50(7):1779–1783, 2002.

[36] G Matthaei, E Jones, and L Young. *Microwave Filters, Impedance-Matching Networks, and Coupling Structures (Artech Microwave Library)*. Norwood, MA, USA: Artech House, 1980.

[37] Raafat R Mansour. Filter technologies for wireless base stations. *IEEE Microwave Magazine*, 5(1):68–74, 2004.

[38] Dan Swanson and Giuseppe Macchiarella. Microwave filter design by synthesis and optimization. *IEEE Microwave Magazine*, 8(2):55–69, 2007.

[39] Milton Dishal. Alignment and adjustment of synchronously tuned multiple-resonant-circuit filters. *Proceedings of the IRE*, 39(11):1448–1455, 1951.

[40] Daniel G Swanson. Narrow-band microwave filter design. *IEEE Microwave magazine*, 8(5):105–114, 2007.

[41] Kenneth V Puglia. A general design procedure for bandpass filters derived from lowpass prototype elements: Part i. *Microwave journal - Euroglobal edition*, 43(12):22–38, 2000.

[42] Kenneth V Puglia. A general design procedure for bandpass filters derived from low pass prototype elements: Part ii. *Microwave journal - Euroglobal edition*, 44(1):114–137, 2001.

[43] J-S Hong. Couplings of asynchronously tuned coupled microwave resonators. *IEE Proceedings-Microwaves, Antennas and Propagation*, 147(5):354–358, 2000.

[44] John W Bandler, Radoslaw M Biernacki, Shao Hua Chen, Piotr A Grobelny, and Ronald H Hemmers. Space mapping technique for electromagnetic optimization. *IEEE Transactions on Microwave Theory and Techniques*, 42(12):2536–2544, 1994.

[45] John W Bandler, Radoslaw M Biernacki, Shao Hua Chen, Ronald H Hemmers, and Kaj Madsen. Electromagnetic optimization exploiting aggressive space mapping. *IEEE Transactions on Microwave Theory and Techniques*, 43(12):2874–2882, 1995.

[46] Mohamed H Bakr, John W Bandler, Kaj Madsen, and Jacob Søndergaard. Review of the space mapping approach to engineering optimization and modeling. *Optimization and Engineering*, 1(3):241–276, 2000.

[47] John W Bandler, Qingsha S Cheng, Sameh A Dakroury, Ahmed S Mohamed, Mohamed H Bakr, Kaj Madsen, and Jacob Sondergaard. Space mapping: the state of the art. *IEEE Transactions on Microwave theory and techniques*, 52(1):337–361, 2004.

[48] Giuseppe Macchiarella and Daniele Traina. A formulation of the cauchy method suitable for the synthesis of lossless circuit models of microwave filters from lossy measurements. *IEEE microwave and wireless components letters*, 16(5):243–245, 2006.

[49] RR Mansour and PD Laforge. Multiband superconducting filters. In *2016 IEEE MTT-S International Microwave Symposium (IMS)*, pages 1–4. IEEE, 2016.

[50] Lin-Chuan Tsai and Ching-Wen Hsue. Dual-band bandpass filters using equal-length coupled-serial-shunted lines and z-transform technique. *IEEE Transactions on Microwave Theory and Techniques*, 52(4):1111–1117, 2004.

[51] Jorge A Ruiz-Cruz, Mohamed M Fahmi, and Raafat R Mansour. Triple-conductor combline resonators for dual-band filters with enhanced guard-band selectivity. *IEEE Transactions on Microwave Theory and Techniques*, 60(12):3969–3979, 2012.

[52] Mustafa S Bakr, Saad WO Luhaib, Ian C Hunter, and Wolfgang Bosch. Dual-mode dual-band conductor-loaded dielectric resonator filters. In *2017 47th European Microwave Conference (EuMC)*, pages 908–910. IEEE, 2017.

[53] Yunchi Zhang, Kawthar A Zaki, Jorge A Ruiz-Cruz, and Ali E Atia. Analytical synthesis of generalized multi-band microwave filters. In *2007 IEEE/MTT-S International Microwave Symposium*, pages 1273–1276. IEEE, 2007.

[54] V Lunot, Stéphane Bila, and Fabien Seyfert. Optimal synthesis for multi-band microwave filters. In *2007 IEEE/MTT-S International Microwave Symposium*, pages 115–118. IEEE, 2007.

[55] Juseop Lee and Kamal Sarabandi. A synthesis method for dual-passband microwave filters. *IEEE Transactions on Microwave Theory and Techniques*, 55(6):1163–1170, 2007.

[56] Juseop Lee and Kamal Sarabandi. Design of triple-passband microwave filters using frequency transformations. *IEEE Transactions on Microwave Theory and Techniques*, 56(1):187–193, 2008.

[57] Giuseppe Macchiarella and Stefano Tamiazzo. Design techniques for dual-passband filters. *IEEE Transactions on Microwave Theory and Techniques*, 53(11):3265–3271, 2005.

[58] Fei Xiao. Direct synthesis technique for dual-passband filters: Superposition approach. *IEEE Transactions on Circuits and Systems II: Express Briefs*, 60(5):267–271, 2013.

[59] Evaristo Musonda and Ian Hunter. Synthesis of general chebyshev characteristic function for dual (single) bandpass filters. In *2015 IEEE MTT-S International Microwave Symposium*, pages 1–4. IEEE, 2015.

[60] Robert J Wenzel. Synthesis of combline and capacitively loaded interdigital bandpass filters of arbitrary bandwidth. *IEEE Transactions on Microwave Theory and Techniques*, 19(8):678–686, 1971.

[61] J Bingham. A new method of solving the accuracy problem in filter design. *IEEE Transactions on Circuit Theory*, 11(3):327–340, 1964.

[62] Gabor C Temes and Sanjit Kumar Mitra. Modern filter theory and design. *New York, Wiley-Interscience, 1973. 569 p*, 1973.

[63] H Orchard and G Temes. Filter design using transformed variables. *IEEE Transactions on Circuit Theory*, 15(4):385–408, 1968.

[64] H Bell. Transformed-variable synthesis of narrow-bandpass filters. *IEEE Transactions on Circuits and Systems*, 26(6):389–394, 1979.

[65] Ralph Levy. Synthesis of general asymmetric singly-and doubly-terminated cross-coupled filters. *IEEE transactions on microwave theory and techniques*, 42(12):2468–2471, 1994.

[66] Richard Woo. *Final report on RF voltage breakdown in coaxial transmission lines*. Jet Propulsion Laboratory, California Institute of Technology, 1970.

[67] J Rodney M Vaughan. Multipactor. *IEEE Transactions on electron devices*, 35(7):1172–1180, 1988.

[68] Seymour B Cohn. Design considerations for high-power microwave filters. *IRE Transactions on Microwave Theory and Techniques*, 7(1):149–153, 1959.

[69] Ming Yu. Power-handling capability for rf filters. *IEEE microwave magazine*, 8(5):88–97, 2007.

[70] JJ McCabe and RH Stone. Survey of high-power microwave filters. *IEEE Transactions on Aerospace and Electronic Systems*, (2):84–95, 1965.

[71] D Anderson, U Jordon, M Lisak, T Olsson, and M Ahlander. Microwave breakdown in resonators and filters. *IEEE transactions on microwave theory and techniques*, 47(12):2547–2556, 1999.

[72] L Young. Peak internal fields in direct-coupled-cavity filters. *IRE Transactions on Microwave Theory and Techniques*, 8(6):612–616, 1960.

[73] Christooph Ernst and Vasil Postoyalko. Prediction of peak internal fields in direct-coupled-cavity filters. *IEEE Transactions on Microwave Theory and Techniques*, 51(1):64–73, 2003.

[74] Christoph Ernst, Vasil Postoyalko, and Nafizah G Khan. Relationship between group delay and stored energy in microwave filters. *IEEE Transactions on Microwave Theory and Techniques*, 49(1):192–196, 2001.

[75] Apu Sivadas, Ming Yu, and Richard Cameron. A simplified analysis for high power microwave bandpass filter structures. In *2000 IEEE MTT-S International Microwave Symposium Digest (Cat. No. 00CH37017)*, volume 3, pages 1771–1774. IEEE, 2000.

[76] Chi Wang and Kawthar A Zaki. Analysis of power handling capacity of band pass filters. In *2001 IEEE MTT-S International Microwave Sympsoium Digest (Cat. No. 01CH37157)*, volume 3, pages 1611–1614. IEEE, 2001.

[77] Christoph Ernst and Vasil Postoyalko. Comparison of the stored energy distributions in a qc-type and a tc-type prototype with the same power transfer function. In *1999 IEEE MTT-S International Microwave Symposium Digest (Cat. No. 99CH36282)*, volume 3, pages 1339–1342. IEEE, 1999.

[78] Christoph Ernst, Vasil Postoyalko, Richard Parry, and Ian Hunter. Filter topologies with minimum peak stored energy. In *2001 IEEE MTT-S International Microwave Sympsoium Digest (Cat. No. 01CH37157)*, volume 3, pages 1631–1634. IEEE, 2001.

[79] BS Senior, IC Hunter, V Postoyalko, and R Parry. An optimised network topology to minimise e-fields occuring in coaxial resonator filters. In *2002 32nd European Microwave Conference*, pages 1–4. IEEE, 2002.

[80] James MacQueen et al. Some methods for classification and analysis of multivariate observations. In *Proceedings of the fifth Berkeley symposium on mathematical statistics and probability*, volume 1, pages 281–297. Oakland, CA, USA, 1967.

[81] Gareth James, Daniela Witten, Trevor Hastie, and Robert Tibshirani. *An introduction to statistical learning*, volume 112. Springer, 2013.

[82] Anil K Jain. Data clustering: 50 years beyond k-means. *Pattern recognition letters*, 31(8):651–666, 2010.

[83] Zhexue Huang. Extensions to the k-means algorithm for clustering large data sets with categorical values. *Data mining and knowledge discovery*, 2(3):283–304, 1998.

[84] Zhexue Huang. A fast clustering algorithm to cluster very large categorical data sets in data mining. *DMKD*, 3(8):34–39, 1997.

[85] Peter J Rousseeuw. Silhouettes: a graphical aid to the interpretation and validation of cluster analysis. *Journal of computational and applied mathematics*, 20:53–65, 1987.

[86] Christoph Ernst. *Energy Storage in Microwave Cavity Filter Networks*. PhD thesis, The University of Leeds, 2000.